The non-linear regime of quantum chromodynamics in the context of relativistic heavy-ion collisions

---

Pablo Guerrero Rodríguez

Universidad de Granada
Programa de Doctorado en Física y Ciencias del Espacio

Advisor: Prof. Javier López Albacete

Universidad de Granada
Departamento de Física Teórica y del Cosmos & CAFPE

Editor: Universidad de Granada. Tesis Doctorales
Autor: Pablo Guerrero Rodríguez
ISBN: 978-84-1306-335-5
URI: http://hdl.handle.net/10481/57446

El trabajo presentado en esta memoria de tesis ha sido financiado parcialmente por la beca FP7-PEOPLE-2013-CIG de la comisión europea (referencia QCDense/631558), así como por el proyecto FPA2016-78220 concedido por el Ministerio de Economía, Industria y Competitividad. La segunda mitad del proyecto fue financiado por la beca 'Posgrado en Europa' de la fundación bancaria La Caixa.

Resumen

Entre los principales problemas abiertos en QCD está el de la comprensión de las interacciones fuertes en el régimen de muy alta energía de colisión. Argumentos teóricos fundamentales relacionados con la unitariedad de la teoría y avalados por diversos estudios empíricos indican que a muy altas energías la descripción estándar (basada en teoremas de factorización colineal) deja de ser válida. En su lugar se entra en un régimen de muy altas densidades de gluones y campos de color intensos gobernado por efectos no lineales, tales como la recombinación de gluones. Dicho régimen –conocido como *régimen de saturación* de QCD– tiene especial relevancia en la descripción de colisiones de iones pesados a muy altas energías. Este tipo de experimentos son realizados en la actualidad en dos aceleradores de partículas: el Relativistic Heavy Ion Collider (RHIC) y el Large Hadron Collider (LHC). El análisis del enorme volumen de datos obtenido en estas instalaciones proporciona información fundamental sobre el sistema generado en estas colisiones. En particular, estos análisis sugieren la formación de un fluido caracterizado por temperaturas y densidades extremadamente altas, en el que los grados de libertad fundamentales de QCD –quarks y gluones– no dan muestras de confinamiento. Este estado se denomina plasma de quarks y gluones (QGP).

El estudio de la generación, expansión y desintegración de esta sustancia plantea numerosos retos a nuestro actual conocimiento de QCD. De hecho, uno de los obstáculos principales lo plantea la descripción del estado inicial del sistema (inmediatamente después de la colisión). Esta tarea requiere, por una parte, un conocimiento profundo de las funciones de onda nucleares en los instantes previos a la colisión, y por la otra, una descripción precisa de los múltiples procesos de colisión que le siguen. El enfoque típico a este problema se basa en el uso de modelos fenomenológicos diseñados para generar condiciones iniciales para simulaciones Monte Carlo del QGP. Dichos modelos se definen en base a una serie de parámetros cuyos valores numéricos son deducidos a partir de comparaciones con datos experimentales. No obstante, los valores extraídos mediante esta estrategia pueden llegar a variar ampliamente de un modelo a otro. Esta discrepancia genera una gran incertidumbre tanto en la precisión como en la interpretación de los estudios fenomenológicos del QGP.

No obstante, el hecho de que los núcleos colisionados son sistemas profundamente *saturados* brinda la oportunidad de realizar cálculos analíticos basados en métodos de la teoría de perturbaciones de QCD. La densidad de gluones que caracteriza a estos núcleos los hace aptos para una descripción mediante aproximaciones semiclásicas, en las que representamos los gluones mediante distribuciones aleatorias de campos de color (modelo de McLerran-Venugopalan, MV). Las correcciones cuánticas a este modelo son introducidas por un conjunto de ecuaciones de renormalización, las ecuaciones B-JIMWLK, que permiten obtener la evolución de la estructura hadrónica a valores decrecientes de la variable x de Bjorken (equivalentemente, a energías de colisión crecientes y escalas de momento transversas moderadas). Las ecuaciones B-JIMWLK incluyen efectos de emisión de gluones así como posibles efectos de recombinación gluónica, de naturaleza no lineal y relevantes en condiciones de alta densidad de gluones. Estos elementos se engloban dentro de la teoría efectiva Color Glass Condensate (CGC), que proporciona el marco teórico adecuado para estudiar QCD a muy altas energías de colisión y altas densidades de gluones.

La teoría CGC ha sido abundantemente empleada en la descripción de la fase inicial de colisiones de iones pesados. El sistema físico presente durante esta etapa se denomina Glasma, y supone un paso intermedio entre la colisión y la generación del QGP. Debido al carácter inherentemente aleatorio de la colisión, las propiedades físicas del Glasma fluctúan de evento a evento, lo que ha demostrado ser

un aspecto fundamental en la descripción de la formación y expansión del QGP. Estas fluctuaciones son, por tanto, una de las características básicas que los modelos fenomenológicos mencionados anteriormente tratan de reproducir. Una de las prestaciones principales del CGC es que proporciona herramientas analíticas para la descripción cuantitativa de fluctuaciones de evento a evento. Esto se lleva a cabo mediante el cálculo de correladores, definidos como promedios sobre el 'ruido ambiental' generado por las distribuciones aleatorias de campos de color clásicos. Esta descripción teórica del estado inicial, exclusivamente basada en principios fundamentales de QCD, puede ser aplicada como condición inicial de las simulaciones Monte Carlo utilizadas en fenomenología del QGP.

El objetivo principal de esta tesis es profundizar y mejorar nuestra comprensión del régimen de saturación de QCD. Abordamos esta tarea en el contexto de dos problemas fundamentales: la descripción teórica de la fase inicial de las colisiones de iones pesados, y el análisis fenomenológico de producción de partículas en experimentos de aceleradores. Nuestros estudios se basan en el formalismo CGC, el cual extendemos y modificamos a lo largo del desarrollo de la tesis. Con nuestras modificaciones aspiramos a conseguir una descripción más realista de los sistemas físicos implicados, y al mismo tiempo ampliar las potenciales aplicaciones de nuestros resultados a estudios fenomenológicos del QGP.

Empezamos realizando un cálculo analítico de los correladores de uno y dos puntos del tensor energía-momento correspondiente al Glasma. Estos objetos caracterizan la media y la varianza de la distribución de densidad de energía generada inmediatamente después de la colisión. En este cálculo asumimos una dependencia explícita en el parámetro de impacto, lo que nos permite describir colisiones entre núcleos finitos. Además, prescindimos de la asunción de interacciones locales en el plano transversal al eje de colisión. Estos aspectos de nuestro cálculo suponen una generalización del modelo MV. Sin embargo, una de las cualidades más importantes de nuestro enfoque es el hecho de que *no* aplicamos las aproximaciones más extendidas en este tipo de estudios. Concretamente, en nuestro cálculo prescindimos de la aproximación *Glasma Graph*, actualmente establecida como paso esencial de la implementación práctica del modelo MV. Nuestro planteamiento implica asumir una serie de importantes complejidades técnicas originadas en el carácter intrínsecamente no lineal del Glasma.

Aplicamos esta misma estrategia a otra propiedad fundamental del Glasma: la posibilidad de generación de carga axial a partir de fluctuaciones de evento a evento. En el contexto del CGC, la descripción cuantitativa de esta cualidad implica el cálculo del correlador de dos puntos de la divergencia de la corriente Chern-Simons.

En los resultados de ambos estudios observamos una notable discrepancia con respecto a los cálculos realizados a partir de la aproximación Glasma Graph. Concretamente, nuestros resultados predicen correlaciones de (relativamente) largo alcance en el plano transversal, lo cual podría entrar en conflicto directo con las hipótesis comúnmente adoptadas por la comunidad. Las expresiones obtenidas en esta tesis admiten una aplicación directa en numerosos estudios fenomenológicos del QGP, lo cual supone un potencial impacto tanto en sus resultados numéricos como su interpretación.

En las secciones fenomenológicas de esta tesis exploramos la influencia del régimen de saturación de QCD en el estudio de procesos de producción de partículas en el LHC. Concretamente, realizamos un análisis de los datos de producción inclusiva de piones neutros obtenidos por la colaboración LHCf. Estos datos son medidos en la región de rapidities ultra-altas de colisiones protón-protón y protón-núcleo a alta energía. Dicha región cinemática es sensible tanto al sector *diluido* de QCD como al régimen de saturación. Para nuestro análisis empleamos un código Monte Carlo que incorpora, por una parte, una descripción de colisiones a nivel partónico basada en el *formalismo híbrido* del CGC, y por la otra, una implementación del proceso de hadronización en el marco del modelo de fragmentación de Lund. Nuestro planteamiento incluye, además, una descripción de la dependencia con la energía de colisión basada en las ecuaciones de evolución no lineales del CGC. Esta estrategia resulta en un notable acuerdo entre modelo y datos, lo que supone una clara indicación de la importancia de la física de saturación para la descripción de interacciones entre núcleos diluidos y densos.

Los contenidos de esta tesis están basados en los siguientes artículos:

- [1] J.L.Albacete, Yasushi Nara y P.G.R., "Ultra-forward particle production from CGC+Lund fragmentation", Physical Review D Volumen 94 (2016) tomo 5, 054004.
- [2] J.L.Albacete, Cyrille Marquet y P.G.R., "Initial correlations of the Glasma energy-momentum tensor", Journal of High Energy Physics 1901 (2019) 073.
- [3] P.G.R., "Topological charge fluctuations in the Glasma", aceptado para publicación en Journal of High Energy Physics.

Contents

Resumen **7**

I Introduction **13**

II Quantum Chromodynamics of Heavy Ion Collisions **18**

1 ABCs of QCD **19**
1.1 The QCD Lagrangian 19
1.2 Running coupling 21
1.3 Deep Inelastic Scattering, the parton model 21

2 Linear evolution equations **25**
2.1 DGLAP evolution 25
2.2 BFKL evolution 29
2.3 Breakdown of linear evolution, saturation 30

3 The Color Glass Condensate **33**
3.1 The McLerran-Venugopalan model 33
3.2 Non-linear evolution equations 35

4 Heavy ion collisions: The Quark Gluon Plasma **37**
4.1 The QCD phase diagram 37
4.2 Experimental signatures of QGP 38
4.2.1 Strangeness enhancement 39
4.2.2 Quarkonium suppression 39
4.2.3 Jet quenching 40
4.2.4 Anisotropic collective flow 41
4.3 Stages of a heavy ion collision 42
4.4 Initial state of HICs 43
4.5 What about thermalization? 45

5 The topological structure of QCD **47**
5.1 The chiral symmetry 48
5.2 The chiral anomaly 51
5.3 Topological charge fluctuations 51
5.4 Axial charge generation in HICs 52

III Theoretical characterization of the Glasma phase **54**

6 Solution of the Yang-Mills equations at $\tau = 0^+$ **55**
6.1 Gluon fields carried by a single nucleus 56

6.2 Glasma fields at $\tau = 0^+$ . . . 60

7 Early properties of the Glasma 65
7.1 The Energy-Momentum Tensor of Glasma at $\tau = 0^+$ . . . 65
7.2 The Divergence of the Chern-Simons current at $\tau = 0^+$ . . . 67

IV Early correlations of the Glasma 69

8 Energy density fluctuations of the Glasma 70
8.1 The EMT one-point correlator in the MV model . . . 70
8.2 The EMT two-point correlator in the MV model . . . 74
8.2.1 Correlators of n Wilson lines and m external color sources . . . 74
8.2.2 The connected function . . . 77
8.2.3 The disconnected function . . . 81
8.2.4 The correlator of four Wilson lines in the adjoint representation . . . 84
8.2.5 Connected and disconnected functions (revisited) . . . 90
8.2.6 Covariance of the Glasma energy density . . . 92
8.2.7 N_c-expansion in the MV model . . . 94

9 Topological charge fluctuations of the Glasma 98
9.1 One-point correlator of the divergence of the Chern-Simons current . . . 98
9.2 Two-point correlator of the divergence of the Chern-Simons current . . . 98
9.2.1 N_c-expansion . . . 100

10 Comparison with previous results 102

V Color Glass Condensate phenomenology 106

11 Ultra-forward particle production in CGC 107
11.1 CGC description of high energy multiparticle production . . . 107
11.2 The hybrid formalism . . . 110
11.3 Multiple parton scattering . . . 112
11.4 The Lund fragmentation model . . . 113
11.5 Inclusive hadron transverse momentum spectra at RHIC . . . 114
11.6 Inclusive hadron transverse momentum spectra at LHCf . . . 115
11.7 Nuclear modification factor at LHCf . . . 116

VI Conclusions and prospects 123

Conclusiones 127

A Light-cone coordinates 131

B Comoving coordinates 133

C Kinematics of DIS **135**

D Derivation of the Wilson Line **137**

E Transverse differentiation of Wilson lines **139**

F Calculation of chromo-electric and -magnetic fields **141**

G Identities relating Wilson line representations **142**

H Operations involving the 2-D Laplacian Green's function **144**

I Baryon production models **149**

Part I

Introduction

You're probably wondering why I'm here (and so am I, so am I)
— Frank Zappa in "You're Probably Wondering Why I'm Here"

Our current understanding of physical phenomena is formulated in terms of four fundamental interactions: electromagnetic, gravitational, weak and strong. These are assumed to be the most basic forces of nature, dictating its behavior and structure at any scale. Throughout history, the ever-growing precision and reach of experimental techniques have motivated the development of increasingly sophisticated theories seeking to describe these interactions. For instance, the observation of magnetic induction inspired the unification of electric and magnetic forces, embodied in Maxwell's equations. Half a century later, the Michelson-Morley experiment ruled out the existence of the ubiquitous ether implicit in said equations, leading Einstein to devise the theory of special relativity. This was the first step towards the formulation of general relativity, which provides the modern description of the gravitational force.

Similarly, in the case of strong interactions the advent of new experimental facilities and detection techniques has been a decisive driving force of theoretical advances. Back in the 1930s, the strong interaction was postulated as the one responsible of binding together the constituents of atomic nuclei (protons and neutrons), then believed to be fundamental particles. An early effort to describe this force was made in 1935 by Hideki Yukawa, who proposed a mechanism based on the exchange of massive particles called mesons (analogous to the role played by photons in electromagnetism). The massive character of the mediating particles explained the short range of the interaction. This theory was accepted and applied with relative success until the early 1960s, when the devising of new detectors (spark and bubble chambers) gave rise to the discovery of an overwhelming amount of particles both in accelerators and cosmic ray observatories. The sheer volume of data inspired a discussion on whether the new particles, known as hadrons, were all fundamental or rather bound states of smaller components. This line of research resulted in the formulation of the quark model (proposed independently by Murray Gell-mann and George Zweig in 1964), which states that the most fundamental degrees of freedom are not hadrons but point-like particles called quarks and gluons. In the late 1960s, the first Deep Inelastic Scattering experiments performed at the Stanford Linear Accelerator Center (SLAC) provided experimental evidence of the existence of quarks[1]. In the early 1970s, the study of the interactions between quarks and gluons (generically called partons) adopted the relativistic quantum field formalism previously applied to Quantum Electrodynamics (QED), thus becoming the theory known as Quantum Chromodynamics. This was the last piece to be incorporated to the Standard Model paradigm, which provides a common framework for the description of the electromagnetic, weak and strong interactions.

Quantum Chromodynamics (QCD) states that the property determining the strength of partonic interactions –analogous to mass in gravity or electric charge in electromagnetism– is color charge. The carriers of color charge are the fundamental degrees of freedom of the theory: quarks and gluons. Quarks are fermions with fractional electric charge and a mass range that goes from very light (10 MeV for up and down quarks) to very heavy (around 175 GeV for top), and gluons are massless bosons that mediate the interaction between quarks. In addition to these basic aspects, QCD exhibits a series of highly non-trivial features, some of them still not fully understood to this day. One is the fact that strong interactions seem to 'forbid' the existence of asymptotic colored states. This is known as color confinement, and it implies that we can not observe isolated partons. Instead, they always appear to be confined in colorless objects: the hadrons. Another essential property of QCD is asymptotic freedom, which is the decrease of the strong coupling constant in

---

[1] The discovery of all fundamental degrees of freedom of the quark model had to wait until 1979, when the electron-positron collisions performed at the Deutsches Elektronen-Synchrotron (DESY) provided evidence for the existence of gluons.

interactions taking place over small distances. Thanks to this feature, processes dominated by large enough momentum transfers (and thus governed by small distance phenomena) can be appropriately described by means of perturbative methods. These have proven hugely successful in describing experimental data from processes such as Deep Inelastic Scattering at moderate Bjorken-x, Drell-Yan annihilation and jet production with great accuracy. In contrast, interactions characterized by low momentum exchanges feature a large coupling constant[2], thus making perturbation theory inapplicable. This poses serious limitations to the description of hadronic structure, as it is largely determined by long range phenomena (over distances of the order of the proton size).

Fortunately, there are ways to work around this obstacle. Although a first-principles analytical description of hadronic structure has proven elusive thus far, perturbative techniques can be successfully applied to describe its *evolution*, namely the way it transforms as we vary the resolution scales at which we observe it. Such observation can be performed through the aforementioned Deep Inelastic Scattering (DIS) experiment, which directly probes the partonic degrees of freedom with a resolution scale roughly proportional to the inverse of the collision energy (under certain conditions). DIS provides a snapshot of hadronic structure that serves as starting point for the application of perturbative renormalization group equations. The simplest and most widely used in practical applications are the ones that describe evolution through linear radiation processes (i.e. DGLAP, BFKL equations). However, they become inadequate at high energies, predicting a fast increase of gluons that leads to the violation of unitarity. In this limit, nucleons become highly dense systems where the possibility of gluon recombination processes must be taken into account. This is achieved through the introduction of non-linear terms in the evolution equations, which have the effect of taming the unphysical gluon growth in the hadronic wave function. Apart from playing a key role in the consistency of the theory[3], these non-linearities also have a great impact in the phenomenology of research areas such as heavy ion physics and (potentially) ultra-high energy cosmic rays[4].

The dynamical regime dominated by large gluon densities and non-linear phenomena –referred to as the gluon saturation regime of QCD– is relevant in the description of highly energetic Heavy Ion Collisions (HICs). Currently there are two particle accelerators conducting this kind of experiments: the Relativistic Heavy Ion Collider (RHIC) and the Large Hadron Collider (LHC). The vast volume of HICs data collected in these facilities has provided striking evidence of collective phenomena at macroscopic scales. These observations hint at the emergence of a highly dense and extremely hot state of matter where quarks and gluons appear to be deconfined. This is known as the Quark Gluon Plasma (QGP). Virtually every stage of the generation, expansion and decay of this substance poses serious qualitative and quantitative challenges to our understanding of QCD. In fact, one of the main obstacles lies in the characterization of the very initial state of HICs, as it requires precise knowledge of the nuclear wave functions prior to the collision and the multiple scattering processes

---

[2] Note that this property (often referred to as *infrared slavery*) is not a sufficient explanation for confinement. As will be detailed later, the former can be theoretically obtained through the calculation of the beta function that describes the running of the QCD coupling parameter, while the latter is a non-refuted hypothesis that states that only color singlets can be observed in nature.

[3] The introduction of non-linear dynamics in evolution successfully removes unphysical results in the computation of forward scattering amplitudes. However, it does not completely solve the problem, as the predicted total cross section still grows more rapidly than allowed by unitarity. It is likely that non-perturbative effects are partially responsible for this violation. However, this falls out of the scope of this thesis.

[4] Given the high energy scales involved in the collisions between these astroparticles and the atmosphere, it has been proposed that the study of the non-linear regime of QCD might be applicable to their detection and characterization. However, this is currently a subject open to debate.

that take place immediately after. A typical approach to this problem relies on the use of a broad variety of phenomenological models that provide initial conditions for Monte Carlo simulations of the expanding QGP. The numerical values of the parameters required as input by these models are constrained by agreement with data, sometimes varying largely from one model to another. Such discrepancy introduces a significant amount of uncertainty in both the precision and physical interpretation of most phenomenological studies of the expansion and cooling of QGP.

Nevertheless, the fact that the colliding nuclei are deeply saturated objects provides the opportunity to perform analytical, first-principles calculations based on perturbative methods. As will be detailed later, such systems allow for a description by means of a semi-classical approximation where gluons are represented by randomly distributed background color fields (McLerran-Venugopalan model). Quantum corrections to the classical fields are introduced by perturbative non-linear evolution equations (the B-JIMWLK equations). This approach is proposed within an effective theory that approximates QCD at high energies and densities: the Color Glass Condensate (CGC).

The CGC framework has been extensively applied in the description of the early, non-equilibrium stage of HICs, known as Glasma. Because of the inherently random nature of the positions and partonic content of the colliding nucleons, the Glasma phase is characterized by event-by-event fluctuations of the energy and momentum deposited in the collision area. This feature has been shown to play a key role in the formation and expansion of QGP, and thus it is one of the aspects that the aforementioned phenomenological models seek to reproduce. A main feature of the CGC framework is that it provides analytical tools to describe the early event-by-event fluctuations. These can be quantified through the calculation of correlators, defined as functional averages of observables over the background color fields. This first-principles characterization of the initial state, purely based on QCD interactions, can be used as an analytical input to the hydrodynamical simulations employed in QGP phenomenology.

In a broad sense, the main goal of this thesis is to improve and deepen our understanding of the saturation regime of QCD. With this aim in mind, we perform a study of the dynamical behavior of the Glasma fields that populate the earliest stages of HICs. This phase emerges from multiple interactions between the constituents of two deeply saturated nuclei, which can be described by means of the CGC effective theory. Within this framework we study a series of physical features of Glasma through the statistical properties of its event-by-event fluctuations. Specifically, we analyze the average and variance of the energy, momentum, and topological charge distributions (respectively computed within CGC as the one- and two-point correlators). We do so in a complete analytical approach that entails a significant step beyond the standard approximations adopted for this kind of calculations. In addition, we employ an extended version of our calculation framework with the aim of expanding the possibilities for phenomenological applications. After discussing in detail these theoretical studies, we explore the impact of saturation physics in the analysis of multiparticle production in RHIC and LHC. To this end, we focus on the ultra-forward rapidity region of the spectra, sensitive to both dilute and saturated regimes of QCD. Our analysis relies in a Monte Carlo event generator that combines a CGC-based treatment of elementary parton scatterings with a well-established implementation of the hadronization process.

This report is organized by chapters arranged in separate parts. The chapters included in Part II deepen into the essential aspects of QCD, emphasizing those that are more relevant to the calculations and results presented in subsequent sections (such as small-x physics, the QGP, and the topological structure of QCD). Special attention is paid to the CGC effective theory (introduced in

Chapter 3), which comprises the basic principles and techniques extensively applied and built upon throughout the thesis. In Part III this framework is employed in the theoretical characterization of the system generated right after a high energy collision of large nuclei. The results reached here serve as a starting point for Part IV, which deals with the fluctuating behavior of the energy density and topological charge distributions originated in the early phase of the collision. The conclusions and future prospects are presented in Part VI. Throughout the development of this thesis a number of outstanding technical challenges were faced, some of them posing too much of a detour from the general lines of the report. These problems are analyzed in depth in the appendices section.

Part II

Quantum Chromodynamics of Heavy Ion Collisions

The universe works on a math equation that never even ever really even ends in the end...

— Modest Mouse in “Never Ending Math Equation”

In the following chapters we briefly discuss some of the fundamental aspects of QCD, emphasizing those that are more relevant to high energy collisions and heavy ion phenomenology. The present section is not, by any means, an exhaustive review of QCD or the vast body of experimental results that sustains it. Rather, the goal of this part is to provide –to the extent possible– a self-contained description of the concepts and techniques that will be applied throughout the rest of the thesis. Such concepts include, but are not limited to, the small-x regime of QCD, the McLerran-Venugopalan model, the CGC effective theory, the Glasma state, and the QGP. For a more detailed and general overview of QCD the reader is referred to [4].

Chapter 1

ABCs of QCD

Before introducing the theoretical core of this thesis (presented in Chapter 3), in this and the following sections we will unfold the path that leads from the very basics of QCD to the onset of the gluon saturation regime. Note that in the ensuing discussion we intentionally leave out color confinement, rather focusing on those properties that have thus far been inferred from (or successfully embedded into) the analytical body of the theory.

1.1 The QCD Lagrangian

QCD is a non-Abelian gauge theory based on the symmetry group $SU(N_c)$ with $N_c=3$. Its fundamental degrees of freedom are point-like, spin-1/2, massive particles called quarks; and massless vector bosons (with spin 1) called gluons. Their dynamics are encoded in the following Lagrangian density:

$$\mathcal{L}_{\text{QCD}} = \sum_f \bar{\psi}_{f,i}(i\gamma_\mu D^\mu_{ij} - m_f\delta_{ij})\psi_{f,j} - \frac{1}{4}F^a_{\mu\nu}F^{\mu\nu,a}, \tag{1.1}$$

which we refer to as the *classical* QCD Lagrangian (as we are omitting the gauge fixing and Faddeev-Popov ghost terms). The first term contains the quark and antiquark fields, which are summed over the flavor index f. This index takes six values corresponding to the known quark flavors $f=u,d,s,c,b,t$, each one characterized by a certain quark mass m_f and a four-component Dirac spinor $\psi_{f,j}$ ($\bar{\psi}_{f,i}$ for the antiquarks). These fields belong to the fundamental representation of $SU(3)$ and thus are labeled by the color indices $i,j=1,...,N_c=3$ (typically dubbed as red, green and blue). The gluons, represented by the gauge fields $A^{\mu,a}$, enter the Lagrangian through the covariant derivative:

$$D^\mu_{ij} = \delta_{ij}\partial^\mu + igt^a_{ij}A^{\mu,a} \tag{1.2}$$

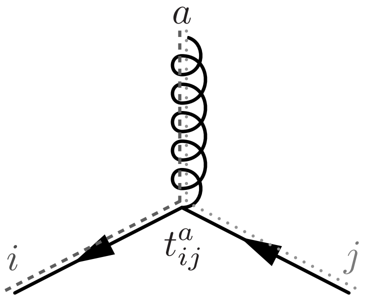

Figure 1.1: Diagrammatic representation of the color charge flow in a gluon-quark vertex.

and the gluon field strength tensor:

$$F^{\mu\nu,a} = \partial^\mu A^{\nu,a} - \partial^\nu A^{\mu,a} - g f^{abc} A^{\mu,b} A^{\nu,c}. \tag{1.3}$$

Here, g is the QCD coupling constant and the matrices t^a_{ij} are the $SU(3)$ generators in the fundamental representation. The structure constants f^{abc} determine the Lie algebra of the group, defined by the commutation relation $[t^a, t^b] = i f^{abc} t^c$. They also serve as generators of the adjoint representation of $SU(3)$, which is where the gluon fields $A^{\mu,a}$ are defined (the color index a thus taking values from 1 to $N_c^2 - 1 = 8$).

A fundamental difference between QED and QCD lies in the fact that the mediating particles of the latter do carry color charge, whereas photons are electrically neutral. Specifically, gluons transport color and anti-color charges, which can be inferred from the quark-gluon interaction vertex brought in by the covariant derivative. One can interpret the emission (or absorption) of a gluon to induce a 'shift' in the color of a quark from j to i (as represented in Fig. 1.1). This feature emerges from the non-Abelian character of $SU(3)$, which also gives rise to gluonic self-interactions in the last term of Eq. (1.1). Said term, known as the Yang-Mills Lagrangian, encodes the dynamics of a theory that contains only gluons.

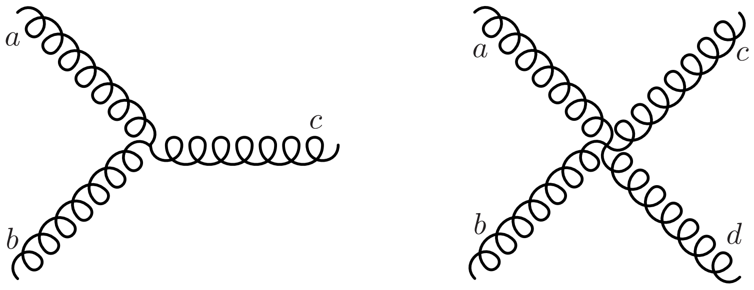

$$-\frac{g^2}{2} f^{abc} (\partial^\mu A^{\nu,a} - \partial^\nu A^{\mu,a}) A^b_\mu A^c_\nu \qquad -\frac{g^2}{4} f^{abe} f^{cde} A^a_\mu A^b_\nu A^{\mu,d} A^{\nu,c}$$

Figure 1.2: Diagrammatic representation of the 3-gluon and 4-gluon vertices that result from substituting Eq. (1.3) into the Yang-Mills Lagrangian.

1.2 Running coupling

QCD is a renormalizable theory and, as such, the value of its coupling 'constant' depends on the momentum scale Q at which the interaction takes place. This dependence is described by the beta function:

$$Q^2 \frac{\partial \alpha_s}{\partial Q^2} = \beta(\alpha_s) = -\beta_0 \alpha_s^2 (1 + \beta_1 \alpha_s + \beta_2 \alpha_s^2 + ...), \tag{1.4}$$

where $\alpha_s = g^2/4\pi$ is defined as a strong 'fine structure' constant in analogy with QED. After the second equality we show a perturbative expansion whose terms are obtained by computing loop corrections to the gluon propagator. The aforementioned self-couplings of the gluon fields (represented in Fig. 1.2) play a crucial role in this calculation, as the loops that include these vertices make a positive contribution to the beta function. Physically, this suggests an anti-screening scenario –as the spatial resolution increases (corresponding to smaller momentum exchanges), the interaction becomes more sensitive to gluonic fluctuations in the vacuum, which have the effect of 'enhancing' the fundamental color charges. This phenomenon competes with quark-antiquark fluctuations, which yield a color screening effect and thus make a negative contribution to the beta function. This constitutes yet another fundamental difference with QED, where only negative contributions (electron-positron fluctuations, known as vacuum polarization effects) are present at leading order. Considering all one-loop corrections in a theory with N_c colors and N_f active flavors (i.e. those that can be assumed as massless at the scale Q^2), the running of the coupling constant yields:

$$\alpha_s(Q^2) = \frac{4\pi}{\beta_0 \ln\left(Q^2/\Lambda^2_{\text{QCD}}\right)} = \frac{12\pi}{(11N_c - 2N_f)\ln\left(Q^2/\Lambda^2_{\text{QCD}}\right)}. \tag{1.5}$$

This expression yields a renormalized coupling constant α_s that decreases as the momentum transfer grows (as can be seen in Fig. 1.3). The renormalization mechanism introduces a scale Λ_{QCD} at which our perturbative expansion Eq. (1.4) loses validity. It is experimentally extracted to be of the order of the typical hadronic size, $\Lambda_{\text{QCD}} \approx 200$ MeV.

Eq. (1.5) implies that at high enough energies ($Q \gg \Lambda_{\text{QCD}}$) QCD is a weakly coupled theory and thus amenable to be approximated via perturbative techniques. This property, known as asymptotic freedom, comes in quite handy for the study of high energy collisions, which is –in a broad sense– the main topic of this thesis. However, Eq. (1.5) also poses a fundamental problem, namely that the long distance phenomena that dictates hadronic structure can not in principle be described perturbatively. As any given hadronic collision experiment is sensitive to both perturbative and non-perturbative processes, we need to be able to 'separate' them in such a way that a systematic, analytical study is possible. This is the main feature (and, in some cases, assumption) of factorization schemes such as collinear factorization, primarily applied in the description of DIS processes.

1.3 Deep Inelastic Scattering, the parton model

In a DIS process (represented in Fig. 1.4) we probe the partonic content of a hadron h through its interaction with a lepton, which to first order is described as the exchange of a single virtual vector boson (γ, $W^{\pm}$ or Z^0) carrying a momentum q. The spatial resolution scale of such a probe can be estimated from the uncertainty principle as $\lambda \sim 1/Q$, where $Q^2 = -q^2 > 0$ is defined as its *virtuality*.

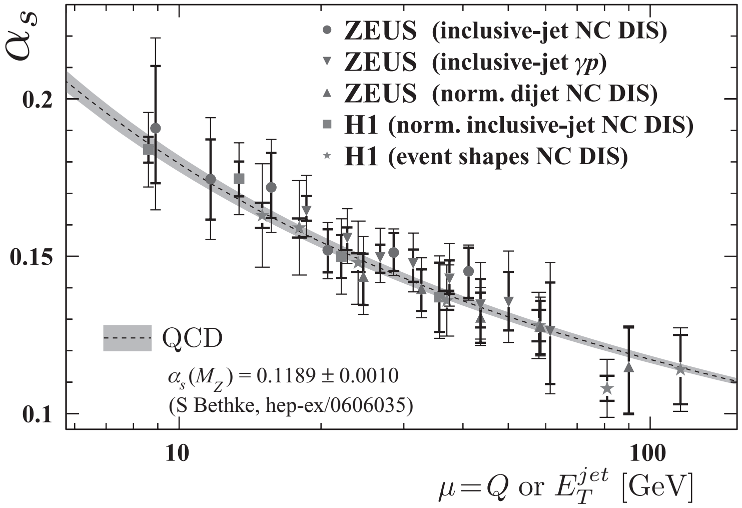

Figure 1.3: Compilation of α_s extractions from DIS experiments at HERA. The dashed line corresponds to the theoretically predicted values. Depending on the specific final states observed, the corresponding data points are obtained as functions of the momentum exchange Q or the energy carried by groups of hadrons sprayed from the collision (jets). Figure extracted from [5].

In a DIS process the virtuality of the exchanged particle greatly exceeds the mass of the struck hadron, $Q^2 \gg m_h^2$, which allows us to resolve its partonic constituents. This interaction results in the fragmentation of the hadron, whose scattered pieces are recombined (through a highly non-trivial process known as hadronization) into a new hadronic system that we denote by X. These final states are integrated out, as we only measure the energy and recoil angle of the scattered lepton (we will focus on inclusive DIS processes).

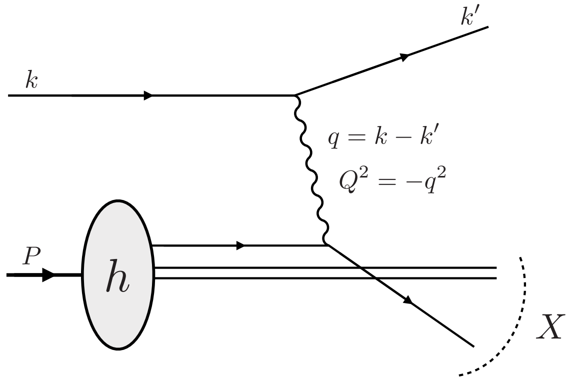

Figure 1.4: Diagrammatic representation of a DIS.

Typically, the two main independent Lorentz invariant quantities used to characterize DIS processes are the virtuality Q^2 and the Bjorken-x variable, defined as:

$$x = \frac{Q^2}{2P \cdot q}\,, \tag{1.6}$$

where P is the momentum of the incoming hadron. This variable quantifies the inelasticity of the process and can be roughly related to the time resolution of the probe, $\Delta t \sim 1/x$. For convenience we will also define the following quantity:

$$y = \frac{P \cdot q}{P \cdot k}\,, \tag{1.7}$$

which (in the rest frame of the hadron) corresponds to the fractional energy loss of the incoming lepton. In order to connect this discussion with experimental results, we will henceforth focus on the particular case where the interaction happens between an electron and a proton via a virtual photon exchange. Using the set of variables presented above (and considering the limit $Q^2 \gg m^2 y^2$), we can write the inclusive double differential cross section of DIS as:

$$\frac{d^2\sigma^{e^- P \to e^- X}}{dx\, dQ^2} = \frac{4\pi\alpha^2}{Q^4}\left[F_1\left(x,\, Q^2\right)\left(1 + (1-y)^2\right) + \left(F_2\left(x,\, Q^2\right) - 2xF_1\left(x,\, Q^2\right)\right)\left(\frac{1-y}{x}\right)\right], \tag{1.8}$$

where α corresponds to the QED coupling constant and F_1, F_2 are dimensionless scalar functions known as structure functions[1]. These objects of undetermined analytical form contain all the information about the internal structure of the struck hadron. The DIS experiments conducted in the late 1960s at SLAC-MIT provided the first measurements of the proton structure functions, revealing them to be approximately Q^2-invariant [6] as previously proposed by Bjorken [7][2]. This scaling behavior, along with the large scattering angles observed in the electrons, motivated Feynman to introduce in 1969 the first formulation of hadronic structure in terms of point-like constituents: the parton model [8].

In this framework, the physical picture underlying DIS is that of an incoherent elastic scattering between the electron and *one* parton. Such an interpretation is possible in a reference frame where the proton moves very fast: the Infinite Momentum Frame (IMF). Due to Lorentz time-dilation, the characteristic time scale of interactions between partons in this frame is much larger than the duration of the interaction with the virtual photon, which allows us to assume an incoherent and instantaneous scattering of a single parton[3]. The cross section of this interaction is related to that of the DIS process by the following formula:

$$\frac{d^2\sigma^{e^- P \to e^- X}}{dx\, dQ^2} = \sum_f \int_0^1 d\xi\, f_f(\xi) \frac{d^2\sigma^{e^- q_f \to e^- q_f}}{dx\, dQ^2} \equiv \sum_f \int_0^1 d\xi\, f_f(\xi)\hat{\sigma}(\xi), \tag{1.9}$$

where $d\xi f_f(\xi)$ gives the probability of the probe interacting with a parton of type f (quark, antiquark or gluon) carrying a fraction ξ of the total longitudinal momentum of the parent proton. Note that this quantity does not depend on the transverse momentum of the probe, which conveys the physical picture of an interaction with point-like particles. This is known as Bjorken scaling. The Parton Distribution Function (PDF) $f_f(\xi)$ contains all the information about the long-distance phenomena that governs hadronic structure, and hence it is an inherently non-perturbative object. In contrast, the cross section of the electron-parton scattering $\hat{\sigma}$ is computable in perturbative theory. To first non-trivial order it reads:

$$\hat{\sigma} = \frac{4\pi\alpha^2}{Q^4}\frac{1}{2}e_q^2\delta(x-\xi)\left[1 + (1-y)^2\right], \tag{1.10}$$

---

[1] In the case where the exchanged particles are $W^\pm$ or Z^0 bosons, this formula includes a third structure function.

[2] Although the article was published after the relevant experimental results, the Bjorken scaling proposal was made before the measurements.

[3] For a more detailed discussion on the kinematics of DIS, see Appendix C.

where e_q is the electric charge of the quark q. Here we implicitly take into account that, as gluons are not electrically charged, only quarks will couple to the virtual photon. The expressions Eq. (1.8), Eq. (1.10) along with the factorization ansatz Eq. (1.9) allow us to perform an explicit computation of the structure functions of the proton:

$$F_2 = 2xF_1 = \sum_{q\bar{q}} e_q^2 x f_q(x). \tag{1.11}$$

The first equality in this expression, known as the Callan-Gross relation, directly stems from the spin-1/2 nature of the probed quarks (it would read $F_1 = 0$ for spin-0 particles). The observation of this relation in the SLAC-MIT experiment allowed to identify Feynman's partons with the quarks previously postulated by Gell-Mann. This is recognized as one of the main achievements of the parton model.

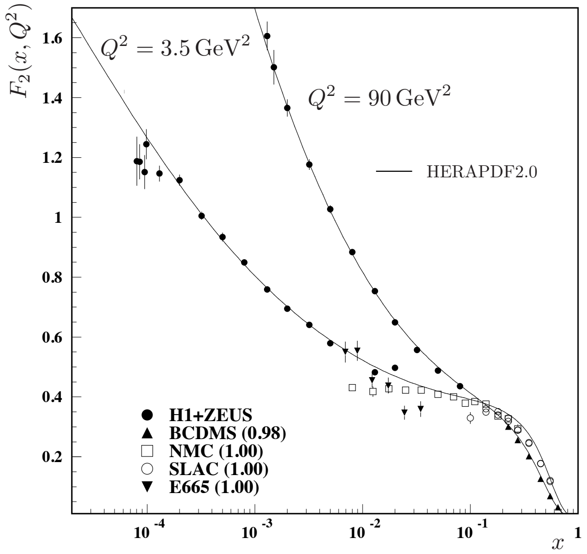

Figure 1.5: Compilation of F_2 data measured in DIS experiments. Bjorken scaling violation is explicitly displayed for Bjorken-x values under 10^{-1}. The curves correspond to the PDF parameterization from the HERAPDF analysis [9], which includes quantum corrections to be discussed in the next chapter. Figure extracted from [10].

The parton model features both a useful physical picture of DIS and a first instance of factorization of long-distance and short-distance phenomena (embodied in Eq. (1.9)). Although it does not provide a satisfactory theoretical description of hadronic structure, this is not so much a problem of the model itself as it is a general shortcoming of perturbative QCD, which can not produce analytical information in the large coupling regime.

However, even if we consider the parton model merely as a useful approximation under which we can interpret DIS processes, it quickly becomes insufficient as we move to higher center of mass energies (or equivalently, smaller values of Bjorken-x), where data displays a violation of the scaling behavior of structure functions. Another intriguing feature displayed by HERA data is the dramatic increase of the proton structure function F_2 with decreasing Bjorken-x values, which suggests an enhancement of the partonic density of the proton. Both properties can be observed in Fig. 1.5. As will be discussed in the next chapter, these effects emerge from the quantum fluctuations that continuously rearrange the hadronic structure.

Chapter 2

Linear evolution equations

The parton model does not take into account any QCD interaction and thus it can be considered as the zeroth order of a perturbative expansion in orders of α_s. The first order corrections enter through the quantum fluctuations represented in Fig. 2.1. These depict how, in a given DIS process, the quark struck by the virtual boson may have emitted a gluon before the interaction (real correction) or fluctuated into itself via an emission-absorption sequence (virtual corrections). Other possible diagrams show how the virtual photon might even encounter a quark emitted in a prior radiation process[1]. All such fluctuations are present in any interaction vertex, and DIS data becomes more sensitive to them as we move towards smaller values of Bjorken-x. In the IMF this effect is interpreted as an enhancement of the time resolution of the DIS probe ($\Delta t \sim 1/x$) that allows it to interact with short-lived quantum fluctuations (see Appendix C for details). This in turn introduces a dependence on the transverse resolution $1/Q$ that, as will be shown below, can be studied via perturbative QCD techniques.

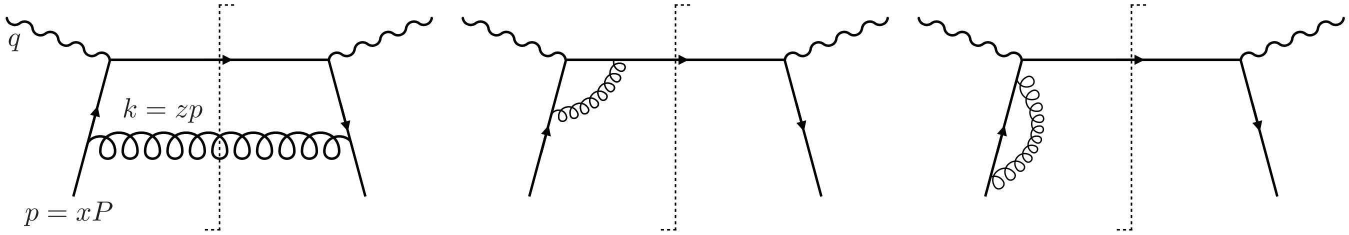

Figure 2.1: $\mathcal{O}(\alpha_s)$ corrections to the squared amplitude of the elastic quark-electron scattering. P is the momentum of the parent proton.

2.1 DGLAP evolution

Let us consider a quark emitting a gluon carrying transverse momentum $k_\perp$ and a small fraction x of the longitudinal momentum of the parent quark. The differential probability for such an emission reads:

$$dP_i \sim \alpha_s \frac{dx_i}{x_i} \frac{d^2 k_\perp}{k_\perp^2}. \tag{2.1}$$

When integrated over the available phase space this probability leads to logarithmic divergences of different nature. The limit $x \to 0$ yields the 'soft' divergence, which for this kind of emission is exactly canceled by the contributions of the virtual corrections (central and right diagrams in Fig. 2.1). The

---

[1] Of course, not *all* possible $\mathcal{O}(\alpha_s)$ corrections are represented here. In addition to complex conjugates (which would look like mirror images of these diagrams), one can also consider other real contributions that, unlike Fig. 2.1 (a), do not resemble the rungs of a ladder. However, we will neglect these terms in the present discussion, as their contribution can be accounted for by an appropriate choice of gauge (the so-called 'physical' gauges).

remaining singularity, known as ‘collinear’ divergence, appears when $|k_\perp| \to 0$. The large logarithms stemming from this limit enhance the quantum corrections in such a way that, even in the small coupling regime, a naive perturbative expansion in powers of α_s becomes ill-behaved. In order to deal with this issue we perform a strategic rearrangement of said logarithmically enhanced terms. This process is called resummation and is at the basis of the Dokshitzer-Gribov-Lipatov-Altarelli-Parisi (DGLAP) evolution equations, whose derivation we will briefly outline below.

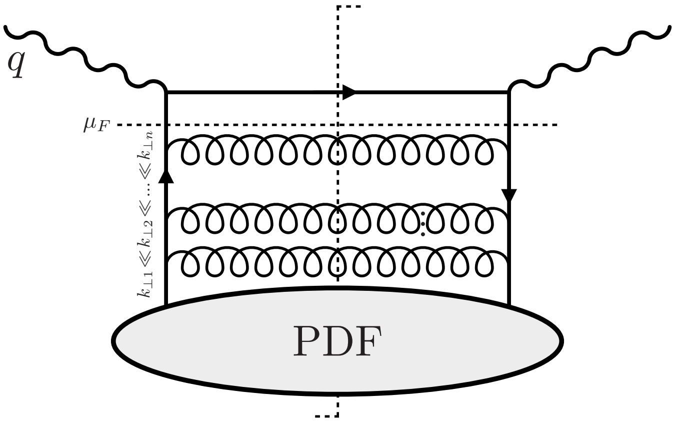

Figure 2.2: Diagrammatic representation of the DGLAP scheme: gluon emissions with $k_\perp$ under a certain factorization scale μ_F are absorbed in the definition of the PDFs. The considered emissions are strongly ordered to all orders in α_s.

In order to connect with the previous DIS calculations, let us consider quantum corrections to the quark-electron scattering. Considering all orders in α_s, the dominant contributions to this process come from those ladder-like diagrams where the transverse momenta of the successive emitted gluons are strongly ordered (see Fig. 2.2):

$$\frac{1}{R_h} \ll k_{\perp 1} \ll k_{\perp 2} \ldots \ll k_{\perp n} \ll \mu_F, \tag{2.2}$$

with moderately small values of x (in such a way that $\ln(1/x)$ factors do not yield a big enhancement). Here R_h is the transverse radius of the struck hadron and μ_F is an arbitrary momentum scale above which we consider interactions to be *hard*. We will only consider this kind of diagrams, as the remaining terms are suppressed by extra factors of α_s. This is known as the leading logarithmic approximation (LLA). Computing the probability of emitting n gluons under such strict ordering condition, we obtain large logarithmic contributions:

$$dP_n \sim \left[\alpha_s(Q^2) \ln\left(\frac{Q^2}{\mu_0^2}\right)\right]^n, \tag{2.3}$$

where $\alpha_s \ln(Q^2/\mu_0^2) \sim 1$ to all orders. Here, μ_0 is an initial perturbative scale that we introduce as a cut-off in the momentum integration. In the context of a DIS process, these large logarithms enter the calculation of the structure functions through the *hard* factor $\hat{\sigma}$, thus explicitly violating Bjorken scaling. Let us, for instance, consider F_2 at first non-trivial order in QCD. We have:

$$F_2(x, Q^2) = \sum_{q\bar{q}} x e_q^2 \left[f_q^{(0)}(x) + \int_x^1 \frac{dz}{z} \frac{\alpha_s}{2\pi} f_q^{(0)}(z) \left\{ P_{qq}\left(\frac{x}{z}\right) \ln\left(\frac{Q^2}{\mu_0^2}\right) + \ldots \right\} \right], \tag{2.4}$$

where the omitted terms inside the curly brackets do not contain collinear divergences. Here $f_q^{(0)}(x)$ corresponds to the 'bare' PDF from the naive parton model. The splitting function $P_{qq}(x)$ gives the probability of having a quark (or antiquark) emitting a gluon with fractional longitudinal momentum x. In the same spirit as Eq. (1.9), we factorize the divergent long-distance contribution (implicit in the limit $\mu_0 \to 0$) by absorbing it in the definition of the PDFs, such as:

$$f_q(x,\mu_F^2) = f_q^{(0)}(x) + \int_x^1 \frac{dz}{z}\frac{\alpha_s}{2\pi} f_q^{(0)}(z) \left\{ P_{qq}\left(\frac{x}{z}\right) \ln\left(\frac{\mu_F^2}{\mu_0^2}\right) + ... \right\}, \tag{2.5}$$

and thus:

$$F_2(x,Q^2) = \sum_{q\bar{q}} x e_q^2 f_q(x,Q^2). \tag{2.6}$$

Eq. (2.5) features the factorization scale μ_F mentioned above, which explicitly separates perturbative from non-perturbative physics. This is an arbitrary scale and thus observables like the structure functions should not depend on its value. The renormalization group equation that imposes such condition is the DGLAP equation:

$$\frac{\partial f_q(x,\mu_F^2)}{\partial \ln \mu_F^2} = \frac{\alpha_s}{2\pi} \int_x^1 \frac{dz}{z} f_q(z,\mu_F^2) P_{qq}\left(\frac{x}{z}\right), \tag{2.7}$$

which yields the evolution of the PDF with μ_F. Taking into account that the proton contains both quarks and gluons that can fluctuate into each other one arrives at the complete DGLAP equations, which can be compactly expressed in matrix form:

$$\frac{\partial}{\partial \ln \mu_F^2} \begin{bmatrix} \Sigma(x,\mu_F^2) \\ f_g(x,\mu_F^2) \end{bmatrix} = \frac{\alpha_s}{2\pi} \int_x^1 \frac{dz}{z} \begin{bmatrix} P_{qq}(z) & 2N_f P_{qg}(z) \\ P_{gq}(z) & P_{gg}(z) \end{bmatrix} \times \begin{bmatrix} \Sigma(x/z,\mu_F^2) \\ f_g(x/z,\mu_F^2) \end{bmatrix}, \tag{2.8}$$

with $\Sigma = f_q + f_{\bar{q}}$. The factorization ansatz outlined above has been widely applied in a variety of QCD calculations. Take, for instance, the differential cross section of an inclusive proton-proton collision (represented in Fig. 2.3):

$$\frac{d\sigma^{pp\to X}}{dp_1 dp_2} = \sum_{i,j} \int dx_1 dx_2 f_i(x_1,\mu_F^2) f_j(x_2,\mu_F^2) \hat{\sigma}(p_1,p_2,\alpha_s,Q^2/\mu_F^2). \tag{2.9}$$

Here the perturbative factor $\hat{\sigma}$ is the only element that depends on the specific process studied. In contrast, the PDFs are universal objects that, once measured and treated with Eq. (2.8), can be used as input to a wide variety of predictive calculations. This 'measurement' is performed by proposing a parameterization for the PDF at an initial scale μ_0 and fixing the parameter values through a fit to data (typically from DIS or Drell-Yan processes). Then, the DGLAP equations evolve the PDFs from μ_0 up to the experimental scale of interest. This procedure has been successfully tested against experimental data in a number of QCD processes (see [11] for a review centered in DIS data).

However, this is not the whole story. Eq. (2.8) shows how quark and gluon distributions are mixed through evolution. This mixing is described by the splitting functions (represented in Fig. 2.4), which we compute perturbatively:

$$P_{ij}(x,Q^2) = P_{ij}^{\mathrm{LO}}(x) + \alpha_s(Q^2) P_{ij}^{\mathrm{NLO}}(x) + ... \tag{2.10}$$

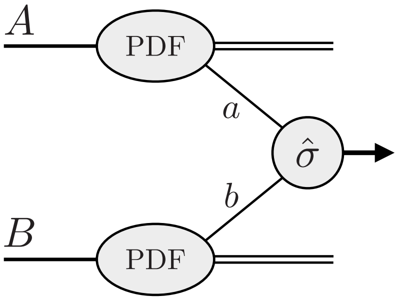

Figure 2.3: Sketch of the collinear factorization of the hadron-hadron cross section introduced in Eq. (2.9).

Let us first consider only the LO terms. Two of these functions exhibit a soft divergence: the ones that describe gluon-gluon and gluon-quark splitting (P_{gg}^{LO} and P_{gq}^{LO})[2]. In consequence, if we were to use LO DGLAP at very small values of x (i.e. below $x = 10^{-4}$, although such values are outside its range of validity), we would find that gluons become the dominant contribution to the PDFs, growing as:

$$f_g(x, Q^2) \sim x^{-\lambda} \tag{2.11}$$

with $\lambda > 0$. This asymptotic behavior is also reproduced at NNLO, which constitutes the current state-of-the-art accuracy of DGLAP analyses. Eq. (2.11) leads to a singular growth of the structure function F_2 that falls short in comparison with the datasets obtained at HERA [12, 13]. These results suggest that, as we reach higher energies (smaller values of x), the DGLAP picture becomes increasingly inadequate. In this limit the resummation scheme adopted thus far fails to take into account large logarithmic contributions from terms proportional to $\alpha_s \ln(1/x)$, which, again, lead to an ill-behaved definition of the perturbative series. This is where the BFKL picture enters.

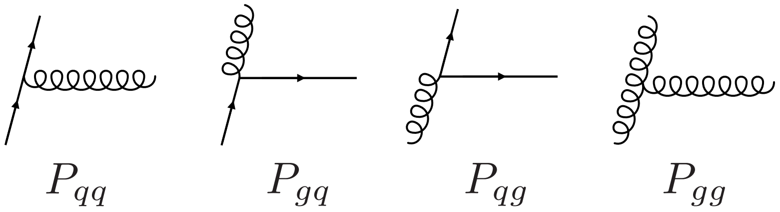

Figure 2.4: Diagrammatical representation of the four LO splitting functions.

It is worth remarking that the previous derivation is a simplified (and arguably incomplete) sketch of a rigorous and very well documented procedure. For a more formal and detailed derivation the reader is referred to [5, 14].

---

[2] Note that these divergences do not get canceled by the virtual terms mentioned at the beginning of this section, as they are corrections to different types of emission. The divergences that do get canceled enter through the splitting functions P_{gg}^{LO} and P_{qq}^{LO}, which get regularized through the standard ‘plus-prescription’ method.

2.2 BFKL evolution

The soft divergence of the splitting functions induces a fast growth of gluon distributions in the high energy limit, which demands for the formulation of alternative evolution schemes beyond DGLAP. We thus take the complementary limit, which corresponds to fixed photon virtuality Q^2 and decreasing x. In this limit the relevant degrees of freedom are gluons and the leading mechanism for evolution is gluon radiation.

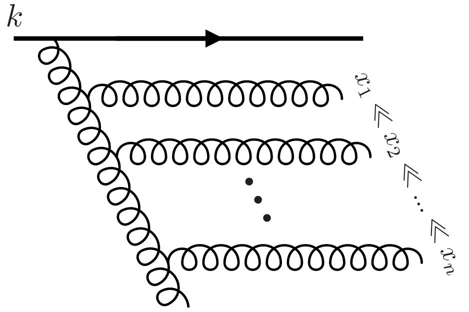

Figure 2.5: Schematic representation of the dominant diagrams for BFKL evolution.

We will thus consider diagrams such as the one shown in Fig. 2.5, where a radiated gluon emits in turn more gluons. As we did in the previous section, we will resum the dominant contributions to this process (LLA), which in this case correspond to diagrams showing a strong ordering in the energy fractions carried by the radiated gluons:

$$x_1 \gg x_2 \gg ... \gg x_n. \tag{2.12}$$

We are thus abandoning the strong ordering in transverse momenta characteristic of the DGLAP radiative cascade[3], considering instead a random walk in $k_\perp$-space. Under these conditions, the large logarithms that we resum are $\alpha_s \ln(1/x) \sim 1$. This approach yields the Balitsky-Fadin-Kuraev-Lipatov (BFKL) evolution equation:

$$\frac{\partial \phi(k,Y)}{\partial \ln(1/x)} = \frac{\alpha_s N_c}{\pi} \int \frac{d^2q}{(k-q)^2} \left[\frac{\phi(q,Y)}{q^2} - \frac{\phi(k,Y)}{q^2+(k-q)^2} \right], \tag{2.13}$$

where the evolution variable is the rapidity $Y = \ln(1/x)$. Technically, the evolved object for such an equation must be a function of $k_\perp$ whose value depends on the measurement scale Y (in contrast to the PDFs, where transverse momentum and energy play the opposite roles). This object is the unintegrated Gluon Distribution $\phi(k_\perp, Y)$, which provides the number of gluons per unit phase space with transverse momentum $k_\perp$ in the wave function of a hadron probed at rapidity Y. Its definition in terms of the usual (integrated) gluon distribution can be written as:

$$x f_g(x,Q^2) = \int^{Q^2} d^2k_\perp \frac{dN_g}{dY d^2k_\perp} = \int^{Q^2} d^2k_\perp \phi(x,k_\perp). \tag{2.14}$$

---

[3] Considering both orderings simultaneously yields the double log approximation (DLA) of DGLAP, applicable when both $\ln Q^2$ and $\ln x$ are large. The results obtained in this limit with regards to gluon growth show qualitative agreement with BFKL evolution, and thus we will only mention it here.

Nevertheless, despite the equality sign in the previous expression, there is no unique direct relation between integrated and unintegrated Gluon Distributions (uGDs). This is not a major issue, as neither are observable quantities but undetermined mathematical objects that we measure through fits to data[4]. The relation Eq. (2.14) is established in a model-dependent way that connects the definition of the uGDs to specific physical processes (for a detailed discussion on the interpretation of different uGDs, see [16]). In the case of DIS, the BFKL equation at NLO succesfully predicted the rapid growth of the cross section with increasing energies, which was subsequently observed experimentally. However, the solution to the BFKL equations yields a gluon distribution that shows an even more singular behavior in the small-x limit than DGLAP did:

$$\phi(k_\perp, x) \sim x^{-\frac{4N_c \ln 2}{\pi}\alpha_s}, \tag{2.15}$$

which, as will be detailed below, leads to unphysical results. The origin of this malfunction is the linear character of the evolution mechanisms considered thus far.

For a detailed derivation of the BFKL equations the reader is referred to [5].

2.3 Breakdown of linear evolution, saturation

In the previous sections we discussed how both linear evolution schemes, DGLAP and BFKL, point towards a singular growth of gluon densities in the small-x limit (although only in the BFKL case we should consider this a prediction). Such asymptotic behavior leads to the violation of unitarity, which is a fundamental requirement of any quantum field theory. In the context of particle collision experiments, the unitarity condition manifests as a strict constraint of the energy dependence of total hadron-hadron cross-sections. This is known as the Froissart bound, which reads:

$$\sigma_{\rm tot}^{hh}(s) \leq \frac{1}{m_\pi^2} \ln^2 s, \tag{2.16}$$

where m_π is the pion mass and s is the squared center of mass energy of the collision. The power growth displayed by the solutions of the linear evolution equations violates this bound, thus being forbidden by the unitarity requirement[5]. Although the Froissart bound is indeed a powerful condition, we must not overlook the fact that one of the key ideas used on its derivation is the existence of a mass gap m_π between the vacuum and the next lowest energy state of QCD (see e.g. [5] for details). As such concepts are extraneous to the perturbative framework outlined in this chapter, it is thus convenient to discuss unitarity in different terms.

In a perturbative context unitarity is more appropriately discussed in terms of the S-matrix, related to the total cross-section by the following expression:

$$\sigma_{\rm tot}^{hh} = 2 \int d^2 b_\perp \left[1 - {\rm Re}\, S(s, b_\perp)\right], \tag{2.17}$$

---

[4] A more precise definition can be achieved by using light-front quantization [15]. However, this is out of the scope of this thesis.

[5] Note that although the Froissart bound does not directly allude DIS, the universal character of PDFs and uGDs extends the singularity problem to any physical process where these objects are used.

where $b_\perp$ is the impact parameter of the interaction (defined as the transverse distance between the centers of the two colliding hadrons) and $S(s, b_\perp)$ is the forward matrix element of the S-matrix. This fundamental object has a probabilistic interpretation and is therefore bounded between $[0, 1]$. This implies a unitarity bound $d\sigma/d^2b_\perp \leq 2$, which is equivalent to the *black disk limit*[6]. The asymptotic power-law behavior displayed by the solutions to the BFKL equation Eq. (2.15) implies a total cross-section that grows as a power of s:

$$\sigma_{\text{tot}}^{\text{BFKL}} \sim s^{\frac{4N_c \ln 2}{\pi}\alpha_s}, \tag{2.18}$$

thus violating the black disk bound (note that a similar result is obtained for DGLAP). Unitarity can be partially restored by taking into account evolution mechanisms beyond gluon radiation. In the DGLAP and BFKL approaches only radiative processes are considered, which suggests a physical picture where partons only act as sources for even more quarks and gluons. From the point of view of DIS, this suggests that the virtual boson only resolves one parton at a time, which is plausible only in the case where the probed hadron is a dilute system. Linear evolution schemes thus assume that hadrons stay dilute throughout the whole evolution process, allowing us to neglect parton-parton interactions. At small-x this hypothesis breaks down, as gluon densities become too large. Under such conditions we must take into account gluon recombination processes, which (as will be shown in the following chapter) introduce non-linear terms in the evolution equations. Such terms contribute negatively to the evolution of the gluon density, taming its otherwise uncontrolled growth. In turn, they effectively transform the asymptotic curve Eq. (2.15) into a logarithm, which respects the unitarity bounds of the S-matrix.

However, $S \leq 1$ is a necessary but not sufficient condition for the restoration of unitarity. Despite the introduction of non-linear evolution schemes, the predicted total cross section still grows more rapidly than allowed by Eq. (2.16). In order to better understand the physics implied in this violation of unitarity one has to deepen into non-perturbative properties of QCD, which falls out of the scope of this thesis.

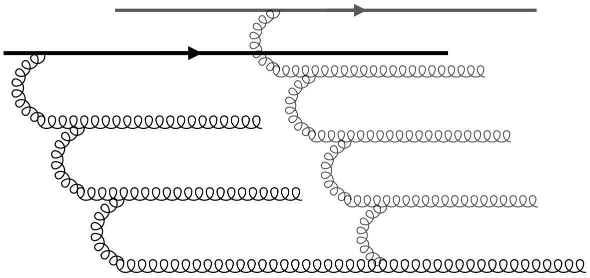

Figure 2.6: Schematic representation of the fusion of two BFKL ladders into a single radiation cascade, a process accounted for by the introduction of non-linear terms in the evolution equations.

Including gluon recombination processes in evolution implies the emergence of a dimensionful scale at which they become relevant. This is the saturation scale Q_s, which signals the transverse momentum at which the linear and non-linear terms of the evolution equations become parametrically of the same order. Q_s can be estimated through a simple geometrical argument. The probability of

---

[6] This limit is computed through the collision between a particle and a circular, totally absorptive target modeled as an infinite potential well.

having two gluons recombine can be computed as:

$$\kappa = \rho^g \sigma^{gg} \sim \frac{x f_g(x, Q^2)}{\pi R_h^2} \frac{\alpha_s}{Q^2}, \tag{2.19}$$

where ρ^g is the transverse gluon density and σ^{gg} is the typical gluon-gluon interaction cross section. We can define the saturation regime as the region of phase space where κ is of order 1, which yields:

$$Q_s^2 \sim \frac{\alpha_s}{\pi R_h^2} x f_g(x, Q_s^2) \sim x^{-\lambda}, \tag{2.20}$$

where we substituted the asymptotic behavior of the DGLAP solution for the gluon PDF (Eq. (2.11)). From this simple derivation we learn that Q_s is a dynamical scale that depends on the value of x. This was verified through fits to data obtained in DIS experiments performed at HERA, which provide a value of $\lambda \sim 0.3$ [17]. Another fundamental property of the saturation scale is its relation to the mass number of the probed hadron. Considering that the gluon densities in nuclei correspond to A times those of nucleons and taking into account the approximate relation between radii $R_A = A^{1/3} R_N$, we obtain:

$$Q_{sA}^2 \sim A^{1/3} Q_{sN}^2. \tag{2.21}$$

This approximate relation shows how saturation effects are enhanced in the wave functions of nuclei with respect to those of individual nucleons.

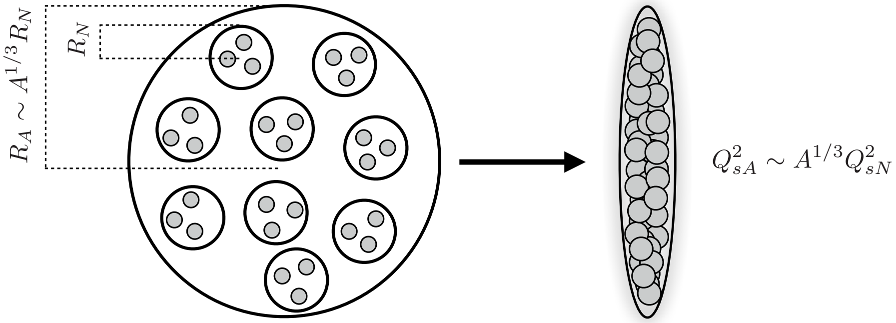

Figure 2.7: Sketch depicting the enhancement of the saturation constant from nucleons to nuclei. The arrow represents a boost to the IMF.

Saturation effects are implemented in the CGC effective theory, which approximates QCD at high energies and large gluon densities. This framework introduces evolution equations that include non-linear terms accounting for gluon recombination processes. This is the theory on which the results presented in this thesis are based. In the following chapter we present a brief review of its main aspects.

Chapter 3

The Color Glass Condensate

Including non-linear effects in the description of hadronic structure at high energies is both required by theoretical considerations and supported by experimental observations. Arguably, the most complete theoretical approach to this task is embodied in the CGC effective field theory. The CGC framework relies in semi-classical methods for the description of the large gluon densities carried by nuclei in the small-x regime. In such systems, the occupation number of gluons with transverse momentum under the saturation scale $N_{k<Q_s}$ is much larger than the commutator of creation $a(k)$ and annihilation $a^\dagger(k)$ operators:

$$N_{k<Q_s} = a^\dagger(k)a(k) \sim \frac{1}{\alpha_s} \gg [a^\dagger(k), a(k)] \sim 1. \tag{3.1}$$

This defines an inherently classical scenario, as one can neglect the non-commutativity of $a(k)$ and $a^\dagger(k)$ and treat them as complex numbers. In turn, this condition allows us to treat the small-x gluons as a classical gauge field, an approach first applied by McLerran and Venugopalan to the calculation of parton distributions of large ultra-relativistic nuclei [18–20].

3.1 The McLerran-Venugopalan model

The McLerran-Venugopalan (MV) model describes the parton content of a nucleus in the IMF, where, by convention, we see it moving in the positive x^3 direction with a very large light-cone momentum $P^+ \gg \Lambda_{\text{QCD}}$ (see Appendix A for a detailed introduction to the light-cone coordinate system). The IMF motivates a separation between 'fast' and 'soft' modes, as one can consider partons that carry a large momentum fraction $p^+ = xP^+$ and thus are much more sharply localized around the light cone (within a distance $\Delta x^- \sim 1/p^+$) and long-lived (with mean lifetime $\Delta x^+ \propto p^+$) than the rest. In the MV model said modes are identified with valence partons, which act as radiative sources of the small-x gluons carried by ultra-relativistic nuclei. The separation between them is explicitly performed at an arbitrary momentum Λ^+ at which we define the theory. Each of these two groups of partons is described through different approximations. Whereas the soft gluons are represented by classical gauge fields $A^{\mu,a}$, the fast degrees of freedom enter as a color current $J^{\mu,a}$ whose form is fixed based on kinematic considerations:

$$J^{\mu,a}(x^-, x_\perp) = \delta^{\mu+}\rho^a(x^-, x_\perp), \tag{3.2}$$

ρ^a being the color charge density. $J^{\mu,a}$ is usually[1] assumed to be independent of the light-cone time x^+ due to the mean lifetime of the emitted gluons being much shorter than that of the valence quarks (which is considerably extended by time dilation). Hence, the valence quarks appear to the observer as a static, 'frozen' ensemble of SU(N_c) charges sitting on $x^- = 0$. The fact that $J^{\nu,a}$ generates

---

[1] There are several strategies for the calculation of the gauge fields $A^{\mu,a}$. One of the aspects in which they differ is the ansatz adopted for $J^{\mu,a}$. Since this technical discussion is more relevant for the calculation method than for the description of the model itself, we will leave it for Part III.

a color current only in the + direction suggests a physical picture where the fast valence partons do not recoil from their light-cone trajectory as the gluons they continuously exchange with the medium are too soft to affect their motion (eikonal approximation). The dynamics of such scenario are encoded in the following action:

$$\mathcal{S} = \int d^4x \left(-\frac{1}{2} F^a_{\mu\nu} F^{a,\mu\nu} + J^a_\mu A^{a,\mu} \right), \tag{3.3}$$

where the small-x gluons are described according to the classical Yang-Mills action and the interaction term $J^a_\mu A^{a,\mu}$ corresponds to a QED-like minimal coupling between soft and fast modes. Minimizing this action we obtain the Yang-Mills equations of motion:

$$[D_\mu, F^{\mu\nu}] = J^{\nu,a}\, t^a = \delta^{\mu +} \rho^a(x^-, x_\perp)\, t^a, \tag{3.4}$$

where ρ^a acts as the source of the classical gauge fields. This variable is taken as a stochastic quantity with a certain probability distribution $W[\rho]$ associated as weight function. Thus, in order to calculate physical observables that depend on ρ^a we need to perform a functional average over all possible color charge configurations:

$$\langle \mathcal{O}[\rho] \rangle = \frac{1}{\mathcal{N}} \int [d\rho] W[\rho] \mathcal{O}[\rho], \tag{3.5}$$

where $\mathcal{N}$ is a normalization constant equal to $\int [d\rho] W[\rho]$. The main assumption adopted in the MV model is that in nuclei with large mass numbers the valence partons that enter Eq. (3.4) through ρ^a emerge from a large number of separate nucleons and therefore are uncorrelated[2] . Thus, invoking the central limit theorem, the MV model approximates $W[\rho]$ with a Gaussian distribution:

$$\langle \mathcal{O}[\rho] \rangle_{\text{MV}} = \frac{\int [d\rho] \exp\left\{ -\int dx^- d^2x_\perp \frac{1}{2\mu^2(x^-)} \text{Tr}\left[\rho^2(x^-, x_\perp)\right] \right\} \mathcal{O}[\rho]}{\int [d\rho] \exp\left\{ -\int dx^- d^2x_\perp \frac{1}{2\mu^2(x^-)} \text{Tr}\left[\rho^2(x^-, x_\perp)\right] \right\}}. \tag{3.6}$$

Here $\mu^2(x^-)$ is a parameter proportional to the color source number density that acts as the variance of the Gaussian weight. The main implication of the Gaussian ansatz is given by the following correlators:

$$\langle \rho^a(x^-, x_\perp) \rangle_{\text{MV}} = 0 \tag{3.7}$$

$$\langle \rho^a(x^-, x_\perp) \rho^b(y^-, y_\perp) \rangle_{\text{MV}} = \mu^2(x^-) \delta^{ab} \delta(x^- - y^-) \delta^2(x_\perp - y_\perp), \tag{3.8}$$

which greatly simplify the calculations involved in the average process Eq. (3.5). However, while Eq. (3.7) plainly states the average color neutrality of the nucleus, Eq. (3.8) presents a extremely naive picture of color charge correlations (local in both color and space-time) and nuclei (transversely infinite, uniform sheets of color charge) that does not precisely describe reality. In Part IV we will introduce a generalization of the previous correlator with the twofold aim of achieving a more realistic description and expanding the phenomenological applications of our results. Nevertheless, despite

---

[2] It is assumed that the large transverse momentum scale at which we are probing nuclei results in transverse resolution scales that are very small compared to a fermi. The argument is sometimes extended to nuclei with smaller mass numbers (or even single nucleons) by assuming that on such scales we perceive locally uncorrelated quarks whose charges add together in a random walk in color space.

the crudeness of the Gaussian ansatz, the MV model is able to qualitatively reproduce the saturation of uGDs.

As mentioned at the beginning of this section, the MV model is defined for a momentum scale $\Lambda^+ = xP^+$ that controls the distinction between fast ($p^+ > \Lambda^+$) and soft partons ($q^+ < \Lambda^+$). As will be shown below, the dependence on Λ^+ enters through the functional weight $W[\rho] \equiv W_\Lambda[\rho]$, which gives the probability of observing a certain configuration of color charge sources in the nucleus at this scale, thus playing a similar role as the PDFs do in the collinear factorization framework. As was also the case with the PDF and the arbitrary factorization scale μ_F, the dependence on Λ^+ should not permeate the observables computed in this theory. The renormalization group equation that solves this issue, yielding the evolution of $W_\Lambda[\rho]$ with decreasing values of Λ^+, is the B-JIMWLK equation.

3.2 Non-linear evolution equations

The framework described above does not include any *explicit* dependence on Λ^+. However, it implicitly requires the described small-x modes to stand close to this artificial scale, with $x \sim \Lambda^+/P^+$. As we probe smaller values of x, gluons are less likely to have been emitted by the partons we arbitrarily defined as sources, but by other gluons also lying in the small-x regime. These interactions between soft modes are taken into account by computing quantum corrections to the classical field (which become large with decreasing values of x, growing like $\ln 1/b$ for gluons with $x' = bx$). Note that this computation is necessarily constrained by the Λ^+ cut, as it is the maximum light-cone momentum allowed for the gluons inside the loops[3]. This is another instance of a quantum theory introducing an explicit dependence on an artificial scale separating hard and soft degrees of freedom. Again, we treat the issue by resumming the quantum fluctuations and absorbing them into the redefinition of an intrinsically non-perturbative object, which in this case is the functional weight $W_\Lambda[\rho]$. This procedure yields the following renormalization group equation:

$$\frac{\partial W_x[\rho]}{\partial \ln 1/x} = \alpha_s \left\{ \frac{1}{2} \frac{\delta^2}{\delta \rho_x^a \delta \rho_y^b} \left[W_x \psi_{xy}^{ab} \right] - \frac{\delta}{\delta \rho_x^a} \left[W_x \sigma_x^a \right] \right\}, \tag{3.9}$$

known as the B-JIMWLK equation[4]. Eq. (3.9) evolves $W_\Lambda[\rho]$ from Λ^+ to a new value $\Lambda'^+ < \Lambda^+$ by incorporating the modes contained in the momentum strip $\Lambda'^+ < p^+ < \Lambda^+$ as new color sources. By doing so we effectively introduce quantum corrections into our theory while preserving its inherent classical nature. This procedure makes observables independent of Λ^+. In the B-JIMWLK framework, the MV model defined by Eq. (3.6) acts as an initial condition for the evolution.

On a surface level, the main difference between Eq. (3.9) and the renormalization group equations introduced so far lies in the presence of a negative non-linear term that we can associate to gluon recombination. This term emerges from the resummation process, which is performed at leading logarithmic accuracy in the parameter $\alpha_s \ln 1/x$ (accounting for radiative, BFKL-like corrections) and to all orders in the background classical fields (which, being *strong* fields, do not allow for a perturbative expansion). The latter corrections yield the non-linear effects that tame the rapid

---

[3] Otherwise we would be double counting the large-x degrees of freedom, which in the MV framework act as external sources.

[4] Conceived by Balitsky, Jalilian-Marian, Iancu, McLerran, Weigert, Leonidov and Kovner.

growth of the gluon density in hadronic wave functions in the small-x limit. In the low density/weak field limit the non-linear term vanishes, and thus we recover the BFKL evolution equation [21].

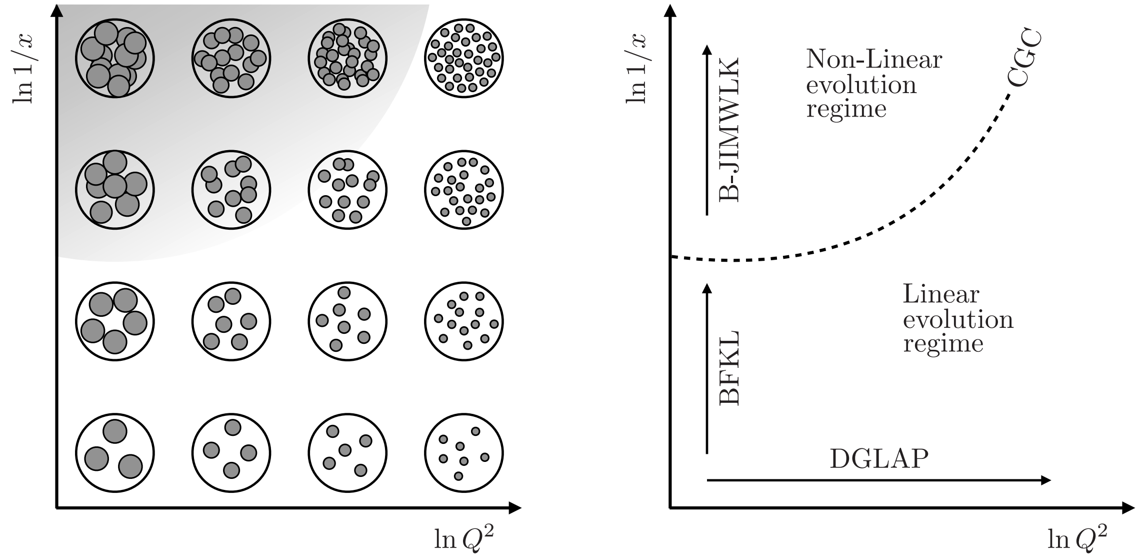

Figure 3.1: Two sketches of the $\ln Q^2$, $\ln 1/x$ plane representing parton densities (left) and evolution regimes (right). Non-perturbative region not represented.

Being notoriously difficult to solve, the practical use of the B-JIMWLK equation has thus far been restricted to different analytical or numerical approximations. The latter are based on a reformulation of Eq. (3.9) as a Langevin equation, which allows for numerical studies on the lattice [22, 23]. As for analytical approximations, a common example in phenomenological analyses is the large-N_c and mean field limit, which yields the so-called Balitsky-Kovchegov (BK) equation [24, 25]. It has been shown that the difference between the solutions of the BK and (numerical) B-JIMWLK equations is strikingly small, of the order of 0.1 % [26].

Chapter 4

Heavy ion collisions: The Quark Gluon Plasma

In this chapter we perform a brief incursion into one of the research fields where saturation physics plays a bigger role: HICs. Our goal with the following sections is to provide a general context to QGP phenomenology, as it is the main area of application of the results presented in Part IV of this thesis. Specifically, we focus on the relevance of the previously discussed CGC effective theory in the characterization of the initial state fluctuations of HICs.

4.1 The QCD phase diagram

In Chapter 1 we discussed that one of the main features of QCD is asymptotic freedom, namely the decrease of the coupling constant in interactions characterized by large momentum exchanges (or happening over small distances). This property, along with the assumption that one can factorize perturbative from non-perturbative phenomena, allows us to build the evolution frameworks outlined in chapters 2 and 3. However, we have not yet considered how the running coupling impacts the bulk thermodynamic properties of QCD matter. This is a highly non-trivial topic, as its research requires precise knowledge of strongly-coupled dynamics.

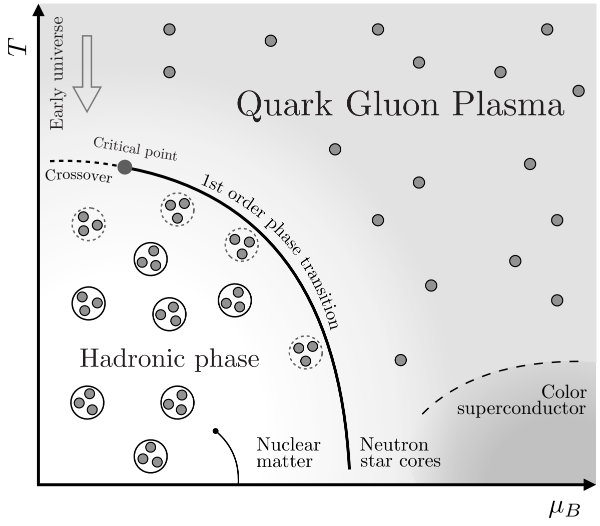

Figure 4.1: Qualitative sketch of the QCD phase diagram. Lattice simulations of QCD predict a transition at high temperature from a phase where quarks and gluons are bound into hadrons (as usual in nature) to a phase where they appear to be deconfined; the QGP.

Currently, the only available first-principles approach to non-perturbative physics is based on numerical simulations of QCD on the lattice. In this formalism the expectation values of observables are obtained as path integrals where we discretize the Euclidean space-time into a hypercubic grid. In contrast to perturbative QCD, lattice methods do not impose any constraint on the value of the coupling constant. This allows us to study the properties of the non-perturbative regime of QCD, thus supplementing the information obtained from the previously discussed factorization frameworks.

But lattice techniques are not devoid of limitations. At non-zero baryonic density ($\mu_B \neq 0$)[1], the numerical computations involved become increasingly unpractical due to the Euclidean QCD action adopting complex values. This is the well-known sign problem, which restricts the application of lattice methods to those regions of phase space where baryonic density is very low[2] ($\mu_B \sim 0$). Beyond this regime, the available knowledge about the QCD phase diagram is subject to a considerable amount of uncertainty, stemming from a variety of model calculations, perturbative computations (in asymptotic regimes) and empirical evidence from nuclear physics. Therefore, it is not surprising that the fine details of sketches like the one shown in Fig. 4.1 are not yet globally agreed upon. Some of the most controversial aspects of the structure of the QCD phase space are the nature and location of phase transitions, critical points, and the modifications induced by external magnetic fields (for a comprehensive review of these topics, see [29]). However, the emergence of QGP at extremely high temperatures and densities is a common point in all contemporary pictures of the QCD phase diagram.

The available theoretical estimates suggest that the early universe was in a QGP state located in the $\mu_B = 0$ axis of the QCD phase diagram. This has inspired a direct comparison between the first stages of cosmological evolution and those of the system generated in HICs (which are sometimes referred to as 'Little Bangs' [30]). Such an analogy is a great source of motivation for heavy ion physics, as it links fundamental research in QCD with open problems in cosmology that otherwise might not be possible to study in an experimentally controlled way (e.g. baryon asymmetry, inflation). Other occurrences of the QGP in nature are expected in the core of neutron stars (*cold* QGP) [31] and in collisions of ultra high energy cosmic rays with the atmosphere [32].

The QGP phase can be experimentally accessed in high energy collisions of heavy nuclei such as the ones performed at RHIC and LHC. In the following section we will briefly outline some of the main signs of QGP emergence observed in these colliders.

4.2 Experimental signatures of QGP

The QGP is a state of matter where the fundamental degrees of freedom of QCD no longer appear to be bound into color neutral hadrons, but inside a macroscopic, strongly-interacting blob of quarks and gluons. Therefore, it is obvious that its direct observation is forbidden by confinement. What is actually observed in HIC experiments is a shower of color neutral particles (an average of 10^4 per event for Pb-Pb collisions at a center of mass energy of 2.76 TeV) that includes hadrons, leptons, photons and other vector bosons. The momentum spectra, chemical composition and correlations of these final products provide indirect information about the QGP phase.

---

[1] The baryo-chemical potential μ_B is a measure of how the energy of a system increases as one adds another baryon to it. At non-zero temperature, $\mu_B = 0$ describes a system where the number of baryons and antibaryons is identical, while $\mu_B > 0$ is associated to a baryon-dominated medium. For the present qualitative discussion, baryonic density and baryo-chemical potential are virtually interchangeable concepts, as they are proportional.

[2] Despite this obstacle, lattice methods rely on well-motivated extrapolations to access experimentally relevant values of μ_B. For a general review of lattice QCD, see [27]. For a more recent and HICs-centered approach to the subject, see [28].

Below we briefly describe some of the most notorious and historically relevant QGP observables proposed so far. In practice, these are systematically compared to analogous measurements in proton-proton collisions, which are assumed to be a reliable baseline for QGP searches.

4.2.1 Strangeness enhancement

Being able to distinguish between a QGP and a dense gas of hadrons was one of the first challenges posed by HIC experiments. For this purpose, in [33] it was proposed that the QGP phase would exhibit an enhanced strangeness content with respect to regular hadronic matter at the same temperature. It was argued that, due to the expected abundance of up and down quarks in the QGP, $u\bar{u}$ and $d\bar{d}$ fluctuations would be suppressed by the Pauli principle, thus favoring the generation of $s\bar{s}$ pairs despite their larger mass.

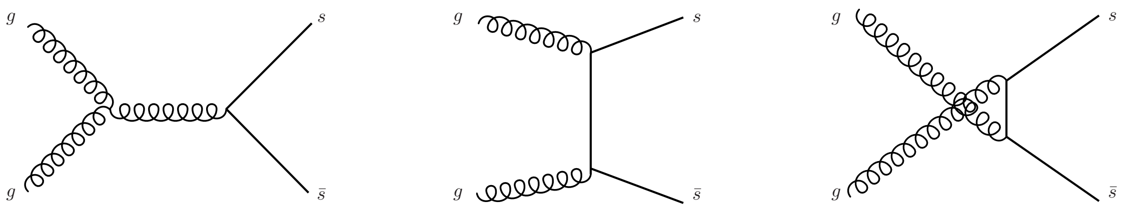

Figure 4.2: Feynman diagrams representing gluon fusion processes.

Another source of enhancement was identified in the prevailing gluonic component assumed in the QGP phase, which would yield a rapid $s\bar{s}$ pair production via gluon fusion processes (see Fig. 4.2). The proposed signal for this phenomenon was the enhancement of the ratios of multi-strange hadrons over light hadrons, which was subsequently observed in a series of experiments conducted at CERN between the 1980s and the year 2000 (when CERN announced the discovery of QGP [34]). For a critical review of QGP observables centered in strangeness enhancement effects, see [35].

4.2.2 Quarkonium suppression

Quarkonium states are defined as bound states of heavy[3] quark-antiquark pairs. Although they interact strongly with other hadrons, their interaction cross sections are reduced relative to those of lighter mesons due to their smaller size. Therefore, the formation of quarkonium states in the presence of a gas of hadrons would be enhanced and relatively easy to observe experimentally, as they decay electromagnetically to lepton pairs of definite mass. However, it was predicted that quarkonium production would be suppressed by color screening in a QGP [36]. This effect reduces the range of attractive forces between quark-antiquark pairs, preventing the formation of bound states whose size exceeds a certain critical length (i.e. Debye length) whose value grows with the temperature of the medium. Therefore, the 'largest' quarkonium states were expected to dissolve first in the QGP as its temperature increases, as depicted in Fig. 4.3. The ensuing sequential suppression can be naively assumed to serve as an estimator of the temperature of the QGP.

In practice, however, this observable turns out to be much more complex than explained above. There is a number of phenomena unrelated to QGP (known as Cold Nuclear Matter effects) that

---

[3] The definition of *heavy* in this context is rather narrow; in practice it only includes charm and bottom quarks. The top quark does not appear in quarkonium states, as it is not expected to hadronize at all.

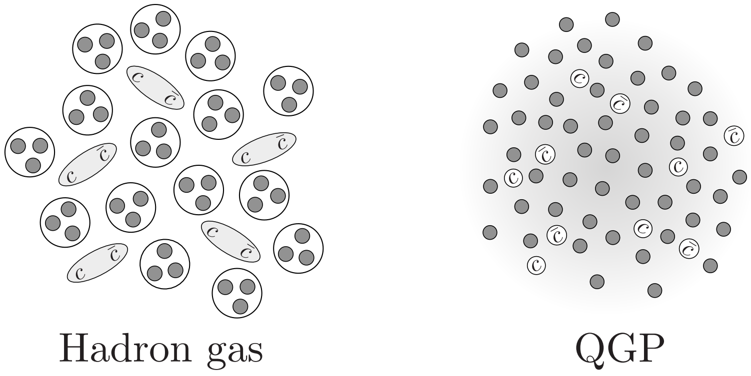

Figure 4.3: Naive picture of the ‘melting’ of $c\bar{c}$ pairs in a QGP (right), in contrast to the situation expected in a confined phase, where they manage to bond into J/ψ states (left). Note that the relative sizes of the J/ψ states and the other hadrons in this sketch are not intended to reflect reality –the former would actually be smaller.

can either enhance or suppress the generation of quarkonia. In addition, there are some processes fueled by the presence of deconfined matter –such as recombination– that work against suppression effects, thus hampering the interpretation of data. As a result, many experimental observations seem to disagree with the naive picture outlined above (e.g. a similar amount of J/ψ suppression at SPS, RHIC and LHC [37]). For a recent review of quarkonium suppression observables in the QGP, see [38].

4.2.3 Jet quenching

Hard scatterings give rise to partons with large transverse momenta. Throughout their propagation they radiate more partons, which can themselves undergo successive radiation processes. The resulting particle cascade goes through hadronization, giving rise to a collimated spray of hadrons in the final state of the collision: a *jet*. The energy loss caused by the interaction between the hard partons and a dense colored medium such as the QGP can influence the jet spectra in different ways. These effects are labeled as jet quenching, and they constitute one of the main signals of the presence of a QGP in HICs.

Arguably the simplest example of an observable sensitive to jet quenching is the nuclear modification factor:

$$R_{AA} = \frac{1}{\langle N_{coll} \rangle} \frac{dN_{AA}/d^2p_\perp dy}{dN_{pp}/d^2p_\perp dy}, \tag{4.1}$$

which is defined as the ratio of the production rates in nucleus-nucleus and proton-proton collisions normalized by the average number of binary nucleon-nucleon collisions[4], $\langle N_{coll} \rangle$. Jet quenching manifests through this observable getting values lower than 1 at high $p_\perp$. This was observed in the first HIC experiments conducted at RHIC [39, 40] (and later reproduced at LHC energies [41–43]) and it was one of the key measurements referenced in the announcement of the QGP discovery.

---

[4] This factor is obtained through comparisons to Monte Carlo simulations based on a geometric picture of the collision known as the Glauber formalism. It depends on the centrality of the collision.

4.2.4 Anisotropic collective flow

Some of the strongest signals of the presence of QGP in HICs are those that stem from its collective expansion, typically referred to as its *flow*. This feature translates into non-trivial correlations between the particles of the final state. One of the key observables sensitive to collective flow is the azimuthal momentum asymmetry of the produced particles with respect to the reaction plane, which is defined by the impact parameter and the beam direction[5] (see Fig. 4.4). This is known as azimuthal anisotropy, and it is characterized by means of the Fourier expansion of the invariant triple differential distributions:

$$E\frac{d^3N}{d^3p} = \frac{1}{2\pi}\frac{d^2N}{p_\perp dp_\perp dy}\left(1 + 2\sum_{n=1}^{\infty} v_n \cos\left[n(\phi - \Psi_{RP})\right]\right), \tag{4.2}$$

where E is the energy of the particle, y its rapidity, p its momentum, $p_\perp$ its transverse momentum, ϕ its azimuthal angle, and Ψ_{RP} the reaction plane angle. As we assume symmetric collisions with respect to the reaction plane, the sine terms of the expansion vanish. The Fourier coefficients of Eq. (4.2) are known as harmonic flow coefficients, and are given by:

$$v_n = \langle \cos\left[n(\phi - \Psi_{RP})\right]\rangle. \tag{4.3}$$

Here the angular brackets denote an average over all particles, summed over all events in the considered $(p_\perp, y)$ bin. The coefficients v_2 and v_3 are referred to as elliptic and triangular flow, respectively.

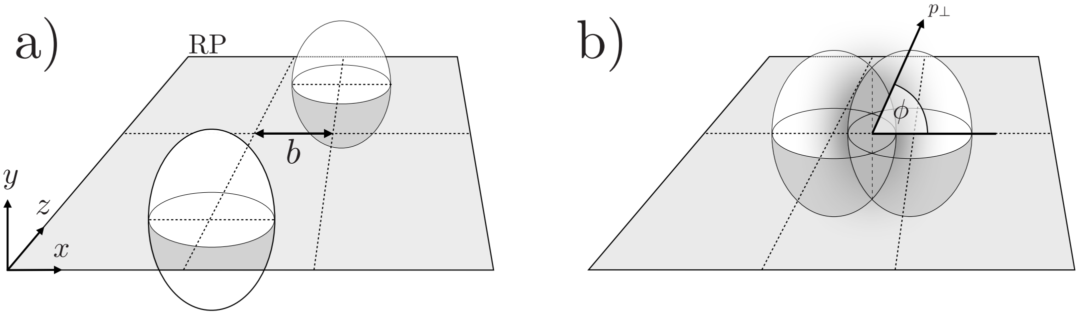

Figure 4.4: Sketch of a non-central collision of two large nuclei, showing a) the projectiles approaching each other, and b) the initial spatial anisotropy that characterizes the overlap region.

The experimental measurements of v_2 in both RHIC [46] and LHC [47] (specially the latter) point towards a quasi-ideal fluid behavior of the generated medium. In this scenario, anisotropies can be naturally explained through a purely geometrical approach. Considering a non-central collision (as depicted in Fig. 4.4), we assume that the almond-shaped nuclear overlap region delimits the generated QGP. Treating this area as a fluid, its initial spatial anisotropy transforms into a final state momentum space anisotropy through the hydrodynamical evolution of the system.

Before getting into the details of the implementation of QGP in phenomenological studies, it is convenient to put it in the context of a wider framework that comprises the different phases of a HIC.

---

[5] Note that both reaction plane and impact parameter are non-accessible experimentally, having to be estimated through different methods. For a detailed review of analysis methods of azimuthal anisotropy in HICs, see [44, 45].

4.3 Stages of a heavy ion collision

The collision of large nuclei constitutes a particularly involved example of many-body problem, with extra difficulties arising from the non-perturbative properties of QCD. Notwithstanding the underlying complexity of these experiments, over the last decade the HIC community has devised a well-established paradigm that describes the different processes involved and sorts them in a sequence of distinct evolution phases. The resulting framework, known as *standard model of HICs*, defines a highly interdisciplinary approach where each evolution stage is treated according to its most prominent physical features. Within this paradigm (represented in Fig. 4.5), the different phases experienced by the system generated in a HIC are:

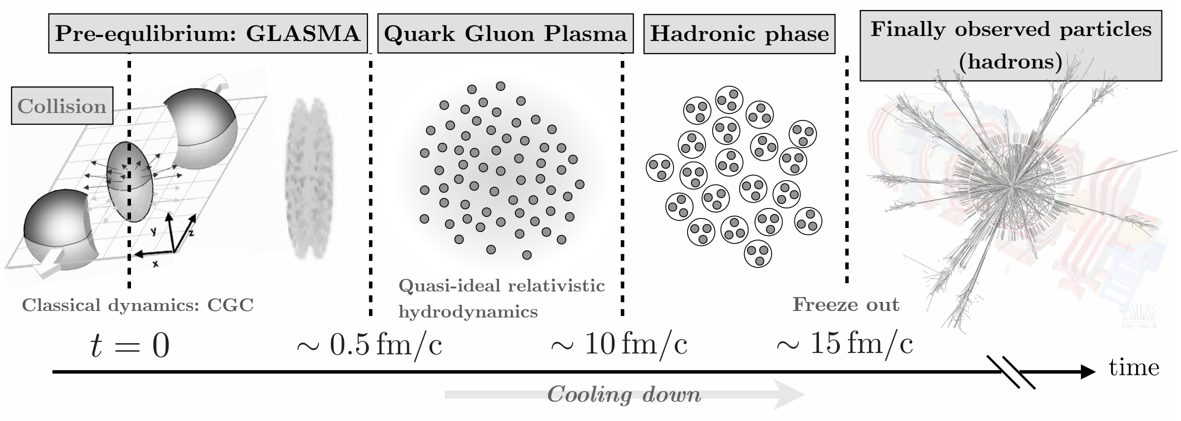

Figure 4.5: Standard model of HICs. Even though this paradigm is theoretically well motivated, the numerical values for time and temperature shown in this diagram are currently subject to a considerable degree of uncertainty, and hence they must be taken only as estimates.

- **The initial state.** Usually defined from $t = 0$ up until an infinitesimal proper time after the collision ($\tau = 0^+$). In this phase, the interactions between the small-x gluons carried by the colliding nuclei give rise to a coherent, highly dense state known as *Glasma*. As will be discussed later, a detailed understanding of this early stage is essential for a proper characterization of the medium generated in HICs. The large occupation number characterizing this phase makes it amenable to the semi-classical description provided by the previously discussed CGC effective theory.

- **Pre-equilibrium.** The Glasma state undergoes a complex evolution process driven by a large number of interactions between its constituents. Within a very short time (~ 0.5 fm/c), these scatterings induce a redistribution of energy density and momentum that leads the system to local thermal equilibrium. This highly non-trivial process is known as **thermalization**, and its precise theoretical description remains one of the most fundamental open problems of the field.

- **The QGP phase.** Once the system thermalizes, the mean free path of its constituents has become much smaller than its size, and thus it can be described in terms of macroscopic variables. Under such conditions, the dynamical evolution of the fireball is implemented within the framework of quasi-ideal relativistic hydrodynamics. Through the comparison between hydrodynamical simulations and experimental data one is able to obtain numerical values of transport properties of QGP such as its shear and bulk viscosities. As will be detailed later, establishing the initial conditions for these simulations requires precise knowledge of the earliest stage of evolution.

- **Hadronic phase.** The QGP expands and cools down, smoothly transitioning into the confined phase approximately 10 fm/c after the collision. Throughout this process the hydrodynamical description gradually breaks down, as the ensuing hot hadron gas can no longer be described by means of macroscopic variables. Once hadronization is completed, the hadron cascade model (implemented in a variety of Monte Carlo codes) provides a description of evolution based on microscopic degrees of freedom.
- **Free streaming.** Although there are different views on this particular point, the general consensus is that the hadronic system described above is produced out of chemical equilibrium. As the hadron gas expands and cools down, it quickly becomes dilute and the collision rate between its constituents decreases, which successively leads to chemical and kinematic **freeze-outs** (approximately 15 fm/c after the collision). After this point, only resonance decays and annihilations can modify the particle yields. The resulting system streams outwards freely, eventually reaching the detectors. The description of this phase typically relies on the kinetic theory framework.

The studies presented in this report focus on the former of these five phases –the initial state of HICs. A proper theoretical characterization of this stage of the collision requires precise knowledge of the partonic composition of the projectile nuclei. As mentioned above, the CGC effective theory plays a fundamental role in this task. In the following section we will expand on the relevance of initial state studies to QGP phenomenology.

4.4 Initial state of HICs

Over the last years it has become clear that the bulk observables in HICs not only reflect the transport properties of the QGP, but also the dynamical features of the initial state of the collision. This was not a sudden realization of the heavy ion community, nor was it the conclusion of a single experiment. Rather, the study of nuclear structure in the high-energy limit (and its implications in collider experiments) was already a long-term concern of QCD by the time the QGP was first observed. Although the relevance of this topic was always acknowledged in the context of HIC phenomenology, most of the early efforts in the field focused on describing the thermal properties of the newly discovered state.

Initial state studies started to gain more notoriety in the community after the first Pb-Pb experiments were performed at LHC. Just the shape of the measured $p_\perp$-spectra already provided strong indications of the importance of the earliest stages of the collision. As mentioned before, in a typical Pb-Pb collision at 2.76 TeV an average of 10^4 particles are produced, and, more importantly, $\sim$99% of them carry a relatively small transverse momentum. This simple observation suggests that most of the particles generated in HICs arise from partons carrying a small fraction x of the light-cone momentum of the parent nucleon. Therefore, a detailed understanding of the small-x gluons that dominate the wave functions of the colliding nuclei is essential for a proper description of HICs.

More recently, QGP phenomenology has also provided important evidence on the relevance of the initial state of HICs. Through fits to data, hydrodynamical simulations of the QGP expansion provide quantitative information about transport properties of the medium, such as its shear viscosity. The very small ratios of shear viscosity over entropy density obtained from both RHIC and LHC data ($\eta/s \sim 0.1$ and $\eta/s \sim 0.2$, respectively [48]) intuitively suggest a low dissipation of the dynamics mapping early and late times of the collision [49]. It is also worth mentioning that phenomenological studies of collective flow favor a non-zero value for azimuthal anisotropy in the initial state, as the traditional (geometrical) picture outlined in the previous section is not enough to explain the relatively large values of triangular flow v_3 by itself [50].

From a technical view point, the dependence on the early stages of HICs necessarily enters through the initial conditions required by hydrodynamical simulations. The multiple interactions happening during the thermalization phase drive the system to local equilibrium and determine the initial energy density and velocity profiles of the QGP. The systematic study of this fundamental input poses a huge challenge, as there is currently no consensus about the theoretical description of pre-equilibrium dynamics. Instead, the standard practice relies on the use of a broad variety of phenomenological models whose main goal is to initialize QGP simulations (see [51] for a review). The numerical values of the physical parameters defined within these models are constrained by agreement with data, sometimes varying greatly from one model to the other. Such discrepancies introduce a significant amount of uncertainty in both the precision and physical interpretation of most phenomenological studies of the expansion and cooling of QGP. Moreover, in some cases a meaningful comparison between models is not possible, as they might be based on vastly different physical pictures. The most remarkable example of this issue (and one of the focus points of the research presented in this thesis) lies in the characterization of the early event-by-event fluctuations of the energy and momentum deposited in the collision area.

Event-by-event fluctuations are a fundamental part of the early dynamics of HICs. Stretching the previously mentioned 'Little Bang' analogy, we could argue that they play a similar role as quantum fluctuations do during the inflationary period of cosmology [52, 53], triggering the large-scale matter fluctuations that eventually result in the formation of galaxies. Likewise in the context of HIC phenomenology, event-by-event fluctuations provide a natural source of energy density inhomogeneity in the initial state, which is mapped into final-state anisotropies through hydrodynamical evolution.

All the aforementioned phenomenological models include mechanisms to implement event-by-event fluctuations in the initial conditions. However, the dynamical origin and practical description of this feature vary largely from model to model. The most widely applied approach proposes reproducing these fluctuations by randomly sampling the positions of nucleons in the transverse plane. Other models achieve a similar effect by considering fluctuations only in the subnucleonic degrees of freedom. However, the outcome of these prescriptions is a partonic distribution that must be mapped onto an energy density profile –a process that is also subject to a large degree of phenomenological modeling.

In the remaining chapters of this report, we will argue that the inherent uncertainty associated to the modeling of the initial state of HICs can be reduced by application of first-principles techniques from QCD. For this purpose, we will follow the classical approach embodied in the previously discussed CGC effective theory. This framework has been extensively applied to the study of Glasma properties, providing fundamental information about its energy, momentum and topological structures [54–57]. The starting point for this kind of studies is the resolution of the classical equations of motion for the produced gluon field in the presence of two external color sources –the valence degrees of freedom of the two colliding nuclei– at an infinitesimal proper time after the collision, $\tau = 0^+$. In Part III we explicitly reproduce this calculation, showing an emerging picture of Glasma as a strongly correlated, maximally anisotropic system dominated by strong classical fields. Having computed said fields, the CGC effective theory allows us to provide explicit results quantifying the size and extent of their transverse correlations (in Part IV).

The CGC framework provides the theoretical tools to characterize event-by-event fluctuations through the calculation of correlators. In the works presented in this report we specifically focus on the one- and two-point functions of the energy, momentum, and topological charge distributions characterizing the Glasma phase. These objects correspond, respectively, to the average and variance of the transverse distributions describing said properties. The only source of fluctuations in our approach is that of the incoming valence partons, as the collision dynamics are fully deterministic under the classical approximation. This allows us to achieve analytical results that can be straightforwardly applied to phenomenological analyses of data with a minimal numerical effort.

4.5 What about thermalization?

The extremely swift decay of the Glasma state into a QGP has been a subject of open debate and intense investigation over the last years. This line of research aims at finding a mechanism that consistently matches the medium descriptions provided by CGC at the initial state and by quasi-ideal hydrodynamics at thermalization time. The task of reconciling these two frameworks is highly non-trivial, as each one presents a radically different physical picture of the medium. As will be shown in Part III, the Glasma is characterized as a coherent, highly anisotropic state dominated by classical fields, which is considerably far from being a quasi-ideal fluid in thermal equilibrium.

Within the CGC framework, the evolution of Glasma at later times is provided by the classical Yang-Mills equations, where the fields at $\tau = 0^+$ act as initial conditions. As no analytical solution has been found to this day, the computation is performed either numerically or within certain approximations. However, Yang-Mills evolution causes the system to expand and become dilute over time, in such a way that the description in terms of classical fields breaks down. From the uncertainty principle we can estimate this limit to be reached at $t \sim 1/Q_s$ (which at RHIC energies corresponds to ~ 0.2 fm/c). The results reached so far within this approach, although promising, are still far from providing a smooth matching between CGC and hydrodynamics at such an early time. For a review of this topic the reader is referred to [58, 59].

Some alternative approaches to this fundamental problem are currently being explored. For instance, on a series of recent works [60] the possibility of matching the CGC description with effective kinetic theory as an intermediate dynamical step before the hydrodynamization of the system is studied. Another alternative approach, based on the AdS/CFT correspondence, suggests that one can gain valuable insight on the thermalization problem by considering it in the context of a $\mathcal{N} = 4$ supersymmetric Yang-Mills theory [61, 62].

However, achieving a detailed description of the dynamics of thermalization is out of the scope of this thesis. Rather, our goal is to explore the properties of the strictly classical Glasma dynamics, which, as will be shown in the following chapters, already poses a quite challenging task. Despite our decision to bypass this fundamental phase of the system evolution, the results reached here are still suitable for a large variety of phenomenological applications that will be detailed later on. This ties up with a widely extended practice in the field, which consists in using the $p_\perp$-integrated distribution of particles produced at the Glasma stage to directly initialize hydrodynamic simulations of QGP. Such a strategy is valid as long as one is interested only in $p_\perp$-independent features over length scales larger than the thermalization time.

Chapter 5

The topological structure of QCD

One important feature of the classical QCD Lagrangian Eq. (1.1) is the fact that it is invariant under the combined transformations of charge conjugation (C) and parity (P), i.e. it is CP-symmetric. There are, however, CP-violating terms that could be naturally included in Eq. (1.1), as they are allowed by Lorentz and gauge invariance. Arguably the most notorious one is the so-called θ-term:

$$\mathcal{L}_\theta = \theta \frac{g^2}{32\pi^2} F_{\mu\nu}(x)\tilde{F}^{\mu\nu}(x), \tag{5.1}$$

with $F^{\mu\nu}$ and $\tilde{F}^{\mu\nu} = \frac{1}{2}\epsilon^{\mu\nu\rho\sigma}F_{\rho\sigma}$ corresponding respectively to the gluon field strength tensor and its dual. The fact that no experiment has provided any evidence of CP-violation in the QCD sector so far suggests an extremely small –or even null– value for the θ parameter of Eq. (5.1). This in turn poses a fine tuning problem for which several solutions have been proposed. Nevertheless, this issue does not only affect the self-consistency of QCD as a theory; it is in fact related to one of the long-term concerns of physics at large.

The search for signals of CP-violation in experiments is mainly motivated by one of the fundamental puzzles of particle physics: the fact that we observe much more matter than antimatter in the universe, i.e. the baryon asymmetry. Most attempts at explaining this imbalance are based on the occurrence of CP-odd fluctuations during the first instants after the Big Bang. However, the currently known sources of CP-violation within the standard model –mainly stemming from the weak sector– are too small to account for baryon asymmetry by themselves. The development of theoretical mechanisms for the generation of additional CP-odd fluctuations is thus a subject of intense research within the particle physics community.

A possible source of CP violation stems from the topological structure of QCD. As will be detailed throughout this chapter, the transitions between topologically inequivalent states of the vacuum –labeled by the so-called winding number Q_w– are closely connected to the anomalous violation of the chiral symmetry, which in turn induces the generation of CP-odd matter. Off-central HICs (those that take place with $|b_\perp| > 0$) provide an appropriate environment for the observation of such effects. These collisions give rise to large background electromagnetic fields [63], which in the presence of deconfined chirally-imbalanced matter may induce a separation of positive and negative charges along the direction of angular momentum [64] (see Fig. 5.1). This effect –known as the Chiral Magnetic Effect (CME)– thus creates a preferential direction for the emission of charged particles that would in turn translate into non-trivial azimuthal correlations in the hadron spectrum. The search for such signatures of this and other transport phenomena connected to the chiral anomaly (generically called *anomalous transport phenomena*) has been carried at both RHIC and LHC [65].

Although these experiments have provided numerous measurements that are indeed compatible with said phenomena [66–70], the presence of large background effects (e.g. transverse momentum [71] and local charge [72] conservation, which also give rise to intrinsic back-to-back correlations; and final state interactions [73]) prevent from drawing definite conclusions. Hence, there is a strong interest from the high energy QCD community in reducing this uncertainty. Significant

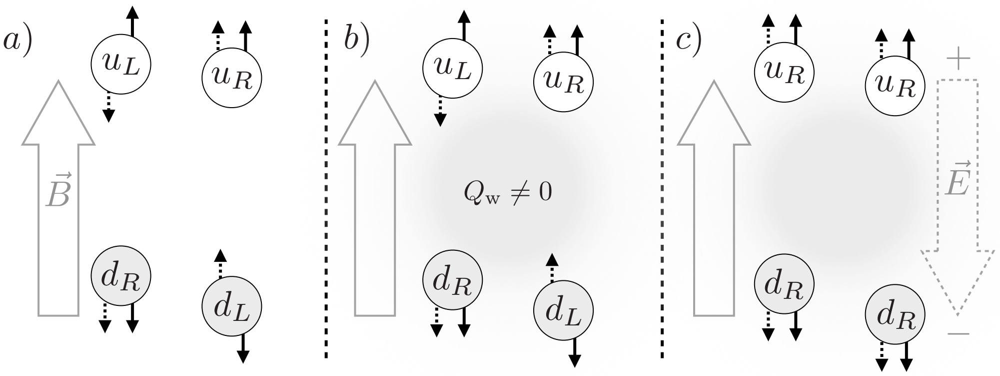

Figure 5.1: Qualitative sketch of CME [64]. The full and dashed arrows represent the spin and momentum of the quarks, respectively. The large magnetic field $\vec{B}$ induces the quarks to move along its direction. The parity of the quarks determines whether their momentum is aligned with their spin, or in the opposite direction. The initial state (a) is chirally symmetric, meaning that there are as many right-handed and left-handed quarks. In (b) the presence of a gauge configuration with non-zero Q_w gives rise to a chirally imbalanced state (c), where the movement of the quarks generates a separation of charges.

advances have been achieved on the experimental side, including the development of different detection techniques [74–77] and, most recently, the implementation of an isobaric collision program at RHIC aimed at the isolation of the CME background [78]. Still, a thorough approach to this task demands for better theoretical constraints on the dynamical origin of correlations between detected particles. With this aim in mind, in Chapter 9 we perform a detailed study of the potential contributions emerging from the initial state of HICs. As will be shown later, the event-by-event fluctuations featured in the Glasma phase play a main role in this respect. Before going into more detail about this work, it is convenient to briefly introduce the basic ideas underlying anomalous transport phenomena.

5.1 The chiral symmetry

We will first outline the concept of chirality of a particle. To that end, let us briefly return to the QCD Lagrangian:

$$\mathcal{L}_\mathrm{QCD} = \sum_f \bar{\psi}_{f,i}(i\gamma_\mu (D^\mu)_{ij} - m_f \delta_{ij})\psi_{f,j} - \frac{1}{4}F^a_{\mu\nu}F^{\mu\nu,a}, \tag{5.2}$$

where in this occasion we will consider only *light* quarks ($f = u, d, s$). Such an approximation is reasonable when considering matter at temperatures around the typical QCD scale $T \sim \Lambda_\mathrm{QCD}$, where we expect effects due to heavy quark flavors to be negligible. Note that within this effective theory we are able to study the basic constituents of all ordinary matter, since protons and neutrons are composed solely of u and d quarks. We will also momentarily neglect the mass term, thus obtaining:

$$\mathcal{L} = i\sum_f \bar{\psi}_{f,i}\gamma_\mu (D^\mu)_{ij}\psi_{f,j} - \frac{1}{4}F^a_{\mu\nu}F^{\mu\nu,a}. \tag{5.3}$$

This expression is invariant under global flavor $SU(3)_L \times SU(3)_R$ transformations:

$$\psi_{R(L)} \to \exp\left\{ i\frac{\tau_j \theta^j_{R(L)}}{2} \right\} \psi_{R(L)}, \tag{5.4}$$

also known as chiral rotations. Here τ_j are the Pauli matrices and $\theta^j_{R(L)}$ some arbitrary parameters. We also defined

$$\psi_{R(L)} = \frac{1 \pm \gamma^5}{2}\psi = P_{R(L)}\psi \tag{5.5}$$

as the right-handed and left-handed components of the quark fields, $\psi_{R(L)} = \begin{pmatrix} u_{R(L)} & d_{R(L)} & s_{R(L)} \end{pmatrix}^{\mathrm{T}}$. Performing an expansion of the quark fields of Eq. (5.3) in terms of Eq. (5.5), we obtain a Lagrangian where the right-handed and left-handed sectors are unmixed:

$$\mathcal{L} = i\bar{\psi}_R \not{D} \psi_R + i\bar{\psi}_L \not{D} \psi_L - \frac{1}{4} F^a_{\mu\nu} F^{\mu\nu,a}. \tag{5.6}$$

This expression conveys a scenario where particles with different chiralities (right- or left-handed, represented by $\psi_{R(L)}$), have an equivalent physical description, as Eq. (5.6) is trivially symmetric under chiral rotations. Although this invariance is explicitly broken by the quark mass term (which mixes chiralities), the fact that we are considering very small masses should make the chiral symmetry approximately satisfied even at low energies. However, we do not observe this behavior in nature[1], which is due to the chiral symmetry being spontaneously broken.

In order to show this, it is convenient to introduce the vector and axial symmetries. According to Noether's theorem, for each symmetry of the Lagrangian there exists an associated conserved current. We define the vector and axial currents V^μ_j, A^μ_j in terms of the Noether currents corresponding to chiral symmetry:

$$j^\mu_{V,j} = j^\mu_{R,j} + j^\mu_{L,j} \tag{5.7}$$

$$j^\mu_{A,j} = j^\mu_{R,j} - j^\mu_{L,j}\,. \tag{5.8}$$

In turn, these are associated to the following $SU(3)_V \times SU(3)_A$ transformations:

$$\psi \to \exp\left\{ i\frac{\tau_j \theta^j}{2} \right\} \psi \tag{5.9}$$

$$\psi \to \exp\left\{ i\gamma^5 \frac{\tau_j \theta^j}{2} \right\} \psi, \tag{5.10}$$

under which the massless QCD Lagrangian is invariant[2]. $SU(3)_V$ corresponds to an empirically observed symmetry of strong interactions: isospin. Conversely, the axial symmetry $SU(3)_A$ does not seem to manifest in nature in any way, and thus it was hypothesized to be spontaneously broken.

---

[1] If chiral symmetry was not broken, we should expect to find a meson with opposite parity and same mass for every member of the meson multiplets.

[2] Note that the vector and axial symmetries are just convenient rearrangements of the chiral symmetry and thus they do not provide new information about the Lagrangian. Nevertheless, they convey a more natural picture in relation to spontaneous symmetry breaking.

In general, a symmetry is spontaneously broken when it is not satisfied by the ground state of the theory, i.e. the vacuum. In the case of QCD, the vacuum is populated by quark-antiquark and gluonic fluctuations. The presence of this material medium has the two-fold effect of modifying the force law between color-charged particles (resulting in the running coupling of QCD) and, in the case of quark-antiquark pair fluctuations, breaking chiral symmetry[3]. This is only a partial breakdown –as mentioned above, the fact that we can classify the hadron spectra in $SU(3)_V$ representations motivates a violation that only affects the axial sector. The spontaneous symmetry breaking mechanism gives rise to eight pseudo-scalar Goldstone states (corresponding to the eight broken generators of the axial symmetry group) that can be identified with the lightest[4] hadronic states: π^+, π^-, π^0, K^+, K^-, K^0, $\bar{K}^0$ and η.

It is theoretically well established that the density of the 'ether' of virtual quark-antiquark pairs described above is sensitive to the conditions of bulk QCD matter in such a way that it becomes negligible at large temperatures, hence giving rise to the restoration of chiral symmetry. This process is controlled by the expectation value $\langle\bar{\phi}\phi\rangle_q$, typically referred to as the *chiral condensate*. Lattice simulations indicate that this quantity displays a smooth fall (see Fig. 5.2) that is usually interpreted as the cross-over transition between hadronic matter and the QGP.

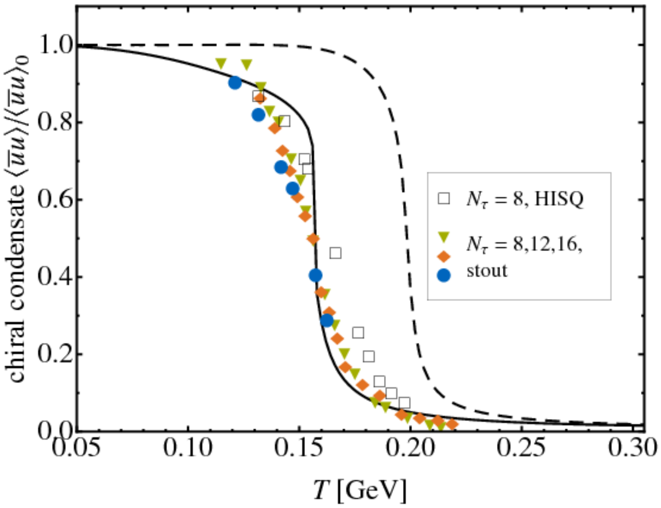

Figure 5.2: Compilation of lattice data on the temperature dependence of the chiral condensate (defined for the up quark) extracted from [80–83]. Curves obtained in the PNJL model. Figure extracted from [84].

The chiral condensate is not the only quantity proposed to be the order parameter that signals the transition towards QGP. Another notorious example is the Polyakov loop, associated to the deconfinement phase transition of QCD. The clear identification of the onset of the QGP phase –both in qualitative and quantitative grounds– is currently subject to an intense debate that is out of the scope of this thesis. For the following discussion it will suffice to bear in mind that the QGP is a chirally-symmetric phase.

---

[3] These virtual particle pairs necessarily contain a net chiral charge in order to preserve momentum conservation.

[4] There is a mass gap of about 630 MeV separating the pseudo-scalar octet from the rest of the hadron spectrum. This allows to build a low-energy effective theory where these hadrons act as the dynamical degrees of freedom (instead of quarks and gluons): the Chiral Perturbation Theory. For a brief review of this topic, see [79].

5.2 The chiral anomaly

Noether's theorem holds only at tree level. This implies that for any symmetry of the classical Lagrangian we must check whether it is broken by quantum corrections in higher orders of the theory. These symmetry violations are known as *quantum anomalies*.

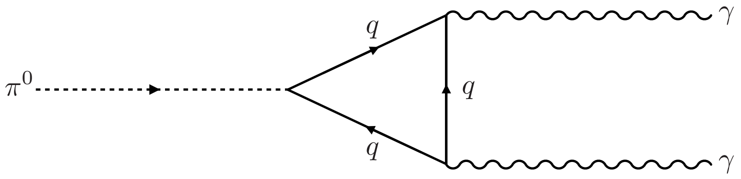

Figure 5.3: Feynman diagram representing a quark loop correction of the neutral pion decay.

Quantum anomalies in global symmetries have the effect of introducing a corrective term into the conservation equation of the corresponding current[5]. This is precisely the case of the chiral symmetry. The quantum correction represented in Fig. 5.3 introduces the following anomalous term:

$$\partial_\mu j^\mu_A = -\frac{g^2 N_f}{8\pi^2}\mathrm{Tr}\left\{F_{\mu\nu}(x)\tilde{F}^{\mu\nu}(x)\right\}. \tag{5.11}$$

Note that in this expression we combine the anomalous terms corresponding to all light flavors (hence the N_f factor). In the massless fermion limit Eq. (5.11) is the only source of chiral symmetry violation. The presence of this correction induces a transformation of left- into right-handed quarks at the following rate:

$$\frac{dN_5}{dt} \equiv \frac{d(N_R - N_L)}{dt} = \int d^3x\, \partial_\mu j^\mu_A = -\frac{g^2 N_f}{8\pi^2}\int d^3x\, \mathrm{Tr}\left\{F_{\mu\nu}(x)\tilde{F}^{\mu\nu}(x)\right\}, \tag{5.12}$$

where we defined the axial charge N_5 as the difference between the net numbers of right- (N_R) and left-handed (N_L) quarks. In order to describe the axial charge generation mechanism it is crucial to understand the structure of the gauge fields entering on the right-hand side of Eq. (5.12). This term implicitly contains different contributions to axial charge production, one of them stemming directly from the underlying topological structure of QCD.

5.3 Topological charge fluctuations

Gauge field configurations can be classified in distinct classes characterized by their corresponding value of the following topological invariant:

$$Q_\mathrm{w} = \frac{g^2}{16\pi^2}\int d^4x\, \mathrm{Tr}\left\{F_{\mu\nu}(x)\tilde{F}^{\mu\nu}(x)\right\}, \tag{5.13}$$

known as topological charge or winding number. This quantity labels degenerate but topologically inequivalent vacuum states separated by potential barriers with heights of order Λ_QCD. At low

---

[5] The situation is much more delicate when quantum anomalies affect a local gauge symmetry. In this case, both the renormalizability and unitarity of the theory get compromised, making it unusable for phenomenological purposes.

temperatures the transitions between different topological configurations require tunneling through these barriers, and they are therefore highly suppressed. Such transitions are mediated by localized field configurations called *instantons*. On the other hand, at high temperatures (such as the ones reached in the QGP phase), these transitions can be performed classically over the potential barrier, and thus they are not suppressed anymore. The corresponding field configurations are then known as *sphalerons* (for a review of the topological aspects of gauge field theories, the reader is referred to [85]).

The contribution of the topological fluctuations discussed above to the axial charge production rate can be straightforwardly obtained from Eq. (5.13) and Eq. (5.12):

$$\frac{dN_5}{dt} = -2N_f \frac{dQ_{\mathrm{w}}}{dt} = -\frac{g^2 N_f}{8\pi^2} \int d^3x \, \mathrm{Tr}\left\{ F_{\mu\nu}(x) \tilde{F}^{\mu\nu}(x) \right\}. \tag{5.14}$$

Because of this relation (and committing an abuse of language), throughout this report we treat the terms 'topological charge' and 'axial charge' in a virtually interchangeable fashion. However, let us highlight here that the former (or rather its fluctuations) represents a dynamical source for the latter.

It is convenient to rewrite Eq. (5.14) in terms of the Chern-Simons current:

$$K^\mu = \epsilon^{\mu\nu\rho\sigma} A^a_\nu \left(F^a_{\rho\sigma} + \frac{g}{3} A^b_\rho A^c_\sigma \right), \tag{5.15}$$

whose 4-divergence satisfies:

$$\dot{\nu}(x) \equiv \partial_\mu K^\mu = -\frac{1}{4} \mathrm{Tr}\left\{ F_{\mu\nu}(x) \tilde{F}^{\mu\nu}(x) \right\}. \tag{5.16}$$

The divergence of the Chern-Simons current is the main object of study of Chapter 9, whose results will be directly compared to a previous study [86] in Chapter 10. For this reason (and also to simplify our formulas), we consider it appropriate to adopt the short notation proposed in said work, $\dot{\nu}(x) \equiv \partial_\mu K^\mu$. Let us now rewrite Eq. (5.14) in terms of $\dot{\nu}$:

$$\frac{dN_5}{dt} = \frac{g^2 N_f}{2\pi^2} \int d^3x \, \dot{\nu}(x). \tag{5.17}$$

Based on this relation, we will take the divergence of the Chern-Simons current as the fundamental object controlling the generation of chirally-imbalanced matter.

5.4 Axial charge generation in HICs

As mentioned at the beginning of this chapter, chirally-imbalanced QGP in the presence of a large electromagnetic field may induce a separation of electric charges that gives rise to non-trivial correlations in the final state of HICs. This phenomenon has attracted much interest from the high energy QCD community throughout the last decade. Unfortunately, the identification of CME signals is severely hindered by the presence of large background effects. The task of reducing this uncertainty demands for a precise theoretical characterization of the different sources of axial charge.

That is precisely the aim of the study reported in Chapter 9, where we explore the potential contributions emerging from the initial stage of HICs. As will be shown, the dynamical properties of the Glasma phase (which result in a vanishing average value of $\dot{\nu}$) do not allow for direct topological charge generation. However, the event-by-event fluctuations that characterize the initial stage dynamics –albeit unrelated to the underlying topological structure of QCD– can provide sizable fluctuations of $\dot{\nu}$ that result in local imbalances of axial charge. The size and extent of these early fluctuations are characterized by the two-point correlator $\langle \dot{\nu}_0(x_\perp)\dot{\nu}_0(y_\perp)\rangle$, which we compute in the CGC framework. This object is of particular importance for those hydrodynamical descriptions that mimic the effects induced by the chiral anomaly [87–89] since event-by-event fluctuations are expected to contribute a significant fraction of the initial axial charge densities.

This source of topological charge competes with the previously discussed sphaleron transitions. Although the latter are known to dominate axial charge production in the QGP phase, throughout the pre-equilibrium stage both mechanisms are likely to yield a significant contribution. It has been argued that in the early stage of the collision sphaleron transitions are suppressed due to the boost invariance of the generated fields [90]. However, as the system evolves towards thermalization and boost invariance wears down, they would be significantly enhanced [90,91]. Whether or not event-by-event fluctuations dominate over this or other mechanisms of axial charge production –like thermal fluctuations of the field strength– is out of the scope of this thesis. For more exhaustive discussions on this topic, the reader is referred to the aforementioned studies. It any case, it is essential to understand and quantitatively constrain the influence of each source in the experimentally observed correlations.

Part III

Theoretical characterization of the Glasma phase

They're suspended like a prism splitting floodlight
To poles of primary colors clawing the veil of the vacuum

— Battles in "Ddiamondd"

In this part we reproduce the analytical computation of the Glasma fields generated immediately after an ultra-relativistic HIC in the MV model. Such task requires solving the Yang-Mills equations with one and two sources (Chapter 6). We then compute the energy-momentum tensor and the divergence of the Chern-Simons current of the Glasma at an infinitesimal proper time $\tau = 0^+$ (Chapter 7). These objects respectively characterize the early deposition of energy density and the generation of axial charge in the plane transverse to the collision axis. The calculations shown in this part serve as preamble and starting point of Part IV, where the main results of the thesis are presented.

Chapter 6

Solution of the Yang-Mills equations at $\tau = 0^+$

In the MV model the description of the medium generated in a collision of two large ultra-relativistic nuclei is formulated via the Yang-Mills equations with two external sources:

$$[D_\mu, F^{\mu\nu}] = J_1^\nu + J_2^\nu, \tag{6.1}$$

where indices 1, 2 label the colliding nuclei. This expression poses a quite crucial problem, namely that it has no general analytical solution. However, in the inner surface of the light-cone, $\tau = 0^+$ (i.e. an infinitesimal proper time after the collision), it is possible to find an analytical expression of the gauge fields[1]. In order to do so, it is convenient to divide the space-time into four quadrants as indicated in Fig. 6.1.

The MV model provides the appropriate framework to compute the gauge fields that characterize each nuclei before the collision. As they inhabit causally disconnected regions of space-time (quadrants 1 and 2), the dynamics of their corresponding fields are described independently by the Yang-Mills equations with a single source. This is the case we will study on Section 6.1. Further on we will detail how these fields define the boundary conditions for the solution in the future light-cone (quadrant 3), where we need to take into account both color sources simultaneously. As for the points where both x^+, x^- are negative (quadrant 0), they represent a region where none of the projectiles have arrived yet. We will see that gauge freedom allows us to choose gluon fields to be zero in this region.

The calculations shown in this chapter were first performed in [92] and later revisited by many other authors. In the following section we will discuss some of the most relevant approaches proposed in the literature, pointing out their fundamental differences.

---

[1] If our goal was to study the generated medium at any value of τ, we would need to turn to either analytical or numerical approximations. The solution at $\tau = 0^+$ (the focus of the present chapter) is an appropriate starting point for such methods.

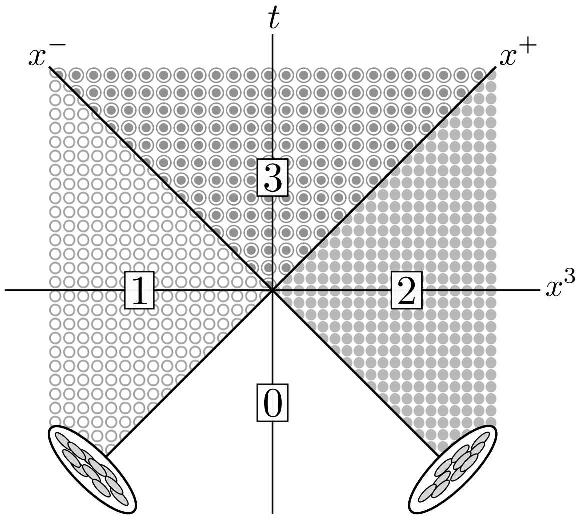

Figure 6.1: Space-time diagram of the collision of two large ultra-relativistic nuclei. The two diagonal lines represent their trajectories (located on top of the light cone).

6.1 Gluon fields carried by a single nucleus

Let us first focus on the case of a single nucleus moving in the positive x^3 direction. We start by coming back to the Yang-Mills equations with one source:

$$[D_\mu, F^{\mu\nu}] = \partial_\mu F^{\mu\nu} - ig[A_\mu, F^{\mu\nu}] = J^{\nu,a}t^a, \tag{6.2}$$

which comprise the dynamical relation between 'fast' and 'soft' nuclear degrees of freedom (valence quarks and gluon fields, respectively) in the MV model. Due to the identity $[D_\mu, [D_\nu, F^{\nu\mu}]] = 0$, these equations imply the covariant conservation of the current:

$$[D_\mu, [D_\nu, F^{\nu\mu}]] = [D_\mu, J^\mu] = \partial_\mu J^\mu - ig\,[A_\mu, J^\mu] = 0, \tag{6.3}$$

where $J^\nu \equiv J^{\nu,a}t^a$ (from now on we assume contracted color indices unless otherwise stated). This equation encodes the effect that radiating the gauge fields has over the color sources and, from a technical point of view, significantly constrains the analytical behavior of the function J^μ. By choosing J^μ to generate a color current only in the + direction (eikonal approximation), we have that Eq. (6.3) yields:

$$\frac{\partial}{\partial x^+} J^+ = ig\left[A^-, J^+\right], \tag{6.4}$$

thus setting its light-cone time evolution. Let us write the solution to this equation by assuming that the x^+-independent ansatz Eq. (3.2) corresponds to J^μ at some initial value x_0^+:

$$J^{\mu,a}(x^+, x^-, x_\perp) = W(x^+, x_0^+) J^{\mu,a}(x_0^+, x^-, x_\perp) W^\dagger(x^+, x_0^+) = \delta^{\mu+} W \rho^a(x_\perp, x^-) W^\dagger. \tag{6.5}$$

Here we introduced the gauge links W. These operators, whose role is to maintain covariant conservation, evolve the color source densities from a certain reference point x_0^+ to x^+. In the eikonal approximation they have the following form:

$$W(x^+, x_0^+; x^-, x_\perp) = \mathrm{P}^+ \exp\left\{ ig \int_{x_0^+}^{x^+} dz^+ A^-(z^+, x^-, x_\perp) \right\}, \tag{6.6}$$

and are called Wilson lines[2]. We will come back to this object later on. The Yang-Mills equations get very complicated when substituting Eq. (6.5) into them, as they become non-local in x^+. Instead, we might choose to work in a gauge where A^- vanishes and in turn $W=1$, thus making our color current static. Note that in such a gauge Eq. (6.4) becomes the ordinary current conservation $\partial_\mu J^\mu = 0$, which is trivially satisfied by Eq. (3.2) and decoupled from the Yang-Mills equations. Then, Eq. (6.2) can be solved by proposing a purely transverse ansatz A^i. This is the traditional procedure, followed in [92–94].

However, in this section we will apply the method first presented in [95], where the covariant gauge (defined by $\partial_\mu \tilde{A}^\mu = 0$) is temporarily adopted in order to solve the Yang-Mills equations in a more systematic approach. We use a tilde to denote the gluon field $\tilde{A}$ and the color source density $\tilde{\rho}$ in the covariant gauge[3], where Eq. (6.2) takes the following form:

$$\Box \tilde{A}^\nu = J^\nu + ig\Big[\tilde{A}_\mu, F^{\mu\nu} + \partial^\mu \tilde{A}^\nu\Big]. \tag{6.7}$$

The system composed of Eq. (6.4) and Eq. (6.7) can be solved iteratively by expanding in orders of $\tilde{\rho}$. This is convenient as both $F^{\mu\nu}$ and $\tilde{A}^\mu$ are at least order one in $\tilde{\rho}$, which makes the commutators in these equations at least one order higher than the rest of the terms (and therefore do not appear in the first iteration). Assuming that Eq. (3.2) corresponds to the lowest non-trivial order of the color current[4], the order $\tilde{\rho}^1$ of Eq. (6.4) reads:

$$\partial^- J^+_{(1)} = 0, \tag{6.8}$$

which is automatically satisfied due to our ansatz being light-cone time independent. Then, Eq. (6.7) becomes:

$$-\nabla_\perp^2 \tilde{A}^\nu_{(1)} = J^\nu_{(1)} = \delta^{\nu +} \tilde{\rho}(x^-, x_\perp). \tag{6.9}$$

This is a Poisson's equation, which can be trivially solved in momentum space: $\tilde{A}^\nu_{(1)} = \delta^{\nu+}\tilde{\rho}/p_\perp^2$. In coordinate space the solution usually appears as:

$$\tilde{A}^\nu_{(1)} = -\delta^{\nu+} \frac{1}{\nabla_\perp^2} \tilde{\rho}(x^-, x_\perp), \tag{6.10}$$

which is a convenient abuse of mathematical language. The actual explicit expression in coordinate space is:

$$\tilde{A}^\nu_{(1)}(x^-, x_\perp) = \delta^{\nu+} \int \frac{d^2 z_\perp}{2\pi} \log(|z_\perp - x_\perp|) \tilde{\rho}(x^-, z_\perp). \tag{6.11}$$

---

[2] On Appendix D we show a detailed derivation of the Wilson line based on the solution of a slightly simpler equation, Eq. (6.21).

[3] Both must be affected by the change of gauge in order to keep the gauge invariance of the Yang-Mills Lagrangian (as can be inferred from the coupling term in Eq. (3.3)).

[4] Note that due to the feedback between gauge fields and currents encoded in Eq. (6.3), J^ν could in principle receive higher order contributions in $\tilde{\rho}$.

This expression is obtained by solving the Poisson's equation via the Green's function for the 2-dimensional Laplace operator G, which satisfies:

$$\partial_\perp^2 G(x_\perp - y_\perp) = \delta(x_\perp - y_\perp). \tag{6.12}$$

This function admits a simple Fourier representation:

$$G(x_\perp - y_\perp) = -\int \frac{d^2k_\perp}{(2\pi)^2} \frac{e^{ik_\perp \cdot (x_\perp - y_\perp)}}{k_\perp^2}, \tag{6.13}$$

that allows us to rewrite Eq. (6.11) as the following convolution:

$$\tilde{A}^\nu_{(1)}(x^-, x_\perp) = \delta^{\nu +}\int dz_\perp^2 G(z_\perp - x_\perp)\tilde{\rho}(x^-, z_\perp). \tag{6.14}$$

This notation will prove useful later on. At order $\tilde{\rho}^2$ the equation system reads:

$$\Box \tilde{A}^\nu_{(2)} = J^\nu_{(2)} + ig\left[\tilde{A}_{(1)\mu}, F^{\mu\nu}_{(1)} + \partial^\mu \tilde{A}^\nu_{(1)}\right] \tag{6.15}$$

$$\partial_\mu J^\mu_{(2)} = 0. \tag{6.16}$$

The latter reduces to $\partial_+ J^+_{(2)} = 0$ if we assume that the current is generated only in the + direction to all orders in $\tilde{\rho}$ (the factor $\delta^{\mu +}$ would then be common to all terms of the $\tilde{\rho}$ expansion). If we impose this term to vanish in the remote past ($x^+ \to -\infty$), the solution is $J^\mu_{(2)} = 0$. As for Eq. (6.15), it takes the following form:

$$\Box \tilde{A}^\nu_{(2)} = 0. \tag{6.17}$$

As the commutator vanishes, there are no sources for this term. By imposing that it also vanishes in the remote past, we have $\tilde{A}^\nu_{(2)} = 0$. This argument can be extended to all orders in $\tilde{\rho}$, resulting in:

$$J^\mu(x^-, x_\perp) = \delta^{\mu +}\tilde{\rho}(x^-, x_\perp) \tag{6.18}$$

$$\tilde{A}^\mu(x^-, x_\perp) = -\delta^{\mu +}\frac{1}{\nabla_\perp^2}\tilde{\rho}(x^-, x_\perp) = \delta^{\mu +}\int dz_\perp^2 G(z_\perp - x_\perp)\tilde{\rho}(x^-, z_\perp). \tag{6.19}$$

Although the covariant gauge provides a systematic way of obtaining the classical fields $\tilde{A}^\mu$, for the upcoming calculations we will find it more convenient to work in the light-cone gauge, defined by the condition $A^+ = 0$. We must find the appropriate gauge rotation:

$$A^\mu = \Omega^\dagger \tilde{A}^\mu \Omega + \frac{i}{g}\Omega^\dagger \partial^\mu \Omega. \tag{6.20}$$

The light-cone gauge condition $A^+ = 0$ yields the following equation for the SU(N_c) element Ω:

$$\partial^+ \Omega = ig\tilde{A}^+ \Omega. \tag{6.21}$$

The solution to this equation is the following ordered exponential (see Appendix D for an explicit derivation):

$$\Omega(x^+, x^-, x_\perp) = \Theta(x^+, x_\perp)\,\mathrm{P}^- \exp\left\{ig\int_{x_0^-}^{x^-} dz^- \tilde{A}^+(z^-, x_\perp)\right\} \equiv \Theta(x^+, x_\perp)\, U(x^-, x_\perp), \tag{6.22}$$

which includes the Wilson line $U(x^-, x_\perp)$. Physically, this object encodes the effect of the interaction with the classical gluon fields over the fast-moving partons in the eikonal approximation (i.e. a rotation in color space). The lower integration limit x_0^- is arbitrary, being determined by the chosen condition for gauge fixing. By only imposing the light-cone gauge condition we get the following fields:

$$A^+ = 0 \tag{6.23}$$

$$A^- = \frac{i}{g}\Theta^\dagger \partial^- \Theta \tag{6.24}$$

$$A^i = \frac{i}{g}\left(\Theta^\dagger U^\dagger (\partial^i U)\Theta + \Theta^\dagger \partial^i \Theta\right). \tag{6.25}$$

As in Eq. (6.21) the factor Θ cancels, the condition $A^+ = 0$ does not constrain Θ in any way and thus the transformation is still undetermined. This residual gauge freedom allows us to choose $\Theta \equiv 1$, resulting in:

$$\begin{aligned} A^\pm &= 0 \\ A^i &= \frac{i}{g} U^\dagger \partial^i U, \end{aligned} \tag{6.26}$$

which is a pure gauge field (i.e. a gauge transformation of the vacuum) in the transverse plane. As mentioned above, there is some arbitrariness stemming from the initial point x_0^-. Different choices of x_0^- give us solutions A^i connected by gauge transformations. We shall adopt $x_0^- \to -\infty$, which corresponds to retarded boundary conditions in x^- ($A^i \to 0$ with $x^- \to -\infty$). Coming back to Fig. 6.1, we see that this choice implies that the fields in quadrant 0 (the backward light cone) should vanish. As no color sources have yet arrived to this region, the dynamics there are described by the homogeneous Yang-Mills equations $[D_\mu, F^{\mu\nu}] = 0$, which also admit a solution of the form Eq. (6.26). We can choose this solution to be 0, hence agreeing with the retarded boundary conditions of quadrants 1, 2 and giving rise to a discontinuity between gauge fields located on the sheet $x^- = 0$.

The physical interpretation of the discontinuity typically stems from the assumption that the x^--dependence of the color sources factorizes as $J^\mu = \delta^{+\mu}\delta(x^-)\rho(x_\perp)$. This expression suggests that, due to the Lorentz contraction experienced by relativistic nuclei, the valence charges are confined on the light-cone surface $x^- = 0$. In such a scenario this infinitely thin sheet contains all physical information and is the only region of space-time where the field strength F^{ij} does not vanish. Although in our derivation we chose not to make any explicit assumption about the longitudinal structure of the nuclei (other than a certain narrowness around $x^- = 0$), we will draw on the prior considerations to rewrite Eq. (6.26) as:

$$A^i = \theta(x^-)\frac{i}{g} V^\dagger \partial^i V \equiv \theta(x^-)\alpha^i(x_\perp), \tag{6.27}$$

where we take the limit $x^- \to \infty$ in the Wilson lines ($V(x_\perp) \equiv U(\infty, x_\perp)$) and factorize the x^--dependence of A^i to a theta function. This solution makes explicit our choice to have vanishing gauge fields in quadrant 0. Note that this is not the only option: instead of a θ, one could in principle choose a smoother function providing that it vanishes at $x_0^- \to -\infty$. However, taking Eq. (6.27) has the advantage of providing an analytically simple approximation that in turn conveys an appropriate physical picture in the high energy limit.

The transverse differentiation present in Eq. (6.26) and Eq. (6.27) can be performed explicitly (which we do in Appendix E). However, the fact that F^{i+} has a particularly simple expression in the covariant gauge yields a good shortcut to the calculation of A^i. We first notice that, in the light-cone gauge, $F^{i+}=-\partial^+ A^i$, so:

$$A^i = -\int_{-\infty}^{x^-} dz^- F^{i+}(z^-). \tag{6.28}$$

We relate F^{i+} to $\tilde{F}^{i+}$ via a gauge transformation (driven by the Wilson lines):

$$F^{i+} = U^\dagger \tilde{F}^{i+} U = U^\dagger \partial^i \tilde{A}^+ U = -U^\dagger \frac{\partial^i \tilde{\rho}}{\nabla_\perp^2} U, \tag{6.29}$$

and thus:

$$A^i = \int_{-\infty}^{x^-} dz^- U^\dagger(z^-, x_\perp) \frac{\partial^i \tilde{\rho}(z^-, x_\perp)}{\nabla_\perp^2} U(z^-, x_\perp). \tag{6.30}$$

Rewriting this expression in the same way as Eq. (6.27) we get to our final result:

$$A^i = \theta(x^-) \int_{-\infty}^{\infty} dz^- U^\dagger(z^-, x_\perp) \frac{\partial^i \tilde{\rho}(z^-, x_\perp)}{\nabla_\perp^2} U(z^-, x_\perp) \equiv \theta(x^-) \alpha^i(x_\perp). \tag{6.31}$$

This calculation provides the starting point for the characterization of the gluon fields formed at the initial stage of a collision between two ultra-relativistic nuclei, which is the topic of the following section.

6.2 Glasma fields at $\tau = 0^+$

We now consider the collision between the nucleus studied in the previous section and another one moving in the negative x^3 direction (which we label respectively as nuclei 1 and 2). Let us (again) start by rewriting the Yang-Mills equations:

$$[D_\mu, F^{\mu\nu}] = \sum_{m=1,2} W[A_m](x, z_m(x))\, J_m^\nu(z_m(x))\, W^\dagger[A_m](x, z_m(x)), \tag{6.32}$$

where the factors $W[A_m](x, z_m(x))$ are the gauge link operators introduced in Eq. (6.5) (evolving the currents of each nucleus from a certain reference point $z_{1,2}(x) = x|_{x^\pm=0}$ to x) and $A_{1,2}$ are the classical fields carried by each nucleus. As mentioned at the beginning of this chapter, solving these equations demands that we distinguish between those regions of space-time that are in causal contact with the collision ($x^0=0$) and those that are not. Let us first focus on the latter, which correspond to the space-time points outside the light cone (quadrants 1 and 2 in Fig. 6.1). In the present section we will work in the Fock-Schwinger gauge, which acts as a sort of interpolation of the light-cone gauges of each nuclei. This gauge is defined by the following condition:

$$(x^+ A^- + x^- A^+)/\tau = 0. \tag{6.33}$$

It is easy to check that the solution found in the previous section still holds in the Fock-Schwinger gauge. As we did before, we start from the covariant gauge solution Eq. (6.19) and perform a transformation:

$$A^\mu = \Omega^\dagger \tilde{A}^\mu \Omega + \frac{i}{g} \Omega^\dagger \partial^\mu \Omega. \tag{6.34}$$

A trivial way to satisfy Eq. (6.33) is to have both $A^+ = A^- = 0$. We can get A^- to vanish simply by taking Ω as light-cone time independent. In order to make $A^+ = 0$ we must solve Eq. (6.21), which, as shown earlier, yields:

$$\Omega(x^-, x_\perp) \equiv \Theta(x_\perp)\, U(x^-, x_\perp), \tag{6.35}$$

with $U(x^-, x_\perp)$ given by Eq. (6.22) and $\Theta(x_\perp)$ an arbitrary function that, again, we choose to be $\Theta(x_\perp) = 1$. Therefore, we arrive at the same result obtained in the light-cone gauge, Eq. (6.31). The case of nucleus 2, moving in the negative x^3 direction (with very large p^-), yields identical expressions up to an index sign inversion:

$$\begin{aligned} A_2^{\pm} &= 0 \\ A_2^i &= \theta(x^+)\alpha_2(x_\perp), \end{aligned}$$

where:

$$\begin{aligned} \alpha_2(x_\perp) &= \int_{-\infty}^{\infty} dz^+ U_2^\dagger(z^+, x_\perp) \frac{\partial^i \tilde{\rho}_2(z^+, x_\perp)}{\nabla_\perp^2} U_2(z^+, x_\perp) \\ U_2(x^+, x_\perp) &= P^+ \exp\left\{ ig \int_{-\infty}^{x^+} dz^+ \tilde{A}_2^-(z^+, x_\perp) \right\} \\ \tilde{A}_2^\nu(x^+, x_\perp) &= -\delta^{\nu -} \frac{1}{\nabla_\perp^2} \tilde{\rho}_2(x^+, x_\perp). \end{aligned}$$

These fields have the property of making the gauge links in the Yang-Mills equations drop out, which allows us to rewrite them simply as:

$$[D_\mu, F^{\mu\nu}] = J^\nu, \tag{6.36}$$

with:

$$J^{\pm} = \rho_{1,2}(x^{\mp}, x_\perp) \tag{6.37}$$

$$J^i \; = 0. \tag{6.38}$$

The solution found for these equations outside the light cone can be compactly expressed as:

$$A^{\pm} = 0 \tag{6.39}$$

$$A^i \; = \theta(x^-)\theta(-x^+)\alpha_1^i(x_\perp) + \theta(x^+)\theta(-x^-)\alpha_2^i(x_\perp). \tag{6.40}$$

The new θ factors account for the regions of space-time where the field generated by each nucleus exists (quadrants 1 and 2 for nuclei 1 and 2, respectively). As these regions of space-time are causally disconnected, the Yang-Mills equations are solved separately for each nucleus without interference (see previous section). However, in the forward light-cone we must take into account both nuclei simultaneously, as they are in causal contact. In this region the best one can do analytically is to obtain the gauge fields just above the forward light-cone, at a proper time $\tau = 0^+$. As the valence color charge densities vanish everywhere except at the very light-cone, in this region the Yang-Mills equations become homogeneous:

$$[D_\mu, F^{\mu\nu}] = 0. \tag{6.41}$$

An appropriate strategy to find a solution consists in proposing the following boost invariant ansatz (see Fig. 6.2):

$$\begin{aligned} A^{\pm} &= \pm x^{\pm}\alpha(\tau=0^+, x_\perp) \\ A^{i} &= \alpha^{i}(\tau=0^+, x_\perp), \end{aligned} \tag{6.42}$$

and invoking a physical 'matching condition' that requires the Yang-Mills equations to be regular at $\tau=0$. As anticipated, this implies using the gauge fields outside the light-cone Eq. (6.40) as boundary conditions. Let us first write Eq. (6.41) in terms of α and α^i. In order to do this, we compute the elements of the field strength tensor $F^{\mu\nu}$:

$$\begin{aligned} F^{+-} &= -\frac{\partial}{\partial x^-}(x^-\alpha) - \frac{\partial}{\partial x^+}(x^+\alpha) = -\frac{1}{\tau}\left(2\tau\alpha + \tau^2\partial_\tau\alpha\right) = -\frac{1}{\tau}\partial_\tau(\tau^2\alpha) \\ F^{i\pm} &= \pm\, x^{\pm}\partial^i\alpha - \frac{\partial\alpha}{\partial\tau}\frac{\partial\tau}{\partial x^{\mp}} \mp ig\, x^{\pm}\left[\alpha^i,\alpha\right] = -x^{\pm}\left(\frac{1}{\tau}\,\partial_\tau\alpha^i \mp \left[D^i,\alpha\right]\right) \\ F^{ij} &= \partial^i\alpha^j - \partial^j\alpha^i - ig\left[\alpha^i,\alpha^j\right]. \end{aligned} \tag{6.43}$$

It will prove useful to adopt proper-time τ and rapidity $\eta = \frac{1}{2}\log\left(x^+/x^-\right)$ as the coordinates inside the light-cone. This is known as the comoving coordinate system (see Appendix B for an introduction). Note that this coordinate system is quite convenient for our ansatz, as we have $A^\tau = 0$ and $A^\eta = \alpha(\tau, x_\perp)$. In order to obtain $F^{\mu\nu}$ in the comoving system we need to perform the transformation $F^{\mu\nu}(\tau,\eta,\perp) = \frac{\partial x^\mu}{\partial x^\rho}\frac{\partial x^\nu}{\partial x^\sigma}F^{\rho\sigma}(+,-,\perp)$. We get the following non-trivial components:

$$\begin{aligned} F^{\tau\eta} &= \frac{\partial\tau}{\partial x^+}\frac{\partial\eta}{\partial x^-}F^{+-} + \frac{\partial\tau}{\partial x^-}\frac{\partial\eta}{\partial x^+}F^{-+} = \frac{1}{\tau^2}\partial_\tau(\tau^2\alpha) \\ F^{\tau i} &= \frac{\partial\tau}{\partial x^\pm}\frac{\partial x^i}{\partial x^\sigma}F^{\pm\sigma} = \frac{x^-}{\tau}F^{+i} + \frac{x^+}{\tau}F^{-i} = \partial_\tau\alpha^i \\ F^{\eta i} &= \frac{\partial\eta}{\partial x^\pm}\frac{\partial x^i}{\partial x^\sigma}F^{\pm\sigma} = \frac{1}{2}\frac{1}{x^+}F^{+i} - \frac{1}{2}\frac{1}{x^-}F^{-i} = -\left[D^i,\alpha\right]. \end{aligned} \tag{6.44}$$

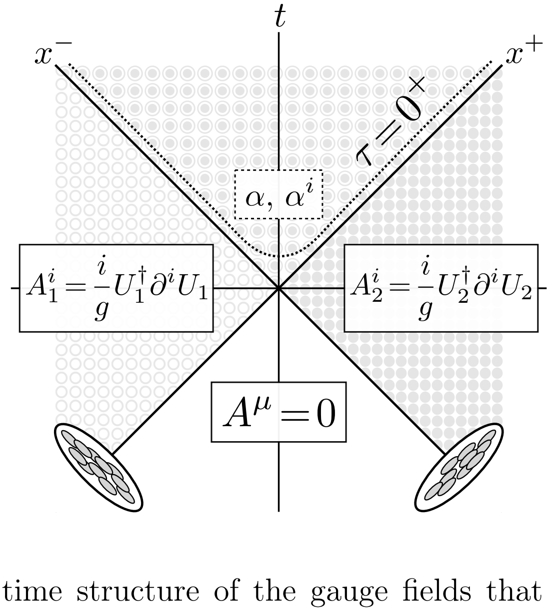

Figure 6.2: Sketch of space-time structure of the gauge fields that describe high energy nuclear collisions. In the forward light cone we indicate the ansatz proposed for $\tau = 0^+$ (Eq. (6.42)).

Now, expanding the homogeneous Yang-Mills equations $\partial_\mu F^{\mu\nu} - ig\left[A_\mu, F^{\mu\nu}\right] = 0$ in their $(\tau,\, \eta)$ components we get:

$$\frac{1}{\tau}\partial_\tau(\tau F^{\tau\nu}) + ig\tau^2\left[\alpha, F^{\eta\nu}\right] + \left[D_i, F^{i\nu}\right] = 0. \tag{6.45}$$

Note that to obtain the previous expansion we have made use of the formula for the divergence operator in the comoving coordinate system (see Appendix B):

$$\nabla \cdot A = \partial_\mu A^\mu = \frac{1}{\tau}\left(\partial_\tau(\tau A^\tau) + \partial_\eta A^\eta + \partial_i(\tau A^i)\right). \tag{6.46}$$

The separate components of Eq. (6.45) yield:

$$\begin{aligned}
&\nu = \tau \longrightarrow ig\tau\left[\alpha, \partial_\tau\alpha\right] - \frac{1}{\tau}\left[D^i, \partial_\tau\alpha^i\right] = 0\\
&\nu = \eta \longrightarrow \frac{1}{\tau}\partial_\tau\frac{1}{\tau}\partial_\tau(\tau^2\alpha) - \left[D^i, \left[D^i, \alpha\right]\right] = 0\\
&\nu = j \longrightarrow \frac{1}{\tau}\partial_\tau(\tau\partial_\tau\alpha^j) - ig\tau^2\left[\alpha, \left[D^j, \alpha\right]\right] - \left[D^i, F^{ij}\right] = 0.
\end{aligned} \tag{6.47}$$

By requiring the regularity of the Yang-Mills equations at $\tau = 0$ we obtain the boundary conditions generated by the sources. To do so we must consider the gauge field over the entire space-time, which takes the following form:

$$\begin{aligned}
A^+ &= \theta(x^+)\theta(x^-)x^+\alpha(\tau, x_\perp)\\
A^- &= -\theta(x^+)\theta(x^-)x^-\alpha(\tau, x_\perp)\\
A^i &= \theta(x^-)\theta(-x^+)\alpha_1^i(x_\perp) + \theta(x^+)\theta(-x^-)\alpha_2^i(x_\perp) + \theta(x^+)\theta(x^-)\alpha^i(\tau, x_\perp).
\end{aligned} \tag{6.48}$$

Substituting Eq. (6.48) in the Yang-Mills equations and taking the limit $x^\pm \to 0$ we encounter some singularities that disappear providing that:

$$\alpha^i(\tau = 0^+, x_\perp) = \alpha_1^i(x_\perp) + \alpha_2^i(x_\perp) \tag{6.49}$$

$$\alpha(\tau = 0^+, x_\perp) = \frac{ig}{2}\left[\alpha_1^i(x_\perp), \alpha_2^i(x_\perp)\right]. \tag{6.50}$$

The Yang-Mills equations Eq. (6.47), along with the conditions Eq. (6.49), Eq. (6.50) pose a boundary value problem whose general solution is not known yet. Several approximations of both analytical and numerical nature have been applied in the literature for the evolution in τ. However, this is out of the scope of the work presented in this thesis, which is focused in the properties of the Glasma fields at $\tau = 0^+$.

Eq. (6.49) and Eq. (6.50) reveal a rather non-trivial physical picture of the collision process and the resulting gluon fields at early times. As the two sheets of color charge pass through each other, the ensuing transverse component arises from the sum of the gluon fields they carry. Moreover, a longitudinal component $A^\eta = \alpha$ emerges as a consequence of the non-linear character of the Yang-Mills equations. From these expressions we can compute the Glasma chromo-electric and -magnetic fields, defined as:

$$E^i = -F^{0i} \tag{6.51}$$

$$B^k = \frac{1}{2}\epsilon^{ijk}F^{ij}. \tag{6.52}$$

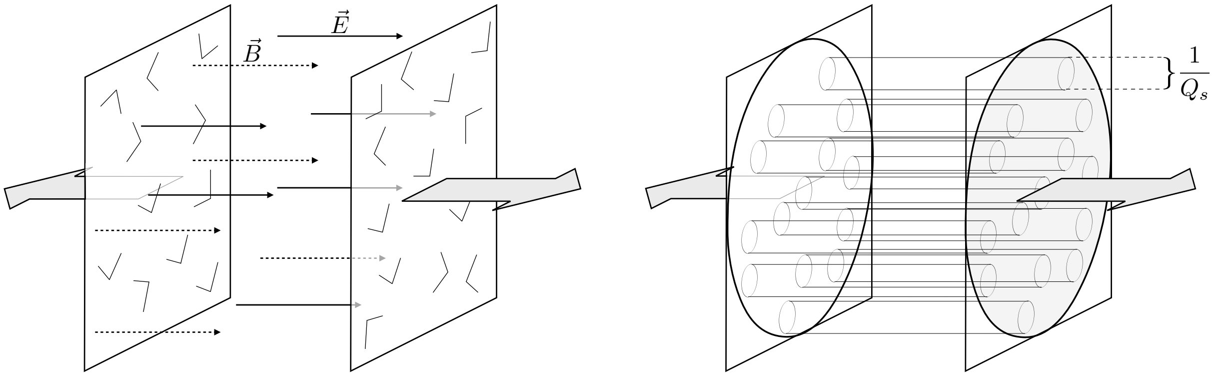

Figure 6.3: LEFT: Representation of chromo-electric and -magnetic fields formed after the collision of two ultra-relativistic hadrons. RIGHT: Schematic picture of Glasma flux tubes.

The i, j, k indices correspond to the spatial Cartesian coordinates, which we denote as 1, 2 and $3 = z$. To compute these fields at $\tau = 0^+$ we substitute Eq. (6.49) and Eq. (6.50) in the previous definitions and take the limit $x^\pm \to 0$. Remarkably, only the longitudinal components of both fields survive:

$$E^z(\tau = 0^+) = -ig\delta^{ij} \left[\alpha_1^i(x_\perp), \alpha_2^j(x_\perp)\right] = 2A^\eta \tag{6.53}$$

$$B^z(\tau = 0^+) = -ig\epsilon^{ij} \left[\alpha_1^i(x_\perp), \alpha_2^j(x_\perp)\right] . \tag{6.54}$$

(See Appendix F for an explicit derivation). At $\tau = 0^+$ the color charge sheets become sources for chromo-electric and -magnetic fields flowing in parallel to the collision axis. This peculiar configuration of boost-invariant longitudinal fields motivates the Glasma flux tube picture (see right panel of Fig. 6.3), which predicts relatively short-range transverse correlations (of order $1/Q_s$ rather than $1/\Lambda_{\text{QCD}}$) [96]. In the following chapter we will see how this structure is at the origin of a series of remarkable features of the Glasma phase.

Summary:

- In this chapter we reproduce the calculation of the gauge fields representing the Glasma phase generated immediately after a highly energetic collision of two large nuclei.
- For this task, we first compute the gluon fields carried by the nuclei before the collision moment in the MV model.
- Then, we solve the Yang-Mills equations with two sources at an infinitesimal proper time after the collision, $\tau = 0^+$.
- The Glasma fields are obtained as boundary conditions for the general resolution of the Yang-Mills equations (at larger values of τ).
- Moreover, we compute the corresponding chromo-electric and -magnetic fields. The characteristic longitudinal structure featured by these fields motivates a physical picture of the Glasma reminiscent of strings or flux tubes stretching between the crossing nuclei.

Chapter 7

Early properties of the Glasma

In this chapter we will compute the Energy-Momentum Tensor $T^{\mu\nu}$ and the divergence of the Chern-Simons current $\dot{\nu}$ corresponding to the previously obtained gauge fields. These objects characterize different properties of the Glasma phase, namely the energy and momenta carried by the classical fields (in the case of $T^{\mu\nu}$) and the rate of axial charge generation (in the case of $\dot{\nu}$). As will be detailed in subsequent chapters of the thesis, these aspects of Glasma are relevant in a variety of phenomenological studies. The calculations presented here constitute a preliminary step for the computation of correlators (Part IV), which provide the statistical behavior of said quantities over a randomly fluctuating background of color sources.

7.1 The Energy-Momentum Tensor of Glasma at $\tau = 0^+$

The Energy-Momentum Tensor $T^{\mu\nu}$ is a mathematical object that contains all information about the density, flux density, energy and momentum of a field. Its components are:

$$\begin{array}{cc} & \begin{array}{cc} \text{Energy density} & \text{Momentum density} \end{array} \\ \text{Momentum density} & \left(\begin{array}{c|ccc} \boxed{T^{00}} & T^{01} & T^{02} & T^{03} \\ \hline T^{10} & T^{11} & T^{12} & T^{13} \\ T^{20} & T^{21} & T^{22} & T^{23} \\ T^{30} & T^{31} & T^{32} & T^{33} \end{array}\right) \\ & \text{Momentum flux} \end{array} . \tag{7.1}$$

In a Yang-Mills theory this operator can be expressed in terms of the field strength tensor $F^{\mu\nu,a}$ as:

$$T^{\mu\nu} = \frac{1}{4} g^{\mu\nu} F^{\alpha\beta,a} F^{a}_{\alpha\beta} - F^{\mu\alpha,a} F^{\nu,a}_{\ \alpha}, \tag{7.2}$$

with the metric tensor defined as $g^{\mu\nu} = [\mathrm{diag}(1,-1,-1,-1)]^{\mu\nu}$ in the Cartesian coordinate system. The previous formula can be written in terms of the color-contracted field strength tensor ($F^{\mu\nu} \equiv F^{\mu\nu,a} t^a$) by means of a color trace:

$$\begin{aligned} 2\,\mathrm{Tr}\left\{\frac{1}{4} g^{\mu\nu} F^{\alpha\beta} F_{\alpha\beta} - F^{\mu\alpha} F^{\nu}_{\ \alpha}\right\} &= 2\,\mathrm{Tr}\left\{\frac{1}{4} g^{\mu\nu} F^{\alpha\beta,a} t^a F^{b}_{\alpha\beta} t^b - F^{\mu\alpha,a} t^a F^{\nu,b}_{\ \alpha} t^b\right\} \\ &= 2\frac{\delta^{ab}}{2}\left(\frac{1}{4} g^{\mu\nu} F^{\alpha\beta,a} F^{b}_{\alpha\beta} - F^{\mu\alpha,a} F^{\nu,b}_{\ \alpha}\right) = \frac{1}{4} g^{\mu\nu} F^{\alpha\beta,a} F^{a}_{\alpha\beta} - F^{\mu\alpha,a} F^{\nu,a}_{\ \alpha} = T^{\mu\nu}, \end{aligned} \tag{7.3}$$

which is equivalent to the sum over $SU(N_c)$ indices implicit in Eq. (7.2) by the Einstein notation. For simplicity, we will momentarily omit both the trace and the factor 2 in our expressions. The components of $T^{\mu\nu}$ can be expressed in terms of the previously computed chromo-electric and -magnetic fields E_i and B_i. Let us start with the energy density, $\epsilon \equiv T^{00}$:

$$\begin{aligned}\epsilon &= \frac{1}{4}(-2|E|^2 + (\epsilon^{ijk}B^k)(\epsilon^{ijm}B^m)) + |E|^2 \\ &= \frac{1}{4}(2|E|^2 + 2\delta^{km}B^kB^m) = \frac{1}{2}(|E|^2 + |B|^2).\end{aligned} \tag{7.4}$$

For the T^{0i} terms (which are the three components of the momentum density, i.e. the Poynting vector) we get:

$$T^{0i} = -F^{0j}F^{i}_{\ j} = E^jF^{i}_{\ j} = -\epsilon^{ijk}E_jB_k = [E \times B]^i\,. \tag{7.5}$$

Note that the definition of the cross product includes a metric tensor that rises the i index, and therefore, a change of sign. Finally, for the T^{ij} terms (momentum flux) we have:

$$T^{ij} = \frac{\delta^{ij}}{2}\left(|E|^2 + |B|^2\right) - (E^iE^j + B^iB^j). \tag{7.6}$$

Now we can explicitly calculate $T^{\mu\nu}$ by substituting Eq. (6.53), Eq. (6.54) into Eq. (7.4), Eq. (7.5) and Eq. (7.6). Remarkably, only the diagonal terms survive this substitution. As both the chromo-electric and chromo-magnetic fields are longitudinal (and therefore parallel) at $\tau = 0^+$, the cross product featured in Eq. (7.5) vanishes. In the case of Eq. (7.6) with $i \neq j$:

$$T^{ij}(\tau = 0^+) \equiv T_0^{ij} = -(E^iE^j + B^iB^j) = 0. \tag{7.7}$$

(From now on we will write $E^i(\tau=0^+)$ and $B^i(\tau=0^+)$ simply as E^i, B^i). This expression features a product of two different components for each field. Again, as both E^i and B^i have only one nonzero component (i.e. z), these terms vanish. This is not the case for the diagonal terms $i=j=1,2$:

$$T_0^{11} = T_0^{22} = \frac{1}{2}\left(|E|^2 + |B|^2\right) \tag{7.8}$$

and $i = j = 3$:

$$T_0^{33} = \frac{1}{2}(|E|^2 + |B|^2) - (|E|^2 + |B|^2) = -\frac{1}{2}\left(|E|^2 + |B|^2\right). \tag{7.9}$$

Hence:

$$T_0^{\mu\nu} = \frac{1}{2}\left(|E|^2 + |B|^2\right) \times \mathrm{diag}(1,1,1,-1) \equiv \epsilon_0 \times t^{\mu\nu}, \tag{7.10}$$

where we defined $t^{\mu\nu} \equiv [\mathrm{diag}(1,1,1,-1)]^{\mu\nu}$. As expected in a classical approximation, this tensor is traceless. Note that the characteristic diagonal structure of $T_0^{\mu\nu}$ is a feature of the specific proper time at which we are setting our calculation. The ensuing time evolution brings non-trivial off-diagonal corrections that largely modify this initial form[1]. At $\tau = 0^+$, however, the classical approximation yields a remarkably simple, diagonal Energy-Momentum Tensor.

What is most remarkable about this object is the maximum pressure anisotropy denoted by the negative value in the longitudinal direction, which makes it very different to the characteristic

---

[1] As indicated by the higher order terms of the τ-expansion proposed in [97].

Energy-Momentum Tensor of an ideal fluid (where all the components of the pressure would be equal and positive). The negative pressure tends to slow down the longitudinal expansion of the system, while the remaining components force it to expand in the transverse directions. This picture is quite problematic for a smooth matching to quasi-ideal hydrodynamics, which makes the description of thermalization a remarkably complex endeavor.

In terms of the previously obtained gluon fields, Eq. (7.10) reads:

$$T_0^{\mu\nu} = -g^2(\delta^{ij}\delta^{kl} + \epsilon^{ij}\epsilon^{kl})\mathrm{Tr}\left\{[\alpha_1^i, \alpha_2^j][\alpha_1^k, \alpha_2^l]\right\} \times t^{\mu\nu}, \tag{7.11}$$

where we have explicitly restored the color trace introduced in Eq. (7.3). In order to compute it we need to expand the color structure of our fields:

$$\begin{aligned}\alpha^i(x_\perp) = \int_{-\infty}^{\infty} dz^- U^\dagger(z^-, x_\perp)\frac{\partial^i\tilde{\rho}(z^-, x_\perp)}{\nabla^2}U(z^-, x_\perp) &= \int_{-\infty}^{\infty} dz^- \frac{\partial^i\tilde{\rho}^a}{\nabla^2}U^\dagger t^a U \\ &= \int_{-\infty}^{\infty} dz^- \frac{\partial^i\tilde{\rho}^a}{\nabla^2}U^{ab}t^b \equiv \alpha^{i,b}(x_\perp)t^b.\end{aligned} \tag{7.12}$$

Here we used the relation between Wilson lines in the fundamental and adjoint representations $U^\dagger t^a U = U^{ab}t^b$ (see Appendix G for a proof). Substituting in Eq. (7.11) we get:

$$\begin{aligned}T_0^{\mu\nu} &= -g^2(\delta^{ij}\delta^{kl} + \epsilon^{ij}\epsilon^{kl})\,\alpha_1^{i,a}\alpha_2^{j,b}\alpha_1^{k,c}\alpha_2^{l,d}\,\mathrm{Tr}\left\{[t^a, t^b][t^c, t^d]\right\} \times t^{\mu\nu} \\ &= g^2(\delta^{ij}\delta^{kl} + \epsilon^{ij}\epsilon^{kl})\,f^{abm}f^{cdn}\alpha_1^{i,a}\alpha_2^{j,b}\alpha_1^{k,c}\alpha_2^{l,d}\,\mathrm{Tr}\left\{t^m t^n\right\} \times t^{\mu\nu} \\ &= \frac{g^2}{2}(\delta^{ij}\delta^{kl} + \epsilon^{ij}\epsilon^{kl})f^{abm}f^{cdm}\,\alpha_1^{i,a}\alpha_2^{j,b}\alpha_1^{k,c}\alpha_2^{l,d} \times t^{\mu\nu}.\end{aligned} \tag{7.13}$$

7.2 The Divergence of the Chern-Simons current at $\tau = 0^+$

As explained in Chapter 5, the divergence of the Chern-Simons current $\dot{\nu}$ characterizes the early fluctuations of axial charge density in the plane transverse to the collision axis. This object plays a crucial role in the description of anomalous transport phenomena such as the Chiral Magnetic Effect, as will be detailed later on. Its expression in terms of the Glasma chromo-electric and -magnetic fields reads:

$$\dot{\nu}(\tau = 0^+, x_\perp) \equiv \dot{\nu}_0(x_\perp) = \mathrm{Tr}\{E(\tau = 0^+, x_\perp)B(\tau = 0^+, x_\perp)\}. \tag{7.14}$$

By expanding this expression in terms of the gluon fields α^i and explicitly computing the color trace we obtain:

$$\begin{aligned}\dot{\nu}_0(x_\perp) &= -g^2\delta^{ij}\epsilon^{kl}\mathrm{Tr}\{[\alpha^i_{1\,x}, \alpha^j_{2\,x}][\alpha^k_{1\,x}, \alpha^l_{2\,x}]\} \\ &= -g^2\delta^{ij}\epsilon^{kl}\alpha^{i,a}_{1\,x}\alpha^{j,b}_{2\,x}\alpha^{k,c}_{1\,x}\alpha^{l,d}_{2\,x}\mathrm{Tr}\{[t^a, t^b][t^c, t^d]\} \\ &= \frac{g^2}{2}\delta^{ij}\epsilon^{kl}f^{abn}f^{cdn}\alpha^{i,a}_{1\,x}\alpha^{j,b}_{2\,x}\alpha^{k,c}_{1\,x}\alpha^{l,d}_{2\,x}.\end{aligned} \tag{7.15}$$

Both Eq. (7.13) and Eq. (7.15) display a remarkably complex index structure. For instance, each expression features two $SU(N_c)$ structure constants f^{abc} whose indices are contracted with those of gluon fields corresponding to different nuclei. As will be shown in Part IV, the color algebra operations derived from this particular configuration (specially for the calculation of two-point correlators) will be the source of many technical challenges that will –in some cases– require the use of computational methods.

Summary:

- In this chapter we obtain the expressions of the Energy-Momentum Tensor and the divergence of the Chern-Simons current in term of the previously computed Glasma fields.
- Both expressions feature a notably complicated index structure, involving two $SU(N_c)$ structure constants and different combinations of Dirac deltas and Levi-Civita tensors.
- Remarkably, the structure of the Energy-Momentum Tensor at $\tau = 0^+$ is far from that of an ideal fluid (which the Glasma is expected to resemble after the thermalization process). However, this issue is out of the scope of the studies presented in this report.

Part IV

Early correlations of the Glasma

[13 minutes of screeching noise]
— Kazumoto Endo in "While You Were Out"

This part of the thesis is devoted to the theoretical characterization of the early event-by-event fluctuations of Glasma. This feature is described in the CGC framework through the functional average previously discussed in Chapter 3. As a preamble, on Section 8.1 we present a generalization of the two-point function of the MV model with relaxed transverse locality and explicit impact parameter dependence. Such extensions allow for a more realistic description of color charge correlations, while expanding the potential phenomenological applications of our results. In this framework, we first study the energy and momentum deposited in the transverse plane to the collision axis in the initial stage of the collision (Chapter 8). Specifically, we compute the one- and two-point correlators of the energy-momentum tensor characterizing the system generated at an infinitesimally small proper time $\tau = 0^+$. We then focus on the generation of topological charge induced by event-by-event fluctuations, which is described by the two-point correlator of the divergence of the Chern-Simons current (Chapter 9). In Chapter 10 we compare our results with previous calculations performed in the so-called Glasma Graph approximation.

Chapter 8

Energy density fluctuations of the Glasma

In this chapter we present a first-principles analytical calculation of the covariance of the Energy-Momentum Tensor (EMT) associated to the Glasma phase. This object involves the two-point and single-point correlators ($\langle T^{\mu\nu}(x_\perp)T^{\sigma\rho}(y_\perp)\rangle$ and $\langle T^{\mu\nu}(x_\perp)\rangle$, respectively) of the EMT at proper time $\tau = 0^+$. Our approach is based on the previously discussed CGC effective theory, which provides the tools to map the fluctuations of the valence color sources from the colliding nuclei to those of the EMT of the produced gluon fields (computed in Part III). We will start by computing the one-point function, which describes the average energy density deposited in the collision area.

8.1 The EMT one-point correlator in the MV model

Although the results shown in this section have been –for the most part– derived previously in the literature [55], this preface allows us to introduce the generalized MV model that we will be extensively using throughout our calculations, as well as to establish the employed notation. The proposed extensions to the MV model are embodied in the following two-point correlator:

$$\boxed{\begin{aligned}\langle \rho^a(x^-, x_\perp)\rho^b(y^-, y_\perp)\rangle &= \mu^2(x^-)h(b_\perp)\delta^{ab}\delta(x^- - y^-)f(x_\perp - y_\perp)\\ &\equiv \lambda(x^-, b_\perp)\delta^{ab}\delta(x^- - y^-)f(x_\perp - y_\perp),\end{aligned}} \tag{8.1}$$

which generalizes the ansatz presented in Eq. (3.8). This expression allows for the possibility of finite, non-homogeneous nuclei by explicitly introducing an impact parameter ($b_\perp = (x_\perp + y_\perp)/2$)

dependence, as previously done in [98]. Also, the assumption that interactions are local in the transverse plane is dropped by the introduction of an undetermined function $f(x_\perp - y_\perp)$ instead of a Dirac delta. This generalization was first explored in [99] and later applied in the implementation of BK evolution within the so-called Gaussian truncation framework [26, 100–102]. Both these extensions of the MV model could prove useful in subsequent phenomenological applications of our results. The specific analytical behavior assumed for $h(b_\perp)$ and $f(x_\perp - y_\perp)$ will be briefly discussed later on (and is treated in depth on Appendix H).

The starting point of our calculation is the Glasma EMT, computed in Section 7.1. Applying Eq. (8.1) to this object we obtain $\langle T_0^{\mu\nu}(x_\perp)\rangle = \langle \epsilon_0(x_\perp)\rangle \times t^{\mu\nu}$, with:

$$\langle \epsilon_0(x_\perp)\rangle = \frac{g^2}{2}(\delta^{ij}\delta^{kl} + \epsilon^{ij}\epsilon^{kl}) f^{abm} f^{cdm} \left\langle \alpha^{i,a}(x_\perp)\alpha^{k,c}(x_\perp)\right\rangle_1 \left\langle \alpha^{j,b}(x_\perp)\alpha^{l,d}(x_\perp)\right\rangle_2. \tag{8.2}$$

Here we factorize the average over color source densities $\tilde{\rho}_1$ and $\tilde{\rho}_2$, as in the MV model we assume the source fluctuations in each nuclei to be independent of each other:

$$\langle \mathcal{O}[\rho_{1,2}]\rangle = \frac{1}{\mathcal{N}_1}\frac{1}{\mathcal{N}_2}\int [d\rho_1] W_\mu[\rho_1] \int [d\rho_2] W_\mu[\rho_2]\, \mathcal{O}[\rho_{1,2}]. \tag{8.3}$$

Also note that, as in Eq. (7.13) all indices are explicit, the $\alpha^{i,a}$ coefficients can be freely permuted in order to perform said factorization. The building block of $\langle \epsilon_0\rangle$ is the average of two gauge fields evaluated in the same transverse coordinate: $\langle \alpha^{i,a}(x_\perp)\alpha^{j,b}(x_\perp)\rangle$. Nevertheless, it will prove useful to perform this calculation for different transverse positions $x_\perp$, $y_\perp$ and eventually take the limit $y_\perp \to x_\perp$:

$$\left\langle \alpha^{i,a}(x_\perp)\alpha^{j,b}(y_\perp)\right\rangle = \int_{-\infty}^{\infty} dz^- dz^{-\prime} \left\langle \frac{\partial^i \tilde{\rho}^{a'}(z^-, x_\perp)}{\nabla^2} U^{a'a}(z^-, x_\perp) \frac{\partial^j \tilde{\rho}^{b'}(z^{-\prime}, y_\perp)}{\nabla^2} U^{b'b}(z^{-\prime}, y_\perp)\right\rangle. \tag{8.4}$$

The average in the right hand side of this expression contains, for each transverse position, an infinite product of $\tilde{\rho}$ factors, one being *external* and the rest being arranged *inside* the Wilson lines. Since the MV model assumes the color sources to obey Gaussian statistics, we can apply Wick's theorem, which under such condition states that any correlator can be expressed in terms of products of two-point functions. In our particular case, the only non-vanishing terms of the infinite possibilities available are the ones that correspond to a factorization of the external sources from those inside the Wilson lines[1]:

$$\left\langle \alpha^{i,a}(x_\perp)\alpha^{j,b}(y_\perp)\right\rangle = \int_{-\infty}^{\infty} dz^- dz^{-\prime} \left\langle \frac{\partial^i \tilde{\rho}^{a'}(z^-, x_\perp)}{\nabla^2} \frac{\partial^j \tilde{\rho}^{b'}(z^{-\prime} y_\perp)}{\nabla^2}\right\rangle \left\langle U^{a'a}(z^-, x_\perp) U^{b'b}(z^{-\prime}, y_\perp)\right\rangle. \tag{8.5}$$

As the differential operators $1/\nabla^2$, ∂^i commute with the average operation $\langle ...\rangle$, the factor involving the external sources can be calculated through an almost direct application of the two-point correlator. In the original MV model (Eq. (3.8)) this yields a quite simple expression:

$$\left\langle \frac{\partial^i \tilde{\rho}^{a'}(x^-, x_\perp)}{\nabla^2} \frac{\partial^j \tilde{\rho}^{b'}(y^-, y_\perp)}{\nabla^2}\right\rangle_{\text{MV}} = \delta^{a'b'} \mu^2(x^-)\delta(x^- - y^-)\partial_x^i \partial_y^j L(x_\perp - y_\perp)_{\text{MV}}, \tag{8.6}$$

---

[1] Later on (in Section 8.2.1), we will perform a general analysis of the decomposition of the correlator of n Wilson lines and m external sources.

with:

$$\frac{1}{\nabla_x^2}\frac{1}{\nabla_y^2}\delta^2(x_\perp - y_\perp) = \int dz_\perp^2 du_\perp^2 G(z_\perp - x_\perp)G(u_\perp - y_\perp)\delta^2(z_\perp - u_\perp)$$
$$= \int d^2 z_\perp G(z_\perp - x_\perp)G(z_\perp - y_\perp) \equiv L(x_\perp - y_\perp)_{\rm MV}. \tag{8.7}$$

However, the generalized version Eq. (8.1) yields:

$$\frac{1}{\nabla_x^2}\frac{1}{\nabla_y^2}\left(h(b_\perp)f(x_\perp - y_\perp)\right) = \int dz_\perp^2 du_\perp^2 G(z_\perp - x_\perp)G(u_\perp - y_\perp)h\left(\frac{z_\perp + u_\perp}{2}\right)f(z_\perp - u_\perp)$$
$$\approx h(b_\perp)\int dz_\perp^2 du_\perp^2 G(z_\perp - x_\perp)G(u_\perp - y_\perp)f(z_\perp - u_\perp)$$
$$\equiv h(b_\perp)L(x_\perp - y_\perp), \tag{8.8}$$

and then:

$$\partial_x^i\partial_y^j\left(h(b_\perp)L(x_\perp - y_\perp)\right) \approx h(b_\perp)\partial_x^i\partial_y^j L(x_\perp - y_\perp), \tag{8.9}$$

resulting in:

$$\left\langle \frac{\partial^i\tilde{\rho}^{a'}(x^-, x_\perp)}{\nabla^2}\frac{\partial^j\tilde{\rho}^{b'}(y^-, y_\perp)}{\nabla^2}\right\rangle = \delta^{a'b'}\lambda(x^-, b_\perp)\delta(x^- - y^-)\partial_x^i\partial_y^j L(x_\perp - y_\perp). \tag{8.10}$$

In the same spirit than [98], in Eq. (8.8) we implicitly assume that the impact parameter profile $h(b_\perp)$ introduced earlier is a slowly varying function over distances of the order of an infrared length scale $1/m$ (or smaller). This length is taken as an intermediate scale between the inverse saturation scale and the nuclear radius R_A:

$$\boxed{\frac{1}{Q_s} \ll \frac{1}{m} \ll R_A\,.} \tag{8.11}$$

In our calculation $1/m$ acts as a cut-off that imposes color neutrality at the nucleon size. Another assumption implicit in the previous expressions is that $f(x_\perp - y_\perp)$ behaves in such a way that its Fourier transform $\hat{f}(k_\perp)$ tends to unity in the infrared limit. This requirement, along with the assumed 'slow' behavior for $h(b_\perp)$, result in this factor being approximately unaffected by the differential operators in both Eq. (8.8) and Eq. (8.9) (see Appendix H for a more detailed discussion about these assumptions). Substituting in Eq. (8.5) we obtain:

$$\left\langle\alpha^{i,a}(x_\perp)\alpha^{j,b}(y_\perp)\right\rangle = \int_{-\infty}^{\infty} dz^-\lambda(z^-, b_\perp)\partial_x^i\partial_y^j L(x_\perp - y_\perp)\left\langle U^{a'a}(z^-, x_\perp)U^{a'b}(z^-, y_\perp)\right\rangle, \tag{8.12}$$

where the last factor corresponds to the dipole function in the adjoint representation [103]:

$$\left\langle U^{a'a}(x^-, x_\perp)U^{a'b}(x^-, y_\perp)\right\rangle = \delta^{ab}\exp\left\{-g^2\frac{N_c}{2}\Gamma(x_\perp - y_\perp)\bar{\lambda}(x^-, b_\perp)\right\}$$
$$\equiv \delta^{ab}C^{(2)}_{\rm adj}(x^-; x_\perp, y_\perp). \tag{8.13}$$

Here we introduce the factor

$$\Gamma(x_\perp - y_\perp) = 2(L(0_\perp) - L(x_\perp - y_\perp)) \tag{8.14}$$

and the integrated color charge density $\bar{\lambda}(x^-, b_\perp) = \int_{-\infty}^{x^-} dz^- \lambda(z^-, b_\perp)$. Note that in Eq. (8.13) the same approximations as in Eq. (8.8) were applied in order to obtain the factorization of $h(b_\perp)\Gamma(x_\perp - y_\perp)$. Substituting:

$$\left\langle \alpha^{i,a}(x_\perp)\alpha^{j,b}(y_\perp)\right\rangle = \delta^{ab}\int_{-\infty}^{\infty} dz^- \lambda(z^-, b_\perp)\partial_x^i \partial_y^j L(x_\perp - y_\perp) C^{(2)}_{\text{adj}}(z^-; x_\perp, y_\perp). \tag{8.15}$$

Now, taking the limit $y_\perp \to x_\perp$:

$$\begin{aligned}\left\langle \alpha^{i,a}(x_\perp)\alpha^{j,b}(x_\perp)\right\rangle &= -\frac{1}{2}\delta^{ab}\delta^{ij}\int_{-\infty}^{\infty} dz^- \lambda(z^-, x_\perp)\partial^2 L(0_\perp) = -\frac{1}{2}\delta^{ab}\delta^{ij}\bar{\lambda}(x_\perp)\partial^2 L(0_\perp) \\ &= -\frac{1}{2}\delta^{ab}\delta^{ij}\bar{\mu}^2 h(x_\perp)\partial^2 L(0_\perp),\end{aligned} \tag{8.16}$$

where we defined $\bar{\lambda}(b_\perp) = \bar{\lambda}(\infty, b_\perp) = \bar{\mu}^2 h(b_\perp)$ (in general, we will identify functions integrated in the longitudinal direction from $-\infty$ to ∞ by simply omitting their longitudinal dependence) and substituted the following expression:

$$\lim_{r\to 0} \partial_x^i \partial_y^j L(r_\perp) = \frac{\delta^{ij}}{2}\int \frac{d^2 q_\perp}{(2\pi)^2}\hat{f}(q_\perp)\frac{1}{q^2} \equiv -\frac{1}{2}\delta^{ij}\partial^2 L(0_\perp), \tag{8.17}$$

with $r = |r_\perp| = |x_\perp - y_\perp|$. Here the double derivative $\partial^2 L(0_\perp)$ is a model-dependent constant that yields a logarithmic divergence in the strict MV model:

$$\partial^2 L(0_\perp)_{\text{MV}} = \frac{1}{4\pi}\lim_{r\to 0}\left[\ln\left(\frac{m^2 r^2}{4}\right)\right]. \tag{8.18}$$

Note that in our generalized framework one could in principle search for a function $f(x_\perp)$ that regularizes said divergence. We will come back to this later. By applying Eq. (8.16) for both nuclei in Eq. (8.2), we obtain:

$$\begin{aligned}\langle \epsilon_0(x_\perp)\rangle &= \frac{g^2}{2} f^{abm} f^{cdm}(\delta^{ij}\delta^{kl} + \epsilon^{ij}\epsilon^{kl})\frac{1}{4}\delta^{ac}\delta^{ik}\delta^{bd}\delta^{jl}\bar{\mu}_1^2\,\bar{\mu}_2^2\, h_1(x_\perp)h_2(x_\perp)(\partial^2 L(0_\perp))^2 \\ &= g^2 N_c^2 C_F \bar{\lambda}_1(x_\perp)\bar{\lambda}_2(x_\perp)(\partial^2 L(0_\perp))^2,\end{aligned} \tag{8.19}$$

whose dependence on the transverse position is a consequence of our generalized MV model approach. Note that we label both factors μ^2 and h according to the corresponding nucleus, which allows for the use of different nuclear profiles for target and projectile. We absorb these quantities, along with the factor $\partial^2 L(0_\perp)$, in the definition of the following momentum scale:

$$\bar{Q}_s^2(x_\perp) \equiv \alpha_s N_c\, \bar{\lambda}(x_\perp)\left(-4\pi\partial^2 L(0_\perp)\right), \tag{8.20}$$

which characterizes each colliding nucleus. Performing this substitution we finally obtain:

$$\boxed{\langle \epsilon_0(x_\perp)\rangle = \frac{C_F}{g^2}\bar{Q}_{s1}^2(x_\perp)\bar{Q}_{s2}^2(x_\perp).} \tag{8.21}$$

Due to Eq. (8.18), in the strict MV model the average energy density is a logarithmically divergent quantity. At the origin of this issue is the Gaussian ansatz, which does not hold for very small resolution distances ($r \to 0$). Indeed, under this approximation it is assumed that the color charge sources at two given points emerge from different nucleons and are therefore uncorrelated, which is not a reasonable assumption at short enough distances. As mentioned before, this shortcoming could in principle be 'treated' by relaxing the locality of correlations in the transverse plane. However, such possibility was not explored in the work presented in this thesis. Instead, we absorb the divergent factors into the definition of momentum scales characterizing each nucleus, $\bar{Q}_{s1,2}$, which later on will be shown to be related to their saturation scales (as made apparent by the chosen notation).

8.2 The EMT two-point correlator in the MV model

The next step in our calculation is the computation of $\langle T_0^{\mu\nu}(x_\perp)T_0^{\sigma\rho}(y_\perp)\rangle = \langle\epsilon_0(x_\perp)\epsilon_0(y_\perp)\rangle \times t^{\mu\nu}t^{\sigma\rho}$. Whereas the one-point function expresses the average energy density of a fluctuating medium, the two-point correlator characterizes how such event-by-event fluctuations give rise to non-trivial correlations between the energy densities at two given points of the transverse plane. We start by expanding the product of energy densities:

$$\begin{aligned}\epsilon_0(x_\perp)\epsilon_0(y_\perp) &= g^4(\delta^{ij}\delta^{kl}+\epsilon^{ij}\epsilon^{kl})\mathrm{Tr}\left\{\left[\alpha_1^i(x_\perp),\alpha_2^j(x_\perp)\right]\left[\alpha_1^k(x_\perp),\alpha_2^l(x_\perp)\right]\right\}\\ &\quad\times(\delta^{i'j'}\delta^{k'l'}+\epsilon^{i'j'}\epsilon^{k'l'})\mathrm{Tr}\left\{\left[\alpha_1^{i'}(y_\perp),\alpha_2^{j'}(y_\perp)\right]\left[\alpha_1^{k'}(y_\perp),\alpha_2^{l'}(y_\perp)\right]\right\}\\ &= \frac{g^4}{4}(\delta^{ij}\delta^{kl}+\epsilon^{ij}\epsilon^{kl})(\delta^{i'j'}\delta^{k'l'}+\epsilon^{i'j'}\epsilon^{k'l'})f^{abn}f^{cdn}f^{a'b'm}f^{c'd'm}\underbrace{\alpha_1^{i,a}\alpha_2^{j,b}\alpha_1^{k,c}\alpha_2^{l,d}}_{x_\perp}\underbrace{\alpha_1^{i',a'}\alpha_2^{j',b'}\alpha_1^{k',c'}\alpha_2^{l',d'}}_{y_\perp}\\ &\equiv \mathcal{A}^{ik;i'k'}_{jl;j'l'}\mathcal{F}^{ac;a'c'}_{bd;b'd'}\alpha^{i,a}_{1\,x}\alpha^{k,c}_{1\,x}\alpha^{i',a'}_{1\,y}\alpha^{k',c'}_{1\,y}\alpha^{j,b}_{2\,x}\alpha^{l,d}_{2\,x}\alpha^{j',b'}_{2\,y}\alpha^{l',d'}_{2\,y}\,. \end{aligned} \tag{8.22}$$

Here we define the transverse and color structure tensors respectively as:

$$\mathcal{A}^{ik;i'k'}_{jl;j'l'} = (\delta^{ij}\delta^{kl}+\epsilon^{ij}\epsilon^{kl})(\delta^{i'j'}\delta^{k'l'}+\epsilon^{i'j'}\epsilon^{k'l'}) \tag{8.23}$$

$$\mathcal{F}^{ac;a'c'}_{bd;b'd'} = \frac{g^4}{4}f^{abn}f^{cdn}f^{a'b'm}f^{c'd'm}, \tag{8.24}$$

and adopted a shorthand notation for the gluon fields $\alpha^{i,a}(x_\perp)\equiv\alpha^{i,a}_x$. As the average operation is performed independently for both nuclei, the building block of $\langle\epsilon_0(x_\perp)\epsilon_0(y_\perp)\rangle$ reads:

$$\begin{aligned}\langle\alpha^{i,a}(x_\perp)\alpha^{k,c}(x_\perp)\alpha^{i',a'}(y_\perp)\alpha^{k',c'}(y_\perp)\rangle &= \int_{-\infty}^{\infty}dz^-dw^-dz^{-\prime}dw^{-\prime}\left\langle\frac{\partial^i\tilde{\rho}^e(z^-,x_\perp)}{\nabla^2}U^{ea}(z^-,x_\perp)\right.\\ &\left.\frac{\partial^k\tilde{\rho}^f(w^-,x_\perp)}{\nabla^2}U^{fc}(w^-,x_\perp)\frac{\partial^{i'}\tilde{\rho}^{e'}(z^{-\prime},y_\perp)}{\nabla^2}U^{e'a'}(z^{-\prime},y_\perp)\frac{\partial^{k'}\tilde{\rho}^{f'}(w^{-\prime},y_\perp)}{\nabla^2}U^{f'c'}(w^{-\prime},y_\perp)\right\rangle. \end{aligned} \tag{8.25}$$

This is an extended, more complex version of Eq. (8.4), with twice as many color sources depending on different longitudinal coordinates. In order to compute this object, it will prove useful to analyze the general case of correlators with n Wilson lines and m external color sources. In the following subsection we will focus on the relevant case for our specific computation, where m is an even number.

8.2.1 Correlators of n Wilson lines and m external color sources

The correlator featured in Eq. (8.25) can be computed by application of the techniques derived in [104]. In said work they analyze the general case of the correlator of n Wilson lines and m color charge densities, denoted as $F^{m,n}$. The following decomposition formula (represented in Fig. 8.1) is provided[2]:

$$
\begin{aligned}
F^{m,n}(b^-,a^-) \equiv{}& G^m H^{0,n} \\
&+\sum_{i,j,i<j} G^{m-2}_{(1,...,i-1,\{i\},i+1,...,j-1,\{j\},j+1,...,m)} H^{2,n}_{(\{1,...,i-1\},i,\{i+1,...,j-1\},j,\{j+1,...,m\})} \\
&+\sum_{i,j,k,l,i<j<k<l} G^{m-4}_{(1,...i-1,\{i\},i+1,...,j-1,\{j\},j+1,...,k-1,\{k\},k+1,...,l-1,\{l\},l+1,...,m)} \\
&\times H^{4,n}_{(\{1,...,i-1\},i,\{i+1,...,j-1\},j,\{j+1,...,k-1\},k,\{k+1,...,l-1\},l,\{l+1,...,m\})} \\
&+...+\sum_{i,j,i<j} G^{2}_{(\{1,...,i-1\},i,\{i+1,...,j-1\},j,\{j+1,...,m\})} H^{2,n}_{(1,...,i-1,\{i\},i+1,...,j-1,\{j\},j+1,...,m)} + H^{m,n},
\end{aligned}
\tag{8.26}
$$

where

$$
G^{m-1}_{(1,...,j-1,\{j\},j+1,...,m)} \equiv \langle \rho_1 ... \rho_{j-1} \rho_{j+1} ... \rho_m \rangle \tag{8.27}
$$

is the correlator of $m-1$ color charge densities.

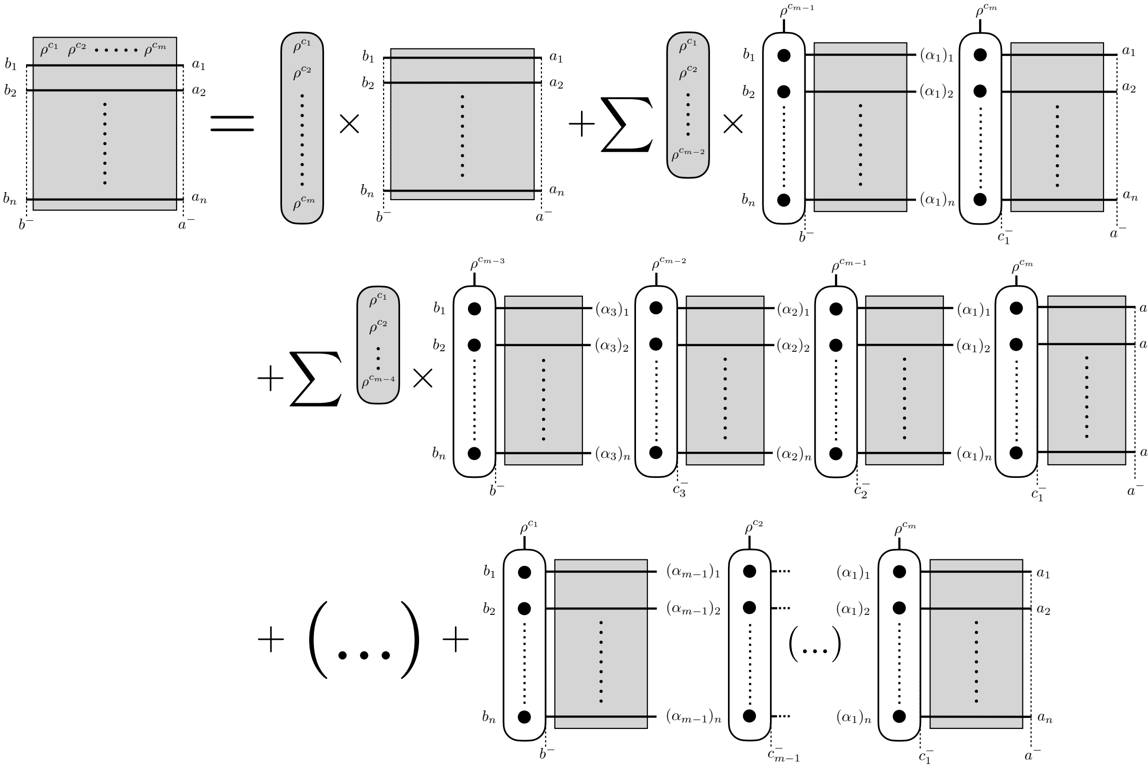

Figure 8.1: Schematic representation of the decomposition of the correlator $F^{m,n}$ (Eq. (8.26)) for an even value of m. The gray oblong shapes represent correlators of color source densities. On the other hand, the white oblong shapes represent the sum of all possible contractions between an external source and n Wilson lines, whose correlators are represented as gray squares (see Fig. 8.3).

---

[2] Eq. (8.26) is derived for the cases where m is even. In [104] the odd m formula is also provided.

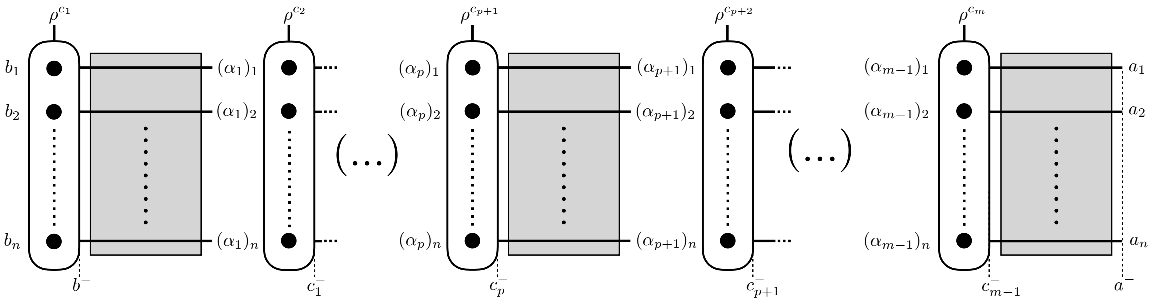

Figure 8.2: Schematic representation of the connected correlator $H^{m,n}$ (see Eq. (8.29)) for the particular case featured in our calculation.

In the notation adopted here, the indices corresponding to sources that are 'missing' from the correlators (like ρ_j in Eq. (8.27)) are indicated by brackets $\{...\}$. We also have:

$$H^{j,n}_{(\{1,...,J_1-1\},J_1,\{J_1+1,...,J_2-1\},J_2,\{J_2+1,...\}...\{J_j-1\},J_j,\{J_{j+1},...,m\})} \equiv \langle \rho_{J_1}\rho_{J_2}...\rho_{J_j}U_1...U_n\rangle_c, \tag{8.28}$$

which we will called the 'connected' correlator of n Wilson lines with j insertions of external sources at the positions J_1, J_2, ... J_j (with $J_1 < J_2 < ... < J_j$). This is a special kind of correlator that does not include contractions between color sources outside the Wilson lines. Therefore, when computing it, any of these external sources can only be linked to those arranged inside Wilson lines. This object can be factorized as:

$$H^{m,n}(b^-,a^-|\{b\},\{a\}) = H^{1,n}(b^-,c_1^-|\{b\},\{\alpha_1\})\left[\prod_{p=1}^{m-2} H^{1,n}(c_p^-,c_{p+1}^-|\{\alpha_p\},\{\alpha_{p+1}\})\right] \times H^{1,n}(c_{m-1}^-,a^-|\{\alpha_{m-1}\},\{a\}), \tag{8.29}$$

where $H^{1,n}$ is the basic building block of the connected correlators, having only one external source being linked to those inside the n Wilson lines (see Fig. 8.2). Applying our generalized version of the MV model (embodied in the two-point correlator Eq. (8.1)), $H^{1,n}$ yields the following expression:

$$H^{1,n}(b^-,a^-|\{b\},\{a\}) \equiv g\sum_{j=1}^{n}\mu^2(y^-)F^n(b^-,y^-|\{b\}\{\beta\})|_{\beta_j=d}F^n(y^-,a^-|\{\beta\}\{a\})|_{\beta_j=d'} \times\int dz_\perp G(z_\perp - x_{j\perp})f(z_\perp - y_\perp)h\left(\frac{z_\perp + y_\perp}{2}\right)f^{cdd'}. \tag{8.30}$$

However, a fundamental difference between the calculation discussed here and the one featured in [104] is that in our case the external sources are affected by the differential operators $1/\nabla^2$ and ∂^i. This aspect can be comprised in a redefinition of $H^{1,n}$ as:

$$H^{1,n}(b^-,a^-|\{b\},\{a\})^i \equiv g\sum_{j=1}^{n}\mu^2(y^-)F^n(b^-,y^-|\{b\}\{\beta\})|_{\beta_j=d}F^n(y^-,a^-|\{\beta\}\{a\})|_{\beta_j=d'} \times\partial_y^i\int dz_\perp dw_\perp G(z_\perp - x_{j\perp})G(w_\perp - y_\perp)f(z_\perp - w_\perp)h\left(\frac{z_\perp + w_\perp}{2}\right)f^{cdd'}, \tag{8.31}$$

where F^n denotes the correlator of n Wilson lines. Note that in these formulas the bracketed indices represent a set of n color indices (not indices from 'missing' sources, as in Eq. (8.27) and Eq. (8.28)).

By application of the analytical properties assumed for h (outlined in Appendix H), the previous expression can be rewritten as:

$$\begin{aligned} H^{1,n}(b^-,a^-|\{b\},\{a\})^i &\approx g\sum_{j=1}^{n}\mu^2(y^-)F^n(b^-,y^-|\{b\}\{\beta\})|_{\beta_j=d}F^n(y^-,a^-|\{\beta\}\{a\})|_{\beta_j=d'} \\ &\qquad\qquad\qquad\qquad\qquad\qquad\times h\left(b_\perp\right)\partial_y^i L(x_{j\perp}-y_\perp)f^{cdd'} \\ &= g\lambda(y^-,b_\perp)\sum_{j=1}^{n}\partial_y^i L(x_{j\perp}-y_\perp)f^{cdd'}F^n(b^-,y^-|\{b\}\{\beta\})|_{\beta_j=d}F^n(y^-,a^-|\{\beta\}\{a\})|_{\beta_j=d'}, \end{aligned} \tag{8.32}$$

where $b_\perp=(x_\perp+y_\perp)/2$[3]. Another difference between our calculation and the one performed in the aforementioned paper is that in the latter the insertion of external sources is assumed to take place at a longitudinal position y^- that satisfies $b^-<y^-<a^-$. However, in our particular case the longitudinal coordinate on which the external color source $\tilde{\rho}^a$ depends is the same as the one of the Wilson line that it is attached to, yielding the following simplification of the previous expression (see Fig. 8.3):

$$H^{1,n}(b^-,a^-|\{b\},\{a\})^i = g\lambda(b^-,b_\perp)\sum_{j=1}^{n}\partial_y^i L(x_{j\perp}-y_\perp)f^{c\,b_j b'}F^n(b^-,a^-|\{\beta\}\{a\})|_{\beta_j=b'}. \tag{8.33}$$

Having defined all the basic pieces of the calculation of a correlator with m external sources and n Wilson lines, we can go back to our particular case. The correlator in Eq. (8.25) corresponds to $F^{m,n}$ with $m=4$, $n=4$. By direct application of Eq. (8.26):

$$\boxed{\begin{aligned} &\left\langle \tilde{\rho}_x^{i,e}U_x^{ea}\tilde{\rho}_x^{k,f}U_x^{fc}\tilde{\rho}_y^{i',e'}U_y^{e'a'}\tilde{\rho}_y^{k',f'}U_y^{f'c'}\right\rangle = \left\langle \tilde{\rho}_x^{i,e}\tilde{\rho}_x^{k,f}\tilde{\rho}_y^{i',e'}\tilde{\rho}_y^{k',f'}\right\rangle\left\langle U_x^{ea}U_x^{fc}U_y^{e'a'}U_y^{f'c'}\right\rangle \\ &+\langle \tilde{\rho}_x^{i,e}\tilde{\rho}_x^{k,f}\rangle\left\langle \tilde{\rho}_y^{i',e'}\tilde{\rho}_y^{k',f'}U_x^{ea}U_x^{fc}U_y^{e'a'}U_y^{f'c'}\right\rangle_{\mathrm{c}} + \left\langle \tilde{\rho}_y^{i',e'}\tilde{\rho}_y^{k',f'}\right\rangle\left\langle \tilde{\rho}_x^{i,e}\tilde{\rho}_x^{k,f}U_x^{ea}U_x^{fc}U_y^{e'a'}U_y^{f'c'}\right\rangle_{\mathrm{c}} \\ &+\left\langle \tilde{\rho}_x^{i,e}\tilde{\rho}_y^{i',e'}\right\rangle\left\langle \tilde{\rho}_x^{k,f}\tilde{\rho}_y^{k',f'}U_x^{ea}U_x^{fc}U_y^{e'a'}U_y^{f'c'}\right\rangle_{\mathrm{c}} + \left\langle \tilde{\rho}_x^{i,e}\tilde{\rho}_y^{k',f'}\right\rangle\left\langle \tilde{\rho}_x^{k,f}\tilde{\rho}_y^{i',e'}U_x^{ea}U_x^{fc}U_y^{e'a'}U_y^{f'c'}\right\rangle_{\mathrm{c}} \\ &+\left\langle \tilde{\rho}_x^{k,f}\tilde{\rho}_y^{i',e'}\right\rangle\left\langle \tilde{\rho}_x^{i,e}\tilde{\rho}_y^{k',f'}U_x^{ea}U_x^{fc}U_y^{e'a'}U_y^{f'c'}\right\rangle_{\mathrm{c}} + \left\langle \tilde{\rho}_x^{k,f}\tilde{\rho}_y^{k',f'}\right\rangle\left\langle \tilde{\rho}_x^{i,e}\tilde{\rho}_y^{i',e'}U_x^{ea}U_x^{fc}U_y^{e'a'}U_y^{f'c'}\right\rangle_{\mathrm{c}} \\ &\qquad\qquad\qquad\qquad\qquad\qquad +\left\langle \tilde{\rho}_x^{i,e}U_x^{ea}\tilde{\rho}_x^{k,f}U_x^{fc}\tilde{\rho}_y^{i',e'}U_y^{e'a'}\tilde{\rho}_y^{k',f'}U_y^{f'c'}\right\rangle_{\mathrm{c}}. \end{aligned}} \tag{8.34}$$

For readability we momentarily adopted a shorthand notation that omits the longitudinal coordinate dependence and the differential operators $1/\nabla^2$, ∂^i. However, it should be kept in mind that the external sources and Wilson lines that share an index depend on the same longitudinal coordinate. In the following subsections we will analyze the different contributions stemming from Eq. (8.34). Let us first focus on those terms that contain the 'connected' correlators introduced in Eq. (8.28).

8.2.2 The connected function

The connected correlator $\langle ...\rangle_{\mathrm{c}}$ accounts for the contribution of correlations between the external color source densities and those arranged inside the Wilson lines. In principle, it can be computed

---

[3] In this step we have made use of the knowledge that all the transverse positions that enter our calculation are either $x_\perp$ or $y_\perp$. Thus, when expanding $h((z_\perp+w_\perp)/2)$ around $h(b_\perp)$ in Eq. (8.31), the linear term of the expansion yields a correction proportional to a product of the form $(x'_\perp-b_\perp)^i\partial^i h(b_\perp)$. Whether $x'_\perp=x_\perp$ or $x'_\perp=y_\perp$, this term is suppressed with respect to $h(b_\perp)$ according to the assumptions detailed in Appendix H.

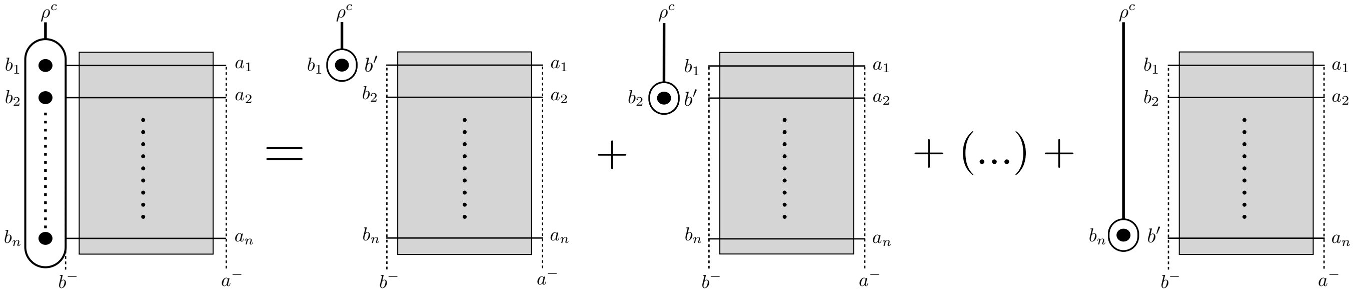

Figure 8.3: Schematic representation of Eq. (8.33). The circles in the right hand of the equation represent couplings of the external source ρ^c to Wilson lines inside the correlator (dark square). Each of these couplings multiplies the correlator by a $g\lambda(b^-, b_\perp)\, f^{cb_jb'}\partial_y L(x_{j\perp} - y_\perp)$ factor.

by application of formulas Eq. (8.29) and Eq. (8.33). However, our case of interest is somewhat more general than the one covered in these equations, as in our correlator each Wilson line depends on a different longitudinal coordinate. Even though this may seem a source of extra difficulty, it actually yields great simplification. For instance, let us take what seems to be the most complicated term of our calculation, namely the fully connected version of the correlator (last term in Eq. (8.34)):

$$\int_{-\infty}^{\infty} dz^- dw^- dz^{-\prime} dw^{-\prime} \Big\langle \frac{\partial^i \tilde{\rho}^e(z^-, x_\perp)}{\nabla^2} \frac{\partial^k \tilde{\rho}^f(w^-, x_\perp)}{\nabla^2} \frac{\partial^{i'} \tilde{\rho}^{e'}(z^{-\prime}, y_\perp)}{\nabla^2} \frac{\partial^{k'} \tilde{\rho}^{f'}(w^{-\prime}, y_\perp)}{\nabla^2}$$
$$\times U^{ea}(z^-, x_\perp) U^{fc}(w^-, x_\perp) U^{e'a'}(z^{-\prime}, y_\perp) U^{f'c'}(w^{-\prime}, y_\perp) \Big\rangle_{\mathrm{c}} . \qquad (8.35)$$

In order to compute this expression we need to consider all regions of integration space[4]. For example, applying Eq. (8.29) in the region where $z^- > w^- > z^{-\prime} > w^{-\prime}$ we have:

$$H^{4,4}(z^-, -\infty | e, f, e', f' \,;\, a, c, a', c') = H^{1,1}(z^-, w^- | e \,;\, \alpha_1)^i H^{1,2}(w^-, z^{-\prime} | \alpha_1, f \,;\, \alpha_2, \beta_1)^k$$
$$\times H^{1,3}(z^{-\prime}, w^{-\prime} | \alpha_2, \beta_1, e' \,;\, \alpha_3, \beta_2, \gamma_1)^{i'}$$
$$\times H^{1,4}(w^{-\prime}, -\infty | \alpha_3, \beta_2, \gamma_1, f' \,;\, a, c, a', c')^{k'}, \qquad (8.36)$$

where, according to Eq. (8.33), the first factor reads:

$$H^{1,1}(z^-, w^- | e \,;\, \alpha_1)^i = g\, \lambda(z^-, b_\perp) \partial_x^i L(0_\perp) f^{ee\alpha} \left\langle U^{\alpha\alpha_1}(z^-, w^-; x_\perp) \right\rangle = 0, \qquad (8.37)$$

which vanishes due to the antisymmetric property of the $SU(N_c)$ structure constants. As we have the same contribution from every region of the integration space, Eq. (8.35) yields 0. In order to

---

[4] Namely the regions where $z^- > z^{-\prime} > w^- > w^{-\prime}$, $z^- > z^{-\prime} > w^{-\prime} > w^-$, etcetera. As is also the case for a single point in a 1-dimensional integral or a line in a 2-dimensional one, the regions where two or more of the coordinates have the same values (for example $z^- = z^{-\prime} > w^- > w^{-\prime}$) yield a negligible contribution. Therefore, we must always consider a certain ordering in our integration variables.

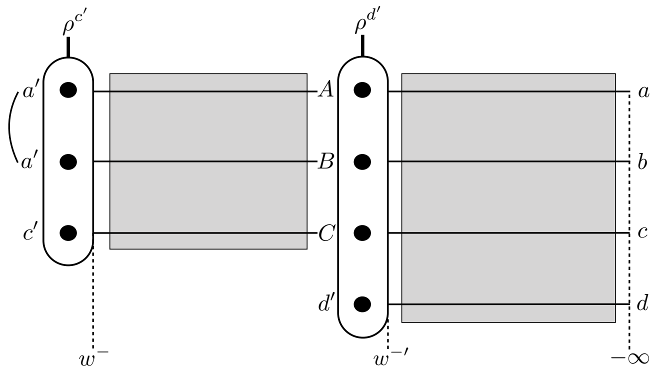

Figure 8.4: Schematic representation of the connected correlator $H^{2,4}$ factorized in Eq. (8.39).

address the remaining six terms we define the ‘connected’ function:

$$\begin{aligned}
C^{ij;kl}_{ab;cd}(u_\perp,u'_\perp,v_\perp,v'_\perp) &= \int_{-\infty}^{\infty} dz^- dz^{-\prime} dw^- dw^{-\prime} \left\langle \frac{\partial^i\tilde{\rho}^{a'}(z^-,u_\perp)}{\nabla^2}\frac{\partial^j\tilde{\rho}^{b'}(z^{-\prime},u'_\perp)}{\nabla^2}\right\rangle \\
\times\Bigg\langle \frac{\partial^k\tilde{\rho}^{c'}(w^-,v_\perp)}{\nabla^2}\frac{\partial^l\tilde{\rho}^{d'}(w^{-\prime},v'_\perp)}{\nabla^2} & U^{a'a}(z^-,u_\perp)U^{b'b}(z^{-\prime},u'_\perp)U^{c'c}(w^-,v_\perp)U^{d'd}(w^{-\prime},v'_\perp)\Bigg\rangle_{\rm c} \\
&= \partial^i_u\partial^j_{u'}L(u_\perp-u'_\perp)\int_{-\infty}^{\infty} dz^- dw^- dw^{-\prime}\lambda(z^-,b_\perp) \\
\times\Bigg\langle \frac{\partial^k\tilde{\rho}^{c'}(w^-,v_\perp)}{\nabla^2}\frac{\partial^l\tilde{\rho}^{d'}(w^{-\prime},v'_\perp)}{\nabla^2} & U^{a'a}(z^-,u_\perp)U^{a'b}(z^-,u'_\perp)U^{c'c}(w^-,v_\perp)U^{d'd}(w^{-\prime},v'_\perp)\Bigg\rangle_{\rm c}\,, \qquad (8.38)
\end{aligned}$$

where $b_\perp = (x_\perp + y_\perp)/2$. The only non-vanishing contributions to this integral come from the regions where $z^- > w^- > w^{-\prime}$ and $z^- > w^{-\prime} > w^-$, as in the other cases Eq. (8.33) introduces a vanishing $H^{1,1}$ factor. For the $z^- > w^- > w^{-\prime}$ region we have (see Fig. 8.4):

$$\begin{aligned}
&\partial^i_u\partial^j_{u'}L(u_\perp-u'_\perp)\int_{-\infty}^{\infty} dz^-\int_{-\infty}^{z^-} dw^-\int_{-\infty}^{w^-} dw^{-\prime}\lambda(z^-,b_\perp)C^{(2)}_{\rm adj}(z^-,w^-;u_\perp,u'_\perp) \\
&\times\left\langle \frac{\partial^k\tilde{\rho}^{c'}(w^-,v_\perp)}{\nabla^2}U^{a'A}(w^-,w^{-\prime};u_\perp)U^{a'B}(w^-,w^{-\prime};u'_\perp)U^{c'C}(w^-,w^{-\prime};v_\perp)\right\rangle_{\rm c} \\
&\times\left\langle \frac{\partial^l\tilde{\rho}^{d'}(w^{-\prime},v'_\perp)}{\nabla^2}U^{Aa}(w^{-\prime},u_\perp)U^{Bb}(w^{-\prime},u'_\perp)U^{Cc}(w^{-\prime},v_\perp)U^{d'd}(w^{-\prime},v'_\perp)\right\rangle_{\rm c}. \qquad (8.39)
\end{aligned}$$

The locality of the two-point function Eq. (8.1) allows us to perform a factorization in the longitudinal direction. We focus on the first connected correlator, which contains one external source and three Wilson lines, thus corresponding to:

$$\begin{aligned}
&H^{1,3}(w^-,w^{-\prime}|a',a',c'\ ;\ A,B,C)^k/(g\,\lambda(w^-,b_\perp)) \\
&= \partial^k_v L(v_\perp - u_\perp)f^{c'a'\alpha}\Big\langle U^{\alpha A}(w^-,w^{-\prime};u_\perp)U^{a'B}(w^-,w^{-\prime};u'_\perp)U^{c'C}(w^-,w^{-\prime};v_\perp)\Big\rangle \\
&+\partial^k_v L(v_\perp - u'_\perp)f^{c'a'\alpha}\Big\langle U^{a'A}(w^-,w^{-\prime};u_\perp)U^{\alpha B}(w^-,w^{-\prime};u'_\perp)U^{c'C}(w^-,w^{-\prime};v_\perp)\Big\rangle + 0. \qquad (8.40)
\end{aligned}$$

Substituting the result for the three-point correlator of Wilson lines in the adjoint representation:

$$\begin{aligned}&\langle U^{aa'}(w^-,x^1_\perp)U^{bb'}(w^-,x^2_\perp)U^{cc'}(w^-,x^3_\perp)\rangle\\ &= \frac{1}{2N_c^2C_F}\left(f^{abc}f^{a'b'c'}+\frac{N_c^2}{N_c^2-4}d^{abc}d^{a'b'c'}\right)\exp\left\{-g^2\frac{N_c}{4}\bar{\lambda}(w^-,b_\perp)\sum_{i>j}\Gamma(x^i_\perp-x^j_\perp)\right\}\\ &\equiv \frac{1}{2N_c^2C_F}\left(f^{abc}f^{a'b'c'}+\frac{N_c^2}{N_c^2-4}d^{abc}d^{a'b'c'}\right)C^{(3)}_{\text{adj}}(w^-;x^1_\perp,x^2_\perp,x^3_\perp),\end{aligned} \tag{8.41}$$

we get to:

$$\begin{aligned}H^{1,3}(w^-,w^{-\prime}|a',a',c'\ ;\ A,B,C)^k &= gf^{ABC}C^{(3)}_{\text{adj}}(w^-,w^{-\prime};u_\perp,u'_\perp,v_\perp)\\ &\times\lambda(w^-,b_\perp)\partial^k_v(L(v_\perp-u'_\perp)-L(v_\perp-u_\perp))\,.\end{aligned} \tag{8.42}$$

Here, the color factor that cancels $(2N_c^2C_F)^{-1}$ emerges from the trace of the product of two structure constants. The remaining correlator, which contains an external source and four adjoint Wilson lines, yields:

$$\begin{aligned}&H^{1,4}(w^{-\prime}|\{A,B,C,d'\},\{a,b,c,d\})^l/(g\,\lambda(w^{-\prime},b_\perp))\\ &=\partial^l_{v'}L(v'_\perp-u_\perp)f^{d'A\alpha}\Big\langle U^{\alpha a}(w^{-\prime},u_\perp)U^{Bb}(w^{-\prime},u'_\perp)U^{Cc}(w^{-\prime},v_\perp)U^{d'd}(w^{-\prime},v'_\perp)\Big\rangle\\ &+\partial^l_{v'}L(v'_\perp-u'_\perp)f^{d'B\alpha}\Big\langle U^{Aa}(w^{-\prime},u_\perp)U^{\alpha b}(w^{-\prime},u'_\perp)U^{Cc}(w^{-\prime},v_\perp)U^{d'd}(w^{-\prime},v'_\perp)\Big\rangle\\ &+\partial^l_{v'}L(v'_\perp-v_\perp)f^{d'C\alpha}\Big\langle U^{Aa}(w^{-\prime},u_\perp)U^{Bb}(w^{-\prime},u'_\perp)U^{\alpha c}(w^{-\prime},v_\perp)U^{d'd}(w^{-\prime},v'_\perp)\Big\rangle+0.\end{aligned} \tag{8.43}$$

Substituting this expression and summing the contribution from the $z^- > w^{-\prime} > w^-$ region the 'connected' function finally yields:

$$\begin{aligned}&C^{ij;kl}_{ab;cd}(u_\perp,u'_\perp,v_\perp,v'_\perp)\\ &=g^2h^3(b_\perp)\partial^i_u\partial^j_{u'}L(u_\perp-u'_\perp)\int_{-\infty}^{\infty}dz^-\int_{-\infty}^{z^-}dw^-\int_{-\infty}^{w^-}dw^{-\prime}\mu^2(z^-)\mu^2(w^-)\mu^2(w^{-\prime})\\ &\times C^{(2)}_{\text{adj}}(z^-,w^-;u_\perp,u'_\perp)\Big(\Big[\partial^k_v(L(v_\perp-u'_\perp)-L(v_\perp-u_\perp))C^{(3)}_{\text{adj}}(w^-,w^{-\prime};u_\perp,u'_\perp,v_\perp)\\ &\times\partial^l_{v'}\left(f^{AeD}f^{CBe}L(v'_\perp-u_\perp)+f^{ACe}f^{DBe}L(v'_\perp-u'_\perp)+f^{ABe}f^{eCD}L(v'_\perp-v_\perp)\right)\\ &\times Q^{ABCD}_{abcd}(w^{-\prime};u_\perp,u'_\perp,v_\perp,v'_\perp)\Big]+\begin{bmatrix}l & \longleftrightarrow & k\\ c & \longleftrightarrow & d\\ v_\perp & \longleftrightarrow & v'_\perp\end{bmatrix}\Big)\,,\end{aligned} \tag{8.44}$$

where we introduced the adjoint Wilson line quadrupole tensor:

$$Q^{aceg}_{bdfh}(w^-;x_\perp,x'_\perp,y_\perp,y'_\perp)=\big\langle U^{ab}(w^-,x_\perp)U^{cd}(w^-,x'_\perp)U^{ef}(w^-,y_\perp)U^{gh}(w^-,y'_\perp)\big\rangle. \tag{8.45}$$

The fact that in our particular case the Wilson lines depend on only two transverse coordinates ($x_\perp$ and $y_\perp$) yields a significant simplification in the final expression. For example, by taking $u_\perp = u'_\perp$ in Eq. (8.44) we can see that the first two connected terms of Eq. (8.34) yield 0. The next four terms take the following form:

$$
\begin{aligned}
&C^{ij;kl}_{ab;cd}(x_\perp, y_\perp, x_\perp, y_\perp) \\
&\quad = 2g^2 h^3(b_\perp)\partial^i_x \partial^j_y L(x_\perp - y_\perp)\int_{-\infty}^{\infty} dz^- \int_{-\infty}^{z^-} dw^- \int_{-\infty}^{w^-} dw^{-\prime} \mu^2(z^-)\mu^2(w^-)\mu^2(w^{-\prime}) \\
&\qquad \times C^{(2)}_{\mathrm{adj}}(z^-, w^-; x_\perp, y_\perp)\partial^k_x (L(x_\perp - x_\perp) - L(x_\perp - y_\perp)) C^{(3)}_{\mathrm{adj}}(w^-, w^{-\prime}; x_\perp, y_\perp, x_\perp) \\
&\qquad \times \partial^l_y (L(y_\perp - y_\perp) - L(y_\perp - x_\perp))\, f^{ACe} f^{BDe} Q^{ABCD}_{abcd}(w^{-\prime}; x_\perp, y_\perp, x_\perp, y_\perp),
\end{aligned}
\tag{8.46}
$$

where we applied the Jacobi identity of SU(N_c):

$$
f^{abe} f^{ecd} + f^{cbe} f^{aed} + f^{dbe} f^{ace} = 0. \tag{8.47}
$$

Although we still need to compute the quadrupole projection $f^{ACe} f^{BDe} Q^{ABCD}_{abcd}$, let us first focus on the first term after the equal sign in Eq. (8.34), which corresponds to a complete factorization of external sources and Wilson lines. We will express this contribution in terms of the 'disconnected' function, whose derivation is detailed in the following subsection.

8.2.3 The disconnected function

The last term from Eq. (8.34) to be discussed corresponds to a complete factorization of the correlations of color source densities and Wilson lines:

$$
\begin{aligned}
&\int_{-\infty}^{\infty} dz^- dw^- dz^{-\prime} dw^{-\prime} \left\langle \frac{\partial^i \tilde{\rho}^e(z^-, x_\perp)}{\nabla^2} \frac{\partial^k \tilde{\rho}^f(w^-, x_\perp)}{\nabla^2} \frac{\partial^{i'} \tilde{\rho}^{e'}(z^{-\prime}, y_\perp)}{\nabla^2} \frac{\partial^{k'} \tilde{\rho}^{f'}(w^{-\prime}, y_\perp)}{\nabla^2} \right\rangle \\
&\qquad\qquad \times \left\langle U^{ea}(z^-, x_\perp) U^{fc}(w^-, x_\perp) U^{e'a'}(z^{-\prime}, y_\perp) U^{f'c'}(w^{-\prime}, y_\perp) \right\rangle .
\end{aligned}
\tag{8.48}
$$

It can be further expanded by application of Wick's theorem, which tells us that the external source correlator breaks down into the following sum of pairwise contractions:

$$
\left\langle \tilde{\rho}^{i,e}_x \, \tilde{\rho}^{k,f}_x \, \tilde{\rho}^{i',e'}_y \, \tilde{\rho}^{k',f'}_y \right\rangle = \langle \tilde{\rho}^{i,e}_x \, \tilde{\rho}^{k,f}_x \rangle \langle \tilde{\rho}^{i',e'}_y \, \tilde{\rho}^{k',f'}_y \rangle + \langle \tilde{\rho}^{i,e}_x \, \tilde{\rho}^{i',e'}_y \rangle \langle \tilde{\rho}^{k,f}_x \, \tilde{\rho}^{k',f'}_y \rangle + \langle \tilde{\rho}^{i,e}_x \, \tilde{\rho}^{k',f'}_y \rangle \langle \tilde{\rho}^{k,f}_x \, \tilde{\rho}^{i',e'}_y \rangle. \tag{8.49}
$$

Following this decomposition, Eq. (8.48) yields three terms that we can address in terms of the 'disconnected' function, which we derive explicitly in the following lines:

$$
\begin{aligned}
&D^{ij;kl}_{ab;cd}(u_\perp, u'_\perp, v_\perp, v'_\perp) \\
&\quad = \int_{-\infty}^{\infty} dz^- dz^{-\prime} dw^- dw^{-\prime} \left\langle \frac{\partial^i \tilde{\rho}^{a'}(z^-, u_\perp)}{\nabla^2} \frac{\partial^j \tilde{\rho}^{b'}(z^{-\prime}, u'_\perp)}{\nabla^2} \right\rangle \left\langle \frac{\partial^k \tilde{\rho}^{c'}(w^-, v_\perp)}{\nabla^2} \frac{\partial^l \tilde{\rho}^{d'}(w^{-\prime}, v'_\perp)}{\nabla^2} \right\rangle \\
&\qquad \times \left\langle U^{a'a}(z^-, u_\perp) U^{b'b}(z^{-\prime}, u'_\perp) U^{c'c}(w^-, v_\perp) U^{d'd}(w^{-\prime}, v'_\perp) \right\rangle \\
&\quad = \int_{-\infty}^{\infty} dz^- dz^{-\prime} dw^- dw^{-\prime} \delta^{a'b'} \lambda(z^-, b_\perp) \delta(z^- - z^{-\prime}) \partial^i_u \partial^j_{u'} L(u_\perp - u'_\perp) \delta^{c'd'} \lambda(w^-, b_\perp) \\
&\qquad \times \delta(w^- - w^{-\prime}) \partial^k_v \partial^l_{v'} L(v_\perp - v'_\perp) \left\langle U^{a'a}(z^-, u_\perp) U^{b'b}(z^{-\prime}, u'_\perp) U^{c'c}(w^-, v_\perp) U^{d'd}(w^{-\prime}, v'_\perp) \right\rangle \\
&\quad = T^{ij;kl}(u_\perp, u'_\perp, v_\perp, v'_\perp) \int_{-\infty}^{\infty} dz^- dw^- \lambda(z^-, b_\perp) \lambda(w^-, b_\perp) \\
&\qquad \times \left\langle U^{a'a}(z^-, u_\perp) U^{a'b}(z^-, u'_\perp) U^{c'c}(w^-, v_\perp) U^{c'd}(w^-, v'_\perp) \right\rangle,
\end{aligned}
\tag{8.50}
$$

Note that both here and in the connected function Eq. (8.44) we substituted the result of Eq. (8.10), which implies that we adopt the same assumptions over $h(b_\perp)$ and $f(x_\perp - y_\perp)$ as in the previous section[5]. In the previous expression we introduced the following function:

$$T^{ij;kl}(u_\perp, u'_\perp, v_\perp, v'_\perp) \equiv \partial^i_u \partial^j_{u'} L(u_\perp - u'_\perp) \partial^k_v \partial^l_{v'} L(v_\perp - v'_\perp), \tag{8.51}$$

where, as was also the case in the connected function Eq. (8.44), we encounter double derivatives of $L(x_\perp - x'_\perp)$. Let us address these factors here. From their symmetries and dimension, we can parameterize them as:

$$\partial^i_x \partial^j_y L(r_\perp) = A(r_\perp)\delta^{ij} + B(r_\perp)\left(\frac{\delta^{ij}}{2} - \frac{r^i r^j}{r^2}\right). \tag{8.52}$$

This formula accounts for an explicit separation of the contributions of the unpolarized $A(r_\perp)$ and linearly polarized $B(r_\perp)$ parts of the gluon distribution. We can express these coefficients in terms of $f(r_\perp)$ explicitly as:

$$A(r_\perp) = \frac{1}{2}\int \frac{d^2q_\perp}{(2\pi)^2} \hat{f}(q_\perp) \frac{e^{iq_\perp \cdot r_\perp}}{q^2} \tag{8.53}$$

$$B(r_\perp) = -\int \frac{d^2q_\perp}{(2\pi)^2} \hat{f}(q_\perp) \frac{e^{iq\,r\cos\theta}}{q^2} \cos(2\theta), \tag{8.54}$$

where $\hat{f}(q_\perp)$ is the Fourier transform of $f(r_\perp)$. In Appendix H we provide an explicit calculation in the specific case of the MV model (where $f(r_\perp) = \delta^{(2)}(r_\perp)$). However, for now we prefer to stay in the most general case and leave them undetermined.

In order to solve the integral present in $D^{ij;kl}_{ab;cd}$ we consider separately the region where $z^- > w^-$ and its complementary. As was also the case with Eq. (8.39), asuming a certain ordering in the integration variables allows us to factorize the Wilson line correlator by applying the locality in rapidity implied in Eq. (8.1). For instance, in the region $z^- > w^-$ (see Fig. 8.5):

$$\begin{aligned}\Big\langle U^{a'a}(z^-, u_\perp) U^{a'b}(z^-, u'_\perp) U^{c'c}(w^-, v_\perp) U^{c'd}(w^-, v'_\perp)\Big\rangle &= \Big\langle U^{a'A}(z^-, w^-; u_\perp) U^{a'B}(z^-, w^-; u'_\perp)\Big\rangle \\ &\times \Big\langle U^{Aa}(w^-, u_\perp) U^{Bb}(w^-, u'_\perp) U^{c'c}(w^-, v_\perp) U^{c'd}(w^-, v'_\perp)\Big\rangle \\ &= C^{(2)}_{\text{adj}}(z^-, w^-; u_\perp, u'_\perp) \Big\langle U^{Aa}(w^-, u_\perp) U^{Ab}(w^-, u'_\perp) U^{c'c}(w^-, v_\perp) U^{c'd}(w^-, v'_\perp)\Big\rangle \\ &= C^{(2)}_{\text{adj}}(z^-, w^-; u_\perp, u'_\perp) Q^{AAc'c'}_{abcd}(w^-; u_\perp, u'_\perp, v_\perp, v'_\perp). \end{aligned} \tag{8.55}$$

Summing the contributions from each integration region $z^- > w^-$ and $w^- > z^-$ we get:

$$\begin{aligned} D^{ij;kl}_{ab;cd}(u_\perp, u'_\perp, v_\perp, v'_\perp) &= T^{ij;kl}(u_\perp, u'_\perp, v_\perp, v'_\perp) \int_{-\infty}^{\infty} dz^- \int_{-\infty}^{z^-} dw^- \lambda(z^-, b_\perp) \lambda(w^-, b_\perp) \\ \times \Big(C^{(2)}_{\text{adj}}(z^-, w^-; u_\perp, u'_\perp) &+ C^{(2)}_{\text{adj}}(z^-, w^-; v_\perp, v'_\perp) \Big) \delta^{AB} \delta^{CD} Q^{ABCD}_{abcd}(w^-; u_\perp, u'_\perp, v_\perp, v'_\perp). \end{aligned} \tag{8.56}$$

---

[5] We also made use (again) of the knowledge that eventually all the transverse positions that enter this expression will be either $x_\perp$ or $y_\perp$, allowing us to approximate h as $h((x_\perp + y_\perp)/2)$. This approximation was also taken in Eq. (8.41), allowing us to extract $\lambda(w^-, b_\perp)$ as a common factor of the sum.

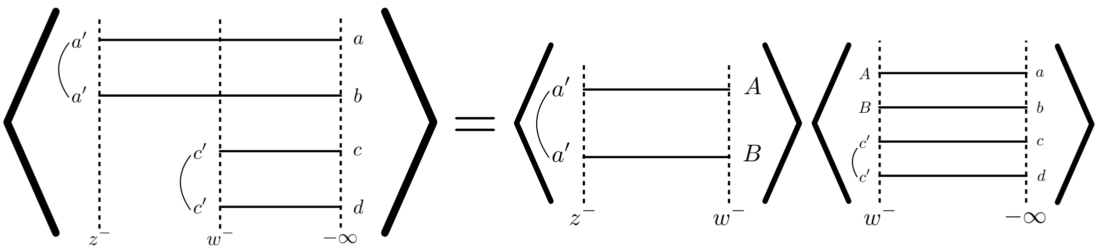

Figure 8.5: Schematic representation of the correlator factorization performed in Eq. (8.55).

Having defined the connected and disconnected functions, we can rewrite our building block compactly Eq. (8.25) as:

$$\boxed{\begin{aligned}\langle\alpha^{i\,a}(x_\perp)\alpha^{k\,c}(x_\perp)\alpha^{i'a'}(y_\perp)\alpha^{k'c'}(y_\perp)\rangle &= D^{ik;i'k'}_{ac;a'c'}(x_\perp,x_\perp,y_\perp,y_\perp)+D^{ii';kk'}_{aa';cc'}(x_\perp,y_\perp,x_\perp,y_\perp)\\ &+D^{ik';ki'}_{ac';ca'}(x_\perp,y_\perp,x_\perp,y_\perp)+C^{ii';kk'}_{aa';cc'}(x_\perp,y_\perp,x_\perp,y_\perp)+C^{ik';ki'}_{ac';ca'}(x_\perp,y_\perp,x_\perp,y_\perp)\\ &+C^{kk';ii'}_{cc';aa'}(x_\perp,y_\perp,x_\perp,y_\perp)+C^{ki';ik'}_{ca';ac'}(x_\perp,y_\perp,x_\perp,y_\perp).\end{aligned}} \tag{8.57}$$

Remarkably, in both $D^{ij;kl}_{ab;cd}$ and $C^{ij;kl}_{ab;cd}$ we find different projections of the adjoint Wilson line quadrupole Eq. (8.45), which is a quite complex object. In some instances, the fact that in our calculation we only consider two transverse coordinates $x_\perp$ and $y_\perp$ yields great simplification. For example, the first term after the equal sign in Eq. (8.57) corresponds to:

$$\begin{aligned}D^{ik;i'k'}_{ac;a'c'}(x_\perp,x_\perp,y_\perp,y_\perp) = 2\,T^{ik;i'k'}(x_\perp,x_\perp,y_\perp,y_\perp)\int_{-\infty}^{\infty}dz^-\int_{-\infty}^{z^-}dw^-\lambda(z^-,b_\perp)\lambda(w^-,b_\perp)\\ Q^{AACC}_{aca'c'}(w^-;x_\perp,x_\perp,y_\perp,y_\perp).\end{aligned} \tag{8.58}$$

In this case, the projection of the adjoint Wilson line quadrupole can be obtained in a straightforward way. Writing it explicitly:

$$Q^{AACC}_{aca'c'}(w^-;x_\perp,x_\perp,y_\perp,y_\perp) = \left\langle U^{Aa}(w^-,x_\perp)U^{Ac}(w^-,x_\perp)U^{Ca'}(w^-,y_\perp)U^{Cc'}(w^-,y_\perp)\right\rangle \tag{8.59}$$

and expanding the first pair of adjoint Wilson lines in terms of fundamental Wilson lines as $U^{ab} = 2\,\mathrm{Tr}\left\{U^\dagger t^a U t^b\right\}$ (see Appendix G for a proof of this identity), we get:

$$U^{Aa}U^{Ac} = 4\,U^\dagger_{ij}t^A_{jk}U_{kl}t^a_{li}U^\dagger_{i'j'}t^A_{j'k'}U_{k'l'}t^c_{l'i'}.$$

Now, applying the Fierz identity $t^a_{ij}t^a_{kl} = \frac{1}{2}(\delta_{il}\delta_{jk} - \frac{1}{N_c}\delta_{ij}\delta_{kl})$:

$$\begin{aligned}&= 2\left(\delta_{jk'}\delta_{kj'} - \frac{1}{N_c}\delta_{jk}\delta_{j'k'}\right)U^\dagger_{ij}U_{kl}t^a_{li}U^\dagger_{i'j'}U_{k'l'}t^c_{l'i'}\\ &= 2\left(U^\dagger_{ij}U_{kl}U^\dagger_{i'k}U_{jl'} - \frac{1}{N_c}U^\dagger_{ij}U_{jl}U^\dagger_{i'j'}U_{j'l'}\right)t^a_{li}t^c_{l'i'}\\ &= 2\left(\delta_{il'}\delta_{i'l} - \frac{1}{N_c}\delta_{il}\delta_{i'l'}\right)t^a_{li}t^c_{l'i'} = 2\left(\mathrm{Tr}\{t^at^c\} - \frac{1}{N_c}\mathrm{Tr}\{t^a\}\mathrm{Tr}\{t^c\}\right) = \delta^{ac}.\end{aligned} \tag{8.60}$$

Therefore:

$$\begin{aligned}D^{ik;i'k'}_{ac;a'c'}(x_\perp,x_\perp,y_\perp,y_\perp) &= 2\,T^{ik;i'k'}(x_\perp,x_\perp,y_\perp,y_\perp)\delta^{ac}\delta^{a'c'}\int_{-\infty}^{\infty}dz^-\int_{-\infty}^{z^-}dw^-\lambda(z^-,b_\perp)\lambda(w^-,b_\perp)\\ &= T^{ik;i'k'}(x_\perp,x_\perp,y_\perp,y_\perp)\delta^{ac}\delta^{a'c'}\bar{\lambda}^2(b_\perp) = \frac{1}{4}\delta^{ik}\delta^{i'k'}\big(\partial^2L(0_\perp)\big)^2\delta^{ac}\delta^{a'c'}\bar{\lambda}^2(b_\perp). \qquad (8.61)\end{aligned}$$

In the two remaining disconnected terms the Wilson lines that share a color index depend on different transverse coordinates, which prevents the Fierz identity from simplifying the expression. To put it differently, while in Eq. (8.58) we have

$$\delta^{AB}\delta^{CD}Q^{ABCD}_{abcd}(w^-;x_\perp,x_\perp,y_\perp,y_\perp) = \delta^{ab}\delta^{cd}, \qquad (8.62)$$

which corresponds to the trivial propagation of an eigenvector in color space, in the other two particular cases of $D^{ij;kl}_{ab;cd}$ we find

$$\delta^{AC}\delta^{BD}Q^{ABCD}_{acbd}(w^-;x_\perp,x_\perp,y_\perp,y_\perp) \qquad (8.63)$$

instead, whose calculation requires expressing $\delta^{AC}\delta^{BD}$ in terms of the eigenvectors of Q^{ABCD}_{acbd}. As for the case present in the connected function $C^{ij;kl}_{ab;cd}$ we have:

$$f^{ACe}f^{BDe}Q^{ABCD}_{abcd}(w^-;x_\perp,y_\perp,x_\perp,y_\perp). \qquad (8.64)$$

In order to compute Eq. (8.63) and Eq. (8.64), in the following subsection we analyze the adjoint Wilson line quadrupole in depth.

8.2.4 The correlator of four Wilson lines in the adjoint representation

Reexponentiation method

Before addressing our case of interest we will briefly describe and apply a general method for the computation of Wilson line correlators. This technique, first applied in [105], is based on the discretization of the x^--direction into n layers of length Δx^-. Due to the properties of path-ordered exponentials, this leads to the factorization of the Wilson line into a product of n independent contributions from each zone:

$$U(x^-,x_\perp)_{ij} \equiv U^{(n)}_{ij} \equiv (U^n(x^-_n,x_\perp)U^{n-1}(x^-_{n-1},x_\perp)...U^1(x^-_1,x_\perp))_{ij}, \qquad (8.65)$$

assuming that Δx^- is equal to or shorter than the correlation length of the gluon field fluctuations. This assumption is trivially satisfied in the MV model (and also in our generalized version), where interactions are local in rapidity, allowing us to take the limit $\Delta x^- \to 0$. As a first step we expand one of these n factors to order g^2:

$$U(x^-,x_\perp)_{ij} \approx \left(\delta_{ik} + ig\tilde{A}^{+a}(x^-_n,x_\perp)t^a_{ik}\Delta x^- - g^2\frac{C_F}{2}\lambda(x^-_n,b_\perp)L(0_\perp)\Delta x^-\delta_{ik}\right)U^{(n-1)}_{kj}, \qquad (8.66)$$

where

$$\tilde{A}^{+a}(x^-,x_\perp) = -\frac{\tilde{\rho}^a(x^-,x_\perp)}{\nabla^2} \qquad (8.67)$$

is the only non-trivial component of the gluon field expressed in the covariant gauge. Note that in the g^2-order term of Eq. (8.66) we already applied the two-point correlator, whose discretized version reads:

$$\langle \tilde{A}^{+a}(x^-,x_\perp)\tilde{A}^{+b}(y^-,y_\perp)\rangle = \lambda(x^-,b_\perp)\delta^{ab}L(x_\perp-y_\perp)\frac{\delta_{x^-y^-}}{\Delta x^-}. \tag{8.68}$$

We iterate this process $n-1$ more times neglecting terms of order $(\Delta x^-)^2$ or higher. Then, we rearrange the resulting terms in the form of the first orders of an expanded exponential. The last step is the reexponentiation, where we assume that the neglected terms complete the expansion. As an example, let us use this technique to calculate the well-known dipole function:

$$\begin{aligned}
&\left\langle \mathrm{Tr}\left\{U(x_\perp)U^\dagger(y_\perp)\right\}\right\rangle \\
&\approx\left\langle U^{(n-1)}_{kl}(x_\perp)U^{(n-1)\dagger}_{lj}(y_\perp)\left(\delta_{ik}+ig\tilde{A}^{+a}(x^-_n,x_\perp)t^a_{ik}\Delta x^- - g^2\frac{C_F}{2}\lambda(x^-_n,b_\perp)L(0_\perp)\Delta x^-\delta_{ik}\right)\right.\\
&\qquad\left.\times\left(\delta_{ji}-ig\tilde{A}^{+b}(x^-_n,y_\perp)t^b_{ji}\Delta x^- - g^2\frac{C_F}{2}\lambda(x^-_n,b_\perp)L(0_\perp)\Delta x^-\delta_{ji}\right)\right\rangle\\
&=\left\langle \mathrm{Tr}\left\{U(x_\perp)U^\dagger(y_\perp)\right\}\right\rangle^{(n-1)}\left(1-\frac{g^2}{2}C_F\Delta x^-\lambda(x^-_n,b_\perp)\Gamma(x_\perp-y_\perp)\right).
\end{aligned} \tag{8.69}$$

In the last step we have made use of the locality in rapidity of the MV model to factorize the correlator of the remaining Wilson line layers $\left\langle \mathrm{Tr}\left\{U(x_\perp)U^\dagger(y_\perp)\right\}\right\rangle^{(n-1)}$. By iterating the process, we arrive at:

$$\begin{aligned}
\left\langle \mathrm{Tr}\left\{U(x_\perp)U^\dagger(y_\perp)\right\}\right\rangle &\approx \left(1-\frac{g^2}{2}C_F\,\Gamma(x_\perp-y_\perp)h(b_\perp)\sum_{i=1}^{n}\Delta x^-\mu^2(x^-_i)\right)\\
&=\left(1-\frac{g^2}{2}C_F\,\Gamma(x_\perp-y_\perp)\bar{\lambda}(x^-,b_\perp)\right).
\end{aligned} \tag{8.70}$$

Lastly, we assume that the neglected higher order terms add up to the following exponential expression:

$$\left\langle \mathrm{Tr}\left\{U(x_\perp)U^\dagger(y_\perp)\right\}\right\rangle = \exp\left\{-\frac{g^2}{2}C_F\,\Gamma(x_\perp-y_\perp)\bar{\lambda}(x^-,b_\perp)\right\}, \tag{8.71}$$

which indeed agrees with the known result.

Diagonalization method

One important shortcoming of the technique described above lies in the fact that there is no unique way in which we can arrange the terms resulting from expanding the Wilson lines. This step becomes more problematic as we increase the number of Wilson lines in the correlator. Nevertheless, we can reduce the inherent arbitrariness of the reexponentiation process by formulating it as a diagonalization problem. This allows us to systematically account for all incoming and outgoing states of the color connections embodied in the medium average $\langle ...\rangle$. In the next subsection we will make use of this technique to obtain the behavior of the following adjoint Wilson line quadrupole:

$$\left\langle U^{Aa}(x_\perp)U^{Bb}(x_\perp)U^{Cc}(y_\perp)U^{Dd}(y_\perp)\right\rangle. \tag{8.72}$$

under different color projections. In order to illustrate the method we will first reproduce the more general result obtained in [105] for three different transverse coordinates:

$$\big\langle U^{ab}(z_\perp)U^{cd}(z_\perp)U^{ef}(x_\perp)U^{gh}(y_\perp)\big\rangle. \tag{8.73}$$

First, we need to expand the adjoint Wilson lines in a longitudinal position x_n^-. For the sake of simplicity in the following calculations we will momentarily adopt a shorthand notation where we absorb the $g\Delta x^-$ factor in the definition of our fields:

$$g\tilde{A}^{+a}(x^-,x_\perp)\Delta x^- \equiv \tilde{A}^{+a}(x^-,x_\perp), \tag{8.74}$$

which yields the following two-point function:

$$\langle \tilde{A}^{+a}(x^-,x_\perp)\tilde{A}^{+b}(y^-,y_\perp)\rangle = \delta_{x^-y^-}\delta^{ab}B_{xy}(x^-,b_\perp), \tag{8.75}$$

where, due to the discretization of the rapidity range, the Kronecker delta $\delta_{x^-y^-}$ now takes the place of the Dirac delta. For simplicity we also introduced:

$$B_{xy}(x^-,b_\perp)\equiv g^2\Delta x^-\lambda(x^-,b_\perp)L(x_\perp-y_\perp). \tag{8.76}$$

Using this notation the expansion to order g^2 of the adjoint Wilson line yields:

$$U^{ab}(x^-,x_\perp) = (U^{ab_1})^{(n-1)}\left(\delta^{b_1b}\left(1-\frac{N_c}{2}B_x(x_n^-,b_\perp)\right) - \tilde{A}^g(x_n^-,x_\perp)f^{b_1gb}\right). \tag{8.77}$$

Performing this expansion for every Wilson line in Eq. (8.73) and neglecting terms of order $(\Delta x^-)^2$ or higher we get:

$$\begin{aligned}
\big\langle U^{ab}(z_\perp)U^{cd}(z_\perp)U^{ef}(x_\perp)U^{gh}(y_\perp)\big\rangle &= \Big\langle U^{aa'}(z_\perp)U^{cc'}(z_\perp)U^{ee'}(x_\perp)U^{gg'}(y_\perp)\Big\rangle^{(n-1)} \\
&\times\left(\delta^{a'b}\delta^{c'd}\delta^{e'f}\delta^{g'h}\left(1-\frac{N_c}{2}\left(2B_z+B_x+B_y\right)\right) + \delta^{a'b}\delta^{c'd}f^{e'mf}f^{g'mh}B_{xy}\right. \\
&+\delta^{a'b}\delta^{e'f}f^{c'md}f^{g'mh}B_{zy} + \delta^{a'b}\delta^{g'h}f^{e'mf}f^{c'md}B_{zx} + \delta^{e'f}\delta^{c'd}f^{a'mb}f^{g'mh}B_{zy} \\
&\left.+\delta^{g'h}\delta^{c'd}f^{e'mf}f^{a'mb}B_{zx} + \delta^{e'f}\delta^{g'h}f^{a'mb}f^{c'md}B_z\right).
\end{aligned} \tag{8.78}$$

We express the previous lines as a matrix equation: $U^{aceg}_{bdfh} = (U^{aceg}_{a'c'e'g'})^{(n-1)}T^{a'c'e'g'}_{bdfh}$, for which we introduce the following color vector basis:

$$\begin{aligned}
&u_1 = \delta^{ea}\delta^{gc} && u_2 = \delta^{ca}\delta^{ge} && u_3 = \delta^{ga}\delta^{ec} \\
&w_1 = d^{eam}d^{gcm} && w_2 = d^{cam}d^{gem} && w_3 = d^{gam}d^{ecm} \\
&z_1 = d^{eam}f^{gcm} && z_2 = d^{cam}f^{gem} && z_3 = d^{gam}f^{ecm}.
\end{aligned} \tag{8.79}$$

It can be shown via color algebra arguments that this ensemble covers all possible connections embodied in $T^{a'c'e'g'}_{bdfh}$ (see [106])[6]. The last three (z_1, z_2, z_3) form a basis that does not mix with

---

[6] In [106], only 8 of these objects are addressed. This is due to the author focusing on the specific case of $N_c=3$. The existence of an extra algebraic relation between $SU(3)$ generators reduces the number of independent rank 4 tensors from 9 to 8.

the rest of the vectors in the Gaussian model we are considering. Thus, if we expressed $T^{a'c'e'h'}_{bdfh}$ in this 9-dimensional space it would look like a block diagonal matrix with a 6×6 part corresponding to the vectors u_i, w_i and a 3×3 sector corresponding to the z_i set. In our specific calculation, the vectors that we are interested in 'live' in the 6-dimensional space defined by the first two sets, and thus it will suffice to consider $T^{a'c'e'h'}_{bdfh}$ in the basis formed by u_i and w_i. In order to build this matrix we propagate these six vectors using Eq. (8.78):

$$\begin{aligned} T^{a'c'e'h'}_{bdfh}\delta^{e'a'}\delta^{g'c'} =& \,\delta^{fb}\delta^{hd}\left(1-\frac{N_c}{2}(2B_z+B_x+B_y-2B_{zx}-2B_{zy})\right) \\ &+ f^{bfm}f^{dhm}\left(B_z+B_{xy}-B_{zx}-B_{zy}\right) \\ =& \,\delta^{fb}\delta^{hd}\left(1-g^2\frac{N_c}{2}\Delta x^-\lambda(x_n^-,b_\perp)(\Gamma(z_\perp-x_\perp)+\Gamma(z_\perp-y_\perp))\right) \\ &+ f^{bfm}f^{dhm}\frac{g^2}{2}\Delta x^-\lambda(x_n^-,b_\perp)\left(\Gamma(z_\perp-x_\perp)+\Gamma(z_\perp-y_\perp)-\Gamma(x_\perp-y_\perp)\right). \end{aligned} \tag{8.80}$$

The SU(N_c) factor $f^{bfm}f^{dhm}$, as well as the ones resulting from permutations of its indices, can be expressed in terms of our basis vectors by means of the following identity:

$$f^{abm}f^{cdm} = \frac{2}{N_c}(\delta^{ac}\delta^{bd}-\delta^{ad}\delta^{bc}) + d^{ace}d^{bde} - d^{ade}d^{bce}. \tag{8.81}$$

Therefore, the propagation of u_1 reads:

$$\begin{aligned} Tu_1 =& \,u_1\left(1-g^2\frac{N_c}{2}\Delta x^-\lambda(x_n^-,b_\perp)(\Gamma(z_\perp-x_\perp)+\Gamma(z_\perp-y_\perp))\right) \\ &+\frac{g^2}{2}\Delta x^-\lambda(x_n^-,b_\perp)\left(\frac{2}{N_c}(u_2-u_3)+w_2-w_3\right)(\Gamma(z_\perp-x_\perp)+\Gamma(z_\perp-y_\perp)-\Gamma(x_\perp-y_\perp)). \end{aligned} \tag{8.82}$$

Repeating this process for the remaining vectors, we obtain:

$$Tu_2 = u_2\left(1-g^2\frac{N_c}{2}\Delta x^-\lambda(x_n^-,b_\perp)\Gamma(x_\perp-y_\perp)\right) \tag{8.83}$$

$$\begin{aligned} Tu_3 =& \,u_3\left(1-g^2\frac{N_c}{2}\Delta x^-\lambda(x_n^-,b_\perp)(\Gamma(z_\perp-x_\perp)+\Gamma(z_\perp-y_\perp))\right) \\ &+\frac{g^2}{2}\Delta x^-\lambda(x_n^-,b_\perp)\left(\frac{2}{N_c}(u_2-u_1)+w_2-w_1\right)(\Gamma(z_\perp-x_\perp)+\Gamma(z_\perp-y_\perp)-\Gamma(x_\perp-y_\perp)) \end{aligned} \tag{8.84}$$

$$\begin{aligned} Tw_1 =& \,w_1\left(1-g^2\frac{N_c}{8}\Delta x^-\lambda(x_n^-,b_\perp)(\Gamma(x_\perp-y_\perp)+3\Gamma(z_\perp-x_\perp)+3\Gamma(z_\perp-y_\perp))\right) \\ &+\frac{g^2}{2}\Delta x^-\lambda(x_n^-,b_\perp)\left(\left(\frac{2}{N_c}-\frac{N_c}{4}\right)(w_2-w_3)+\left(\frac{4}{N_c^2}-1\right)(u_2-u_3)\right) \\ &\times(\Gamma(x_\perp-y_\perp)-\Gamma(z_\perp-x_\perp)-\Gamma(z_\perp-y_\perp)) \end{aligned} \tag{8.85}$$

$$Tw_2 = w_2\left(1-g^2\frac{N_c}{4}\Delta x^-\lambda(x_n^-,b_\perp)\left(\Gamma(x_\perp-y_\perp)+\Gamma(z_\perp-x_\perp)+\Gamma(z_\perp-y_\perp)\right)\right) \tag{8.86}$$

$$Tw_3 = w_3\left(1-g^2\frac{N_c}{8}\Delta x^-\lambda(x_n^-,b_\perp)(\Gamma(x_\perp-y_\perp)+3\Gamma(z_\perp-x_\perp)+3\Gamma(z_\perp-y_\perp))\right)$$

$$+\frac{g^2}{2}\Delta x^-\lambda(x_n^-,b_\perp)\left(\left(\frac{2}{N_c}-\frac{N_c}{4}\right)(w_2-w_1)+\left(\frac{4}{N_c^2}-1\right)(u_2-u_1)\right)$$
$$\times(\Gamma(x_\perp-y_\perp)-\Gamma(z_\perp-x_\perp)-\Gamma(z_\perp-y_\perp)). \tag{8.87}$$

From the previous projections we can write Eq. (8.78) in the following form:

$$U^{aceg}_{bdfh}=(U^{aceg}_{a'c'e'g'})^{(n-1)}T^{a'c'e'g'}_{bdfh}(x_n^-)=(U^{aceg}_{a'c'e'g'})^{(n-1)}(\mathbb{1}+M(x_n^-))^{a'c'e'g'}_{bdfh}, \tag{8.88}$$

where the $M^{a'c'e'g'}_{bdfh}$ matrix is of order 1 in Δx^-. The next step of the method consists in iterating the expansion of the Wilson lines $n-1$ times. By doing this (and neglecting terms of order $(\Delta x^-)^2$ or higher), we get:

$$U^{aceg}_{bdfh}=\mathbb{1}+\sum_{i=1}^{n}M^{a'c'e'g'}_{bdfh}(x_i^-)=\mathbb{1}+\int^{x^-}dz'^-M^{a'c'e'g'}_{bdfh}(z'^-)=\mathbb{1}+\bar{M}(x^-). \tag{8.89}$$

It is worth remarking that we are omitting some of the dependencies of $\bar{M}$ for simplicity; this tensor also depends on the transverse coordinates, $\bar{M}(x^-;z_\perp,x_\perp,y_\perp)$. In order to reproduce the notation of [105], we introduce the following functions:

$$R_a=-\frac{g^2}{2}\bar{\lambda}(x^-,b_\perp)\left(\Gamma(z_\perp-x_\perp)-\Gamma(z_\perp-y_\perp)\right) \tag{8.90}$$
$$R_b=-\frac{g^2}{2}\bar{\lambda}(x^-,b_\perp)\left(\Gamma(x_\perp-y_\perp)\right) \tag{8.91}$$
$$R_d=R_b-R_a, \tag{8.92}$$

and thus we obtain the following expression for $\bar{M}$ (hereby correcting typos in the matrix given in [105]):

$$\begin{bmatrix}
N_cR_a & 0 & -\frac{2}{N_c}R_d & 0 & 0 & R_d\left(\frac{4}{N_c^2}-1\right)\\
\frac{2}{N_c}R_d & N_cR_b & \frac{2}{N_c}R_d & -R_d\left(\frac{4}{N_c^2}-1\right) & 0 & -R_d\left(\frac{4}{N_c^2}-1\right)\\
-\frac{2}{N_c}R_d & 0 & N_cR_a & R_d\left(\frac{4}{N_c^2}-1\right) & 0 & 0\\
0 & 0 & -R_d & \frac{N_c}{4}(3R_a+R_b) & 0 & R_d\left(\frac{2}{N_c}-\frac{N_c}{4}\right)\\
R_d & 0 & R_d & -R_d\left(\frac{2}{N_c}-\frac{N_c}{4}\right) & \frac{N_c}{2}(R_a+R_b) & -R_d\left(\frac{2}{N_c}-\frac{N_c}{4}\right)\\
-R_d & 0 & 0 & R_d\left(\frac{2}{N_c}-\frac{N_c}{4}\right) & 0 & \frac{N_c}{4}(3R_a+R_b)
\end{bmatrix}, \tag{8.93}$$

which we diagonalize using Mathematica:

$$\bar{M}_d=\begin{bmatrix}
N_cR_a & 0 & 0 & 0 & 0 & 0\\
0 & N_cR_b & 0 & 0 & 0 & 0\\
0 & 0 & \frac{1}{2}(R_a+R_b)N_c & 0 & 0 & 0\\
0 & 0 & 0 & \frac{1}{2}(R_a+R_b)N_c & 0 & 0\\
0 & 0 & 0 & 0 & N_cR_a-R_d & 0\\
0 & 0 & 0 & 0 & 0 & N_cR_a+R_d
\end{bmatrix}. \tag{8.94}$$

The final step is the reexponentiation of Eq. (8.89), which is straightforward for a diagonal matrix:

$$U^{aceg}_{bdfh} \doteq (\mathbb{1}+\bar{M}_d)^{aceg}_{bdfh} \;\longrightarrow\; U^{aceg}_{bdfh} \doteq (e^{\bar{M}_d})^{aceg}_{bdfh}. \tag{8.95}$$

Here the dot stresses that in order to use this result we need to work in the basis defined by the eigenvectors of $\bar{M}$, which in the $(u_1, u_2, u_3, w_1, w_2, w_3)$ basis adopts the form:

$$t_1 = \begin{pmatrix} \frac{N_c^2-4}{2N_c} \\ 0 \\ -\frac{N_c^2-4}{2N_c} \\ -1 \\ 0 \\ 1 \end{pmatrix},\; t_2 = \begin{pmatrix} 0 \\ 1 \\ 0 \\ 0 \\ 0 \\ 0 \end{pmatrix},\; t_3 = \begin{pmatrix} -\frac{2}{N_c} \\ 0 \\ \frac{2}{N_c} \\ -1 \\ 0 \\ 1 \end{pmatrix},$$

$$t_4 = \begin{pmatrix} 0 \\ 0 \\ 0 \\ 0 \\ 1 \\ 0 \end{pmatrix},\; t_5 = \begin{pmatrix} \frac{2+N_c}{N_c} \\ -\frac{2}{N_c}\frac{2+N_c}{N_c+1} \\ \frac{2+N_c}{N_c} \\ 1 \\ -\frac{N_c+4}{N_c+2} \\ 1 \end{pmatrix},\; t_6 = \begin{pmatrix} \frac{2-N_c}{N_c} \\ \frac{2}{N_c}\frac{2-N_c}{N_c-1} \\ \frac{2-N_c}{N_c} \\ 1 \\ -\frac{N_c-4}{N_c-2} \\ 1 \end{pmatrix}. \tag{8.96}$$

Remarkably, we have $t_2 = u_2 = \delta^{ca}\delta^{ge}$, $t_3 = -f^{can}f^{gen}$, and $t_4 = w_1 = d^{ean}d^{gcn}$.

Projections of the quadrupole

Let us now go back to our particular case:

$$\left\langle U^{Aa}(x_\perp)U^{Bb}(x_\perp)U^{Cc}(y_\perp)U^{Dd}(y_\perp)\right\rangle, \tag{8.97}$$

which can be obtained from the quadrupole studied in the previous subsection by setting $z_\perp \equiv x_\perp$ and $x_\perp = y_\perp \equiv y_\perp$. This simplifies the above result, as $R_b = 0$ and $R_d = -R_a$. In this limit, $\bar{M}_d$ adopts the following form:

$$\bar{M}_d = \begin{bmatrix} N_cR_a & 0 & 0 & 0 & 0 & 0 \\ 0 & 0 & 0 & 0 & 0 & 0 \\ 0 & 0 & \frac{1}{2}N_cR_a & 0 & 0 & 0 \\ 0 & 0 & 0 & \frac{1}{2}N_cR_a & 0 & 0 \\ 0 & 0 & 0 & 0 & (N_c+1)R_a & 0 \\ 0 & 0 & 0 & 0 & 0 & (N_c-1)R_a \end{bmatrix}. \tag{8.98}$$

As part of the calculation of $\langle T^{\mu\nu}(x_\perp)T^{\sigma\rho}(y_\perp)\rangle$, we need to calculate the following projections of the adjoint Wilson line quadrupole:

$$f^{ABe}f^{DCe}\left\langle U^{Aa}(x_\perp)U^{Bb}(x_\perp)U^{Cc}(y_\perp)U^{Dd}(y_\perp)\right\rangle \tag{8.99}$$

$$\delta^{AC}\delta^{BD}\left\langle U^{Aa}(x_\perp)U^{Bb}(x_\perp)U^{Cc}(y_\perp)U^{Dd}(y_\perp)\right\rangle. \tag{8.100}$$

The first of them corresponds to the propagation of the eigenvector t_3, which is straightforward to compute:

$$\begin{aligned}(e^{\bar{M}_d})^{ABCD}_{abcd}(t_3)^{ABCD} &= (t_3)^{abcd}\exp\left\{\frac{1}{2}N_c R_a\right\} \\ &= f^{abn}f^{dcn}\exp\left\{-g^2\frac{N_c}{2}\Gamma(x_\perp - y_\perp)\bar{\lambda}(x^-, b_\perp)\right\}, \qquad (8.101)\end{aligned}$$

as was also the case with Eq. (8.62). In contrast, Eq. (8.100) corresponds to the propagation of u_1, which is not an eigenvector and thus requires that we express it in terms of the t_i set:

$$u_1 = \frac{1}{N_c}t_1 + \frac{1}{N_c^2-1}t_2 - \frac{1}{N_c}t_3 + \frac{N_c}{N_c^2-4}t_4 + \frac{1}{4}t_5 - \frac{1}{4}t_6. \qquad (8.102)$$

Then:

$$\begin{aligned}(e^{\bar{M}_d})^{ABCD}_{abcd}(u_1)^{ABCD} &= \frac{1}{N_c}(t_1)^{abcd}\exp\left\{-g^2 N_c\Gamma(x_\perp - y_\perp)\bar{\lambda}\right\} + \frac{1}{N_c^2-1}(t_2)^{abcd} \\ &-\frac{1}{N_c}(t_3)^{abcd}\exp\left\{-g^2\frac{N_c}{2}\Gamma(x_\perp - y_\perp)\bar{\lambda}\right\} + \frac{N_c}{N_c^2-4}(t_4)^{abcd}\exp\left\{-g^2\frac{N_c}{2}\Gamma(x_\perp - y_\perp)\bar{\lambda}\right\} \\ &+\frac{1}{4}(t_5)^{abcd}\exp\left\{-g^2(N_c+1)\Gamma(x_\perp - y_\perp)\bar{\lambda}\right\} - \frac{1}{4}(t_6)^{abcd}\exp\left\{-g^2(N_c-1)\Gamma(x_\perp - y_\perp)\bar{\lambda}\right\}, \qquad (8.103)\end{aligned}$$

where we omitted the dependencies of $\bar{\lambda}$ for simplicity. Expanding the eigenvectors in terms of our original basis Eq. (8.79) we obtain:

$$\begin{aligned}&= \delta^{ac}\delta^{bd}\left(\frac{N_c^2-4}{2N_c^2}e^{-g^2N_c\Gamma\bar{\lambda}} + \frac{2}{N_c^2}e^{-g^2\frac{N_c}{2}\Gamma\bar{\lambda}} + \frac{N_c+2}{4N_c}e^{-g^2(N_c+1)\Gamma\bar{\lambda}} + \frac{N_c-2}{4N_c}e^{-g^2(N_c-1)\Gamma\bar{\lambda}}\right) \\ &+\delta^{ab}\delta^{cd}\left(\frac{1}{N_c^2-1} - \frac{N_c+2}{2N_c(N_c+1)}e^{-g^2(N_c+1)\Gamma\bar{\lambda}} + \frac{N_c-2}{2N_c(N_c-1)}e^{-g^2(N_c-1)\Gamma\bar{\lambda}}\right) \\ &+\delta^{ad}\delta^{bc}\left(-\frac{N_c^2-4}{2N_c^2}e^{-g^2N_c\Gamma\bar{\lambda}} - \frac{2}{N_c^2}e^{-g^2\frac{N_c}{2}\Gamma\bar{\lambda}} + \frac{N_c+2}{4N_c}e^{-g^2(N_c+1)\Gamma\bar{\lambda}} + \frac{N_c-2}{4N_c}e^{-g^2(N_c-1)\Gamma\bar{\lambda}}\right) \\ &+d^{acn}d^{bdn}\left(-\frac{1}{N_c}e^{-g^2N_c\Gamma\bar{\lambda}} + \frac{1}{N_c}e^{-g^2\frac{N_c}{2}\Gamma\bar{\lambda}} + \frac{1}{4}e^{-g^2(N_c+1)\Gamma\bar{\lambda}} - \frac{1}{4}e^{-g^2(N_c-1)\Gamma\bar{\lambda}}\right) \\ &+d^{abn}d^{cdn}\left(\frac{N_c}{N_c^2-4}e^{-g^2\frac{N_c}{2}\Gamma\bar{\lambda}} - \frac{N_c+4}{4(N_c+2)}e^{-g^2(N_c+1)\Gamma\bar{\lambda}} + \frac{N_c-4}{4(N_c-2)}e^{-g^2(N_c-1)\Gamma\bar{\lambda}}\right) \\ &+d^{adn}d^{bcn}\left(\frac{1}{N_c}e^{-g^2N_c\Gamma\bar{\lambda}} - \frac{1}{N_c}e^{-g^2\frac{N_c}{2}\Gamma\bar{\lambda}} + \frac{1}{4}e^{-g^2(N_c+1)\Gamma\bar{\lambda}} - \frac{1}{4}e^{-g^2(N_c-1)\Gamma\bar{\lambda}}\right), \qquad (8.104)\end{aligned}$$

where we continue to omit dependencies[7].

8.2.5 Connected and disconnected functions (revisited)

By application of the projections computed above, we are now able to complete the calculations of $C^{ij;kl}_{ab;cd}$ and $D^{ij;kl}_{ab;cd}$. As shown in Eq. (8.101), the former contains a trivial projection of the adjoint

---

[7] Note that in order to apply Eq. (8.104) in the calculation of $D^{ij;kl}_{ab;cd}(x_\perp, y_\perp, x_\perp, y_\perp)$ and $C^{ij;kl}_{ab;cd}(x_\perp, y_\perp, x_\perp, y_\perp)$ one has to permute its indices b and c.

Wilson line quadrupole:

$$f^{ACe}f^{BDe}Q^{ABCD}_{abcd}(w^{-\prime};x_\perp,y_\perp,x_\perp,y_\perp) = f^{ABe}f^{CDe}Q^{ABCD}_{acbd}(w^{-\prime};x_\perp,x_\perp,y_\perp,y_\perp)$$
$$= f^{ace}f^{bde}C^{(2)}_{\text{adj}}(w^{-\prime};x_\perp,y_\perp). \tag{8.105}$$

Also, note that in the case of only two different transverse coordinates the adjoint Wilson line tripole also tends to the dipole function:

$$C^{(3)}_{\text{adj}}(w^-,w^{-\prime};x_\perp,y_\perp,x_\perp) = C^{(2)}_{\text{adj}}(w^-,w^{-\prime};x_\perp,y_\perp). \tag{8.106}$$

Substituting these expressions into Eq. (8.46), we are left with a product of three dipole functions that combine as:

$$C^{(2)}_{\text{adj}}(z^-,w^-;x_\perp,y_\perp)C^{(2)}_{\text{adj}}(w^-,w^{-\prime};x_\perp,y_\perp)C^{(2)}_{\text{adj}}(w^{-\prime};x_\perp,y_\perp)$$
$$= \exp\left\{-g^2\frac{N_c}{2}\Gamma(x_\perp-y_\perp)h(b_\perp)\big(\bar\mu^2(z^-,w^-)+\bar\mu^2(w^-,w^{-\prime})+\bar\mu^2(w^{-\prime})\big)\right\}$$
$$= \exp\left\{-g^2\frac{N_c}{2}\Gamma(x_\perp-y_\perp)h(b_\perp)\left(\int_{w^-}^{z^-}du^-\mu^2(u^-)+\int_{w^{-\prime}}^{w^-}du^-\mu^2(u^-)+\int_{-\infty}^{w^{-\prime}}du^-\mu^2(u^-)\right)\right\}$$
$$= C^{(2)}_{\text{adj}}(z^-;x_\perp,y_\perp), \tag{8.107}$$

and therefore:

$$C^{ij;kl}_{ab;cd}(x_\perp,y_\perp,x_\perp,y_\perp) = \frac{g^2}{2}f^{ace}f^{bde}h^3(b_\perp)\partial^i_x\partial^j_y L(x_\perp-y_\perp)\partial^k_x\Gamma(x_\perp-y_\perp)\partial^l_y\Gamma(y_\perp-x_\perp)$$
$$\times\int_{-\infty}^{\infty}dz^-\int_{-\infty}^{z^-}dw^-\int_{-\infty}^{w^-}dw^{-\prime}\mu^2(z^-)\mu^2(w^-)\mu^2(w^{\prime -})C^{(2)}_{\text{adj}}(z^-;x_\perp,y_\perp). \tag{8.108}$$

Solving the double integral, we obtain:

$$C^{ij;kl}_{ab;cd}(x_\perp,y_\perp,x_\perp,y_\perp) = f^{ace}f^{bde}\partial^i_x\partial^j_y L(x_\perp-y_\perp)\partial^k_x\Gamma(x_\perp-y_\perp)\partial^l_y\Gamma(x_\perp-y_\perp)$$
$$\times\left(\frac{4}{\Gamma^3g^4N_c^3}-\left(\frac{\bar\lambda^2(b_\perp)}{2\Gamma N_c}+\frac{4}{\Gamma^3g^4N_c^3}+\frac{2\bar\lambda(b_\perp)}{\Gamma^2g^2N_c^2}\right)C^{(2)}_{\text{adj}}(x_\perp,y_\perp)\right), \tag{8.109}$$

which concludes the computation of the connected function. In the case of the disconnected function, substituting the result of Eq. (8.63) and solving the double integrals, we obtain:

$$D^{ij;kl}_{ab;cd}(x_\perp,y_\perp,x_\perp,y_\perp) = 2\Bigg(\delta^{ab}\delta^{cd}\left[\frac{N_c^2-4}{2N_c^2}f_1+\frac{2}{N_c^2}f_2+\frac{N_c+2}{4N_c}f_3+\frac{N_c-2}{4N_c}f_4\right]$$
$$+\delta^{ac}\delta^{bd}\left[\frac{1}{N_c^2-1}f_5-\frac{N_c+2}{2N_c(N_c+1)}f_3+\frac{N_c-2}{2N_c(N_c-1)}f_4\right]$$
$$+\delta^{ad}\delta^{bc}\left[-\frac{N_c^2-4}{2N_c^2}f_1-\frac{2}{N_c^2}f_2+\frac{N_c+2}{4N_c}f_3+\frac{N_c-2}{4N_c}f_4\right]$$
$$+d^{abm}d^{cdm}\left[-\frac{1}{N_c}f_1+\frac{1}{N_c}f_2+\frac{1}{4}f_3-\frac{1}{4}f_4\right]+d^{adm}d^{cbm}\left[\frac{1}{N_c}f_1-\frac{1}{N_c}f_2+\frac{1}{4}f_3-\frac{1}{4}f_4\right]$$
$$+d^{acm}d^{bdm}\left[\frac{N_c}{N_c^2-4}f_2-\frac{N_c+4}{4(N_c+2)}f_3+\frac{N_c-4}{4(N_c-2)}f_4\right]\Bigg)T^{ij;kl}(x_\perp,y_\perp,x_\perp,y_\perp), \tag{8.110}$$

where:

$$f_1 = \frac{2}{(N_c g^2\Gamma)^2}(1 - C^{(2)}_{\text{adj}}(x_\perp, y_\perp))^2 \tag{8.111}$$

$$f_2 = \frac{2}{N_c g^2\Gamma}\left(\frac{2}{N_c g^2\Gamma}(1 - C^{(2)}_{\text{adj}}(x_\perp, y_\perp)) - \bar{\lambda}(b_\perp) C^{(2)}_{\text{adj}}(x_\perp, y_\perp)\right) \tag{8.112}$$

$$\begin{aligned} f_3 = &\left(\frac{4}{N_c(N_c+2)g^4\Gamma^2}(1 - C^{(2)}_{\text{adj}}(x_\perp, y_\perp))\right. \\ &\left. - \frac{2}{(N_c+2)(N_c+1)g^4\Gamma^2}(1 - (C^{(2)}_{\text{adj}}(x_\perp, y_\perp))^2 \exp\left\{-g^2\Gamma\bar{\lambda}(b_\perp)\right\})\right) \end{aligned} \tag{8.113}$$

$$\begin{aligned} f_4 = &\left(\frac{4}{N_c(N_c-2)g^4\Gamma^2}(1 - C^{(2)}_{\text{adj}}(x_\perp, y_\perp))\right. \\ &\left. - \frac{2}{(N_c-2)(N_c-1)g^4\Gamma^2}(1 - (C^{(2)}_{\text{adj}}(x_\perp, y_\perp))^2 \exp\left\{g^2\Gamma\bar{\lambda}(b_\perp)\right\})\right) \end{aligned} \tag{8.114}$$

$$f_5 = \frac{2}{N_c g^2\Gamma}\left(\bar{\lambda}(b_\perp) - \frac{2}{N_c g^2\Gamma}(1 - C^{(2)}_{\text{adj}}(x_\perp, y_\perp))\right). \tag{8.115}$$

This concludes the calculation of $\langle \alpha_x^{i,a}\alpha_x^{k,c}\alpha_y^{i',a'}\alpha_y^{k',c'}\rangle$.

8.2.6 Covariance of the Glasma energy density

The final step of this long calculation consists in explicitly expanding the color contractions between said building blocks (one for each nucleus) and the transverse and color structure tensors defined earlier:

$$\langle \epsilon_0(x_\perp)\epsilon_0(y_\perp)\rangle = \mathcal{A}^{ik;i'k'}_{jl;j'l'}\mathcal{F}^{ac;a'c'}_{bd;b'd'}\langle \alpha_x^{i,a}\alpha_x^{k,c}\alpha_y^{i',a'}\alpha_y^{k',c'}\rangle_1 \langle \alpha_x^{j,b}\alpha_x^{l,d}\alpha_y^{j',b'}\alpha_y^{l',d'}\rangle_2. \tag{8.116}$$

The product of the seven terms corresponding to each nucleus (Eq. (8.57)) yields a total of 49 terms, which, by application of the symmetries of the tensors $\mathcal{A}^{ik;i'k'}_{jl;j'l'}$ and $\mathcal{F}^{ac;a'c'}_{bd;b'd'}$, can be reduced to:

$$\begin{aligned} \langle \epsilon_0(x_\perp)\epsilon_0(y_\perp)\rangle = &\left[\frac{1}{2}D_{1\,ac;a'c'}^{\;ik;i'k'}(x_\perp, x_\perp, y_\perp, y_\perp) D_{2\,bd;b'd'}^{\;jl;j'l'}(x_\perp, x_\perp, y_\perp, y_\perp)\mathcal{A}^{ik;i'k'}_{jl;j'l'}\mathcal{F}^{ac;a'c'}_{bd;b'd'}\right. \\ &+ \left(D_{1\,ac;a'c'}^{\;ik;i'k'}(x_\perp, x_\perp, y_\perp, y_\perp) D_{2\,bb';dd'}^{\;jj';ll'}(x_\perp, y_\perp, x_\perp, y_\perp)\right. \\ &\left. + D_{1\,aa';cc'}^{\;ii';kk'}(x_\perp, y_\perp, x_\perp, y_\perp) D_{2\,bb';dd'}^{\;jj';ll'}(x_\perp, y_\perp, x_\perp, y_\perp)\right)\left[\mathcal{A}^{ik;i'k'}_{jl;j'l'}\mathcal{F}^{ac;a'c'}_{bd;b'd'} + \mathcal{A}^{ik;i'k'}_{jl;l'j'}\mathcal{F}^{ac;a'c'}_{bd;d'b'}\right] \\ &+ \left(D_{1\,ac;a'c'}^{\;ik;i'k'}(x_\perp, x_\perp, y_\perp, y_\perp) C_{2\,bb';dd'}^{\;jj';ll'}(x_\perp, y_\perp, x_\perp, y_\perp)\right. \\ &+ 2\,D_{1\,aa';cc'}^{\;ii';kk'}(x_\perp, y_\perp, x_\perp, y_\perp) C_{2\,bb';dd'}^{\;jj';ll'}(x_\perp, y_\perp, x_\perp, y_\perp) \\ &\left. + 2\,C_{1\,aa';cc'}^{\;ii';kk'}(x_\perp, y_\perp, x_\perp, y_\perp) C_{2\,bb';dd'}^{\;jj';ll'}(x_\perp, y_\perp, x_\perp, y_\perp)\right) \\ &\left.\times\left[\mathcal{A}^{ik;i'k'}_{jl;j'l'}\mathcal{F}^{ac;a'c'}_{bd;b'd'} + \mathcal{A}^{ik;i'k'}_{lj;j'l'}\mathcal{F}^{ac;a'c'}_{db;b'd'} + \mathcal{A}^{ik;i'k'}_{jl;l'j'}\mathcal{F}^{ac;a'c'}_{bd;d'b'} + \mathcal{A}^{ik;i'k'}_{lj;l'j'}\mathcal{F}^{ac;a'c'}_{db;d'b'}\right]\right] + [1 \leftrightarrow 2]\,. \end{aligned} \tag{8.117}$$

It is worth mentioning that the terms stemming from the first contraction after the equal sign in Eq. (8.117) are identical to the product of the separate averages of $\epsilon_0(x_\perp)$ and $\epsilon_0(y_\perp)$:

$$\begin{aligned}
D^{ik;i'k'}_{ac;a'c'}(x_\perp,x_\perp,y_\perp,y_\perp)D^{jl;j'l'}_{bd;b'd'}(x_\perp,x_\perp,y_\perp,y_\perp)\mathcal{A}^{ik;i'k'}_{jl;j'l'}\mathcal{F}^{ac;a'c'}_{bd;b'd'}& \\
= g^4(\partial^2 L(0_\perp))^4 N_c^4 C_F^2\,\bar\lambda_1^2(b_\perp)\bar\lambda_2^2(b_\perp)& \\
= \frac{1}{g^4}\alpha_s^4(4\pi\,\partial^2 L(0_\perp))^4 N_c^4 C_F^2\,\bar\lambda_1^2(b_\perp)\bar\lambda_2^2(b_\perp) = \frac{C_F^2}{g^4}\bar Q_{s1}^4\bar Q_{s2}^4 \approx \langle\epsilon_0(x_\perp)\rangle\langle\epsilon_0(y_\perp)\rangle,&
\end{aligned} \tag{8.118}$$

(where we approximated $h(x_\perp)$ and $h(y_\perp)$ with $h(b_\perp)$, as repeatedly done throughout the calculation). Therefore, the result of $\mathrm{Cov}[\epsilon](\tau=0^+;x_\perp,y_\perp)=\langle\epsilon_0(x_\perp)\epsilon_0(y_\perp)\rangle-\langle\epsilon_0(x_\perp)\rangle\langle\epsilon_0(y_\perp)\rangle$ corresponds to the remaining terms. We use the Mathematica package FeynCalc [107, 108] to explicitly perform the index contractions featured in Eq. (8.117). After doing so we arrive at the main result of this chapter:

$$\boxed{\begin{aligned}
&\mathrm{Cov}[\epsilon](\tau=0^+;x_\perp,y_\perp)\equiv\langle\epsilon_0(x_\perp)\epsilon_0(y_\perp)\rangle-\langle\epsilon_0(x_\perp)\rangle\langle\epsilon_0(y_\perp)\rangle = \\
&\quad\frac{\partial_x^i\Gamma\partial_y^i\Gamma(N_c^2-1)A(4A^2-B^2)}{16N_c^2\Gamma^5 g^4}(p_1q_2+p_2q_1) \\
&\quad+\frac{(N_c^2-1)(16A^4+B^4)}{2N_c^2\Gamma^4 g^4}p_1p_2+\frac{(\partial_x^i\Gamma\partial_y^i\Gamma)^2(N_c^2-1)A^2}{64N_c^2\Gamma^6 g^4}q_1q_2 \\
&\quad+\frac{(N_c^2-1)(4A^2+B^2)}{2N_c^2\Gamma^2 g^4}\left(\left[\bar Q_{s1}^4(Q_{s2}^2r^2-4+4e^{-\frac{Q_{s2}^2r^2}{4}})\right]+[1\leftrightarrow 2]\right) \\
&\quad+\frac{(4A^2+B^2)^2}{g^4\Gamma^4N_c^2}\left(\left[\frac{N_c^6+2N_c^4-19N_c^2+8}{(N_c^2-1)^2}-4\frac{N_c^6-3N_c^4-26N_c^2+16}{(N_c^2-1)(N_c^2-4)}e^{-\frac{Q_{s1}^2r^2}{4}}\right.\right. \\
&\quad+\frac{(N_c-1)(N_c+3)N_c^3}{(N_c+1)^2(N_c+2)^2}\left(\frac{N_c}{2}e^{-\frac{(N_c+1)r^2Q_{s2}^2}{2N_c}}+(N_c+2)-2(N_c+1)e^{-\frac{Q_{s2}^2r^2}{4}}\right)e^{-\frac{(N_c+1)r^2Q_{s1}^2}{2N_c}} \\
&\quad+\frac{(N_c+1)(N_c-3)N_c^3}{(N_c-1)^2(N_c-2)^2}\left(\frac{N_c}{2}e^{-\frac{(N_c-1)r^2Q_{s2}^2}{2N_c}}+(N_c-2)-2(N_c-1)e^{-\frac{Q_{s2}^2r^2}{4}}\right)e^{-\frac{(N_c-1)r^2Q_{s1}^2}{2N_c}} \\
&\quad\left.+\frac{r^4}{2}Q_{s1}^2Q_{s2}^2-4r^2Q_{s1}^2\left(1-e^{-\frac{Q_{s2}^2r^2}{4}}\right)+4\frac{(N_c^2-8)(N_c^2-1)(N_c^2+4)}{(N_c^2-4)^2}e^{-\frac{\left(Q_{s1}^2+Q_{s2}^2\right)r^2}{4}}\right] \\
&\quad\left.+[1\leftrightarrow 2]\right),
\end{aligned}} \tag{8.119}$$

where the dependencies have been omitted for readability. Note that the covariance of the full EMT is straightforwardly obtained from the previous expression as $\mathrm{Cov}[T^{\mu\nu}](0^+;x_\perp,y_\perp)=\mathrm{Cov}[\epsilon](0^+;x_\perp,y_\perp)\times t^{\mu\nu}t^{\sigma\rho}$.

Explicit expressions for the factors $A(r_\perp)$ and $B(r_\perp)$ are given in Appendix H and in Eqs. (8.124), (8.125) below for the specific case of the original MV model. Also, in order to make our final result more compact we have defined:

$$p_{1,2}\equiv e^{-\frac{Q_{s1,2}^2r^2}{4}}(Q_{s1,2}^2r^2+4)-4 \tag{8.120}$$

$$q_{1,2}\equiv e^{-\frac{Q_{s1,2}^2r^2}{4}}\left(Q_{s1,2}^4r^4+8Q_{s1,2}^2r^2+32\right)-32. \tag{8.121}$$

For simplicity, in the previous expressions we also defined the following momentum scale:

$$\frac{r^2 Q_s^2}{4} = g^2 \frac{N_c}{2} \Gamma(r_\perp) \bar{\lambda}(b_\perp), \tag{8.122}$$

which is related to the one introduced in Sec. 8.1 by:

$$Q_s^2(r_\perp, b_\perp) \overset{r\to 0}{=} \bar{Q}_s^2(b_\perp). \tag{8.123}$$

(This limit is explicitly computed in Appendix H). Since Eq. (8.119) is somewhat lengthy, in the next sections we discuss a few simplifying limits in the context of the original MV model.

8.2.7 N_c-expansion in the MV model

Our generalization of the classical approach introduces a few elements that had to be left undetermined throughout the calculation. For instance, the function $f(r_\perp)$ featured in the two-point correlator of Eq. (8.1) introduces some ambiguity in the computation of the double derivative of $L(r_\perp)$, which is left in terms of the unknown coefficients $A(r_\perp)$ and $B(r_\perp)$. In the particular case of the MV model, where $f(r_\perp)$ is taken as a Dirac delta, we are able to compute them as:

$$A(r_\perp)_{\text{MV}} = -\frac{1}{2} G(r_\perp) = \frac{1}{4\pi} K_0(mr) \tag{8.124}$$

$$B(r_\perp)_{\text{MV}} = \frac{1}{4\pi}, \tag{8.125}$$

where K_0 is a modified Bessel function. The mass m is an infrared scale that we introduce to regularize the divergent Green's function $G(r_\perp)$. For simplicity we choose m to be the same mass scale introduced earlier in Eq. (8.11). The leading behavior in the $m\to 0$ limit is:

$$A(r_\perp)_{\text{MV}} \approx \frac{1}{8\pi} \ln\left(\frac{4}{m^2 r^2}\right), \tag{8.126}$$

and B_{MV}, being a constant, yields a negligible correction to this logarithm. In the same limit, the leading behavior of $\Gamma(r_\perp)$ and the product of its derivatives corresponds to the following expressions:

$$\Gamma(r_\perp)_{\text{MV}} = \frac{1}{2\pi m^2} - \frac{r}{2\pi m} K_1(mr) \approx \frac{r^2}{8\pi} \ln\left(\frac{4}{m^2 r^2}\right) \tag{8.127}$$

$$\left[\partial_x^i \Gamma \partial_y^i \Gamma\right]_{\text{MV}} \approx -\frac{r^2}{16\pi^2} \ln\left(\frac{m^2 r^2}{4}\right)^2. \tag{8.128}$$

(See Appendix H for a detailed derivation of these expressions). Except for B_{MV}, all these factors exhibit logarithmic divergences of different nature. While Γ and $\partial_x^i \Gamma \partial_y^i \Gamma$ diverge only in the infrared limit $m\to 0$, A and Q_s^2 are divergent in both infrared and ultraviolet $r\to 0$ limits. Then, as the scale $\bar{Q}_s^2$ contains the factor $\partial^2 L(0_\perp) \equiv -2 \lim_{r\to 0} A(r_\perp)$, it is logarithmically divergent in the MV model by definition.

However, the only divergences that we need to deal with are the ones included in the saturation scales Q_s and $\bar{Q}_s$, as all logarithms stemming from A and Γ are cancelled in the pre-factor of Eq. (8.119). Therefore, the overall effect of taking the MV limit on the complete result of the energy density covariance only consists in replacing all r-depending coefficients (except the saturation scales) with constants. As this substitution does not yield a significant simplification to the final formula, instead of showing that result we prefer to display the first orders of its N_c-expansion. Note that in these expressions we are not adopting the strict MV limit, which would imply $h(b_\perp)=1$; instead, we are only assuming locality in the transverse plane (by taking $f(x_\perp - y_\perp)=\delta(x_\perp - y_\perp)$). The leading order of the expansion, of order N_c^0, reads:

$$
\begin{aligned}
\big[\mathrm{Cov}[\epsilon_{\text{MV}}](0^+;x_\perp,y_\perp)\big]_{N_c^0} = \Bigg[\frac{1}{g^4\,r^8}e^{-\frac{r^2}{2}\left(Q_{s1}^2+Q_{s2}^2\right)}\Bigg(16+32e^{\frac{Q_{s1}^2r^2}{2}} \\
-64e^{\frac{Q_{s1}^2r^2}{4}} - 4e^{\frac{r^2}{4}\left(2Q_{s1}^2+Q_{s2}^2\right)}\left(Q_{s2}^4r^4 - 2\bar{Q}_{s1}^4r^4 + 8\,Q_{s2}^2r^2 + 48\right) \\
+\frac{1}{8}e^{\frac{r^2}{4}\left(Q_{s1}^2+Q_{s2}^2\right)}\Big(Q_{s1}^4Q_{s2}^4r^8 + (4\,Q_{s1}^2Q_{s2}^2r^6 + 128\,r^2)\big(Q_{s1}^2+Q_{s2}^2\big) + 16\,r^4\big(Q_{s1}^2+Q_{s2}^2\big)^2 + 1024\Big) \\
+2e^{\frac{r^2}{2}\left(Q_{s1}^2+Q_{s2}^2\right)}\left(\bar{Q}_{s1}^4r^4\big(Q_{s2}^2r^2-4\big)+40\right)\Bigg)\Bigg] + [1\leftrightarrow 2]. \qquad (8.129)
\end{aligned}
$$

The next term, of order N_c^{-2}, reads:

$$
\begin{aligned}
\big[\mathrm{Cov}[\epsilon_{\text{MV}}](0^+;x_\perp,y_\perp)\big]_{N_c^{-2}} = \Bigg[\frac{1}{N_c^2g^4\,r^8}e^{-\frac{r^2}{2}\left(Q_{s1}^2+Q_{s2}^2\right)}\Bigg(2\left(Q_{s1}^2r^2+Q_{s2}^2r^2+8\right)^2 \\
+4\,Q_{s1}^2r^2(8+Q_{s1}^2r^2)e^{\frac{Q_{s2}^2r^2}{2}} - 8(8+Q_{s1}^2r^2)(4+Q_{s1}^2r^2)e^{\frac{Q_{s2}^2r^2}{4}} \\
+4\,e^{\frac{r^2}{4}\left(2Q_{s1}^2+Q_{s2}^2\right)}\Big(Q_{s2}^4r^4 - 2\bar{Q}_{s1}^4r^4 + 8Q_{s2}^2r^2 + 16Q_{s1}^2r^2\Big) \\
-\frac{1}{8}e^{\frac{r^2}{4}\left(Q_{s1}^2+Q_{s2}^2\right)}\Big(Q_{s1}^4Q_{s2}^4r^8 + (4Q_{s1}^2Q_{s2}^2r^6+128r^2)\big(Q_{s1}^2+Q_{s2}^2\big) + 16\,r^4\big(Q_{s1}^2+Q_{s2}^2\big)^2 - 1024\Big) \\
-2\,e^{\frac{r^2}{2}\left(Q_{s1}^2+Q_{s2}^2\right)}\Big(\bar{Q}_{s1}^4r^4(Q_{s2}^2r^2-4) + 32Q_{s1}^2r^2 - 4\,Q_{s1}^2Q_{s2}^2r^4\Big)\Bigg)\Bigg] + [1\leftrightarrow 2]\,. \qquad (8.130)
\end{aligned}
$$

In both these expressions we have already cancelled the previously mentioned logarithms, which leaves us only with saturation scales. Different prescriptions with a varying level of sophistication are available in the literature to treat their divergences. In order to give a general idea of the magnitude and analytical features of our solution, here we will adopt the GBW model, which in practice consists simply in neglecting all logarithmic dependencies. In this framework, on Fig. 8.6 we draw Eqs. (8.129), (8.130) as functions of the dimensionless product rQ_s for $Q_{s1}=Q_{s2}$. Note that, as we are ignoring all logarithmic factors, we also have $Q_s=\bar{Q}_s$.

The N_c^{-2} term yields a small but noticeable negative correction (see red dashed curve of Fig. 8.6). As the next terms are negligible, the first two orders of the N_c-expansion provide a neat approximation to the complete result (see right plot of Fig. 8.6). Comparing this curve with the N_c^0-order term we notice that the large-N_c limit yields a 12.5% error in the $r\to 0$ limit, which is a reasonable approximation. Most remarkably, in the $rQ_s \gg 1$ limit our result vanishes following a $1/r^2$ power-law behavior. The leading term of this limit results from a combination of terms included in the first two orders of the N_c-expansion presented above, Eq. (8.129) and Eq. (8.130):

$$
\lim_{rQ_s\gg 1}\mathrm{Cov}[\epsilon_{\text{MV}}](0^+;x_\perp,y_\perp) = \frac{2\,(N_c^2-1)\left(\bar{Q}_{s1}^4Q_{s2}^2+\bar{Q}_{s2}^4Q_{s1}^2\right)}{g^4N_c^2r^2}. \qquad (8.131)
$$

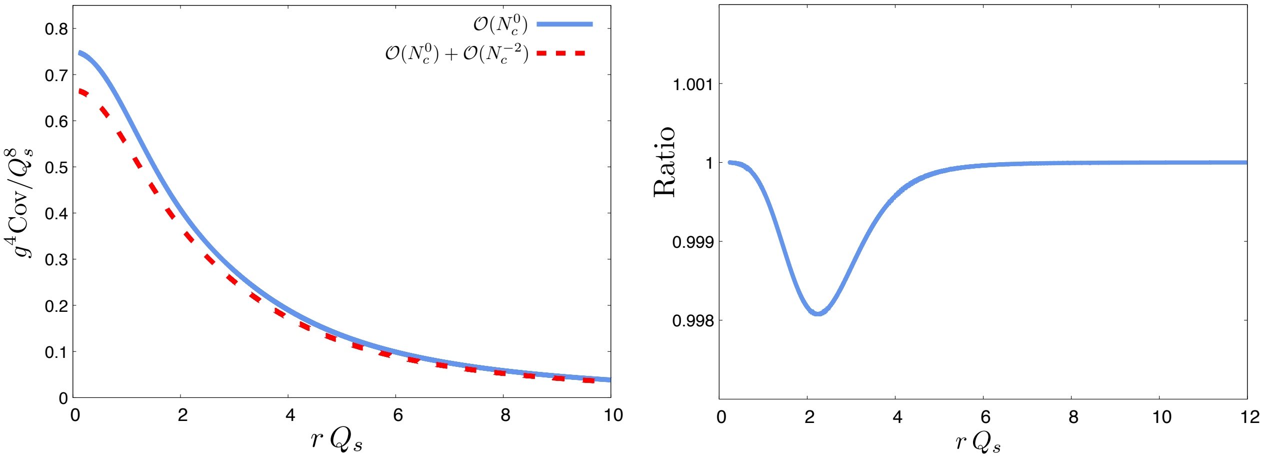

Figure 8.6: LEFT: Sum of the first two orders of the N_c-expansion of the energy density covariance against rQ_s for $Q_{s1}=Q_{s2}$ and $N_c=3$. Blue full curve: N_c^0-order term. Red dashed curve: Sum of N_c^0- and N_c^{-2}-order terms. RIGHT: Ratio between the complete result and the sum of the first two orders of the N_c-expansion.

Note that this power-law tail is a non-trivial feature of our general result that is also displayed in the particular case of the MV model. Normalizing the previous result with a single one-point correlator we obtain the following expression:

$$\lim_{rQ_s\gg 1}\left(\frac{\mathrm{Cov}[\epsilon](0^+;x_\perp,y_\perp)}{\langle\epsilon_0(x_\perp)\rangle}\right)_{\mathrm{MV}}=\frac{4}{g^2N_cr^2}\left(\frac{\bar{Q}_{s1}^2Q_{s2}^2}{\bar{Q}_{s2}^2}+\frac{\bar{Q}_{s2}^2Q_{s1}^2}{\bar{Q}_{s1}^2}\right). \tag{8.132}$$

In the opposite limit, $r\to 0$, the covariance tends to:

$$\lim_{r\to 0}\mathrm{Cov}[\epsilon_{\mathrm{MV}}](0^+;x_\perp,y_\perp)=\frac{C_F}{2N_cg^4}\left(Q_{s1}^4Q_{s2}^4+\left(\bar{Q}_{s1}^4Q_{s2}^4+\bar{Q}_{s2}^4Q_{s1}^4\right)\right)=\frac{3C_F}{2N_cg^4}\bar{Q}_{s1}^4\bar{Q}_{s2}^4, \tag{8.133}$$

and the normalized covariance:

$$\lim_{r\to 0}\left(\frac{\mathrm{Cov}[\epsilon](0^+;x_\perp,y_\perp)}{\langle\epsilon_0(x_\perp)\rangle\langle\epsilon_0(y_\perp)\rangle}\right)_{\mathrm{MV}}=\frac{Q_{s1}^4Q_{s2}^4+\left(\bar{Q}_{s1}^4Q_{s2}^4+\bar{Q}_{s2}^4Q_{s1}^4\right)}{\bar{Q}_{s1}^4\bar{Q}_{s2}^4(N_c^2-1)}=\frac{3}{N_c^2-1}. \tag{8.134}$$

In both expressions we applied Eq. (8.123) in the last step.

Summary:

- We perform an exact analytical calculation of the covariance of the EMT characterizing the Glasma state at $\tau = 0^+$.
- For this task we introduce a generalization of the MV model aimed at expanding the subsequent phenomenological applications of our results.
- Throughout this calculation we face a number of highly non-trivial challenges, like the computation of projections of the correlator of four Wilson lines in the adjoint representation and the decomposition of correlators of an arbitrary number of color sources and Wilson lines.
- The obtained expressions display a power-law tail $1/r^2$ in the limit of long correlation distances $rQ_s \gg 1$. As will be detailed in Chapter 10, this is a non-trivial feature of our exact approach that contrasts with the behavior predicted by the analytical approximations typically applied in the community.
- Our result seems to conflict with the conjectured physical picture of Glasma flux tubes, as it predicts transverse correlation lengths larger than $1/Q_s$ (or rather, logarithmic enhanced by a factor $\ln(Q_s/m)$ sensitive to the infrared).
- The first two orders of the N_c-expansion of our result (N_c^0 and N_c^{-2}) yield a good approximation of the exact expression.

Chapter 9

Topological charge fluctuations of the Glasma

In this chapter we perform an analytical first-principles calculation of the one- and two-point correlators of the divergence of the Chern-Simons current at proper time $\tau = 0^+$, which characterize the early generation of axial charge density in the plane transverse to the collision axis due to event-by-event fluctuations. As discussed in Chapter 5, this object plays a crucial role in the description of anomalous transport phenomena such as the Chiral Magnetic Effect.

9.1 One-point correlator of the divergence of the Chern-Simons current

Before evaluating the two-point function, in this section we will show that the expectation value of the divergence of the Chern-Simons current over the classical background fields is 0, indicating that there is no overall CP violation in the process. The correlator of Eq. (7.15) factorizes like:

$$\langle \dot{\nu}_0(x_\perp) \rangle = \frac{g^2}{2} \delta^{ij} \epsilon^{kl} f^{abn} f^{cdn} \langle \alpha_1^{i,a}(x_\perp) \alpha_1^{k,c}(x_\perp) \rangle \langle \alpha_2^{j,b}(x_\perp) \alpha_2^{l,d}(x_\perp) \rangle. \tag{9.1}$$

As in the case of the one-point function of the EMT, we have that the building block of $\langle \dot{\nu}_0 \rangle$ is the correlator of two gauge fields evaluated in the same transverse position, $\langle \alpha^{i,a}(x_\perp) \alpha^{k,c}(x_\perp) \rangle$. Substituting Eq. (8.16), we get:

$$\boxed{\langle \dot{\nu}_0(x_\perp) \rangle = \frac{g^2}{8} (\partial^2 L(0_\perp))^2 \bar{\lambda}_1(x_\perp) \bar{\lambda}_2(x_\perp) \delta^{ij} \epsilon^{kl} f^{abn} f^{cdn} \delta^{ac} \delta^{ik} \delta^{bd} \delta^{jl} = 0,} \tag{9.2}$$

which vanishes due to the antisymmetric property of the Levi-Civita tensor. As mentioned earlier, this null average accounts for the Glasma state being globally CP-symmetric. However, local axial charge fluctuations are expected to happen on an event-by-event basis. Our object of interest is therefore the two-point correlator of $\dot{\nu}_0$, whose computation we outline in the following section.

9.2 Two-point correlator of the divergence of the Chern-Simons current

In this section we describe the calculation of $\langle \dot{\nu}_0(x_\perp) \dot{\nu}_0(y_\perp) \rangle$. As we did in the previous section, we start by expanding $\dot{\nu}_0$ in terms of the gluon fields:

$$\dot{\nu}_0(x_\perp) \dot{\nu}_0(y_\perp) = \frac{g^4}{4} \delta^{ij} \epsilon^{kl} \delta^{i'j'} \epsilon^{k'l'} f^{abn} f^{cdn} f^{a'b'm} f^{c'd'm} \alpha_{1x}^{i,a} \alpha_{2x}^{j,b} \alpha_{1x}^{k,c} \alpha_{2x}^{l,d} \alpha_{1y}^{i',a'} \alpha_{2y}^{j',b'} \alpha_{1y}^{k',c'} \alpha_{2y}^{l',d'}, \tag{9.3}$$

then, the correlator reads:

$$\langle \dot{\nu}_0(x_\perp) \dot{\nu}_0(y_\perp) \rangle = \frac{g^4}{4} \epsilon^{kl} \epsilon^{k'l'} f^{abn} f^{cdn} f^{a'b'm} f^{c'd'm} \langle \alpha_x^{i,a} \alpha_x^{k,c} \alpha_y^{i',a'} \alpha_y^{k',c'} \rangle_1 \langle \alpha_x^{i,b} \alpha_x^{l,d} \alpha_y^{i',b'} \alpha_y^{l',d'} \rangle_2. \tag{9.4}$$

Color algebra-wise, this expression presents the same level of complexity than the previously computed two-point correlator of the energy density. However, it features a much simpler transverse index structure, which we can rewrite as:

$$\epsilon^{kl}\epsilon^{k'l'} = \delta^{kk'}\delta^{ll'} - \delta^{kl'}\delta^{lk'}, \tag{9.5}$$

yielding:

$$\begin{aligned}\langle \dot{\nu}_0(x_\perp)\dot{\nu}_0(y_\perp)\rangle = \frac{g^4}{4} f^{abn} f^{cdn} f^{a'b'm} f^{c'd'm} \Big(& \langle \alpha_x^{i,a}\alpha_x^{k,c}\alpha_y^{i',a'}\alpha_y^{k,c'}\rangle_1 \langle \alpha_x^{i,b}\alpha_x^{l,d}\alpha_y^{i',b'}\alpha_y^{l,d'}\rangle_2 \\ & - \langle \alpha_x^{i,a}\alpha_x^{k,c}\alpha_y^{i',a'}\alpha_y^{l,c'}\rangle_1 \langle \alpha_x^{i,b}\alpha_x^{l,d}\alpha_y^{i',b'}\alpha_y^{k,d'}\rangle_2 \Big).\end{aligned} \tag{9.6}$$

The building block for this computation is the correlator of four gluon fields in two different transverse positions, which was computed in the previous chapter. Substituting said result in Eq. (9.6) and performing the ensuing index contractions (for which, again, we use the Mathematica package FeynCalc), we obtain the main result of this chapter:

$$\boxed{\begin{aligned} \langle \dot{\nu}_0(x_\perp)\dot{\nu}_0(y_\perp)\rangle = {} & \frac{16A^4 - B^4}{g^4\Gamma^4 N_c^2}\Bigg(\Bigg[\frac{N_c^6 + 2N_c^4 - 19N_c^2 + 8}{2(N_c^2-1)^2} - 2\frac{N_c^6 - 3N_c^4 - 26N_c^2 + 16}{N_c^4 - 5N_c^2 + 4} e^{-\frac{Q_{s1}^2 r^2}{4}} \\ & + (N_c^2-1)\left(1 - e^{-\frac{Q_{s1}^2 r^2}{4}}\left(1 + \frac{Q_{s1}^2 r^2}{4}\right)\right)\left(1 - e^{-\frac{Q_{s2}^2 r^2}{4}}\left(1 + \frac{Q_{s2}^2 r^2}{4}\right)\right) \\ & + \frac{r^4}{4} Q_{s1}^2 Q_{s2}^2 - 2r^2 Q_{s1}^2\left(1 - e^{-\frac{Q_{s2}^2 r^2}{4}}\right) + 2\frac{(N_c^2-8)(N_c^2-1)(N_c^2+4)}{(N_c^2-4)^2} e^{-\frac{(Q_{s1}^2+Q_{s2}^2)r^2}{4}} \\ & + \frac{(N_c-1)(N_c+3)N^3}{2(N_c+1)^2(N_c+2)^2}\left(\frac{N_c}{2} e^{-\frac{(N_c+1)r^2 Q_{s2}^2}{2N_c}} + (N_c+2) - 2(N_c+1)e^{-\frac{Q_{s2}^2 r^2}{4}}\right) e^{-\frac{(N_c+1)r^2 Q_{s1}^2}{2N_c}} \\ & + \frac{(N_c+1)(N_c-3)N^3}{2(N_c-1)^2(N_c-2)^2}\left(\frac{N_c}{2} e^{-\frac{(N_c-1)r^2 Q_{s2}^2}{2N_c}} + (N_c-2) - 2(N_c-1)e^{-\frac{Q_{s2}^2 r^2}{4}}\right) e^{-\frac{(N_c-1)r^2 Q_{s1}^2}{2N_c}}\Bigg] \\ & + [1 \leftrightarrow 2]\Bigg), \end{aligned}} \tag{9.7}$$

where the dependencies have been omitted for readability.

Let us now compute some simplifying limits on Eq. (9.7) in order to obtain more compact formulas. In the limit of small transverse separations $r \to 0$ the two-point function tends to:

$$\lim_{r\to 0} \langle \dot{\nu}_0(x_\perp)\dot{\nu}_0(y_\perp)\rangle_{\text{MV}} = \frac{3(N_c^2-1)}{32 g^4 N_c^2} Q_{s1}^4 Q_{s2}^4. \tag{9.8}$$

The ratio with the product of the energy density averages at each transverse position reads:

$$\lim_{r\to 0}\left(\frac{\langle \dot{\nu}_0(x_\perp)\dot{\nu}_0(y_\perp)\rangle}{\langle \epsilon_0(x_\perp)\rangle\langle \epsilon_0(y_\perp)\rangle}\right)_{\text{MV}} = \frac{3}{8(N_c^2-1)}, \tag{9.9}$$

which displays the characteristic $1/(N_c^2-1)$ suppression factor of non-trivial color correlations. In the opposite limit, $rQ_s \gg 1$, we obtain:

$$\lim_{rQ_s\gg 1} \langle \dot{\nu}_0(x_\perp)\dot{\nu}_0(y_\perp)\rangle_{\text{MV}} = \frac{8\,Q_{s1}^2 Q_{s2}^2}{g^4 N^2 r^4}. \tag{9.10}$$

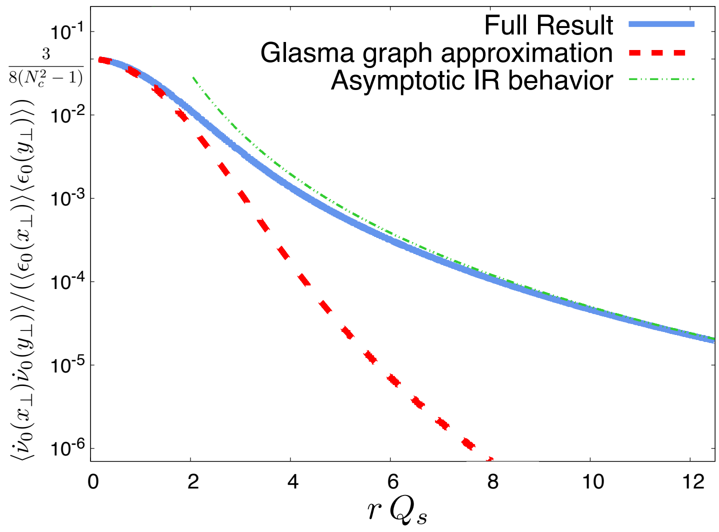

Figure 9.1: Two-point correlator of the divergence of the Chern-Simons current normalized to the product of energy density averages in the exact analytical approach (blue full curve) and the Glasma Graph approximation (red dashed curve). As a visual aid we also indicate the asymptotic behavior in the infrared limit, which is $32/[(N_c^2-1)^2r^4Q_s^4]$ (green dot-dashed curve).

For the sake of comparison with previous results obtained in the Glasma Graph approximation (see Fig. 9.1) we also compute the following limit:

$$\lim_{rQ_s\gg 1}\left(\frac{\langle\dot{\nu}_0(x_\perp)\dot{\nu}_0(y_\perp)\rangle}{\langle\epsilon_0(x_\perp)\rangle\langle\epsilon_0(y_\perp)\rangle}\right)_{\rm MV}=\frac{32\,Q_{s1}^2Q_{s2}^2}{(N_c^2-1)^2r^4\bar{Q}_{s1}^4\bar{Q}_{s2}^4}. \tag{9.11}$$

The limits computed above allow for a straightforward comparison of our approach to other analytical frameworks available in the literature, which is the main subject of the next chapter.

9.2.1 N_c-expansion

In order to complete the analysis of our final expression Eq. (9.7), in this subsection we display its expansion in orders of N_c. The leading order term, of order N_c^0, reads:

$$\begin{aligned}\left[\langle\dot{\nu}_0(x_\perp)\dot{\nu}_0(y_\perp)\rangle\right]_{N_c^0}=&\Bigg[\frac{1}{g^4\,r^8}e^{-\frac{r^2}{2}(Q_{s1}^2+Q_{s2}^2)}\Bigg(8+16e^{\frac{Q_{s1}^2r^2}{2}}-32e^{\frac{Q_{s1}^2r^2}{4}}+24e^{\frac{r^2}{2}(Q_{s1}^2+Q_{s2}^2)}\\&-8e^{\frac{r^2}{4}(2Q_{s1}^2+Q_{s2}^2)}\left(8+Q_{s2}^2r^2\right)+e^{\frac{r^2}{4}(Q_{s1}^2+Q_{s2}^2)}\Big(Q_{s1}^2Q_{s2}^2r^4+4r^2(Q_{s1}^2+Q_{s2}^2)+48\Big)\Bigg)\Bigg]+[1\leftrightarrow 2]\,,\end{aligned} \tag{9.12}$$

and the next term, of order N_c^{-2}, reads:

$$\begin{aligned}\left[\langle\dot{\nu}_0(x_\perp)\dot{\nu}_0(y_\perp)\rangle\right]_{N_c^{-2}}=&\Bigg[\frac{1}{N_c^2g^4\,r^8}e^{-\frac{r^2}{2}(Q_{s1}^2+Q_{s2}^2)}\Bigg(2\,Q_{s1}^2r^2(8+Q_{s1}^2r^2)e^{\frac{Q_{s2}^2r^2}{2}}\\&+8\,e^{\frac{r^2}{4}(2Q_{s1}^2+Q_{s2}^2)}\left(4Q_{s1}^2r^2+Q_{s2}^2r^2-4\right)+4e^{\frac{r^2}{2}(Q_{s1}^2+Q_{s2}^2)}\Big(Q_{s1}^2Q_{s2}^2r^4-4r^2(Q_{s1}^2+Q_{s2}^2)+4\Big)\\&-4(Q_{s1}^4r^4+12Q_{s1}^2r^2+32)e^{\frac{Q_{s2}^2r^2}{4}}-e^{\frac{r^2}{4}(Q_{s1}^2+Q_{s2}^2)}\Big(Q_{s1}^2Q_{s2}^2r^4+4r^2(Q_{s1}^2+Q_{s2}^2)-80\Big)\\&+\left(Q_{s1}^2r^2+Q_{s2}^2r^2+8\right)^2\Bigg)\Bigg]+[1\leftrightarrow 2]\,.\end{aligned} \tag{9.13}$$

As it is also the case for the covariance of the energy density ϵ_0, the first two orders of the N_c-expansion of Eq. (9.7) yield a neat approximation of the complete result (see Fig. 9.2), but not a significant improvement regarding the practicality of the formulas.

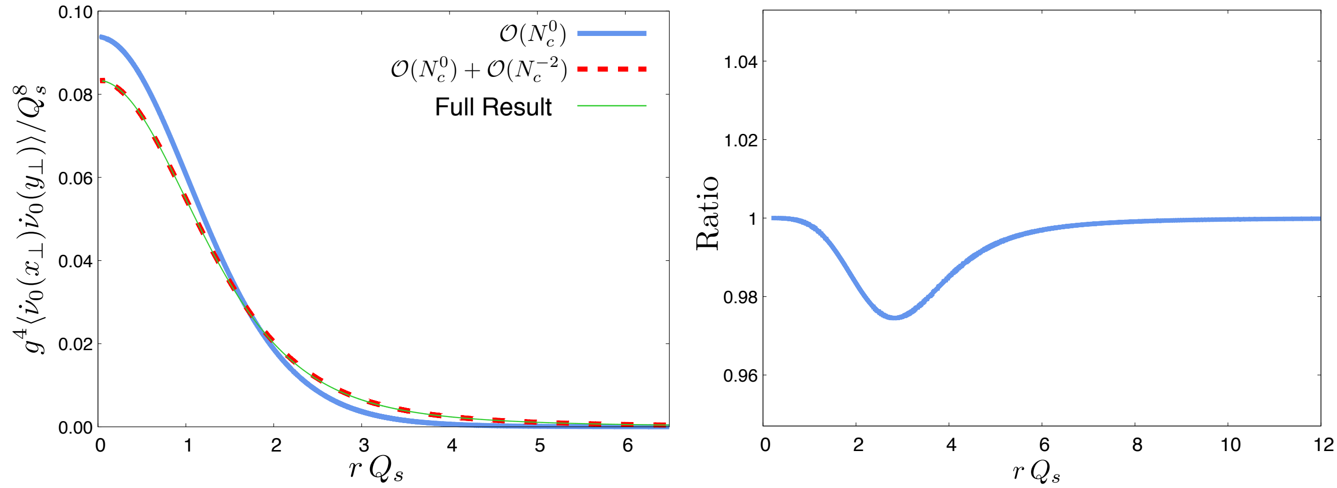

Figure 9.2: LEFT: Comparison of the first two orders of the N_c-expansion of the two-point function of the divergence of the Chern-Simons current against $r\,Q_s$ in the GBW model for $Q_{s1}=Q_{s2}$ and $N_c\!=\!3$. Blue full curve: N_c^0-order term. Red dashed curve: Sum of N_c^0- and N_c^{-2}-order terms. Thin green curve: full result. RIGHT: Ratio between the full result and the sum of the first two orders of the N_c-expansion.

Summary:

- We perform an exact analytical calculation of the one- and two-point correlators of the divergence of the Chern-Simons current characterizing the Glasma state at $\tau\!=\!0^+$.
- For this task we use the same generalized framework applied in Chapter 8.
- Our final expression displays a power-law tail $1/r^4$ in the limit of long correlation distances $rQ_s \gg 1$. As will be detailed in Chapter 10, this result is also in conflict with the one obtained by the standard analytical approach, and thus it supports the conclusions reached in the calculations from Chapter 8.
- As in the case of the EMT, the first two orders of the N_c-expansion of our result (N_c^0 and N_c^{-2}) yield a good approximation of the exact expression.

Chapter 10

Comparison with previous results

An alternative approach to the calculations presented in the previous chapters is proposed in [86] under the so-called Glasma Graph approximation. In its original formulation, this method plays a foundational role in the practical implementation of the MV model.

By proposing a Gaussian ansatz (Eq. (3.6)), the MV model implicitly assumes that the complex color charge correlations underlying the interactions between colliding nuclei can be uniquely determined by the two-point function Eq. (3.8). The Glasma Graph approximation builds upon this assumption and extends it by considering that said interactions are restricted to the exchange of only two gluons per color source. This approach –although expected to be valid only in a gluon-dilute regime– has been adopted as the standard practice in the field, being at the base of a wealth phenomenological studies of HICs [109–117]. Moreover, the Glasma Graph approximation provides some justification to the most widely accepted physical picture of the early stages of HICs, i.e. the Glasma flux tube[1].

The two-gluon exchange ansatz outlined above translates into a factorization of double parton distributions into all possible products of single parton distributions, which yields great simplification in the context of dihadron correlator calculations [86]. In the same spirit, in the aforementioned work it is assumed that the four-point correlation functions of the gluon fields factorize into products of two-point correlation functions such that:

$$\begin{aligned}\langle\alpha^{i,a}(x_\perp)\alpha^{k,c}(x_\perp)\alpha^{i',a'}(y_\perp)\alpha^{k',c'}(y_\perp)\rangle_{\text{GG}} = &\langle\alpha^{i,a}(x_\perp)\alpha^{k,c}(x_\perp)\rangle\langle\alpha^{i',a'}(y_\perp)\alpha^{k',c'}(y_\perp)\rangle\\ &+\langle\alpha^{i,a}(x_\perp)\alpha^{i',a'}(y_\perp)\rangle\langle\alpha^{k,c}(x_\perp)\alpha^{k',c'}(y_\perp)\rangle\\ &+\langle\alpha^{i,a}(x_\perp)\alpha^{k',c'}(y_\perp)\rangle\langle\alpha^{k,c}(x_\perp)\alpha^{i',a'}(y_\perp)\rangle.\end{aligned} \tag{10.1}$$

This Wick theorem-like decomposition is equivalent to assuming that the gluon fields conserve the Gaussian character of the color source distributions[2]. This is not generally correct, as the dynamical generation of the former by the latter (encoded in the Yang-Mills equations) is non-linear. However, as we shall see, this assumption yields a good approximation of the exact result in the limit of small transverse separations $r \to 0$. In this limit an effective linearization of the fields' dynamics takes place, as the connected functions derived in Chapter 8 vanish and the disconnected contributions become equivalent to the two-point function of gluon fields. This results in a mapping of the Gaussian statistics followed by the color source distributions onto the gluon fields.

Let us first focus on the EMT correlators computed in Chapter 8. We compare the normalized covariance from our result (in the strict MV model and with $Q_{s1} = Q_{s2}$) with the one computed according to the decomposition defined in Eq. (10.1). As can be seen in Fig. 10.1, although both

---

[1] The contributions considered in the Glasma Graph approach are expected –on purely parametric grounds– to be highly suppressed for $p_\perp \gg Q_s$, which supports the short correlation range conjectured by the flux tube picture.

[2] This assumption, although giving rise to a formally similar decomposition of correlators, is of a fundamentally different nature than the original Glasma Graph approximation. In this regard, note that the interactions comprised by the two-point correlators from Eq. (10.1) include gluon exchanges to all orders. Ignoring conceptual differences, we will use the name 'Glasma Graph approximation' to refer to said decomposition.

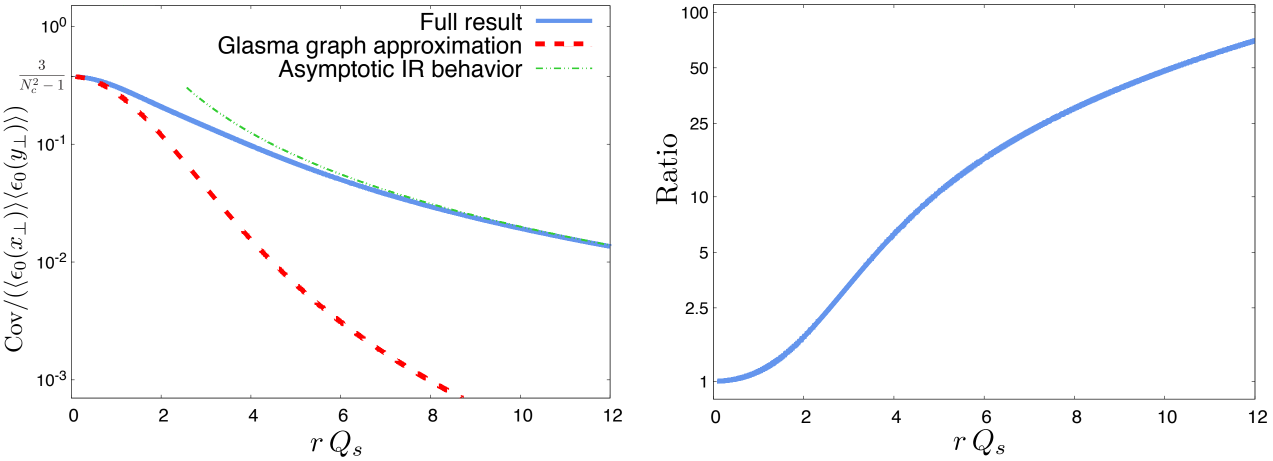

Figure 10.1: LEFT: Comparison of the normalized covariance of energy density ϵ_0 against $r\,Q_s$ for $Q_{s1} = Q_{s2}$, $N_c = 3$ in the exact analytical approach (blue full curve) and the Glasma Graph approximation (red dashed curve). As a visual aid we also indicate the asymptotic behavior in the IR limit, which is $16/[(N_c^2-1)r^2Q_s^2]$ (green dot-dashed curve). RIGHT: Ratio of exact analytical result to the Glasma Graph result.

results agree exactly in the UV limit $r \to 0$, in the rest of the spectrum our computation yields a harder curve. Another remarkable difference is that, while our result for the normalized covariance shows a slowly vanishing behavior in the infrared limit, the Glasma Graph approximation yields a much steeper tail:

$$\lim_{rQ_s\gg1}\left(\frac{\mathrm{Cov}[\epsilon](0^+;x_\perp,y_\perp)}{\langle\epsilon_0(x_\perp)\rangle\langle\epsilon_0(y_\perp)\rangle}\right)_{\mathrm{GG}} = \frac{16(\bar{Q}_{s1}^4+\bar{Q}_{s2}^4)}{r^4(N_c^2-1)\bar{Q}_{s1}^4\bar{Q}_{s2}^4}. \tag{10.2}$$

The $\propto 1/r^4$ decreasing behavior displayed by this expression is in clear contrast with the $\propto 1/r^2$ curve approached by our result in the same limit. A similar thing happens in the case of the divergence of the Chern-Simons current. In Fig. 9.1 and Fig. 10.2 we compare our result with the one computed according to the Glasma Graph approximation. As can be seen in Fig. 9.1, although both results agree exactly in the small transverse separation limit $r \to 0$, in the rest of the spectrum (approximately for $r > 1/Q_s$) our computation yields a significantly harder curve, just as in the case of the EMT correlators. However, in the case of $\dot{\nu}$ this difference is larger (as can be seen in the right panel of Fig. 10.2). While our result shows a $\propto 1/r^4$ decreasing behavior (see Eq. (9.11)), the Glasma Graph approximation yields a much steeper $\propto 1/r^8$ tail:

$$\lim_{rQ_s\gg1}\left(\frac{\langle\dot{\nu}_0(x_\perp)\dot{\nu}_0(y_\perp)\rangle}{\langle\epsilon_0(x_\perp)\rangle\langle\epsilon_0(y_\perp)\rangle}\right)_{\mathrm{GG}} = \frac{96}{(N_c^2-1)r^8\bar{Q}_{s1}^4\bar{Q}_{s2}^4}. \tag{10.3}$$

Such discrepancies potentially imply much different numerical results and physical interpretations for any observable built from any of these quantities. Moreover, they provide further evidence on the inadequacy of the Glasma Graph approximation for correlation distances larger than $1/Q_s$, an outcome that agrees with the expected validity range of this approach. Although this is indeed a remarkable finding, our results conflict with the Glasma Graph approximation in a deeper level, in turn challenging the previously mentioned Glasma flux tube picture.

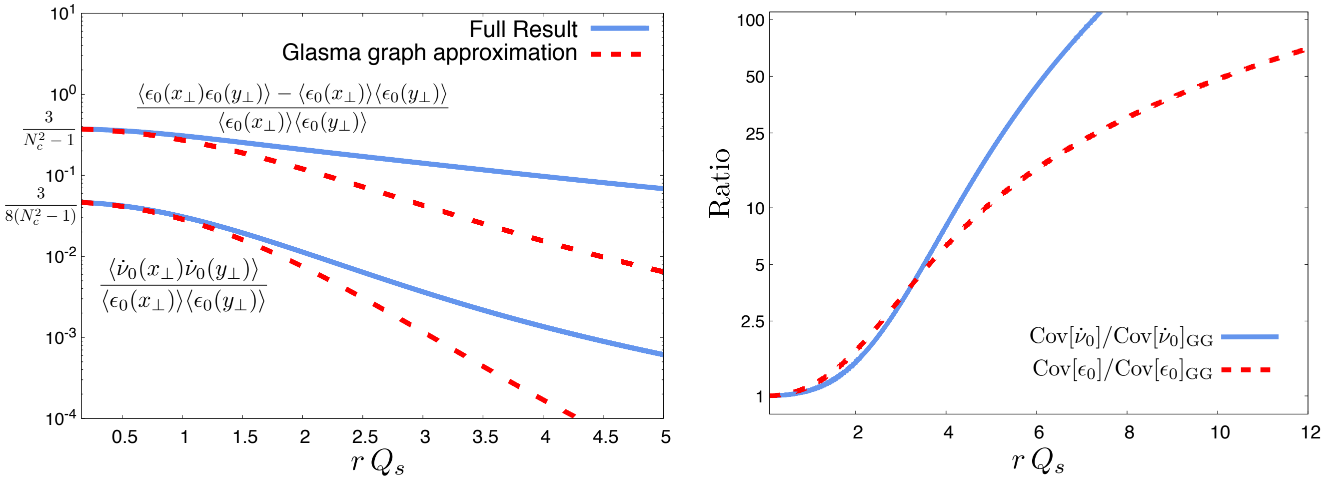

Figure 10.2: LEFT: Comparison of the covariance of the divergence of the Chern-Simons current (lower pair of curves) and the energy density (upper pair of curves) against rQ_s for $Q_{s1} = Q_{s2}$ in the exact analytical approach (blue full curves) and the Glasma Graph approximation (red dashed curves). RIGHT: Ratio of exact analytical result to the Glasma Graph result for the covariance of the divergence of the Chern-Simons current (blue full curve) and the energy density (red dashed curve).

In order to see this, let us return to our result for the EMT correlators. The 2-dimensional transverse integral of Eq. (8.131) is dominated by the upper bound (the infrared cut-off $r \sim 1/m$) rather than the lower bound $r \sim 1/Q_s$, which is what happens under the Glasma Graph approximation [118] due to its $1/r^4$ fall-off. This indicates that the range of the transverse color screening of the correlations, which determines the size of the color domains in the interaction region, is actually bigger than $1/Q_s$, as it features a logarithmic enhancement $\ln(Q_s/m)$ sensitive to the infrared. Similar observations were made in [119] in the context of two-particle correlations: a sensitivity of the color domain size to the infrared was observed numerically, with it getting larger as the infrared cut-off was decreased. In the case of EMT correlations, our qualitative discussion also remains to be quantified with numerical calculations.

The previous feature is not, however, reproduced by the correlators corresponding to the divergence of the Chern-Simons current. The two-dimensional transverse integral of Eq. (9.11) is dominated by the lower bound $r \sim 1/Q_s$, as opposed to the case of the corresponding energy density correlator. This result thus seems somewhat more consistent with the conjectured Glasma flux tube picture [96]. Nevertheless, Eq. (9.11) still displays a remarkably slow fall-off that contrasts with the behavior one could naively expect from correlations between Gaussianly-distributed color charges.

Summary:

- We compare the results from chapters 8 and 9 to previous calculations performed under the widely applied Glasma Graph approximation.
- Although said calculations also exhibit a power-law behavior in the $rQ_s \gg 1$ limit, they yield much more rapidly decaying curves than those obtained in the exact approach ($\propto 1/r^4$ and $\propto 1/r^8$ for the EMT and the divergence of the Chern-Simons current, respectively).
- Remarkably, the gap between the results for the divergence of the Chern-Simons current is even larger than the one showed by those of the energy density.
- The relatively long-range correlations obtained in this part could potentially have a remarkable impact in both physical interpretations and numerical results for any phenomenological work based on these quantities –specially those that require their integration in the transverse plane.
- Our results for the EMT correlators could challenge the conjectured physical picture of Glasma flux tubes, as they lead to an infrared-sensitive logarithmic enhancement of the correlation length.

Part V

Color Glass Condensate phenomenology

What good is it if you don't use it?
It ain't no good to nobody!

— Screamin' Jay Hawkins in "What good is it?"

The calculations carried out in Part IV provide the foundation for a number of phenomenological studies of HICs. For example, the results of Chapter 8 could be directly applied in studies of QGP properties via multi-parametric fits based on Bayesian statistics [120]. Also, upon the proper spectral decomposition, they may allow to perform mode-by-mode studies of the hydrodynamical propagation of initial fluctuations (as proposed in [121, 122]). As for the expressions derived in Chapter 9, they can be directly applied to the Monte Carlo modeling of initial axial charge density [86], a fundamental input for those hydrodynamical simulations that aim at describing anomalous transport phenomena [87–89]. In this final part of the thesis we focus on a specific application explained in Chapter 11. In this work we apply the CGC framework to the description of hadron production in high energy collisions at ultra-forward rapidities, achieving a good description of a variety of observables sensitive to saturation effects, measured at both RHIC and LHC.

Chapter 11

Ultra-forward particle production in CGC

In this chapter we present an analysis of data on single inclusive pion production in high energy proton-proton and proton-nucleus collisions at ultra-forward rapidities ($8.8 \leq y \leq 10.8$), as measured by the LHCf collaboration. We also analyze forward RHIC data for calibration purposes. Our study relies on the use of a Monte Carlo event generator that combines a perturbative description of partonic scatterings based on the hybrid formalism of CGC with an implementation of hadronization in the framework of the Lund string fragmentation model. This strategy allows us to reach values of the momenta of the produced particles as low as detected experimentally, $p_\perp \sim 0.1$ GeV. Before getting into the details of our analysis, let us start with a brief overview of the CGC description of hadron production in high energy collisions.

11.1 CGC description of high energy multiparticle production

Hadron production in high energy collisions is still an open problem in QCD. To this day, there is no framework able to provide a unified, consistent description of hadron spectra in all accessible kinematic ranges. Even at partonic level, we need to rely on different formalisms adapted to the physical conditions of each region of phase space. For example, the standard procedure to analyze the large-$p_\perp$ sector of hadron spectra relies on Monte Carlo implementations of the collinear factorization ansatz Eq. (2.9). As previously discussed (Section 2.3), this formalism breaks down as we move towards the small-x limit, where one can no longer assume the colliding hadrons to be dilute objects. The appropriate framework to be applied in this regime is the CGC effective theory.

Two fundamental approaches to particle production have been proposed within CGC. The calculations reproduced in Part III provide the starting point to one of them, namely the numerical resolution of the classical Yang-Mills equations on the lattice. The other strategy is based on the so-called $k_\perp$-factorization ansatz:

$$\frac{dN_g}{dy d^2p_\perp d^2b_\perp} = \frac{4\pi N_c}{N_c^2-1}\frac{\alpha_s}{p_\perp^2}\int d^2k_\perp \phi_1(k_\perp^2, y, b_\perp)\phi_2(k_\perp^2 - p_\perp^2, y, b_\perp), \tag{11.1}$$

by which the gluon spectra is computed through the integration of the uGDs of the colliding hadrons $\phi_{1,2}$. The motivation behind this expression lies in the experimental observation that most particles generated in HICs carry a relatively low transverse momentum. In the case of the Au-Au collisions performed at $\sqrt{s_{\rm NN}} = 200$ GeV at RHIC, most detected particles carry a transverse momentum approximately below 1 GeV. The fact that this value is quite close to the estimated saturation momentum for such collisions ($Q_s^2 \sim 1 \div 2$ GeV^2) suggests an underlying particle production mechanism largely dominated by saturation effects. Hence, the $k_\perp$-factorization scheme proposes a description of the multiplicity distributions exclusively based on uGDs with a scale dependence given by the evolution equations of CGC.

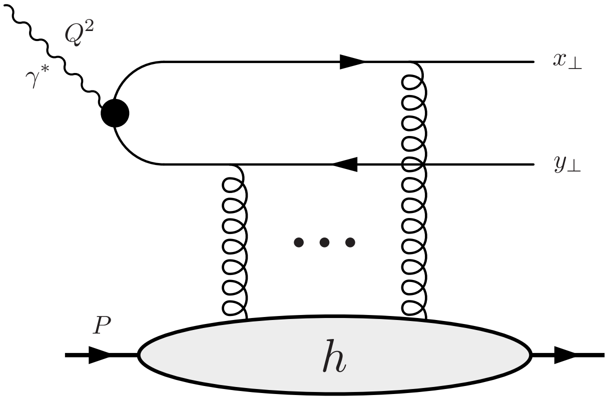

Figure 11.1: Sketch of a DIS process as interpreted in dipole models.

As explained in Section 2.2, the practical description of uGDs is not unique; it is established in a model-dependent way connected to the specific processes in which they are experimentally measured. Arguably the most widely applied prescriptions are those based on the dipole model [123–125], which stems from a relatively simple formulation of DIS experiments. Within this model, DIS is interpreted as a two step process: first, the fast moving virtual photon γ^* fluctuates into a quark-antiquark pair; and then, this dipole scatters off the hadronic target through multiple gluon exchanges[1] (see Fig. 11.1). The uGDs are related to the dipole scattering amplitude in coordinate space via a Fourier transform:

$$\phi_{(F/A)}(x, k_\perp) = \int d^2r_\perp\, e^{-ik_\perp\cdot r_\perp}\left[1 - \mathcal{N}_{(F/A)}(x, r)\right], \tag{11.2}$$

where $\phi_{(F/A)}$ refers to the uGD in either the fundamental or adjoint representation[2]. The dipole scattering amplitude $\mathcal{N}_{(F/A)}$ encodes all the information about the strong interaction of the scattering process (and thus contains all x-dependence). There exist several prescriptions for its modeling,

---

[1] Which in the MV model are described in terms of Wilson lines, as seen in Chapter 6.

[2] The uGD in the adjoint representation is built from the dipole scattering amplitudes corresponding to a gluon dipole. In the large N_c limit these are obtained as $\mathcal{N}_A = 2\mathcal{N}_F - \mathcal{N}_F^2$ [126]. However, in [16] it was shown that this relation is only valid in the local Gaussian approximation adopted in the MV model.

which in turn define different approaches within CGC to experimental data analysis (see [51] for a review of some of the available models).

The $k_\perp$-factorization formula Eq. (11.1) is appropriate for the parton-level description of collisions between two gluon-dense objects. However, the analysis of particle production at very large rapidities –i.e. the ultra-forward region– is sensitive to the wave functions of the colliding hadrons in the extreme limits of phase space. In this kinematic regime, only one of these hadrons is perceived as a gluon-dense system, whereas the other appears as a dilute ensemble of fast-moving quarks (as illustrated in Fig. 11.2). This can be inferred from the relation between the $(p_\perp, y)$ of a particle produced in a hadronic collision at center-of-mass energy $\sqrt{s}$ and the x fraction carried by the participants of the partonic subprocess:

$$x_p \approx \frac{p_\perp}{\sqrt{s}} e^{y} \quad x_t \approx \frac{p_\perp}{\sqrt{s}} e^{-y}, \tag{11.3}$$

where $x_{p,t}$ labels the parent hadrons as *projectile* or *target*. From these expressions we can infer that by analyzing large rapidities we are probing the projectile at large-x values and the target at small-x values. Specifically, in the kinematic range covered by the LHCf experiment one has $\sqrt{s} = 7$ TeV, $p_t \lesssim 1$ GeV and $8.8 \leq y \leq 10.8$, yielding the following Bjorken-x values for projectile and target: $x_p \sim 10^{-1} \sim 1$ and $x_t \sim 10^{-8} \sim 10^{-9}$, the latter being the smallest x values ever accessed experimentally. As discussed in the introductory chapters of this report, a highly asymmetric collision in terms of x is also strongly asymmetric in the density of the colliding objects.

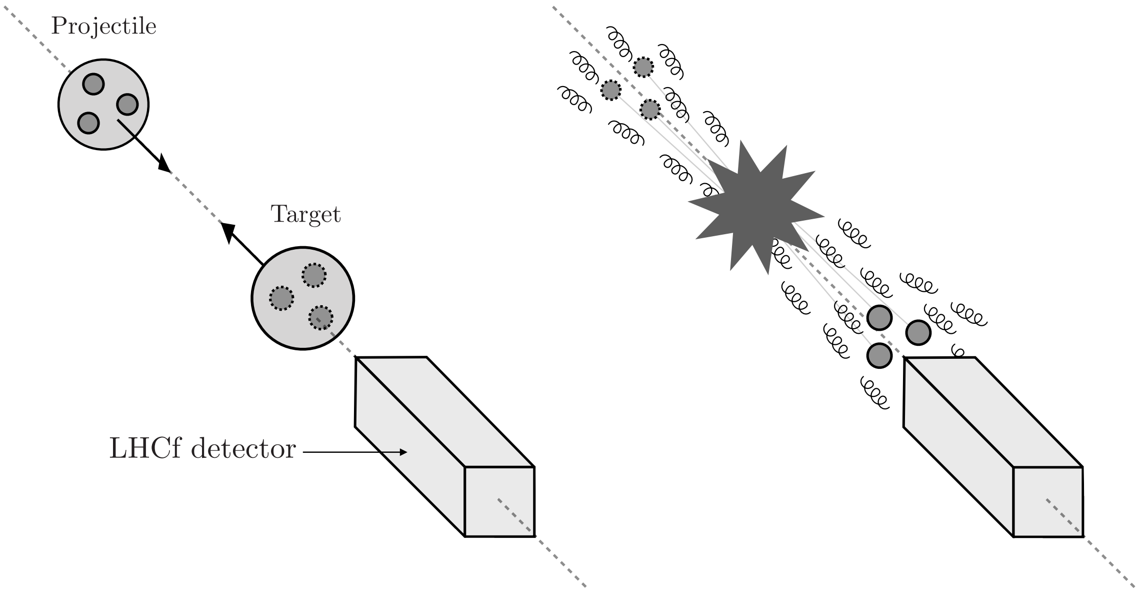

Figure 11.2: Rough sketch of a hadron-hadron collision as perceived in the LHCf experiment. After the collision, the particles that fly very close to the beam axis (ultra-forward rapidity region) correspond to the large-x degrees of freedom of the projectile (its valence partons) and the small-x gluons from the target.

At large (but not too large) x values an appropriate characterization of hadrons is given by the partonic picture discussed in chapters 1 and 2, whereas in the very small-x limit they can be properly described in the CGC framework. These 'dilute-dense processes' can be interpreted at partonic level as mediated by a highly energetic valence quark from the projectile scattering off a 'soft' parton (typically a gluon) from the target. Such a process features a clear separation of scales that allows us to describe each side of the interaction independently. This is the main principle of the *hybrid formalism*, first proposed in [127].

11.2 The hybrid formalism

In the hybrid factorization scheme (depicted in Fig. 11.4) the large-x degrees of freedom (from the projectile) are represented with the usual PDFs of collinear factorization, while the small-x gluons (from the target) are described in terms of uGDs with a scale dependence given by the evolution equations of CGC. In the hybrid formalism the cross section for quark or gluon production in the scattering off a gluon-dense target reads:

$$\frac{d\sigma^{h_1 h_2 \to (q/g) X}}{dy\, d^2 k_\perp} = \frac{K}{(2\pi)^2} \frac{\sigma_0}{2}\, x_1 f_{(q/g)/h_1}(x_1, \mu_{\mathrm{F}}^2) \phi_{(F/A)/h_2}(x_2, k_\perp)\,, \tag{11.4}$$

where $f_{(q/g),h_1}(x_1, \mu^2)$ is the PDF of quarks or gluons in the projectile h_1 evaluated at the scale μ_{F}, while $\phi_{(F/A)/h_2}(x_2, k_t)$ refers to the uGD of the target in either the fundamental or adjoint representation. Eq. (11.4) is known as the DHJ formula (for Dumitru, Hayashigaki, and Jalilian-Marian). This formalism thus combines the previously discussed frameworks of collinear and $k_\perp$-factorization.

In our analysis we use a Monte Carlo event generator set up to simulate partonic hard scatterings ($qg \to q$ and $gg \to g$) according to Eq. (11.4), along with initial and final state radiation based on DGLAP evolution. For the computation of the uGDs we take the parameterization of the dipole scattering amplitude $\mathcal{N}(x, r)$ from the AAMQS fits to data on the structure functions measured in electron-proton scattering at HERA [128,129] (see Fig. 11.3 for a comparison with HERA data). The main dynamical input in those fits is the running coupling BK (rcBK) equation for the description of the x-dependence of the dipole amplitudes [130–132]. The fit parameters are mostly related to the initial conditions for the evolution, set at the initial Bjorken-x value $x_0 = 10^{-2}$. In the AAMQS fits they were chosen in the following form:

$$\mathcal{N}_F(x_0, r) = 1 - \exp\left[-\frac{(r^2 Q_{s0}^2)^\gamma}{4} \log\left(\frac{1}{\Lambda r} + e\right)\right]. \tag{11.5}$$

The AAMQS fits provide a well constrained parameterization of the proton uGD. Similar to what has been done in previous works [133], the uGDs of nuclear targets (lead or gold in our case) are built by simply rescaling the value of the initial saturation scale as previously indicated in Eq. (2.21): $Q_{s0,A}^2 = A^{1/3} Q_{s0,N}^2$, where A is the mass number of the target nucleus. In this work we shall use the AAMQS sets corresponding to $\gamma = 1.101$, $Q_{s0}^2 = 0.157$ GeV^2 and $\gamma = 1.119$, $Q_{s0}^2 = 0.168$ GeV^2. We check that the results for LHCf kinematics are very little sensitive to this particular choice, as other AAMQS sets yield a very similar description of the data.

As for the proton PDFs, we use the CTEQ6 leading order set [135] with a default factorization scale $\mu_{\mathrm{F}} = \max\{k_\perp, Q_s\}$, where $k_\perp$ is the transverse momentum acquired by the incoming parton as it multiply scatters the soft glue of the target. This choice ensures that primary partonic production can be described by means of perturbative tools. We cannot exclude that part of primary particle production could be of genuinely non-perturbative origin –specially for very small transverse

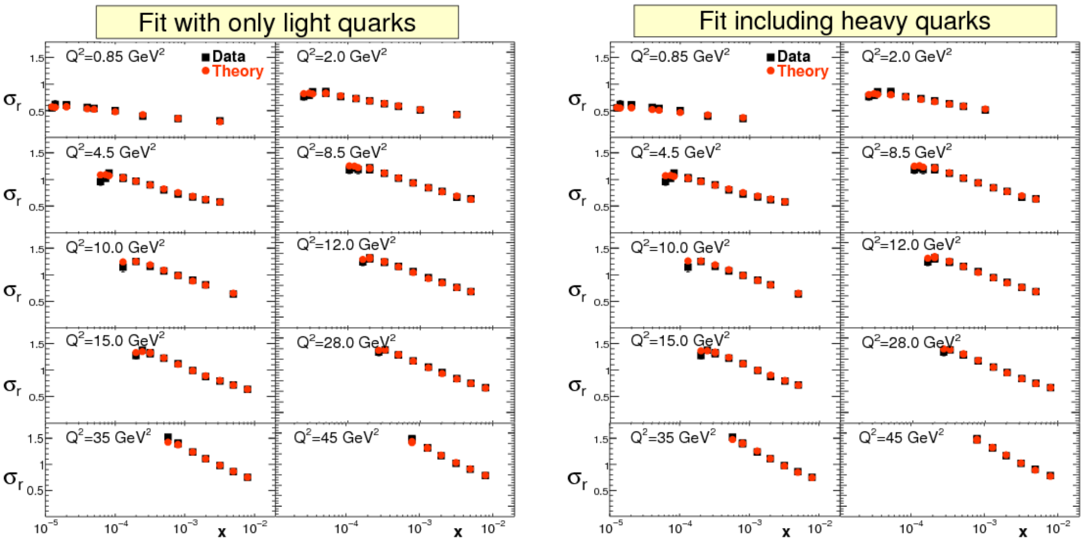

Figure 11.3: Comparison of experimental data for the reduced cross sections measured at HERA [134] (black squares) with results from the AAMQS fits (red circles) in different Q^2 bins. The left plot corresponds to a fit with only light flavors and GBW initial condition, whereas the right plot also includes the contribution of charm and beauty quarks. Figure extracted from [129].

momenta of the produced pions– and hence, not amenable to a description in terms of Eq. (11.4). However, the good description of the data reported below makes us confident that the main dynamical features of the process studied here are well accounted for by our approach. When applied to LHCf kinematics, our ansatz for the factorization scale ensures that it always falls into the perturbative domain $\mu \gtrsim 1$ GeV, since the saturation scale at the LHC ultra-forward region is perturbatively large: $Q_s(x \sim 10^{-8}) \gtrsim 1$ GeV both for proton and lead targets. Such is not the case in RHIC kinematics, where the saturation scale is considerably smaller and closer to its initial values $Q_{s0}^2 \sim 0.2$ GeV. In the latter case, we impose a momentum cut-off on the exchanged transverse momentum $k_{\perp,\min} = 1$ GeV. However, this cut-off is not necessary at the LHCf or, in other words, our results are insensitive to its precise value, as the scattering is dominated by higher transverse momenta (of the order of the saturation scale of the target $k_\perp \sim Q_s(x) \gtrsim 1$ GeV).

Finally, the factor σ_0 in Eq. (11.4) results from the integration over impact parameter implicit in Eq. (11.2). In the mean field approach treatment of the target geometry –proton or nucleus– that we shall adopt, it carries the meaning of the average transverse size of the proton. Its value can be taken from the AAMQS fits where it was one of the free fit parameters ($\sigma_0/2 = 16.5\,\text{mb}$). As for the K-factor in Eq. (11.4), it is not the result of any calculation; it has been added by hand to account for higher order corrections and potential non-perturbative effects. In practice, we use it to adjust the normalization of theoretical curves to experimental data in phenomenological works. In an ideal situation it should be equal to unity.

The degree of accuracy of the hybrid factorization formula as well as that of the non-linear evolution equations describing the Bjorken-x dependence of the uGD of the target –rcBK in our case– have been considerably improved in the recent past. In particular, NLO corrections to the cross-section Eq. (11.4) have been computed in [136, 137]. Also, both the BK and B-JIMWLK evolution equations are now known at full NLO accuracy [138,139]. However, it was quickly noticed that the perturbative expansion of hadronic observables and evolution equations at NLO become unstable in certain regions of phase space [140–142], even leading to negative cross sections. Such unphysical behavior has been identified as due to the increasing importance of double transverse momentum logarithms. Later works showed that the resummation of those collinear logs stabilizes the behavior of the perturbative series [143,144], even allowing a good phenomenological description of electron-proton cross sections measured in HERA [145,146]. Recently, it has been suggested that the kinematic corrections embodied in the resummation of large collinear logs can be accounted for through an appropriate subtraction of the rapidity divergence in the BK evolution for the target [147].

However the notable progress briefly reported above, we shall consider the hybrid formalism *only* at leading logarithmic accuracy (LL) together with LO DGLAP evolution and running coupling BK evolution to describe the scale dependence of the projectile PDF and target uGD respectively. Although a full NLO analysis of forward production data would be desirable –as all theoretical tools are now available– its phenomenological implementation should start by performing a global fit to electron-proton data at full NLO accuracy in order to obtain the uGD of a proton, which has not been carried out to date. Also, as shown in [140,141], NLO effects become increasingly important in the region of high transverse momentum and small to moderate evolution rapidities $Y = \ln(x_0/x)$. In this work we are interested in the opposite kinematic regime of very high evolution rapidities $Y \sim 15$ and small transverse momentum scales, $k_t \lesssim Q_s(x)$. We expect then that the LO implementation of the hybrid factorization captures the main dynamical features of the collision process in the LHCf kinematic regime. This set up could be systematically improved using available theoretical progress, but we leave such task for future works.

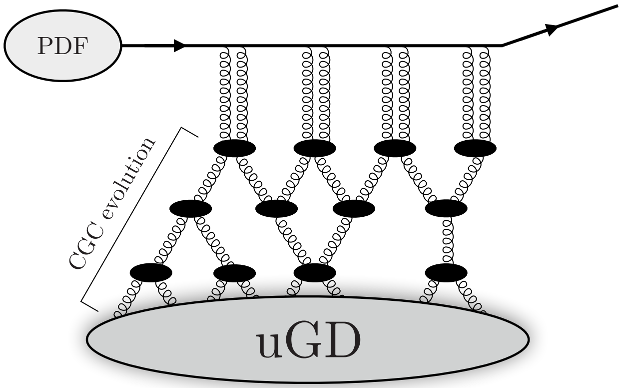

Figure 11.4: Sketch of the hybrid formalism. The multiple gluon exchanges in the lower part of the diagram represent the non-linear small-x evolution of the uGDs, computed within the CGC effective theory.

Let us now go over the additional features implemented in our Monte Carlo code. A fundamental aspect of out set up is the possibility of simulating multiple, simultaneous scatterings of different valence quarks with the dense glue of the target.

11.3 Multiple parton scattering

This feature is implemented in the eikonal model formalism [148–150], where we assume the probability distribution governing the number of independent hard scatterings to be a Poisson of mean

n, with:

$$n(b,s) = T_{\rm pp}(b)\sigma_{\rm DHJ}(s). \tag{11.6}$$

n is the average number of partonic collisions per event. It depends on the invariant mass of the collision s through the integrated cross section $\sigma_{\rm DHJ}$, and on the impact parameter of the collision b through $T_{\rm pp}$, which is the spatial overlap of the colliding protons obtained as the convolution of two Gaussian functions:

$$T_{\rm pp}(b) = \frac{1}{4\pi B}\exp\left(-\frac{b^2}{4B}\right). \tag{11.7}$$

For every event, the impact parameter b is randomly generated in a range between 0 fm and:

$$b_{max} = \sqrt{\frac{\sigma_{nd}}{\pi}}. \tag{11.8}$$

which is the radius of a circle of area defined by the cross section of non-diffractive events, σ_{nd}. For collisions on nuclear targets, we substitute the target profile by a Gaussian with radius $R_{\rm A}^2 = R_{\rm p}^2\, A^{2/3}$. Its convolution with the Gaussian profile of a proton yields:

$$T_{\rm pA}(b) = \frac{A^{2/3}}{\pi R_{\rm p}^2(A^{2/3}+1)}\exp\left(\frac{-b^2}{R_{\rm p}^2(A^{2/3}+1)}\right). \tag{11.9}$$

Which is normalized to $A^{2/3}$. Other options for a nuclear spatial profile like the Woods-Saxon model were not considered in this work. The increase of the maximum impact parameter b_{max} allowed for nuclear targets is accounted for by the substitution of σ_{nd} in Eq. (11.8) by the cross section values for d-Au and p-Pb collisions given in [151, 152].

As a last step of the Monte Carlo simulation, the partonic cascades generated through the implementation of multiple scatterings according to Eq. (11.4) have to be mapped into hadron distributions. In previous analyses of LHC and RHIC forward particle production data (which were also based on the hybrid factorization scheme [140, 141, 153]) this step was performed through the following convolution:

$$\frac{d\sigma^{hadrons}}{dyd^2p_\perp} = \frac{d\sigma^{partons}_{\rm DHJ}}{dyd^2p_\perp} \otimes D_{h/p}, \tag{11.10}$$

where $D_{h/p}$ is known as the fragmentation function. This non-perturbative object provides the probability of a parton p giving rise to a certain hadron h. The description of the hadronization process in terms of fragmentation functions is limited, by construction, to perturbatively large values of the transverse momentum of the produced particle, $p_\perp \sim 1$ GeV, where these functions are defined. However, one of the main novelties of the work discussed in this chapter with respect to previous ones lies precisely on the treatment of the hadronization process, which we implement in the framework of Lund string fragmentation.

11.4 The Lund fragmentation model

The hadronization of the scattered partons into the finally observed hadrons is described in terms of the Lund string fragmentation model as embedded in the PYTHIA event generator. More specifically, PYTHIA6 [154] is used to arrange partons resulting from hard scatterings and initial and final state radiation processes into *strings*; PYTHIA 8.186 [155] is then used to simulate their fragmentation into hadrons in the framework of the popcorn model[3]. This particular choice of hadronization model turns out to be crucial for a good description of the data. Other possible choices, like the diquark model, result in much softer spectra of the produced pions, yielding a worse agreement with data. The remnants of the colliding hadrons are also arranged into strings (stretched between quark-diquark pairs). The fraction of the total energy x carried by the quark is chosen according to the probability density:

$$P(x) \propto \frac{(1-x)^{\alpha}}{\sqrt[4]{x^2 + c_{min}^2}}. \tag{11.11}$$

Where $c_{min} = 2\langle m_q \rangle/\sqrt{s} = 0.6/\sqrt{s}$. For the α parameter we use the PYTHIA6 default value $\alpha = 3$. No primordial $k_\perp$ distribution is considered, as in [156] it was shown to be unnecessary in this framework. This procedure allows us to reach values of the momenta of the produced particles as low as detected experimentally $p_\perp \sim 0.1$ GeV and, therefore, opens the possibility of describing particle multiplicities.

The Monte Carlo code described above was first developed and applied for the description of ultra-forward pion production in proton-proton collisions at the LHC [156]. In the work presented in this chapter we extended it to the case of proton-nucleus collisions and the study of the measured nuclear modification factors. As a preliminary step we perform an analysis of forward production at RHIC.

11.5 Inclusive hadron transverse momentum spectra at RHIC

In this section we compare our results to experimental data in the kinematic range observed by two different RHIC detectors, namely BRAHMS [157] and STAR [158]. The kinematic conditions achieved in the d-Au collisions performed at $\sqrt{s} = 200$ GeV at RHIC are appropriate for a description in terms of the DHJ formula, provided that we focus on the high-rapidity region of the spectra (see Fig. 11.5). These fits act as a reference for calibration, as the datasets used have been largely studied in previous works based on the DHJ formula [153, 156, 159]. We build the PDF of the deuteron from the proton PDFs assuming strict isospin symmetry. For each independent hard scattering we calculate the multiplicity density of produced particles from the Eq. (11.4) for the cross section scaling by the non-diffractive cross-section:

$$\frac{dN^{h_1 h_2 \to (q/g)X}}{dy\, d^2k_\perp} = \frac{1}{\sigma_{nd}} \frac{d\sigma^{h_1 h_2 \to (q/g)X}}{dy\, d^2k_\perp}. \tag{11.12}$$

We assume that the energy dependence of the non-diffractive cross section in Eq. (11.12) cancels off the energy dependence of the σ_0 factor in Eq. (11.4), even if these two objects are not necessarily the same one. Any possible deviation from this assumption is absorbed on the corresponding K-factors.

We take a quite straightforward approach on proton-nucleus collisions. In this particular case, where the colliding particle is a deuteron (a deuterium nucleus, containing a proton and a neutron),

---

[3] For a brief discussion on hadronization models, see Appendix I.

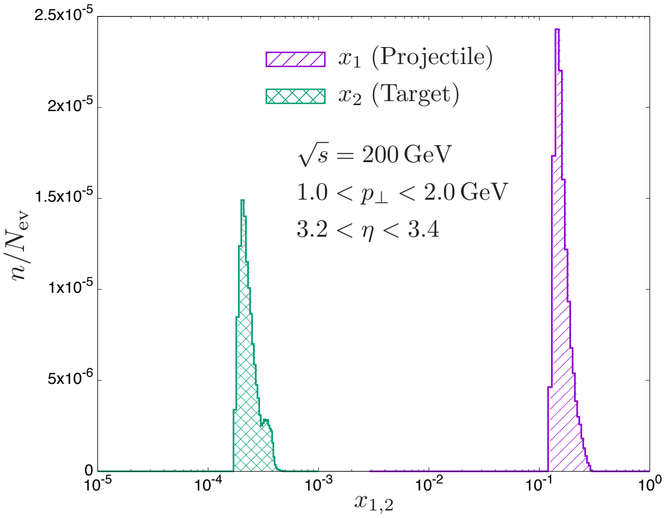

Figure 11.5: Average distribution of Bjorken-x values for projectile and target and pseudo-rapidity of the produced particle $3.2 \leq y \leq 3.4$.

we simply consider its PDF to be increased by a factor of 2 with respect to the proton's. No coherence effects between partons from proton and neutron are considered, as in the kinematic region of interest both nucleons are equally dilute. The only nuclear effect we consider is the boosting of the saturation scale by a factor of approximately $A^{1/3}$. This situation causes the gluon saturation effects to appear at higher transverse momentum scales than for single nucleons. The fact that we get a good description of data by this simple approach (see figure 11.6) tells us that the nonlinear dynamics of the saturation regime are the most prominent feature of proton-nucleus collision in this kinematic region, dominating over other effects like nuclear fluctuations.

We reach a rather good description of d-Au data on the spectra of negatively charged hadrons measured at pseudo-rapidities $\eta = 2.2$ and 3.2 by BRAHMS in minimum bias collisions and also of STAR data on neutral pion production at $\eta = 4$, see Fig 11.6. Our results are little sensitive to the specific value of the number of participants nucleons in the collision which, in the mean field treatment of nuclear geometry performed here, is given by $N_{part} \approx A^{1/3}$. The most remarkable feature of our result is that, by means of the Lund fragmentation mechanism implemented in our Monte Carlo, we can reach values of the transverse momentum of the produced particle as low as detected experimentally $p_{\perp,\text{min}} \sim 0.2$ GeV. As previous approaches relied on the use of fragmentation functions to describe the hadronization process, they could only access the regime of perturbatively high transverse momenta $p_{\perp,\text{min}} \gtrsim 1$ GeV. BRAHMS data is well described with a K-factor $K = 1$. However, STAR data on neutral pions can only be described with a K-factor $K = 0.4$, exactly the same value obtained in previous analyses of data.

11.6 Inclusive hadron transverse momentum spectra at LHCf

In this section we compare our results with data on neutral pion production measured by the LHCf collaboration in p-p and p-Pb collisions at $\sqrt{s} = 7\,\text{TeV}$ and $5.02\,\text{TeV}$ respectively [160]. The rapidity range available in this experiment ($8.8 \leq y \leq 10.8$) is appropriate for a description in terms of the DHJ formula, as shown in Fig. 11.7. In this figure we plot the distributions of Bjorken-x values

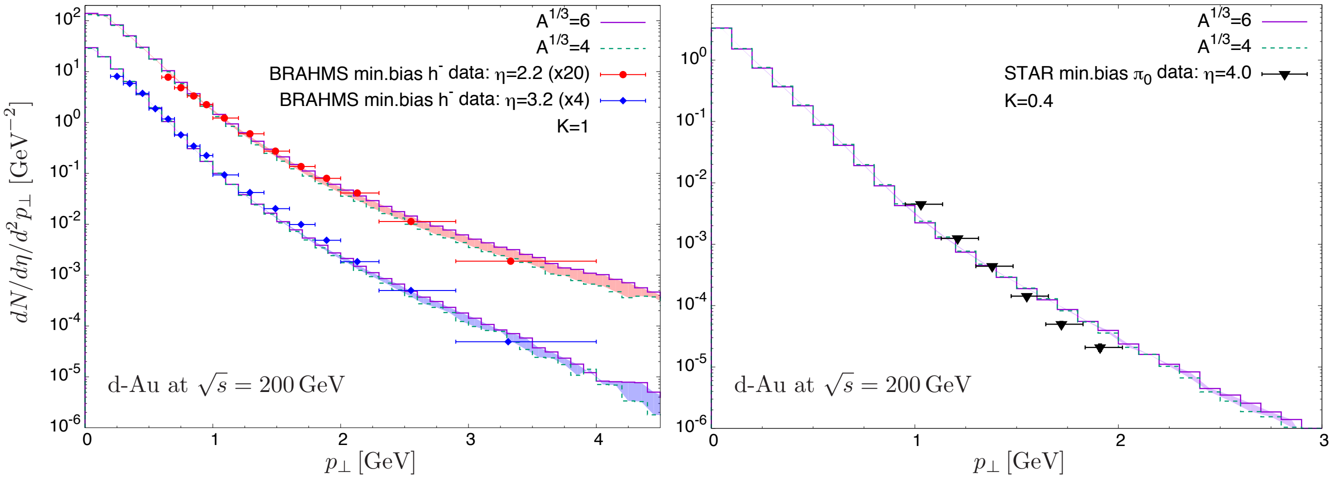

Figure 11.6: Left plot: negatively charged hadron transverse momentum spectra at η =2.2 and 3.2 in d-Au collisions at $\sqrt{s}$ = 200 GeV measured by the BRAHMS collaboration. Right plot: neutral pion spectra at η =4 in d-Au collisions at $\sqrt{s}$ = 200 GeV measured by the STAR collaboration. Scale dependence between $Q_{s0}^2 = 0.157\, A^{1/3}\,\mathrm{GeV}^2$ with $A^{1/3} = 6$ and 4 is shown by the shaded areas.

contributing from projectile and target. They are peaked in $x_p \approx 0.1$ and $x_t \approx 10^{-8}$, which indicates a much stronger dilute-dense asymmetry than in the RHIC case, Fig. 11.5.

Similarly to the previous analysis presented in [156], we obtain a remarkably good description of p-p data for all rapidities, see Fig. 11.9. Importantly, the K-factor used for the description of data is exactly the same as the one used for the description of BRAHMS data, $K = 1$. This is an important result, as it indicates that the energy evolution from RHIC to LHC, equivalent to more than ten units in evolution rapidity, $\Delta Y \gtrsim 14$, is well accounted for by the theoretical tools in our approach, namely the rcBK evolution for the x-dependence of the uGDs. For the sake of illustration in Fig. 11.9 we also show the partonic spectra generated prior to the hadronization process. As a comment, it should be noted that the bump observed for the lowest momentum bin is due to the contribution of projectile remnants not participating into the hard scattering.

We also find a good agreement of the neutral pion spectra measured in p-Pb collisions, see Fig. 11.10. In this case our theoretical result is a bit above the data at the highest values of transverse momenta. Again, we have used a K-factor $K=1$ for its description. As shown in Fig. 11.10, a slightly lower value of the K-factor, $K=0.5$, results in a slightly better description of the data, although we do not have a clear motivation for such choice.

11.7 Nuclear modification factor at LHCf

Finally, in this section we present our results for the nuclear modification factor R_{pPb}, defined as follows:

$$R_{\mathrm{pPb}}^{\pi^0} \equiv \frac{\sigma_{\mathrm{inel}}^{\mathrm{pp}}}{\langle N_{coll}\rangle \sigma_{\mathrm{inel}}^{\mathrm{pPb}}} \frac{E d^3\sigma^{\mathrm{pPb}}/d^3p}{E d^3\sigma^{\mathrm{pp}}/d^3p} = \frac{1}{\langle N_{coll}\rangle} \frac{dN^{\mathrm{pPb}\to\pi^0 X}/dyd^2p_t}{dN^{\mathrm{pp}\to\pi^0 X}/dyd^2p_t}. \tag{11.13}$$

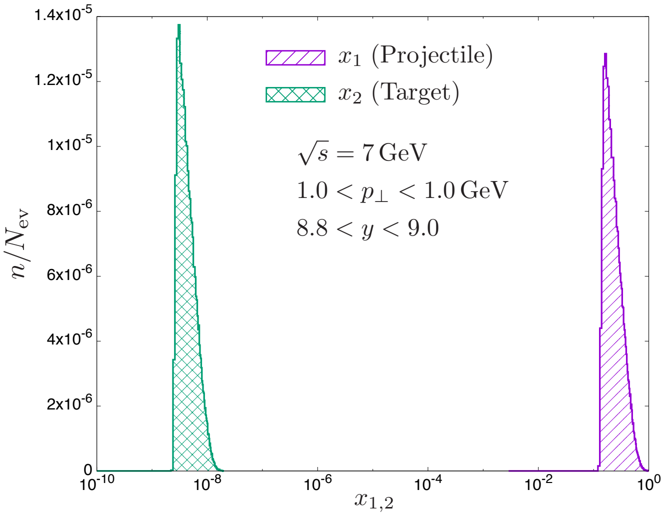

Figure 11.7: Average distribution of Bjorken-x values for projectile and target and rapidity of the produced particle $8.8 \leq y \leq 9.0$.

Where $Ed^3\sigma^{\rm pPb}/dp^3$, $Ed^3\sigma^{\rm pp}/dp^3$ are the inclusive cross sections of neutral pion production in p-Pb and p-p collisions respectively, and $\langle N_{coll}\rangle$ is the average number of nucleon-nucleon scatterings in a p-Pb collision. We shall use the same value of $\langle N_{coll}\rangle$ as the one used in the experimental analysis [160], obtained from a Monte Carlo Glauber simulation: $\langle N_{coll}\rangle = 6.9$. Also, it should be kept in mind that the experimental value for $\sqrt{s} = 5.02$ TeV is obtained after interpolating p-p data from 2.76 and 7 TeV collision energies.

One remarkable feature of experimental data is the approximate flatness of the $R^{\pi^0}_{\rm pPb}$ over all the measured rapidity range (see Fig. 11.11). Actually a constant value $R^{\pi^0}_{\rm pPb} = 1/\langle N_{coll}\rangle \approx 0.15$ is compatible with data for all y. This would immediately imply that the multiplicity density in p-p collisions is approximately equal to the one in p-Pb collisions (see right hand side of Eq. (11.13)):

$$\frac{dN^{pp\to\pi^0 X}}{dyd^2p_t} \approx \frac{dN^{pPb\to\pi^0 X}}{dyd^2p_t}. \tag{11.14}$$

Certainly, a more refined analysis of data would probably indicate a decreasing behavior of $R^{\pi^0}_{\rm pPb}$ with increasing rapidity of the detected pions. However, such rate of change is much smaller than the one observed at RHIC energies in a similar range of transverse momenta. This purely empirical observation is well accounted for by our calculations. In terms of saturation physics this result can be immediately related to the asymptotic properties of the solution of the BK equation, used to describe the x-dependence of the uGDs of the proton and lead targets. At partonic level, Eq. (11.14) can be written as:

$$\langle n_{\rm pPb}\rangle_b N^{\rm Pb}_{(F/A)} \approx \langle n_{\rm pp}\rangle_b N^{\rm p}_{(F/A)}. \tag{11.15}$$

Where $N^{\rm Pb}_{(F/A)}$, $N^{\rm p}_{(F/A)}$ are the uGDs corresponding to proton and nucleus targets, and $\langle n_{\rm pPb}\rangle_b$, $\langle n_{\rm pp}\rangle_b$ are the average number of independent hard collisions per p-p and p-Pb events integrated in impact parameter. Due to the normalization of the spatial overlap function for proton-nucleus collisions T_{pA}, the integration of Eq. (11.6) over b yields:

$$\langle n_{\rm pPb}\rangle_b = A^{2/3}\langle n_{\rm pp}\rangle_b. \tag{11.16}$$

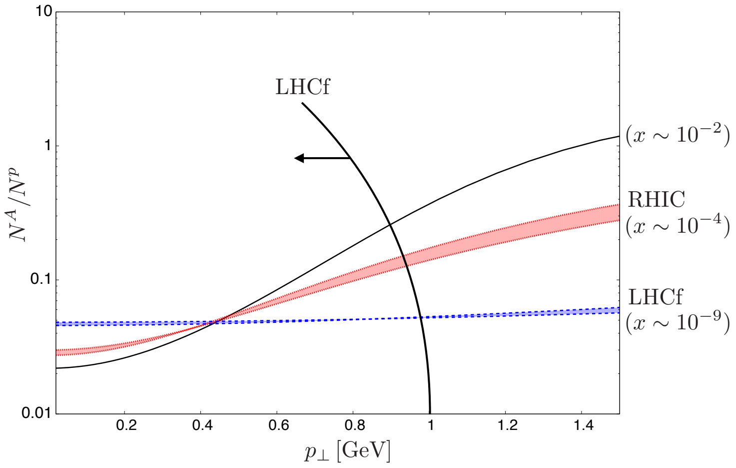

Figure 11.8: Ratio of rcBK-evolved uGDs for proton and lead targets for the different x-ranges observed at RHIC and LHC.

Applying this expression to Eq. (11.15), and also neglecting the difference in the factorization scales for p or Pb scattering we get:

$$\frac{N^{\text{Pb}}_{(F/A)}}{N^{\text{p}}_{(F/A)}} = \frac{1}{A^{2/3}}. \tag{11.17}$$

This behavior is well realized by the BK-evolved uGD's used in this work. As shown in Fig. 11.8, the ratio of lead over proton uGD's takes a constant value $1/A^{2/3} \approx 0.03$ in all the $k_\perp$ range probed by the LHCf data studied here. We interpret the fact that the experimental data on $R^{\pi^0}_{\text{p-Pb}}$ reproduces this constant behavior over the whole range of rapidity as an indication for the prevalence of saturation effects in the probed kinematic regime by the LHCf. In turn, the analogous ratio for the kinematic regime relevant for forward RHIC data also exhibits a growing behavior with increasing transverse momentum, in the very same fashion as the corresponding nuclear modification factor. We conclude that RHIC forward kinematics falls outside the universality regime of small-x evolution. Rather, RHIC kinematics test non-linear evolution in the pre-asymptotic regime.

Aside from the description of data discussed in this work, the fact that the main features of ultra-forward production data –even for very small transverse momentum of the produced particles– can be understood in terms of perturbative tools may open interesting new avenues of research in the field of Ultra-High Energy Cosmic Rays (UHECR). There, the main features of the air showers developed after the primary collisions in the upper atmosphere are determined to a large extent by the hadronic collisions properties –in particular, by the total cross-section, forward multiplicity, charm production and inelasticity [161]. Thus, the availability of theoretically controlled tools to extrapolate from the well constrained collision energy domain probed at the LHC to that of UHECR is necessary to reduce the inherent uncertainty associated to the extrapolation itself and, thereby, also the uncertainty associated to the analysis of the primary mass composition of UHECR. We propose that the use of non-linear renormalization group equations of QCD (like the BK equation employed in this work) can offer insight in this direction.

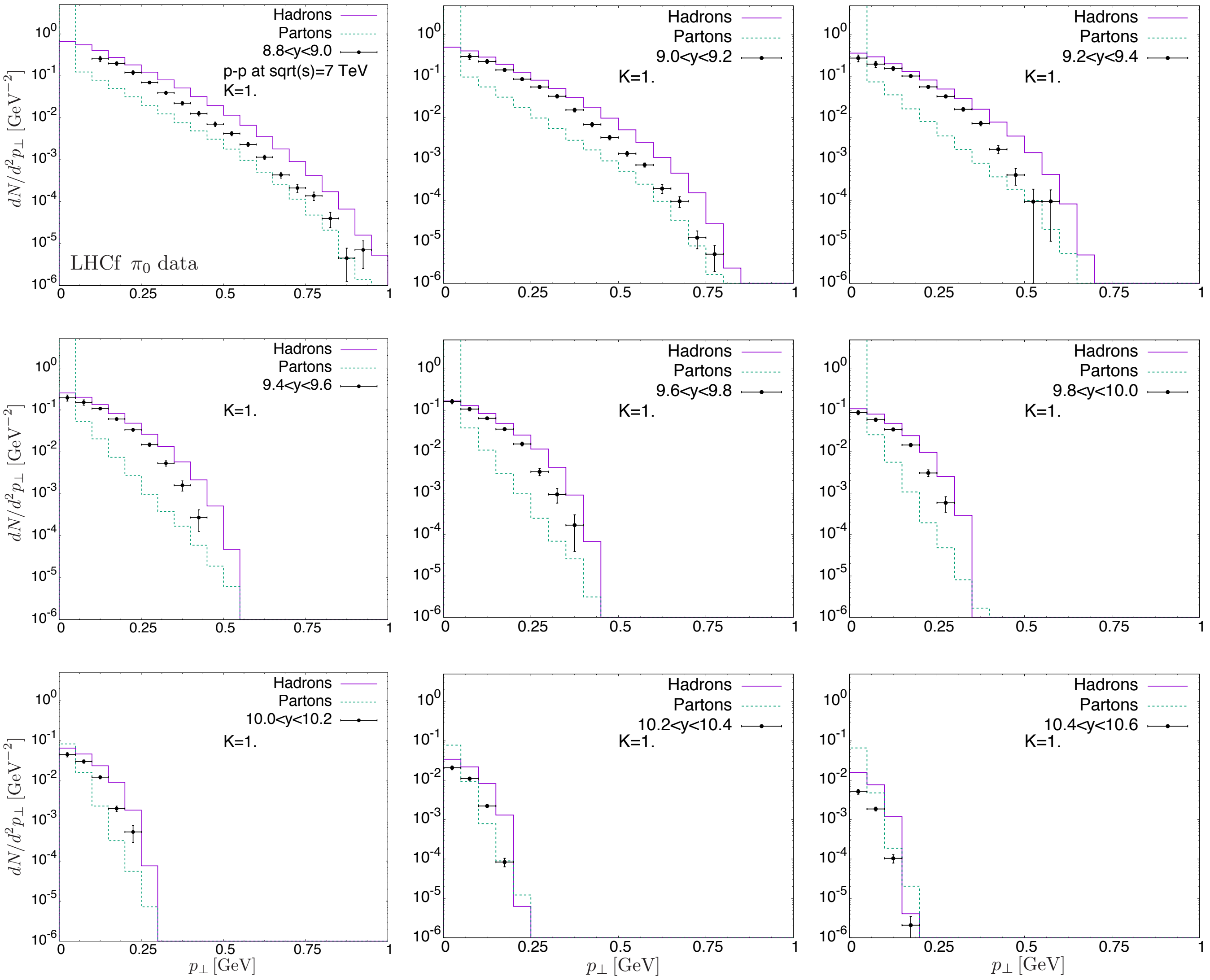

Figure 11.9: Neutral pion transverse momentum spectra in the rapidity range $8.9 < y < 10.6$ in p-p collisions at $\sqrt{s} = 7$ TeV. Also shown is the corresponding partonic spectra (dashed lines).

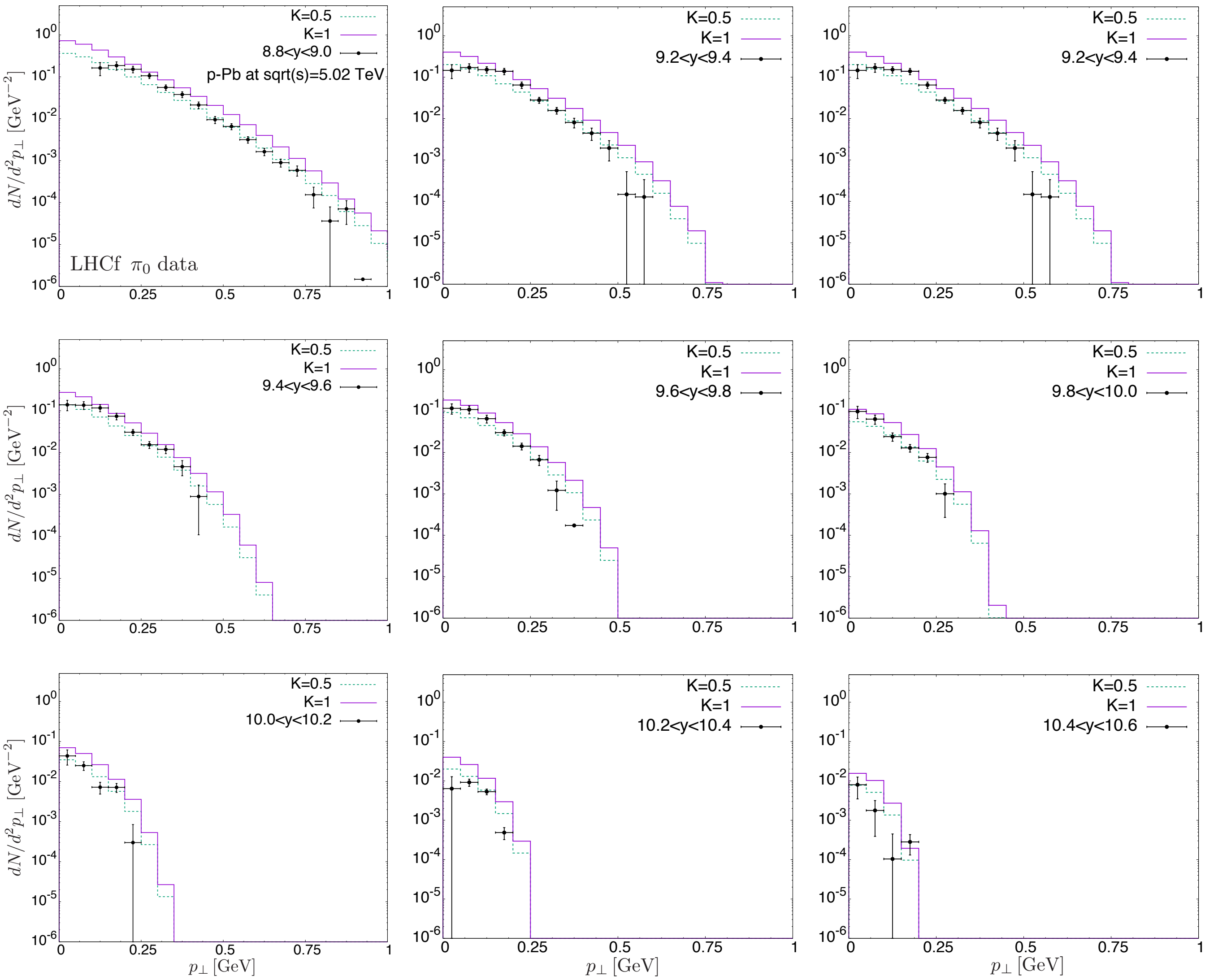

Figure 11.10: Neutral pion transverse momentum spectra in the rapidity range $8.9 < y < 10.6$ in p-Pb collisions at $\sqrt{s_{NN}} = 5.02\,\text{TeV}$ measured at LHCf detector. Solid and dashed lines correspond to K-factors K=1 and K=0.5 respectively.

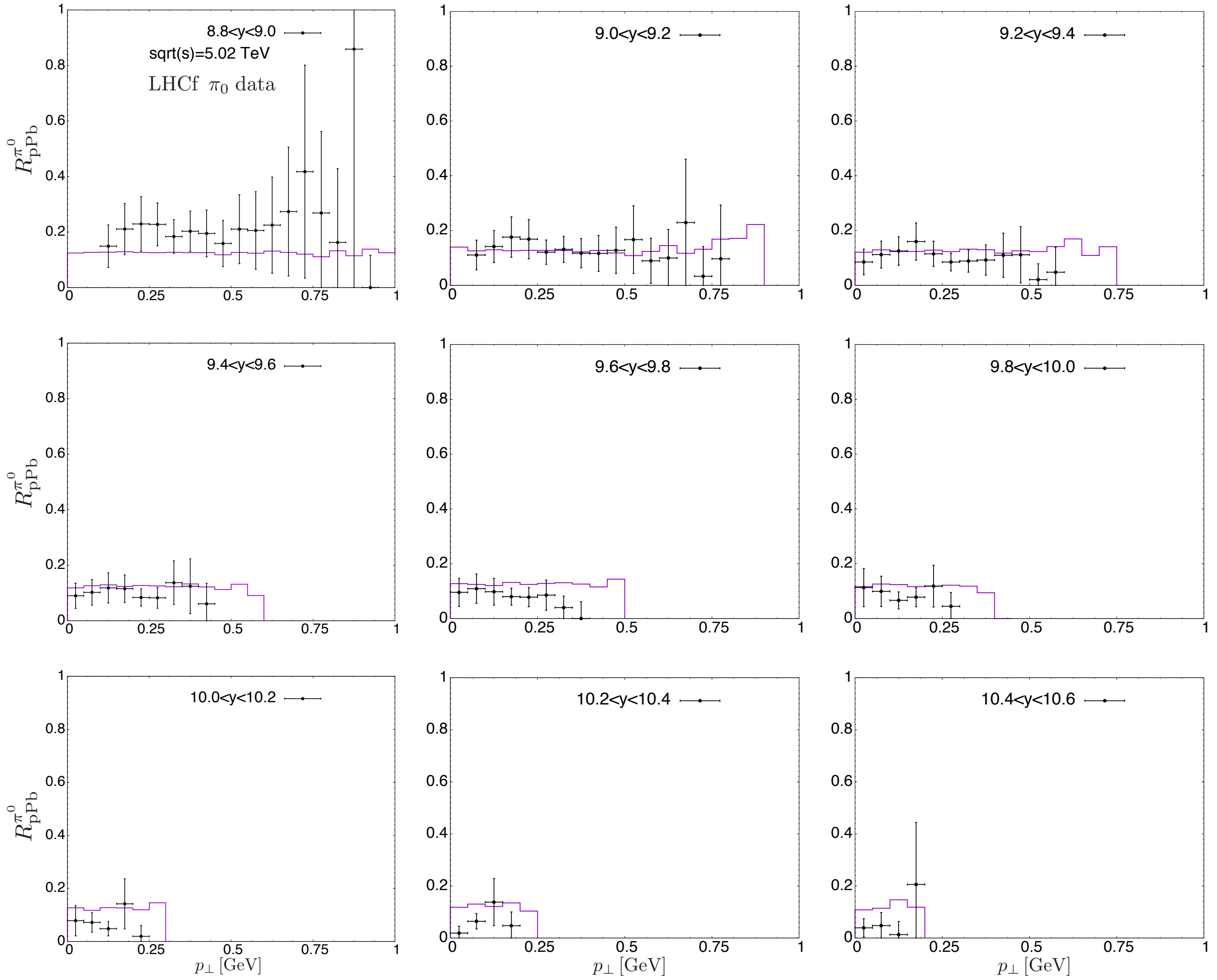

Figure 11.11: Nuclear modification factor for neutral pion production at $\sqrt{s_{NN}} = 5.02\,\text{TeV}$. Data points taken from [160]. Since there is no neutral pion transverse momentum spectra measurement available for p-p collisions at $\sqrt{s} = 5.02\,\text{TeV}$, it is derived by interpolation of datasets obtained from p-p collisions at $\sqrt{s} = 7\,\text{TeV}$ and $2.76\,\text{TeV}$, which are included in that paper.

Summary:

- We perform an analysis of data on hadron production in high energy p-p and p-A collisions at ultra-forward rapidities.
- For this task we use a Monte Carlo event generator that combines a CGC description of elementary partonic scatterings with an implementation of hadronization according to the Lund string fragmentation model.
- Within this approach we achieve a good description of the single neutral pion spectrum in the very forward region of the LHC ($8.8 \leq y \leq 10.8$) and down to the lowest values of transverse momentum experimentally accessed by the LHCf collaboration ($p_\perp \lesssim 0.1$ GeV).
- The flat and approximately constant behavior obtained for the nuclear modification factor R_{pPb} over the wide range of rapidities covered by data can be related to the asymptotic properties of the solutions of the rcBK equation and, in particular, to the existence of universal solutions at sufficiently small-x.
- Our results show that the main dynamical features of a dilute-dense interaction can be reproduced through the saturation-dominated small-x evolution of the uGDs (in our case, given by the rcBK equation).
- Moreover, this approach provides a theoretically controlled way of extrapolating to higher energies, which has a clear potential as a tool for studying Ultra-High Energy Cosmic Rays.

Part VI

Conclusions and prospects

With intensity, the drop evaporates by law
In conclusion, leaving is easy
When you've got some place you need to be.

— Bill Callahan in "Riding for the Feeling"

In this report we address the saturation regime of QCD in the light of two fundamental problems of high energy physics: the theoretical characterization of the initial stage of HICs, and the phenomenological analysis of multiparticle production in collider experiments. Our studies are based on the CGC formalism, which throughout the development of the thesis we extend and modify with the two-fold aim of achieving a more realistic physical picture and expanding the potential applications of our results.

On the theoretical side, we start with a first-principles analytical calculation of the one- and two-point correlators of the Glasma EMT. These objects characterize, respectively, the average and the variance of the distribution of energy density deposited in the plane transverse to the collision axis at an infinitesimal proper time $\tau = 0^+$. In the course of this work we extend the traditional MV model by introducing an explicit impact parameter dependence in the two-point correlator of color source densities, as well as a generalization of the transverse profile of the interaction. Also, and foremost, throughout our calculations we apply a self-consistent approach where we respect the inherently non-linear character of the Glasma field dynamics, thus departing from the approximations adopted as standard practice in this kind of studies (i.e. the Glasma Graph approximation). The results achieved in this way raise a question about the accuracy of the widely accepted flux tube picture of Glasma. Said results can be summed up in four main points:

- Our expression for the two-point correlator of the Glasma EMT displays a remarkably slow vanishing behavior in the limit of long correlation distances $rQ_s \gg 1$: a power-law tail $1/r^2$.
- Although the calculations performed under the Glasma Graph approximation also exhibit a power-law behavior in the same limit, they yield much more rapidly decaying curves than those obtained in the exact approach ($\propto 1/r^2$ vs. $\propto 1/r^4$).
- Our results could conflict with the conjectured physical picture of Glasma flux tubes, as they predict transverse correlation lengths larger than $1/Q_s$ (or rather, logarithmic enhanced by a factor $\ln(Q_s/m)$ sensitive to the infrared).
- The relatively long-range correlations obtained in this work could potentially have a deep impact in both physical interpretations and numerical results for any phenomenological study based on the two-point correlator of the Glasma EMT. An example that is already being explored by the author is the analytical calculation of the moments of the energy density distribution, known as eccentricities. From these quantities we can build a series of dimensionless ratios that have been observed to be proportional to the experimentally measured anisotropic flow coefficients. Our first principles analytical approach proves successful in reproducing data measured at both RHIC and LHC without needing to resort to other less theoretically motivated implementations of initial state fluctuations (e.g. sampling of random nucleon positions).

Then we turn our attention to another fundamental feature of the Glasma phase: the fluctuations of topological charge that in turn give rise to generation of local imbalances of axial charge. Within the CGC framework these fluctuations are characterized by the two-point correlator of the divergence of the Chern-Simons current, which we compute in the same fashion as the previously obtained correlators of the EMT. Remarkably, the obtained expressions yield an even larger discrepancy with those computed under the Glasma Graph approximate approach. To summarize:

- Our result for the two-point correlator of the divergence of the Chern-Simons current exhibits a power-law tail $1/r^4$ in the limit of long correlation distances $rQ_s \gg 1$, whereas the expression obtained under the Glasma Graph approximation decays like $1/r^8$.

- Remarkably, the gap between the results for the divergence of the Chern-Simons current is even larger than the one showed by those of the energy density, suggesting that the non-linear dynamics followed by the gluon fields have an even greater effect over the long-range transverse fluctuations of axial charge density than they do over those of the deposited energy.
- However, despite the notably slow fall-off of our expression, the transverse correlation lengths estimated for this observable are neither sensitive to the infrared nor logarithmically enhanced, an outcome that seems somewhat more consistent with the conjectured Glasma flux tube picture.
- The results of this study can be directly applied in studies of anomalous transport phenomena such as the CME, as they provide a fundamental input for the Monte Carlo modeling of initial conditions of axial charge density.

A common conclusion of both studies is that the commonly adopted Glasma Graph approximation yields the exact same result as our approach in the UV limit $r \to 0$. This seems to indicate that the non-linear nature of the Glasma fields dynamics can be overlooked in this limit, or to a good approximation for correlation distances shorter than $1/Q_s$. This outcome confirms the expected validity range of the Glasma Graph approximation. However, the large discrepancies observed in the rest of the spectra provides analytical evidence on the importance of the non-linear dynamics relating color source densities and gauge field correlators.

In the phenomenological part of the report we study the influence of saturation physics in the analysis of multiparticle production at the LHC. With this goal, we perform an analysis of data on single inclusive pion production measured by the LHCf collaboration in high energy proton-proton and proton-nucleus at ultra-forward rapidities, $8.8 \leq y \leq 10.8$. Our analysis relies on the use of a Monte Carlo event generator that combines a perturbative description of the partonic-level scattering process in the hybrid formalism of CGC with an implementation of hadronization in the framework of the Lund string fragmentation model. The main dynamical input in this set up is the rcBK equation, which is applied in the computation of the x-dependence of dipole amplitudes. The main conclusions of our analysis can be summarized as:

- We achieve a good description of the single neutral pion spectrum in the very forward region of the LHC ($8.8 \leq y \leq 10.8$) and down to the lowest values of transverse momentum experimentally accessed by the LHCf collaboration ($p_\perp \lesssim 0.1$ GeV).
- The fact that we can reproduce such low values is a feature of our particular approach, where we employ the Lund string fragmentation model –instead of fragmentation functions– to describe hadronization. This particular aspect opens the door for a calculation of less inclusive observables dominated by the low-$p_\perp$ region, such as 2-particle correlations or multiplicities.
- The flat and approximately constant behavior obtained for the nuclear modification factor R_{pPb} over the wide range of rapidities covered by data can be interpreted as a consequence of the asymptotic properties of the solutions of the rcBK equation and, in particular, the existence of universal solutions at sufficiently small-x.
- Our results show that the main dynamical features of a dilute-dense interaction can be reproduced through the saturation-dominated small-x evolution of the uGDs (in our case, given by the rcBK equation).
- This approach provides a theoretically controlled way of extrapolating to higher energies, which

could be applied in the study of Ultra-High Energy Cosmic Rays.

The studies described above presents a wide variety of applications and potential follow-up projects. It was already mentioned that our results for the correlations of the Glasma EMT can be applied in the computation of anisotropic flow coefficients. A logical continuation of this project would be the implementation of the obtained expressions into a Monte Carlo code aimed at a fully QCD-based description of primordial fluctuations in HICs.

Another potential application of our previous work is the computation of the dilute-dense limit of the computed correlators. As our set-up allows for different mass numbers A_1, A_2 for the colliding nuclei, it is thus straightforward to repeat the calculation in the case where $A_1 \ll A_2$. This simple project aims at bringing new insight into the theoretical characterization of the system generated in a highly energetic proton-nucleus collision.

A more complex follow-up to the previous works is the analytical calculation of higher order terms in the τ-expansion of the EMT correlators. Said expansion was proposed in [162], where they define the gluon fields generated after a HIC in terms of a power series in τ, which turns the Yang-Mills equations into an infinite system of differential equations that can be solved recursively. This approach provides analytical insight of the early time evolution of essential objects like the energy-momentum tensor and its correlators. A theoretical characterization of how these quantities evolve after the collision is of fundamental interest for the application of our work to phenomenological studies of QGP, as such state is expected to be formed at a proper time of the order of the inverse of the saturation scale.

Besides being the foundation for several applications and follow-up works, the research reported in this thesis can also be subject to improvements, upgrades and expansions. For instance, in the case of the calculation of correlators, a straightforward refinement of our results could come from considering saturation beyond the MV model[4]. Regarding the analysis of ultra-forward particle production, an immediate improvement could come from the implementation of the state-of-the-art precision tools for small-x evolution.

---

[4] In this regard, the undetermined function $f(x_\perp - y_\perp)$ introduced in our generalized approach allows for the implementation of JIMWLK evolution within the so-called Gaussian truncation.

Conclusiones

En esta tesis hemos abordado el estudio del régimen de saturación de QCD desde dos ángulos: uno teórico, realizándose una descripción analítica de la fase inicial de una colisión de iones pesados; y uno fenomenológico, basado en un análisis de la producción de partículas en experimentos de aceleradores (concretamente, el LHC). Estos estudios se llevaron a cabo en el marco del formalismo CGC, al que realizamos una serie de modificaciones.

En la parte teórica presentamos el cálculo de los correladores de uno y dos puntos del tensor energía-momento correspondiente al Glasma. Estos objetos describen cuantitativamente propiedades estadísticas de la distribución de densidad de energía generada inmediatamente después de la colisión (tiempo propio $\tau = 0^+$); concretamente, la media y la varianza. En el desarrollo de este cálculo introducimos dos generalizaciones del modelo MV, a saber: incorporamos una dependencia explícita en el parámetro de impacto, y relajamos la asunción de localidad en las correlaciones a nivel partónico. Asimismo, adoptamos un método *exacto* (dentro de las convenciones del modelo MV) en el que respetamos la naturaleza no lineal de las correlaciones del Glasma, lo que supone un notable paso adelante en relación a las técnicas aproximadas aplicadas rutinariamente en este tipo de cálculos. Los resultados obtenidos mediante esta estrategia ponen en duda la interpretación del Glasma como conjunto de *tubos de flujo* de color, comúnmente aceptada como paradigma del estado inicial de las colisiones de iones pesados. Dichos resultados se pueden resumir en cuatro puntos:

- La expresión obtenida para el correlador de dos puntos del tensor energía-momento tiende a cero en el límite $rQ_s \gg 1$ a un ritmo notablemente lento: siguiendo una curva $1/r^2$.
- Aunque los resultados obtenidos por medio de la aproximación Glasma Graph también exhiben un comportamiento de potencia negativa, su tendencia a 0 es mucho más rápida ($\propto 1/r^2$ vs. $\propto 1/r^4$).
- Nuestros resultados podrían entrar en conflicto con la interpretación del Glasma mencionada anteriormente. A partir de dicha hipótesis se deducen distancias de correlación cortas (del orden de $1/Q_s$), mientras que las correlaciones obtenidas en nuestro cálculo dan lugar a distancias de correlación logarítmicamente amplificadas por un factor $\ln(Q_s/m)$ sensible al infrarrojo.
- Las correlaciones de (relativamente) largo alcance obtenidas en este trabajo podrían tener un impacto profundo tanto en las interpretaciones como en los resultados numéricos de cualquier estudio fenomenológico basado en el correlador de dos puntos del tensor energía-momento del Glasma. Una aplicación específica que está siendo estudiada por el autor en la actualidad es el cálculo analítico de excentricidades, obtenidas como momentos de la distribución de densidad de energía. A partir de estas cantidades se pueden calcular una serie de magnitudes adimensionales que exhiben sendas relaciones de proporcionalidad con los coeficientes de flujo anisotrópico medidos experimentalmente. Nuestra metodología de primeros principios resulta en un excelente acuerdo con datos obtenidos en RHIC y LHC, sin tener que recurrir a modelos fenomenológicos con menos respaldo teórico (por ejemplo, el muestreo de posiciones de nucleones aleatorias).

Nuestro siguiente objeto de estudio es el correlador de dos puntos de la divergencia de la corriente Chern-Simons. Esta cantidad caracteriza la generación de carga axial originada por fluctuaciones de evento a evento en el Glasma. En este cálculo seguimos los mismos principios aplicados en el cálculo de correladores del tensor energía-momento. Notablemente, al comparar con resultados de la aproximación Glasma Graph las expresiones obtenidas dan lugar a una discrepancia aún más significativa que en el caso anterior. En resumen:

- En el límite $rQ_s \gg 1$, nuestro resultado para el correlador de dos puntos de la divergencia de la corriente Chern-Simons tiende a 0 siguiendo una curva $1/r^4$. Por otro lado, la expresión obtenida siguiendo la aproximación Glasma Graph decrece de acuerdo a $1/r^8$.
- Cabe destacar que la discrepancia entre resultados es aún mayor para esta propiedad que para el caso anterior (tensor energía-momento).
- A pesar del comportamiento de la expresión obtenida en el límite $rQ_s \gg 1$, las distancias de correlación estimadas para esta propiedad particular no muestran sensibilidad al infrarrojo, ni están amplificadas de ninguna otra forma. Es, por tanto, un resultado más fácilmente integrable en el paradigma de los tubos de flujo de Glasma.
- Los resultados de este estudio representan una contribución fundamental a la modelización de distribuciones iniciales de carga axial para simulaciones Monte Carlo. Por tanto, pueden ser aplicados directamente en estudios sobre fenómenos de transporte anómalo como el efecto magnético-quiral.

Una observación común a ambos estudios es el hecho de que, en el límite ultravioleta $r \to 0$, nuestro método de cálculo da lugar a exactamente los mismos resultados que la aproximación Glasma Graph. Esto sugiere que el carácter no lineal del Glasma puede ser ignorado en dicho límite, siendo además una buena aproximación para distancias inferiores a $1/Q_s$. Este resultado confirma el rango de validez de la aproximación Glasma Graph, predicho en estudios recientes. No obstante, la significativa discrepancia observada en el resto del espectro evidencia la importancia del carácter no lineal de las correlaciones del Glasma.

En las secciones de fenomenología de esta tesis estudiamos la influencia del régimen de saturación sobre los procesos de producción de partículas observados en el LHC. Específicamente, realizamos un análisis de los datos de producción inclusiva de piones neutros obtenidos por la colaboración LHCf. El rango de rapidities accesible por este experimento se denomina región de rapidities ultra-altas: $8.8 \leq y \leq 10.8$. En esta región observamos una colisión altamente asimétrica en la que uno de los núcleos que colisionan se percibe como saturado. Nuestro análisis se basa en el uso de un código Monte Carlo que combina una descripción de las colisiones a nivel partónico basada en el formalismo híbrido del CGC con una implementación del proceso de hadronización de acuerdo al modelo de fragmentación de cuerdas de Lund. La evolución de la distribución de gluones (uGD) que describe el núcleo saturado con la energía es descrita por medio de la ecuación rcBK del CGC. Los resultados de este análisis se pueden resumir en los siguientes puntos:

- Obtenemos una buena descripción de los datos en todo el espectro de momento transversal, alcanzando incluso los valores más bajos accesibles por la colaboración LHCf ($p_\perp \lesssim 0.1$ GeV).
- Poder reproducir datos correspondientes a momentos tan bajos es una cualidad de la metodología detallada anteriormente, en especial del uso del modelo de hadronización de Lund. Esto supone una ventaja significativa sobre aquellos métodos de análisis basados en el uso de funciones de fragmentación. Este aspecto en particular abre la posibilidad de aplicar nuestro modelo a la descripción de observables menos inclusivos dominados por la región de bajo $p_\perp$, como por ejemplo la multiplicidad.

- El factor de modificación nuclear R_{pPb} se mantiene aproximadamente constante en un amplio margen de rapidities, lo que puede ser interpretado como una consecuencia de las propiedades asintóticas de las soluciones a la ecuación rcBK. Esto sugiere la existencia de soluciones universales a valores de x lo suficientemente bajos.
- Nuestros resultados muestran que los aspectos principales de las interacciones entre sistemas diluidos y densos pueden ser descritos en términos de física de saturación; en particular, por medio de la evolución no lineal de las uGDs.
- La metodología empleada en este estudio propone un método teóricamente motivado de extrapolar a altas energías, lo que encontraría una potencial aplicación en el estudio de rayos cósmicos de ultra-altas energías.

Los estudios presentados en esta tesis plantean una amplia variedad de posibles aplicaciones y proyectos complementarios. Como ha sido mencionado previamente, nuestros resultados sobre las correlaciones del tensor energía-momento del Glasma pueden ser aplicadas en el cálculo de coeficientes de flujo anisotrópico. Una continuación natural de este proyecto sería la implementación de las expresiones obtenidas en un código Monte Carlo para el estudio de fluctuaciones primordiales en colisiones de iones pesados.

Otro posible uso de los resultados obtenidos en dicho trabajo sería el estudio de colisiones con un alto grado de asimetría. Se trata de una aplicación directa del cálculo presentado anteriormente, ya que éste permite asignar distintos números másicos A_1, A_2 a los núcleos. El cálculo del límite $A_1 \ll A_2$ permite una aproximación teórica sencilla al problema de describir el sistema generado en colisiones protón-núcleo.

Otra posible continuación de los estudios anteriores sería el cálculo analítico de términos de una expansión en órdenes de τ en la que los correladores obtenidos aquí actuarían como orden 0. En dicha expansión [162], las ecuaciones Yang-Mills se convierten en un sistema de infinitas ecuaciones diferenciales que puede ser resuelto recursivamente. La computación de órdenes superiores en τ permitiría ganar intuición sobre la evolución temporal de las propiedades fundamentales del Glasma. Este es un aspecto de vital importancia para la conexión entre nuestros estudios y los análisis fenomenológicos del QGP, generado en escalas temporales del orden de $1/Q_s$.

A parte de aportar la base para futuras líneas de investigación, los estudios realizados en esta tesis también son susceptibles de mejoras, y ampliaciones. Por ejemplo, en el caso del cálculo de correladores, una extensión lógica de nuestros resultados vendría de considerar modelos de saturación más allá del modelo MV. Con respecto al análisis de producción de partículas en rapidities ultra-altas, una mejora inmediata sería la incorporación de las herramientas de precisión más recientemente desarrolladas para la descripción de evolución en el régimen de x bajo.

Appendices

Appendix A

Light-cone coordinates

In the calculations presented in this thesis we make extensive use of Dirac's light-cone coordinate system. In order to define it, let us start with the usual Cartesian system of Minkowski space, where 4-positions are expressed by the components $\vec{r}=(x^0,x^1,x^2,x^3)\equiv(x^0,\vec{x}_\perp,x^3)$. We choose the metric tensor to be $g_{\mu\nu}=\mathrm{diag}(1,-1,-1,-1)$. In this framework, the light-cone coordinates are defined as:

$$x^+=\frac{x^0+x^3}{\sqrt{2}} \qquad x^-=\frac{x^0-x^3}{\sqrt{2}}. \tag{A.1}$$

Note that this transformation is equivalent to performing a 45° rotation of the Cartesian system, in such a way that the x^0, x^3 axes fall on top of the light-cone. This does not affect the transverse coordinates x^1, x^2, and thus we can ignore them for now. By differentiation of the previous formulas we obtain the base vectors of the new coordinate system:

$$\vec{r}=x^0\hat{e}_0+x^3\hat{e}_3 \doteq x^+\vec{e}_++x^-\vec{e}_- \tag{A.2}$$

$$\vec{e}_+=\frac{\partial\vec{r}}{\partial x^+}=\frac{1}{\sqrt{2}}\hat{e}_0+\frac{1}{\sqrt{2}}\hat{e}_3 \tag{A.3}$$

$$\vec{e}_-=\frac{\partial\vec{r}}{\partial x^-}=\frac{1}{\sqrt{2}}\hat{e}_0-\frac{1}{\sqrt{2}}\hat{e}_3, \tag{A.4}$$

with the corresponding scale factors $h_+=|\vec{e}_+|=1$ and $h_-=|\vec{e}_-|=1$. The components of a general 4-vector $\vec{A}$ in this coordinate system are straightforwardly obtained as:

$$A^+=\frac{A^0+A^3}{\sqrt{2}} \qquad A^-=\frac{A^0-A^3}{\sqrt{2}}, \tag{A.5}$$

formulas that can be expressed more succinctly using matrix notation:

$$\begin{pmatrix}A^+\\A^-\end{pmatrix}=\frac{1}{\sqrt{2}}\begin{pmatrix}1&1\\1&-1\end{pmatrix}\begin{pmatrix}A^0\\A^3\end{pmatrix}\equiv(S)\begin{pmatrix}A^0\\A^3\end{pmatrix}. \tag{A.6}$$

Here we define the transformation matrix S. We may use S to express the metric tensor in light-cone coordinates:

$$g'_{\mu\nu}=\left(S^{-1}\right)^{\mathrm{T}}g_{\mu\nu}\left(S^{-1}\right)=\frac{1}{2}\begin{pmatrix}1&1\\1&-1\end{pmatrix}\begin{pmatrix}1&0\\0&-1\end{pmatrix}\begin{pmatrix}1&1\\1&-1\end{pmatrix}=\begin{pmatrix}0&1\\1&0\end{pmatrix}. \tag{A.7}$$

Including transverse coordinates the complete light-cone metric tensor reads:

$$g'_{\mu\nu}=\begin{pmatrix}0&1&0&0\\1&0&0&0\\0&0&-1&0\\0&0&0&-1\end{pmatrix}, \tag{A.8}$$

and therefore the scalar product yields:

$$\vec{a}\cdot\vec{b} = a_\mu b^\mu = g'_{\mu\nu} a^\nu b^\mu = a^+ b^- + a^- b^+ - a^1 b^1 - a^2 b^2. \tag{A.9}$$

An important feature of the light-cone coordinates is the fact that they do not mix under Lorentz boosts in the x^3 direction. Whereas in the Cartesian system a boost of rapidity η has the following form:

$$x'^0 = x^0 \cosh\eta - x^3 \sinh\eta \tag{A.10}$$

$$x'^3 = x^3 \cosh\eta - x^0 \sinh\eta, \tag{A.11}$$

in the light-cone system such boost is succinctly expressed as a scaling transformation:

$$x'^+ = e^{-\eta} x^+ \tag{A.12}$$

$$x'^- = e^{\eta} x^-, \tag{A.13}$$

which leaves the product x^+x^- invariant[1]. This yields great simplification when describing highly boosted systems, e.g. nuclei moving at nearly the speed of light. Another notable feature of the light-cone coordinates is given by their derivatives:

$$\frac{\partial}{\partial x^+} = \frac{1}{\sqrt{2}}\left(\frac{\partial}{\partial x^0} + \frac{\partial}{\partial x^3}\right) \tag{A.14}$$

$$\frac{\partial}{\partial x^-} = \frac{1}{\sqrt{2}}\left(\frac{\partial}{\partial x^0} - \frac{\partial}{\partial x^3}\right). \tag{A.15}$$

Let us take $\frac{\partial}{\partial x^+}$ for instance and perform a Lorentz boost in the x^3 direction. We obtain:

$$\begin{aligned}\frac{\partial}{\partial x'^+} &= \frac{1}{\sqrt{2}}\left(\frac{\partial}{\partial x'^0} + \frac{\partial}{\partial x'^3}\right) = \frac{1}{\sqrt{2}}\left(\frac{\partial x^0}{\partial x'^0}\frac{\partial}{\partial x^0} + \frac{\partial x^3}{\partial x'^0}\frac{\partial}{\partial x^3} + \frac{\partial x^0}{\partial x'^3}\frac{\partial}{\partial x^0} + \frac{\partial x^3}{\partial x'^3}\frac{\partial}{\partial x^3}\right)\\ &= (\cosh\eta + \sinh\eta)\frac{1}{\sqrt{2}}\left(\frac{\partial}{\partial x^0} + \frac{\partial}{\partial x^3}\right) = e^{\eta}\frac{\partial}{\partial x^+},\end{aligned} \tag{A.16}$$

which shows that it transforms like the $-$ component of a 4-vector. The reciprocal is also true, $\frac{\partial}{\partial x'^-} = e^{-\eta}\frac{\partial}{\partial x^-}$. Due to this feature of light-cone coordinates, we adopt the notation $\partial^\pm \equiv \partial/\partial x^\mp$.

In the first stage of the calculations featured in this report (part III) we apply light-cone coordinates in the description of a nucleus moving at the speed of light in the positive x^3 direction. Such system is sitting at $x^- = 0$ with x^+ increasing proportionally to the temporal coordinate x^0, which justifies why in this framework x^+ is typically referred to as 'light-cone time'. Later on, when we consider two colliding nuclei, it is useful to use a different system known as 'comoving' coordinates.

---

[1] This is simply the light-cone form of the familiar Lorentz invariance: $x^+x^- = \big((x^0)^2 - (x^3)^2\big)/2$.

Appendix B

Comoving coordinates

High energy collisions are almost invariant under boosts in the longitudinal direction, which motivates the equations of motion derived in Chapter 6.2 (originally in [92]) being independent of rapidity $\eta = \frac{1}{2}\log(x^+/x^-)$[1]. Such invariance makes it convenient to use the comoving coordinate system (sometimes referred to as Bjorken coordinates), defined by the Lorentz-invariant quantities known as proper time τ and rapidity η:

$$\tau = \sqrt{(x^0)^2 - (x^3)^2} = \sqrt{2x^+x^-} \qquad \eta = \frac{1}{2}\log\left(\frac{x^0 + x^3}{x^0 - x^3}\right) = \frac{1}{2}\log\left(\frac{x^+}{x^-}\right). \tag{B.1}$$

Inverting the previous expressions:

$$x^+ = \frac{\tau}{\sqrt{2}}e^{\eta} \qquad x^- = \frac{\tau}{\sqrt{2}}e^{-\eta} \tag{B.2}$$

$$x^0 = \tau\cosh\eta \qquad x^3 = \tau\sinh\eta. \tag{B.3}$$

By differentiation of these formulas we obtain the base vectors of the new coordinate system:

$$\vec{r} = x^+\hat{e}_+ + x^-\hat{e}_- \doteq \tau\vec{e}_\tau + \eta\vec{e}_\eta \tag{B.4}$$

$$\vec{e}_\tau = \frac{\partial\vec{r}}{\partial\tau} = \frac{x^+}{\tau}\hat{e}_+ + \frac{x^-}{\tau}\hat{e}_- \tag{B.5}$$

$$\vec{e}_\eta = \frac{\partial\vec{r}}{\partial\eta} = x^+\hat{e}_+ - x^-\hat{e}_-. \tag{B.6}$$

Note that, in general, curvilinear coordinate systems do not require the natural basis vectors to be of unit length. The corresponding scale factors are $h_\tau = 1$ and $h_\eta = \tau$. By solving the system posed by the previous expressions for $\hat{e}_+$ and $\hat{e}_-$ and substituting:

$$\vec{A} \doteq A^\tau\vec{e}_\tau + A^\eta\vec{e}_\eta \doteq A^+\hat{e}_+ + A^-\hat{e}_- = A^+\left(\frac{x^-}{\tau}(\vec{e}_\tau + \vec{e}_\eta/\tau)\right) + A^-\left(\frac{x^+}{\tau}(\vec{e}_\tau - \vec{e}_\eta/\tau)\right), \tag{B.7}$$

we can obtain the components of general 4-vectors in the comoving coordinate system:

$$A^\tau = \frac{x^-A^+ + x^+A^-}{\tau} \tag{B.8}$$

$$A^\eta = \frac{x^-A^+ - x^+A^-}{\tau^2}. \tag{B.9}$$

Using matrix notation this transformation yields:

$$\begin{pmatrix} A^\tau \\ A^\eta \end{pmatrix} = \begin{pmatrix} \frac{x^-}{\tau} & \frac{x^+}{\tau} \\ \frac{x^-}{\tau^2} & -\frac{x^+}{\tau^2} \end{pmatrix} \begin{pmatrix} A^+ \\ A^- \end{pmatrix} \equiv (S)\begin{pmatrix} A^+ \\ A^- \end{pmatrix}, \tag{B.10}$$

---

[1] In Chapter 6.2 this property emerges as a consequence of our ansatz for the longitudinal structure of the valence quarks inside nuclei

and the metric tensor looks like:

$$g'_{\mu,\nu} = \left(S^{-1}\right)^{\mathrm{T}} g_{\mu,\nu} \left(S^{-1}\right) = \begin{pmatrix} \frac{x^+}{\tau} & \frac{x^-}{\tau} \\ x^+ & -x^- \end{pmatrix} \begin{pmatrix} 0 & 1 \\ 1 & 0 \end{pmatrix} \begin{pmatrix} \frac{x^+}{\tau} & x^+ \\ \frac{x^-}{\tau} & -x^- \end{pmatrix} = \begin{pmatrix} 1 & 0 \\ 0 & -\tau^2 \end{pmatrix}. \tag{B.11}$$

As with the light-cone system, the transverse coordinates are not affected by this transformation and therefore the complete metric reads $g'_{\mu\nu} = \mathrm{diag}(1, -\tau^2, -1, -1)$. Remarkably, the fact that this coordinate system is characterized by a non-trivial scale factor ($h_\eta = \tau$) has an effect over the definition of differential operators such as the divergence of a vector A^μ. The general formula for a curvilinear coordinate system (u_1, u_2, u_3) reads:

$$\nabla \cdot A = \partial_\mu A^\mu = \frac{1}{h_1 h_2 h_3} \left[\frac{\partial}{\partial u_1}(h_2 h_3 A_1) + \frac{\partial}{\partial u_2}(h_1 h_3 A_2) + \frac{\partial}{\partial u_3}(h_1 h_2 A_3) \right], \tag{B.12}$$

where h_1, h_2, h_3 are the respective scale factors of each coordinate. In the comoving system we get:

$$\partial_\mu A^\mu = \frac{1}{\tau} \left(\partial_\tau(\tau A^\tau) + \partial_\eta A^\eta + \partial_i(\tau A^i) \right), \tag{B.13}$$

with $i = 1, 2$. It is also useful to know the relation between simple derivatives in the light-cone and comoving systems:

$$\partial^\pm = \frac{\partial \tau}{\partial x^\mp} \frac{\partial}{\partial \tau} + \frac{\partial \eta}{\partial x^\mp} \frac{\partial}{\partial \eta} = \frac{x^\pm}{\tau} \frac{\partial}{\partial \tau} \mp \frac{x^\pm}{\tau^2} \frac{\partial}{\partial \eta} = \frac{x^\pm}{\tau} \partial_\tau \mp \frac{x^\pm}{\tau^2} \partial_\eta. \tag{B.14}$$

Note the position of the η index after the last equality sign. While rising or lowering the τ index does not introduce new factors, we must be careful when doing the same for η. For example, if we want to express the previous relation using matrix notation:

$$\begin{pmatrix} \partial^+ \\ \partial^- \end{pmatrix} = \left(S^{-1}\right) \begin{pmatrix} \partial^\tau \\ \partial^\eta \end{pmatrix} = \begin{pmatrix} \frac{x^+}{\tau} & x^+ \\ \frac{x^-}{\tau} & -x^- \end{pmatrix} \begin{pmatrix} \partial^\tau \\ \partial^\eta \end{pmatrix}, \tag{B.15}$$

in order to recover the previous notation we must take into account that $\partial^\eta = -\partial_\eta / \tau^2$. The inverse relations read:

$$\partial_\tau = \frac{x^+ \partial^- + x^- \partial^+}{\tau} = \sqrt{\frac{x^+}{2x^-}} \partial^- + \sqrt{\frac{x^-}{2x^+}} \partial^+ \tag{B.16}$$

$$\partial_\eta = x^+ \partial^- - x^- \partial^+. \tag{B.17}$$

In these expressions we can observe that ∂_τ and ∂_η are Lorentz-invariant operators, which is an important feature of this coordinate system.

Appendix C

Kinematics of DIS

The physical picture underlying a DIS process depends on the reference frame we choose to work in. We will focus on the Infinite Momentum Frame (IMF), in which the parton model (discussed in Section 1.3) is formulated. In the IMF the proton moves with a very large longitudinal momentum P in the positive x^3 direction. In cartesian coordinates its 4-momentum reads:

$$P^\mu \approx (P,\, 0,\, 0,\, P), \tag{C.1}$$

where we are neglecting the proton mass m. For the 4-momentum corresponding to the exchanged photon we have:

$$q^\mu = (q^0,\, q^1,\, q^2,\, 0). \tag{C.2}$$

Note that, although sometimes we explicitly refer to an electron-proton scattering, the following discussion is applicable to any case of DIS. These processes are described in terms of the following Lorentz invariants:

$$Q^2 = -q^2 \qquad\qquad x = \frac{Q^2}{2P\cdot q}. \tag{C.3}$$

With the previous definitions, we have $Q^2/x = 2P\cdot q = 2Pq^0$ and therefore:

$$q^0 \approx \frac{Q^2}{2xP}. \tag{C.4}$$

From this expression we can infer that $q^0 \ll Q$ and thus $Q^2 \approx q_\perp^2$. Therefore, from the uncertainty principle we are able to estimate the transverse resolution λ of the DIS probe as:

$$x_\perp \approx \frac{1}{q_\perp} \equiv \frac{1}{Q} \equiv \lambda. \tag{C.5}$$

As in a DIS process we have $Q^2 \gg m$, from the previous expression we infer that the photon can resolve very short distances inside the proton; this allows it to interact with its fundamental degrees of freedom. In the parton model of DIS we assume that said interaction only affects a single parton, and that it is incoherent (i.e. independent of the spectators partons). In order to justify this assumption we need to analyze the different time scales involved in a DIS process. From Eq. (C.4) we can estimate the interaction time between the DIS probe and the target as:

$$t_{\rm DIS} \approx \frac{1}{q^0} \approx \frac{2xP}{Q^2}. \tag{C.6}$$

Let us compare Eq. (C.6) with the typical time scale at which partons interact with each other, $t_{\rm p}$. We can estimate this quantity by performing a boost from the rest frame of the proton, where $(t_{\rm p})_{\rm RF} \sim 1/\Lambda_{\rm QCD}$, to the IMF:

$$t_{\rm p} \approx \frac{1}{\Lambda_{\rm QCD}}\frac{P}{m}. \tag{C.7}$$

The Lorentz factor corresponding to this transformation is P/m, where m is the proton mass. From the DIS condition $Q^2 \gg m$ we can infer that $x\Lambda_{\text{QCD}} m \leq \Lambda_{\text{QCD}} m \ll Q^2$ and therefore:

$$t_{\text{DIS}} \ll t_{\text{p}}. \tag{C.8}$$

This expression tells us that the DIS probe is not sensitive to the interactions of the constituents of the target (in the *naive* parton model). Eq. (C.6) is not, however, the quantity that we identify with the *time resolution* Δt in this report. Rather, we prefer to use a time scale that we can directly compare to the lifetimes of partonic fluctuations inside the proton. We compute this quantity in its rest frame, where:

$$P^\mu = (m, 0, 0, 0) \qquad q^\mu = (q^0, 0, 0, q^3), \tag{C.9}$$

and:

$$q^0 = \frac{Q^2}{2xm}. \tag{C.10}$$

From the DIS condition we can see that $q^0 \gg Q$. Now, from the definition of Q^2:

$$(q^3)^2 - (q^0)^2 = Q^2 \geq 0. \tag{C.11}$$

These expressions pose a hierarchy of scales $q^3 \geq q^0 \gg Q$ that suggests that $q^3 \approx q^0$. This situation is specially suitable for the use of light-cone coordinates (introduced in Appendix A):

$$q^+ = \frac{q^0 + q^3}{\sqrt{2}} \approx \sqrt{2} q^0 \tag{C.12}$$

$$q^- = \frac{q^0 - q^3}{\sqrt{2}}. \tag{C.13}$$

In order to estimate q^-, we use the fact that $2q^+q^- = (q^0)^2 - (q^3)^2 = -Q^2$ to compute:

$$q^- = \frac{1}{q^+} q^+ q^- = -\frac{1}{2q^+} Q^2 \approx -\frac{Q^2}{2\sqrt{2} q^0} = \frac{xm}{\sqrt{2}}. \tag{C.14}$$

Now, from the uncertainty principle (which in light-cone coordinates reads $x^\pm p^\mp \geq 1$), we can estimate the light-cone time resolution of the probe as:

$$x^+ \approx \frac{1}{q^-} \approx \frac{\sqrt{2}}{mx}. \tag{C.15}$$

This quantity is usually referred to as *Ioffe time* in the literature. In our report we identify it as a temporal resolution $\Delta t \sim 1/x$, as it provides the estimate lifetimes of the partonic fluctuations to which the DIS probe is sensitive.

Let us finish this discussion by pointing out a straightforward relation between our DIS invariants Eq. (C.3). By computing the squared center-of-mass energy of the photon-proton reaction:

$$s = (P + q)^2 = 2P \cdot q + q^2 + m^2 = 2P \cdot q - Q^2 + m^2, \tag{C.16}$$

we see that Bjorken-x can be rewritten as:

$$x = \frac{Q^2}{s + Q^2 - m^2}, \tag{C.17}$$

which justifies the identification of the small-x regime with large energies.

Appendix D

Derivation of the Wilson Line

In order to solve Eq. (6.21) we consider a path in the x^- coordinate defined as a curve $\gamma(x^-)$ that goes from an initial point x_0^- to x^-:

$$\frac{\partial}{\partial \gamma(x^-)}\Omega(\gamma(x^-), x^+, x_\perp) = ig\tilde{A}^+(\gamma(x^-), x_\perp)\Omega(\gamma(x^-), x^+, x_\perp). \tag{D.1}$$

We rename this path as $z_1 \equiv \gamma(x^-)$ and integrate:

$$\begin{aligned}\int_{x_0^-}^{x^-} dz_1^- \frac{\partial}{\partial z_1^-}\Omega(z_1^-, x^+, x_\perp) &= ig\int_{x_0^-}^{x^-} dz_1^- \tilde{A}^+(z_1^-, x_\perp)\Omega(z_1^-, x^+, x_\perp)\\ \Omega(x^-, x^+, x_\perp) &= 1 + ig\int_{x_0^-}^{x^-} dz_1^- \tilde{A}^+(z_1^-, x_\perp)\Omega(z_1^-, x^+, x_\perp),\end{aligned} \tag{D.2}$$

where we take the initial point x_0^- so $\Omega(x_0^-, x^+, x_\perp) = 1$. This equation defines an iterative process that starts by substituting $\Omega(z_1^-, x^+, x_\perp)$:

$$\Omega(x^-, x^+, x_\perp) = 1 + ig\int_{x_0^-}^{x^-} dz_1^- \tilde{A}^+(z_1^-, x_\perp) + (ig)^2\int_{x_0^-}^{z_1^-} dz_1^- dz_2^- \tilde{A}^+(z_1^-, x_\perp)\tilde{A}^+(z_2^-, x_\perp)\Omega(z_2^-, x^+, x_\perp), \tag{D.3}$$

where z_2^- defines a new path that goes from x_0^- to z_1^-. Substituting $\Omega(z_2^-, x^+, x_\perp)$ we get:

$$\begin{aligned}\Omega(x^-, x^+, x_\perp) = 1 &+ ig\int_{x_0^-}^{x^-} dz_1^- \tilde{A}^+(z_1^-, x_\perp) + (ig)^2\int_{x_0^-}^{z_1^-} dz_1^- dz_2^- \tilde{A}^+(z_1^-, x_\perp)\tilde{A}^+(z_2^-, x_\perp)\\ &+ (ig)^3\int_{x_0^-}^{z_1^-} dz_1^- dz_2^- \tilde{A}^+(z_1^-, x_\perp)\tilde{A}^+(z_2^-, x_\perp)\int_{x_0^-}^{z_2^-} dz_3^- \tilde{A}^+(z_3^-, x_\perp)\Omega(z_3^-, x^+, x_\perp),\end{aligned} \tag{D.4}$$

and so on. Repeating the process, we obtain:

$$\Omega(x^-, x^+, x_\perp) \equiv \Theta(x^+, x_\perp)\, U(x^-, x_\perp), \tag{D.5}$$

where:

$$U(x^-, x_\perp) = \sum_{n=0}^{\infty}\left[(ig)^n \int_{x^- \geq z_1^- \geq z_2^- \geq \ldots \geq z_{n-1}^- \geq x_0^-} dz_1^- dz_2^- \ldots dz_n^- \tilde{A}^+(z_1^-, x_\perp)\tilde{A}^+(z_2^-, x_\perp)\ldots\tilde{A}^+(z_n^-, x_\perp)\right]. \tag{D.6}$$

We have factorized the x^+ dependence (and some of the $x_\perp$ dependence) into an arbitrary function Θ that does not participate in the previously described iterative process (as this factor cancels out in Eq. (6.21)). We can express U more succinctly by using the fact that in Eq. (D.6) the fields $\tilde{A}^+$ are arranged in a decreasing 'path order' from z_1^- to z_n^-. We introduce the path ordering function

P^-, that rearranges the fields from left to right according to decreasing values of x^-. One of the properties of this function will allow us to rewrite Eq. (D.6) in a more convenient way:

$$\int_{x^- \geq z_1^- \geq z_2^- \geq x_0^-} dz_1^- dz_2^- \tilde{A}^+(z_1^-)\tilde{A}^+(z_2^-) = \frac{1}{2}\int_{x_0^-}^{x^-} dz_1^- \int_{x_0^-}^{x^-} dz_2^- \mathrm{P}^- \left(\tilde{A}^+(z_1^-)\tilde{A}^+(z_2^-)\right), \tag{D.7}$$

as in the right side of the equation there are two cases that contribute equally to the integration ($z_1^- \geq z_2^-$ and $z_2^- \geq z_1^-$). Extending this to the x^--ordered product of n fields featured in Eq. (D.6) we get:

$$\begin{aligned} U(x^-, x_\perp) &= \sum_{n=0}^{\infty} \left[\frac{(ig)^n}{n!} \int_{x_0^-}^{x^-} dz_1^- dz_2^- ... dz_n^- \mathrm{P}^- \left(\tilde{A}^+(z_1^-, x_\perp)\tilde{A}^+(z_2^-, x_\perp)...\tilde{A}^+(z_n^-, x_\perp)\right)\right] \\ &= \sum_{n=0}^{\infty} \frac{(ig)^n}{n!} \mathrm{P}^- \left[\left(\int_{x_0^-}^{x^-} dz^- \tilde{A}^+(z^-, x_\perp) \right)^n \right] \\ &= \mathrm{P}^- \exp\left\{ ig \int_{x_0^-}^{x^-} dz^- \tilde{A}^+(z^-, x_\perp) \right\}, \end{aligned} \tag{D.8}$$

where we have defined the path-ordered exponential. The final form of the solution is:

$$\Omega(x^+, x^-, x_\perp) = \Theta(x^+, x_\perp)\, \mathrm{P}^- \exp\left\{ ig \int_{x_0^-}^{x^-} dz^- \tilde{A}^+(z^-, x_\perp) \right\} \equiv \Theta(x^+, x_\perp)\, U(x^-, x_\perp). \tag{D.9}$$

$U(x^-, x_\perp)$ is the $SU(N_c)$ group element called Wilson line. The initial integration point x_0^- is arbitrary (it could be $x_0^- > x^-$, in which case P^- would stand for a decreasing ordering in x^-) until we establish the condition for gauge fixing. However, residual gauge freedom allows us to choose $\Theta = 1$, resulting in $\Omega(x^+, x^-, x_\perp) = U(x^-, x_\perp)$.

Appendix E

Transverse differentiation of Wilson lines

As a cross-check, in this appendix we explicitly perform the calculation of the covariant gauge field, which includes a derivative of the Wilson line U on the transverse plane: $A^i(x^-,x_\perp) = i/g\, U^\dagger(x^-,x_\perp)\partial^i U(x^-,x_\perp)$. In order to do this calculation it is convenient to expand U as:

$$\begin{aligned}\partial^i U(x^-,x_\perp) &= \partial^i\left[\sum_{n=0}^{\infty}(ig)^n\int_{x_0^-}^{x^-}dz_1^-\int_{x_0^-}^{z_1^-}dz_2^-\ldots\int_{x_0^-}^{z_{n-1}^-}dz_n^-\tilde{A}_1\tilde{A}_2\ldots\tilde{A}_n\right]\\ &= \sum_{n=1}^{\infty}(ig)^n\int_{x_0^-}^{x^-}dz_1^-\int_{x_0^-}^{z_1^-}dz_2^-\ldots\int_{x_0^-}^{z_{n-1}^-}dz_n^-\sum_{m=1}^{n}(\tilde{A}_1\ldots\partial^i\tilde{A}_m\ldots\tilde{A}_n), \qquad \text{(E.1)}\end{aligned}$$

where we have defined $\tilde{A}_i\equiv\tilde{A}(z_i,x_\perp)=\tilde{A}^{a_i}\tilde{\rho}^{a_i}$. Let us write down a few terms of this double sum:

$$\begin{aligned}&0+(ig)\int_{x_0^-}^{x^-}dz_1^-\partial^i\tilde{A}_1+(ig)^2\left(\int_{x_0^-}^{x^-}dz_1^-\int_{x_0^-}^{z_1^-}dz_2^-(\partial^i\tilde{A}_1\tilde{A}_2+\tilde{A}_1\partial^i\tilde{A}_2)\right)\\ &+(ig)^3\left(\int_{x_0^-}^{x^-}dz_1^-\int_{x_0^-}^{z_1^-}dz_2^-\int_{x_0^-}^{z_2^-}dz_3^-(\partial^i\tilde{A}_1\tilde{A}_2\tilde{A}_3+\tilde{A}_1\partial^i\tilde{A}_2\tilde{A}_3+\tilde{A}_1\tilde{A}_2\partial^i\tilde{A}_3)\right)+\ldots \qquad \text{(E.2)}\end{aligned}$$

From this expression it is easy to see that, in general, the sum of all terms proportional to $\partial^i A_m$ takes the following form:

$$\int_{x_0^-}^{x^-}dz_1^-\tilde{A}_1\int_{x_0^-}^{z_1^-}dz_2^-\tilde{A}_2\ldots\int_{x_0^-}^{z_{m-1}^-}dz_m^-\partial^i\tilde{A}_m\left(\sum_{n=m}^{\infty}(ig)^n\int_{x_0^-}^{z_m^-}dz_{m+1}^-\tilde{A}_{m+1}\ldots\int_{x_0^-}^{z_{n-1}^-}dz_n^-\tilde{A}_n\right), \qquad \text{(E.3)}$$

which allows us to reorganize Eq. (E.1) as:

$$\partial^i U(x^-,x_\perp)=\sum_{m=1}^{\infty}\int_{x_0^-}^{x^-}dz_1^-\tilde{A}_1\ldots\int_{x_0^-}^{z_{m-1}^-}dz_m^-\partial^i\tilde{A}_m\left(\sum_{n=m}^{\infty}(ig)^n\int_{x_0^-}^{z_m^-}dz_{m+1}^-\tilde{A}_{m+1}\ldots\int_{x_0^-}^{z_{n-1}^-}dz_n^-\tilde{A}_n\right), \quad \text{(E.4)}$$

which can be expressed as a function of a new Wilson line by using the path ordering function P^-:

$$=\sum_{m=1}^{\infty}\int_{x_0^-}^{x^-}dz_1^-\tilde{A}_1\ldots\int_{x_0^-}^{z_{m-1}^-}dz_m^-\partial^i\tilde{A}_m\left(\sum_{n=m}^{\infty}\frac{(ig)^n}{(n-m)!}\int_{x_0^-}^{z_m^-}dz_{m+1}^-\ldots dz_n^-\mathrm{P}^-(\tilde{A}_{m+1}\ldots\tilde{A}_n)\right) \qquad \text{(E.5)}$$

and redefining the index of the inner summation as $n'=n-m$:

$$\begin{aligned}&=\sum_{m=1}^{\infty}\int_{x_0^-}^{x^-}dz_1^-\tilde{A}_1\ldots\int_{x_0^-}^{z_{m-1}^-}dz_m^-\partial^i\tilde{A}_m(ig)^m\left(\sum_{n'=0}^{\infty}\frac{(ig)^{n'}}{n'!}\int_{x_0^-}^{z_m^-}dz_1^-\ldots dz_{n'}^-P^-(\tilde{A}_1\ldots\tilde{A}_{n'})\right)\\ &=\sum_{m=1}^{\infty}(ig)^m\int_{x_0^-}^{x^-}dz_1^-\tilde{A}_1\int_{x_0^-}^{z_1^-}dz_2^-\tilde{A}_2\ldots\int_{x_0^-}^{z_{m-1}^-}dz_m^-\partial^i\tilde{A}_mU(z_m^-,x_\perp). \qquad \text{(E.6)}\end{aligned}$$

Now, redefining $m'=m-1$:

$$= \sum_{m'=0}^{\infty} (ig)^{m'} \int_{x_0^-}^{x^-} dz_1^- \tilde{A}_1 ... \int_{x_0^-}^{z^-_{m'-1}} dz^-_{m'} \tilde{A}_{m'} \int_{x_0^-}^{z^-_{m'}} dz^- (ig) \partial^i \tilde{A}\, U(z^-, x_\perp).$$

For simplicity, we also renamed the smallest integration variable z_m^- as z^-. Now, by using a theta function we can redefine the upper integration limit of the integration over z^-, as:

$$= \int_{x_0^-}^{x^-} dz^- \left[\sum_{m'=0}^{\infty} (ig)^{m'} \int_{x_0^-}^{x^-} dz_1^- \tilde{A}_1 ... \int_{x_0^-}^{z^-_{m'-1}} dz^-_{m'} \tilde{A}_{m'} (ig) \theta(z^-_{m'} - z^-) \partial^i \tilde{A}\, U(z^-, x_\perp) \right]. \tag{E.7}$$

In this expression it is apparent that the integral has support only for $z^-_{m'}$ greater or equal to z^-, which takes values between x^- and x_0^-. As every other integration variable is greater or equal to $z^-_{m'}$ due to path ordering, we can lose this instrumental theta function by modifying the lower integration limit of the nested integrals:

$$\begin{aligned}
&= \int_{x_0^-}^{x^-} dz^- \left[\sum_{j=0}^{\infty} (ig)^j \int_{z^-}^{x^-} dz_1^- \tilde{A}_1 ... \int_{z^-}^{z^-_{j-1}} dz_j^- \tilde{A}_j \right] ig\, \partial^i \tilde{A}(z^-)\, U(z^-, x_\perp) \\
&= \int_{x_0^-}^{x^-} dz^- \left[\sum_{j=0}^{\infty} \frac{(ig)^j}{j!} \int_{z^-}^{x^-} dz_1^- .. dz_j^- \mathrm{P}^-(\tilde{A}_1 ... \tilde{A}_j) \right] ig\, \partial^i \tilde{A}(z^-)\, U(z^-, x_\perp) \\
&= ig \int_{x_0^-}^{x^-} dz^- U(x^-, z^-; x_\perp) \partial^i \tilde{A}(z^-)\, U(z^-, x_0^-; x_\perp).
\end{aligned} \tag{E.8}$$

Substituting the previous result in the covariant gauge field formula, we get:

$$\begin{aligned}
A^i(x^-, x_\perp) = \frac{i}{g} U^\dagger(x^-, x_\perp) \partial^i U(x^-, x_\perp) &= - \int_{x_0^-}^{x^-} dz^- U^\dagger(x^-, x_0^-; x_\perp)\, U(x^-, z^-; x_\perp) \partial^i \tilde{A}(z^-)\, U(z^-, x_0^-; x_\perp) \\
&= - \int_{x_0^-}^{x^-} dz^- U^\dagger(z^-, x_0^-; x_\perp) \partial^i \tilde{A}(z^-)\, U(z^-, x_0^-; x_\perp) \\
&= \int_{x_0^-}^{x^-} dz^- U^\dagger(z^-, x_0^-; x_\perp) \frac{\partial^i \tilde{\rho}(z^-, x_\perp)}{\nabla_\perp^2} U(z^-, x_0^-; x_\perp).
\end{aligned} \tag{E.9}$$

In the omitted intermediate step we have used $U^\dagger(a, b; x_\perp) = U(b, a; x_\perp)$ and the fact that, due to path ordering, we can 'glue' Wilson lines together as $U(b, c; x_\perp) U(a, b; x_\perp) = U(a, c; x_\perp)$.

Appendix F

Calculation of chromo-electric and -magnetic fields

Starting from the components of $T^{\mu\nu}$ expressed as functions of E^i and B^k, the next step is to calculate these fields at $\tau = 0^+$. We start with the transverse components of the chromo-electric field E^i (with $i = 1, 2$).

$$E^i = -F^{0i} = -\frac{\partial x^0}{\partial x^\sigma}\frac{\partial x^i}{\partial x^\rho}F^{\sigma\rho} = -\left(\frac{\partial x^0}{\partial x^+}F^{+i} + \frac{\partial x^0}{\partial x^-}F^{-i}\right) = -\frac{1}{\sqrt{2}}\left(x^+\left(\frac{1}{\tau}\partial_\tau\alpha^i - [D^i,\alpha]\right)\right.$$
$$\left. + x^-\left(\frac{1}{\tau}\partial_\tau\alpha^i + [D^i,\alpha]\right)\right) = -\cosh{(\eta)}\partial_\tau\alpha^i + \left(\frac{x^+ - x^-}{\sqrt{2}}\right)[D^i,\alpha].$$

Now, taking the limit $x^\pm \to 0$:

$$E^i = -\cosh{(\eta)}\partial_\tau\big(\alpha_1^i(x_\perp) + \alpha_2^i(x_\perp)\big) - \left(\frac{x^+ - x^-}{2\sqrt{2}}\right)\left[D^i, ig[\alpha_{1j}(x_\perp), \alpha_2^j(x_\perp)]\right] = 0.$$

As for the longitudinal field E^z:

$$E^z = -F^{0z} = -\frac{\partial x^0}{\partial x^\sigma}\frac{\partial x^z}{\partial x^\rho}F^{\sigma\rho} = -\left(\frac{\partial x^0}{\partial x^+}\frac{\partial x^z}{\partial x^-}F^{+-} + \frac{\partial x^0}{\partial x^-}\frac{\partial x^z}{\partial x^+}F^{-+}\right) = F^{+-} = -2\alpha - \tau\partial_\tau\alpha.$$

Taking the limit $x^\pm \to 0$:

$$E^z = ig\left[\alpha_{1\,i}(x_\perp), \alpha_2^i(x_\perp)\right] = -ig\left[\alpha_1^i(x_\perp), \alpha_2^i(x_\perp)\right] = -2A^\eta. \tag{F.1}$$

Now we focus on the chromo-magnetic field. Its transverse components B^k (with $k = 1, 2$) read:

$$B^k = \epsilon^{izk}F^{iz} = \epsilon^{izk}\frac{\partial x^i}{\partial x^\sigma}\frac{\partial x^z}{\partial x^\rho}F^{\sigma\rho} = \epsilon^{izk}\left(\frac{\partial x^z}{\partial x^+}F^{i+} + \frac{\partial x^z}{\partial x^-}F^{i-}\right) = \frac{\epsilon^{izk}}{\sqrt{2}}\left(F^{i+} - F^{i-}\right)$$
$$= \frac{\epsilon^{izk}}{\sqrt{2}}\left(x^+\left(\frac{1}{\tau}\partial_\tau\alpha^i - [D^i,\alpha]\right) - x^-\left(\frac{1}{\tau}\partial_\tau\alpha^i + [D^i,\alpha]\right)\right) = \epsilon^{izk}\left(\sinh{(\eta)}\partial_\tau\alpha^i - \left(\frac{x^+ + x^-}{\sqrt{2}}\right)[D^i,\alpha]\right).$$

As it was also the case with E^i, this expression vanishes in the limit $x^\pm \to 0$. Finally, for the longitudinal field B_z:

$$B^z = \frac{1}{2}\epsilon^{ijz}F^{ij} = \frac{1}{2}\left(F^{12} - F^{21}\right) = F^{12}.$$

In order to compute this it is preferable to start from F^{ij}:

$$F^{ij} = \partial^i\alpha^j - \partial^j\alpha^i - ig[\alpha^i, \alpha^j].$$

We take the limit $x^\pm \to 0$:

$$F^{ij} = \partial^i(\alpha_1^j + \alpha_2^j) - \partial^j(\alpha_1^i + \alpha_2^i) - ig[\alpha_1^i + \alpha_2^i, \alpha_1^j + \alpha_2^j] = \partial^i\alpha_1^j + \partial^i\alpha_2^j - \partial^j\alpha_1^i - \partial^j\alpha_2^i - ig\left([\alpha_1^i, \alpha_1^j]\right.$$
$$\left. + [\alpha_1^i, \alpha_2^j] - [\alpha_1^j, \alpha_2^i] + [\alpha_2^i, \alpha_2^j]\right) = \cancel{F_1^{ij}} + \cancel{F_2^{ij}} - ig\left(\left[\alpha_1^i, \alpha_2^j\right] - \left[\alpha_1^j, \alpha_2^i\right]\right).$$

And finally:

$$B^z = F^{12} = -ig\epsilon^{ij}\left[\alpha_1^i(x_\perp), \alpha_2^j(x_\perp)\right]. \tag{F.2}$$

Appendix G

Identities relating Wilson line representations

In general, the tensor product of irreducible representations is not necessarily an irreducible representation. In fact, it can be decomposed into the direct sum of irreducible representations as: $R \otimes R' = \oplus_\alpha R_\alpha$. The Clebsch-Gordan coefficients (CG from now on) $C^{R_\alpha}_{\alpha,ij}$ define the transformation between the unitary bases of each representation space:

$$\hat{e}_{ij} = \sum_{R_\alpha} C^{R_\alpha}_{\alpha,ij}\, \hat{e}^{R_\alpha}_\alpha, \tag{G.1}$$

where $\hat{e}_{ij}$, $\hat{e}^{R_\alpha}_\alpha$ are the basis vectors for the tensor-product space $R \otimes R'$ (with each group identified with indices i, j) and the irreducible representations R_α, respectively[1]. This transformation being unitary implies:

$$\left(C^{R_\alpha}_{\alpha,ij}\right)^* C^{R_\beta}_{\beta,ij} = \delta_{R_\alpha R_\beta}\delta_{\alpha\beta}, \tag{G.2}$$

$$\sum_{R_\alpha} \left(C^{R_\alpha}_{\alpha,ij}\right)^* C^{R_\alpha}_{\alpha,kl} = \delta_{ik}\delta_{jl}. \tag{G.3}$$

The latter can be interpreted as a completeness relation of the projectors built as $P^{R_\alpha}_{ijkl} = \left(C^{R_\alpha}_{\alpha,ij}\right)^* C^{R_\alpha}_{\alpha,kl}$ (which gives rise to the Fierz identities). Any vector $\vec{V}$ of the tensor-product space can be expressed in both bases as $\vec{V} = V_{ij}\hat{e}_{ij} = \sum_{R_\alpha} V^{R_\alpha}_\alpha\, \hat{e}^{R_\alpha}_\alpha$. It is straightforward to use the previous properties of the CG coefficients to obtain the following relations between components:

$$V^{R_\alpha}_\alpha = C^{R_\alpha}_{\alpha,ij}\, V_{ij} \tag{G.4}$$

$$V_{ij} = \sum_{R_\alpha} \left(C^{R_\alpha}_{\alpha,ij}\right)^* V^{R_\alpha}_\alpha. \tag{G.5}$$

We can use these expressions to derive the relation between group elements in different representations. In general, group transformations U affect these coefficients as:

$$V_\alpha \to U^{R_\alpha}_{\alpha\beta} V^{R_\alpha}_\beta \tag{G.6}$$

$$V_{ij} \to U^R_{ik} U^{R'}_{jl} V_{kl}. \tag{G.7}$$

If we perform a transformation in both sides of Eq. (G.4) we get:

$$U^{R_\alpha}_{\alpha\beta} V^{R_\alpha}_\beta = C^{R_\alpha}_{\alpha,ij}\, U^R_{ik} U^{R'}_{jl} V_{kl}. \tag{G.8}$$

By writing $V^{R_\alpha}_\beta$ in the $\{k, l\}$ basis (according to Eq. (G.4)) and crossing out the V_{kl} coefficients in both sides we get to the following useful identity:

$$U^{R_\alpha}_{\alpha\beta} C^{R_\alpha}_{\beta,kl} = C^{R_\alpha}_{\alpha,ij}\, U^R_{ik} U^{R'}_{jl}, \tag{G.9}$$

---

[1] Note that this is a generalization of the expansion coefficients of total angular momentum eigenstates in a tensor product basis.

which tells us how CG coefficients transform. Now let us focus on the particular case of the tensorial product of the fundamental and anti-fundamental groups of $SU(N_c)$ (which may represent a quark-antiquark dipole), whose decomposition in irreducible representations yields the sum of the scalar and adjoint representations:

$$3 \otimes 3 \to 8 \oplus 1\,.$$

The corresponding CG coefficients read:

$$C^{(1)}_{ij} = \frac{1}{\sqrt{N_c}}\delta_{ij} \tag{G.10}$$

$$C^{(8)}_{a,ij} = \sqrt{2}\, t^a_{ji}, \tag{G.11}$$

which, along with Eq. (G.9), give us the expression relating the action of $SU(N_c)$ elements in the fundamental, anti-fundamental and adjoint representations. In particular, for Wilson lines we have:

$$\sqrt{2}\, U^{ab} t^b_{lk} = \sqrt{2}\, t^a_{ji} U_{ik} U^*_{jl} = \sqrt{2}\, t^a_{ji} U_{ik} U^\dagger_{lj} \;\;;\;\; U^\dagger t^a U = U^{ab} t^b. \tag{G.12}$$

Now, from the completeness relation Eq. (G.3) we get the following familiar identity:

$$\frac{1}{N_c}\delta_{ij}\delta_{lk} + 2\, t^a_{ij} t^a_{kl} = \delta_{il}\delta_{jk}, \tag{G.13}$$

which is often referred to as 'the' Fierz identity of the $SU(N_c)$ generators. This identity tells us that the $SU(N_c)$ generators in the fundamental representation complemented with the identity matrix form a complete base of the $N_c \times N_c$ matrix space. Multiplying both sides by $U^*_{ii'} U_{jj'} = U^\dagger_{i'i} U_{jj'}$ and applying Eq. (G.12) we get:

$$\frac{1}{N_c} U^\dagger_{i'i}\delta_{ij} U_{jj'}\delta_{lk} + 2\, U^\dagger_{i'i} t^a_{ij} U_{jj'} t^a_{kl} = U^\dagger_{i'i}\delta_{il}\delta_{jk} U_{jj'} \;;\; \frac{1}{N_c}\delta_{i'j'}\delta_{lk} + 2\, U^{ab} t^b_{i'j'} t^a_{kl} = U^\dagger_{i'l} U_{kj'}, \tag{G.14}$$

a Fierz-like identity that relates Wilson lines in the fundamental and adjoint representations. From here we can obtain a closed expression for the components of U^{ab} in terms of the fundamental Wilson lines by multiplying both sides by $t^a_{lk} t^b_{j'i'}$:

$$\frac{1}{N_c} t^a_{lk} t^b_{j'i'} \delta_{i'j'}\delta_{lk} + 2\, t^a_{lk} t^b_{j'i'}\, U^{ab} t^b_{i'j'} t^a_{kl} = t^a_{lk} t^b_{j'i'} U^\dagger_{i'l} U_{kj'} \;;\; \frac{1}{N_c}\cancel{\mathrm{Tr}\{t^a\}\mathrm{Tr}\{t^b\}} + 2\, U^{ab}\mathrm{Tr}\{t^a t^a\}\mathrm{Tr}\{t^b t^b\} = \mathrm{Tr}\{U^\dagger t^a U t^b\}$$

$$U^{ab} = 2\,\mathrm{Tr}\{U^\dagger t^a U t^b\}. \tag{G.15}$$

As a trivial cross-check, we can obtain Eq. (G.12) from here by contracting one of the indices of U^{ab} with a color matrix and applying the Fierz relation Eq. (G.13):

$$\begin{aligned} U^{ab} t^b &= 2\,\mathrm{Tr}\{U^\dagger t^a U t^b\} t^b = 2 U^\dagger_{ij} t^a_{jk} U_{kl} t^b_{li} t^b_{mn} = U^\dagger_{ij} t^a_{jk} U_{kl}\left(\delta_{ln}\delta_{im} - \frac{1}{N_c}\delta_{li}\delta_{mn}\right) \\ &= U^\dagger_{mj} t^a_{jk} U_{kn} - \frac{1}{N_c}\cancel{\mathrm{Tr}\{U^\dagger t^a U\}}\delta_{mn} = U^\dagger t^a U. \end{aligned} \tag{G.16}$$

The last term cancels due to the cyclic property of the trace, which makes it the same as the trace of a single color matrix (which is zero).

Appendix H

Operations involving the 2-D Laplacian Green's function

Throughout the computation of the covariance of $T_0^{\mu\nu}$ we encounter several non-trivial calculations involving the Green's function for the 2-dimensional Laplace operator $G(x_\perp - y_\perp)$. For instance, when computing the correlator of two gluon fields (Eq. (9.1)), we find:

$$\frac{1}{\nabla_x^2}\frac{1}{\nabla_y^2}\left(h(b_\perp)f(x_\perp - y_\perp)\right) = \int dz_\perp^2 du_\perp^2 G(z_\perp - x_\perp)G(u_\perp - y_\perp)h\left(\frac{z_\perp + u_\perp}{2}\right)f(z_\perp - u_\perp). \tag{H.1}$$

This expression includes two undetermined functions, $h(b_\perp)$ and $f(x_\perp - y_\perp)$, introduced in the two-point correlator (Eq. (9.6)) in order to generalize the MV model. However, we do not take these functions as completely general. For $h(b_\perp)$, in addition to overall good analytical properties, we assume a slowly varying behavior over lengths of the order of a length scale $1/m$ or smaller (as proposed in [98]):

$$|h(b_\perp)| \gg m^{-1}|\partial^i h(b_\perp)| \gg m^{-2}|\partial^i\partial^j h(b_\perp)| \gg ... \tag{H.2}$$

where we take m as the infrared regulator. We require that:

$$\frac{1}{Q_s} \ll \frac{1}{m} \ll R_A, \tag{H.3}$$

where R_A is the nuclear radius. Thus, the interaction distances of interest in our calculation obey $r = |x_\perp - y_\perp| \ll m^{-1}$. This requirement, as well as the assumed behavior for $h(b_\perp)$, yield a significant simplification to Eq. (H.1). To see this, we expand $h\left((z_\perp + u_\perp)/2\right)$ around $b_\perp = (x_\perp + y_\perp)/2$:

$$h(b'_\perp) = h(b_\perp) + (b'_\perp - b_\perp)^i \partial^i h(b_\perp) + ... \tag{H.4}$$

where $b'_\perp = (z_\perp + u_\perp)/2$. Cutting the expansion at first order, Eq. (H.1) yields the following terms:

$$\begin{aligned} &h(b_\perp)\int d^2z_\perp d^2u_\perp G(z_\perp - x_\perp)G(u_\perp - y_\perp)f(z_\perp - u_\perp) \\ &+ \partial^i h(b_\perp)\int d^2z_\perp d^2u_\perp G(z_\perp - x_\perp)G(u_\perp - y_\perp)(b'_\perp - b_\perp)^i f(z_\perp - u_\perp). \end{aligned} \tag{H.5}$$

First, we focus on the leading order term:

$$h(b_\perp)\int d^2z_\perp d^2u_\perp G(z_\perp - x_\perp)G(u_\perp - y_\perp)f(z_\perp - u_\perp) \equiv h(b_\perp)L(x_\perp - y_\perp). \tag{H.6}$$

In order to further transform $L(x_\perp - y_\perp)$ we go to momentum space. The Green's function $G(x_\perp - y_\perp)$ admits a simple Fourier representation:

$$G(x_\perp - y_\perp) = -\int \frac{d^2k_\perp}{(2\pi)^2}\frac{e^{ik_\perp\cdot(x_\perp - y_\perp)}}{k^2}, \tag{H.7}$$

which we substitute in $L(x_\perp - y_\perp)$, yielding:

$$L(x_\perp - y_\perp) = \int \frac{d^2z_\perp}{(2\pi)^2}\frac{d^2u_\perp}{(2\pi)^2}\frac{d^2k_\perp}{k^2}\frac{d^2q_\perp}{q^2} e^{ik_\perp\cdot(z_\perp - x_\perp)} e^{iq_\perp\cdot(u_\perp - y_\perp)} f(z_\perp - u_\perp)$$
$$= \int \frac{d^2q_\perp}{(2\pi)^2}\hat{f}(q_\perp)\frac{e^{iq_\perp\cdot r_\perp}}{q^4}. \tag{H.8}$$

In the last step we introduced the inverse Fourier transform of f, defined as:

$$\hat{f}(q_\perp) = \int d^2w_\perp e^{-iq_\perp\cdot w_\perp} f(w_\perp). \tag{H.9}$$

Now we turn to the linear term of the expansion (second term of Eq. (H.5)), which we want to compare with $h(b_\perp)L(r_\perp)$. By performing a simple variable change, it can be written as:

$$\frac{1}{4}\partial^i h(b_\perp)\int d^2v_\perp d^2w_\perp G\left(\frac{v_\perp + w_\perp}{2} - \frac{r_\perp}{2}\right) G\left(\frac{v_\perp - w_\perp}{2} + \frac{r_\perp}{2}\right)\frac{(v_\perp)^i}{2} f(w_\perp), \tag{H.10}$$

where $v_\perp = z_\perp + u_\perp$ and $w_\perp = z_\perp - u_\perp$. Substituting Eq. (H.7) and performing some transformations, we get to:

$$\frac{1}{8}\partial^i h(b_\perp)\int \frac{d^2v_\perp}{(2\pi)^4}\frac{d^2k_\perp}{k^2}\frac{d^2q_\perp}{q^2} e^{i(k_\perp + q_\perp)\cdot v_\perp} e^{-i(k_\perp - q_\perp)\cdot r_\perp}(v_\perp)^i \hat{f}(q_\perp - k_\perp). \tag{H.11}$$

The integration in $v_\perp$ yields a distribution derivative of the Dirac delta function:

$$\int d^2v_\perp e^{i(k_\perp + q_\perp)\cdot v_\perp}(v)^i = -i(2\pi)^2\partial^i\delta(k_\perp + q_\perp). \tag{H.12}$$

Substituting this result in Eq. (H.11) and integrating by parts, we finally obtain:

$$\frac{1}{2}r_\perp^i\partial^i h(b_\perp)\int \frac{d^2q_\perp}{(2\pi)^2}\hat{f}(q_\perp)\frac{e^{iq_\perp\cdot r_\perp}}{q^4} = \frac{1}{2}r_\perp^i\partial^i h(b_\perp)L(r_\perp), \tag{H.13}$$

and thus, Eq. (H.5) yields:

$$\left(h(b_\perp) + \frac{1}{2}r_\perp^i\partial^i h(b_\perp)\right)L(r_\perp) \approx h(b_\perp)L(r_\perp). \tag{H.14}$$

Here we applied the fact that $r_\perp^i\partial^i h(b_\perp) \leq |r_\perp||\vec{\partial}h(b_\perp)| \ll m^{-1}|\vec{\partial}h(b_\perp)| \ll |h(b_\perp)|$. We will take this expression as a good approximation of Eq. (H.1). The next step in the calculation of the two gluon field correlator Eq. (9.1) is the computation of the double derivative:

$$\partial_x^i\partial_y^j\left(h(b_\perp)L(r_\perp)\right) = (\partial_x^i\partial_y^j h)L + (\partial_y^j h)(\partial_x^i L) + (\partial_x^i h)(\partial_y^j L) + h(\partial_x^i\partial_y^j L)$$
$$\approx h(b_\perp)\partial_x^i\partial_y^j L(r_\perp). \tag{H.15}$$

The reasoning behind the last approximate equality follows from the dimension of $L(r_\perp)$, its IR behavior, and the fact that we imposed an infrared cut-off mass scale m. In order to be able to discuss $L(r_\perp)$ in the infrared region we need to assume a certain behavior of $\hat{f}(q_\perp)$ in this regime. We assume $\hat{f}_{\text{IR}} \sim 1$, just like in the MV model, as we do not expect other possible choices of models to differ in that regime. Then, we can safely assume that $L \propto m^{-2}$, which makes the term $(\partial_x^i \partial_y^j h)L$ suppressed with respect to $\partial_x^i \partial_y^j L$ (a dimensionless object). Also, this takes us to $\partial^i L \propto m^{-1}$, making the terms of the form $(\partial^j h)(\partial^i L)$ negligible as well. Thus, we are left with the following double derivative:

$$\partial_x^i \partial_y^j L(r_\perp) = \int \frac{d^2 q_\perp}{(2\pi)^2} \hat{f}(q_\perp) \frac{e^{iq_\perp \cdot r_\perp}}{q^4} q^i q^j. \tag{H.16}$$

From its symmetries and dimension, the previous expression can be parameterized as:

$$\partial_x^i \partial_y^j L(r_\perp) = A(r_\perp)\delta^{ij} + B(r_\perp)\left(\frac{\delta^{ij}}{2} - \frac{r^i r^j}{r^2}\right). \tag{H.17}$$

A priori, this decomposition is not possible when $r \to 0$. However, as it is a symmetric object in i, j, we can make a different parameterization in this limit:

$$\lim_{r\to 0} \partial_x^i \partial_y^j L(r_\perp) = C\delta^{ij}, \tag{H.18}$$

that we can relate to:

$$\partial_x^i \partial_x^j L(r_\perp) = \frac{\partial}{\partial x^i}\left(\frac{\partial}{\partial y^j}\frac{\partial y^j}{\partial r^j}\frac{\partial r^j}{\partial x^j}\right) L(r_\perp) = -\partial_x^i \partial_y^j L(r_\perp). \tag{H.19}$$

Now, taking the limit $r \to 0$:

$$\lim_{r\to 0} \partial_x^i \partial_x^j L(r_\perp) = -\lim_{r\to 0} \partial_x^i \partial_y^j L(r_\perp) = -C\delta^{ij} \tag{H.20}$$

and contracting with δ^{ij}:

$$\delta^{ij} \lim_{r\to 0} \partial_x^i \partial_x^j L(r_\perp) = -2C \equiv \partial_\perp^2 L(0_\perp), \tag{H.21}$$

we have $C = -\frac{1}{2}\partial_\perp^2 L(0_\perp)$, which is the notation we use in the body of the article (the same as in [163]). We can express these coefficients in terms of $\hat{f}(q_\perp)$ by computing the following projections of Eq. (H.16) and Eq. (H.18):

$$A(r_\perp) = \frac{1}{2}\delta^{ij}\partial_x^i \partial_y^j L(r_\perp) = \frac{1}{2}\int \frac{d^2 q_\perp}{(2\pi)^2} \hat{f}(q_\perp) \frac{e^{iq_\perp \cdot r_\perp}}{q^2} \tag{H.22}$$

$$\begin{aligned} B(r_\perp) &= 2\left(\frac{\delta^{ij}}{2} - \frac{r^i r^j}{r^2}\right)\partial_x^i \partial_y^j L(r_\perp) = \int \frac{d^2 q_\perp}{(2\pi)^2} \hat{f}(q_\perp) \frac{e^{iq_\perp \cdot r_\perp}}{q^4} q^i q^j \left(\delta^{ij} - 2\frac{r^i r^j}{r^2}\right) \\ &= \int \frac{d^2 q_\perp}{(2\pi)^2} \hat{f}(q_\perp) \frac{e^{iq_\perp \cdot r_\perp}}{q^4} \left(q^2 - 2\frac{q^i r^i q^j r^j}{r^2}\right) \\ &= \int \frac{d^2 q_\perp}{(2\pi)^2} \hat{f}(q_\perp) \frac{e^{iq\, r\cos\theta}}{q^2} \left(1 - 2\cos^2\theta\right) = -\int \frac{d^2 q_\perp}{(2\pi)^2} \hat{f}(q_\perp) \frac{e^{iq\, r\cos\theta}}{q^2} \cos(2\theta) \end{aligned} \tag{H.23}$$

$$C = \frac{1}{2}\delta^{ij} \lim_{r\to 0} \partial_x^i \partial_y^j L(r_\perp) = \frac{1}{2}\int \frac{d^2 q_\perp}{(2\pi)^2} \hat{f}(q_\perp) \frac{1}{q^2}. \tag{H.24}$$

Note that, as $\lim_{r\to 0} A(r_\perp) = C$ and $\lim_{r\to 0} B(r_\perp) = 0$, this parameterization of $\partial_x^i \partial_y^j L(r_\perp)$ is continuous in r. We can relate C to the factor Γ, defined as:

$$\Gamma(x_\perp - y_\perp) = 2(L(0_\perp) - L(x_\perp - y_\perp)) = 2\int \frac{d^2 q_\perp}{(2\pi)^2} \frac{\hat{f}(q_\perp)}{q^4}(1 - e^{iq_\perp \cdot r_\perp}), \tag{H.25}$$

by taking the limit $r \to 0$:

$$\lim_{r\to 0}\Gamma(x_\perp - y_\perp) = 2\int \frac{d^2q_\perp}{(2\pi)^2}\frac{\hat{f}(q_\perp)}{q^4}\left(-i(q_\perp\cdot r_\perp)+\frac{1}{2}(q_\perp\cdot r_\perp)^2\right) = \frac{r^2}{2}\int \frac{d^2q_\perp}{(2\pi)^2}\frac{\hat{f}(q_\perp)}{q^2}$$
$$= r^2 C = r^2\left(-\frac{1}{2}\partial_\perp^2 L(0_\perp)\right), \quad \text{(H.26)}$$

where we assumed that $\hat{f}(q_\perp) = \hat{f}(|q_\perp|)$.

The MV model

In the specific case where $f(z_\perp - w_\perp) = \delta^2(z_\perp - w_\perp)$, i.e. the MV model, we have $\hat{f}(q_\perp) = 1$ and thus we can explicitly compute our coefficients:

$$A(r_\perp)_{\text{MV}} = -\frac{1}{2}G(r_\perp) \quad \text{(H.27)}$$

$$B(r_\perp)_{\text{MV}} = -\int_0^\infty\int_0^{2\pi}\frac{dq\,d\theta}{(2\pi)^2}\frac{e^{iq\,r\cos\theta}}{q}\cos(2\theta) = \frac{1}{2\pi}\int_0^\infty\frac{dq}{q}J_2(q\,r) = \frac{1}{4\pi} \quad \text{(H.28)}$$

$$C_{\text{MV}} = \frac{1}{4\pi}\int\frac{dq}{q} = -\frac{1}{2}\lim_{r\to 0}G(r_\perp). \quad \text{(H.29)}$$

Both $A(r_\perp)_{\text{MV}}$ and C_{MV} yield an infrared logarithmic divergence, which we deal with by introducing a regularizing mass in the Fourier representation of $G(r_\perp)$:

$$G(r_\perp) = -\int\frac{d^2q_\perp}{(2\pi)^2}\frac{e^{iq_\perp\cdot r_\perp}}{q^2+m^2} = -\frac{1}{2\pi}K_0(m\,r), \quad \text{(H.30)}$$

where K_0 is a modified Bessel function. For simplicity we choose m to be the same mass scale introduced earlier in Eq. (H.2) (although it could be an unrelated infrared scale). In our calculation we will keep only the leading behavior in the $m \to 0$ limit, which is:

$$A(r_\perp)_{\text{MV}} \approx -\frac{1}{4\pi}\left(\ln\left(\frac{mr}{2}\right)+\gamma\right) \approx -\frac{1}{4\pi}\ln\left(\frac{mr}{2}\right), \quad \text{(H.31)}$$

(where γ is the Euler constant) and thus:

$$\partial_x^i\partial_y^j L(r_\perp)_{\text{MV}} \approx \frac{1}{4\pi}\left[-\delta^{ij}\ln\left(\frac{mr}{2}\right)+\left(\frac{\delta^{ij}}{2}-\frac{r^ir^j}{r_\perp^2}\right)\right]. \quad \text{(H.32)}$$

The coefficient C_{MV} corresponds to the UV limit of the previous expression ($r \to 0$):

$$\lim_{r\to 0}\partial_x^i\partial_y^j L(r_\perp)_{\text{MV}} = C_{\text{MV}}\delta^{ij} \approx \frac{\delta^{ij}}{4\pi}\lim_{r\to 0}\left[\ln\left(\frac{2}{mr}\right)\right], \quad \text{(H.33)}$$

and thus:

$$\partial_\perp^2 L(0_\perp)_{\text{MV}} = \frac{1}{4\pi}\lim_{r\to 0}\left[\ln\left(\frac{m^2r^2}{4}\right)\right], \quad \text{(H.34)}$$

which also exhibits a logarithmic divergence. As for Γ, we have:

$$\Gamma(x_\perp - y_\perp)_{\text{MV}} = 2\int \frac{d^2q_\perp}{(2\pi)^2}\frac{1}{(q^2+m^2)^2}(1-e^{iq_\perp\cdot r_\perp}) = \frac{1}{2\pi m^2} - \frac{r}{2\pi m}K_1(mr). \tag{H.35}$$

The leading behavior of the previous expression in the $m\to 0$ yields:

$$\Gamma(x_\perp - y_\perp)_{\text{MV}} \approx -\frac{r^2}{8\pi}\left(\log\left(\frac{m^2r^2}{4}\right) + 2\gamma - 1\right) \approx \frac{r^2}{8\pi}\log\left(\frac{4}{m^2r^2}\right). \tag{H.36}$$

Appendix I

Baryon production models

In this appendix we outline a brief, qualitative description of the hadronization mechanisms considered within the Lund fragmentation model.

Meson production

In the framework of the Lund fragmentation model, meson production is quite simply described in terms of the breaking of a string between two quark/antiquark endpoints. The breaking mechanism is based on the generation of quark-antiquark fluctuations that are put on-shell by the color field between the string endpoints. The concept of quantum tunneling allows us to give a transverse mass $m_\perp$ to these quarks: we say that the quark-antiquark fluctuation *tunnels out* to the classically allowed region by drifting apart in such a way that the potential between them can be transformed into $m_\perp$. The tunneling probability depends on $m_\perp$ and on the string tension κ as:

$$P \sim \exp\left(-\frac{\pi m_\perp^2}{\kappa}\right) \tag{I.1}$$

Where $\kappa \approx 0.2$ GeV^2. Remarkably, this simple picture implies a suppression in the generation of heavy quarks through this mechanism. Strings keep breaking successively until tunneling is no longer energetically favorable and we are left with a variety of color-singlet bound states.

A consistent description of baryon production in the same terms has not been found yet. However, several prescriptions have been developed.

Baryon production: The diquark model

The simplest possible approach. The diquark in a color anti-triplet state is considered to be an effectively fundamental object (just like an ordinary antiquark), and therefore we consider diquark pair production as an additional string breaking mechanism. Baryons are produced by combining diquarks and quarks. A feature of this model is that baryons and antibaryons are produced adjacently arranged along the string, with no meson production in between. This is the key difference with the next production model:

Baryon production: The popcorn model

In this model, which is more general and relatively closer to QCD, we consider quarks to be the only fundamental objects, and therefore only quark-antiquark fluctuations are considered.

Baryon production in the popcorn framework is based on more complicated color constructions. When the string endpoints are quarks with colors r and $\bar{r}$, the breaking of the string by the generation of a $r\bar{r}$ pair in between would lead to the production of two mesons, but within this model we also consider the possibility that the generated pair is, for example, $g\bar{g}$. Then, as $r+g=\bar{b}$, the generation of a new $b\bar{b}$ pair in between would lead to baryon-antibaryon production in the exact same way as in the diquark model (considering the $\bar{g}\bar{b}$, gb pairs as diquarks). Nevertheless, the main difference with the diquark model is the possibility of mesons being produced between baryons and antibaryons, which may happen through an additional fluctuation. The simple popcorn model only allows for one intermediate meson to be produced, but the *advanced* version allows many.

In order to simulate the popcorn model in a Lund fragmentation-based Monte Carlo, we consider the probabilities of generating baryon-antibaryon pairs with $(P(BMB))$ or without $(P(BB))$ an intermediate meson to be related by the following ratio:

$$\frac{P(BMB)}{P(BMB)+P(BB)}=\frac{\lambda}{0.5+\lambda}. \tag{I.2}$$

This ratio is simply the fraction of events in which a meson is produced between the baryon pair. The default value for the λ parameter in the event generator PYTHIA8 is $\lambda=0.5$, meaning that $P(BMB)=P(BB)$. If we make $\lambda=0$ instead, we get $P(BMB)=0$, meaning that no intermediate meson production is allowed; this situation corresponds to the application of the diquark model.

One conclusion of this comparison is that the energy distribution between mesons and baryons in our Monte Carlo simulations is clearly model-dependent, as many more mesons are generated at every event when using the popcorn model with a relatively high λ value. Another example of a model-dependent observable in the outcome of the simulations presented in Chapter 11 is the baryon-antibaryon transverse momentum correlation.

Bibliography

[1] J. L. Albacete, P. Guerrero Rodríguez and Y. Nara, *Phys. Rev.* **D94** (2016)no. 5 054004 [`arXiv:1605.08334 [hep-ph]`].

[2] J. L. Albacete, P. Guerrero-Rodríguez and C. Marquet, *JHEP* **01** (2019) 073 [`arXiv:1808.00795 [hep-ph]`].

[3] P. Guerrero-Rodríguez, `arXiv:1903.11602 [hep-ph]`.

[4] R. K. Ellis, W. J. Stirling and B. R. Webber, *Camb. Monogr. Part. Phys. Nucl. Phys. Cosmol.* **8** (1996) 1.

[5] Y. V. Kovchegov and E. Levin, *Camb. Monogr. Part. Phys. Nucl. Phys. Cosmol.* **33** (2012) 1.

[6] J. Prentki and J. Steinberger, eds., *Proceedings, 14th International Conference on High-Energy Physics (ICHEP 68)*, (Geneva), CERN, CERN, 1968.

[7] J. D. Bjorken, *Phys. Rev.* **179** (Mar, 1969) 1547.

[8] R. P. Feynman, *Phys. Rev. Lett.* **23** (Dec, 1969) 1415.

[9] **H1, ZEUS** collaboration, H. Abramowicz *et. al.*, *Eur. Phys. J.* **C75** (2015)no. 12 580 [`arXiv:1506.06042 [hep-ex]`].

[10] **Particle Data Group** collaboration, M. Tanabashi *et. al.*, *Phys. Rev.* **D98** (2018)no. 3 030001.

[11] F. Caola, S. Forte and J. Rojo, *Nucl. Phys.* **A854** (2011) 32 [`arXiv:1007.5405 [hep-ph]`].

[12] C. D. White and R. S. Thorne, *Phys. Rev.* **D75** (2007) 034005 [`arXiv:hep-ph/0611204 [hep-ph]`].

[13] R. D. Ball, V. Bertone, M. Bonvini, S. Marzani, J. Rojo and L. Rottoli, *Eur. Phys. J.* **C78** (2018)no. 4 321 [`arXiv:1710.05935 [hep-ph]`].

[14] T. Muta, *Foundations of Quantum Chromodynamics.* WORLD SCIENTIFIC, 3rd ed., 2009.

[15] J. C. Collins, *Acta Phys. Polon.* **B34** (2003) 3103 [`arXiv:hep-ph/0304122 [hep-ph]`].

[16] F. Dominguez, C. Marquet, B.-W. Xiao and F. Yuan, *Phys. Rev. D* **83** (May, 2011) 105005.

[17] K. Golec-Biernat and M. Wüsthoff, *Phys. Rev. D* **59** (Nov, 1998) 014017.

[18] L. McLerran and R. Venugopalan, *Phys. Rev. D* **49** (Mar, 1994) 2233.

[19] L. McLerran and R. Venugopalan, *Phys. Rev. D* **49** (Apr, 1994) 3352.

[20] L. McLerran and R. Venugopalan, *Phys. Rev. D* **50** (Aug, 1994) 2225.

[21] J. Jalilian-Marian, A. Kovner, A. Leonidov and H. Weigert, *Nucl. Phys.* **B504** (1997) 415 [`arXiv:hep-ph/9701284 [hep-ph]`].

[22] J.-P. Blaizot, E. Iancu and H. Weigert, *Nuclear Physics A* **713** (2003)no. 3 441 .

[23] K. Rummukainen and H. Weigert, *Nuclear Physics A* **739** (2004)no. 1 183 .

[24] I. Balitsky, *Nuclear Physics B* **463** (1996)no. 1 99 .

[25] Y. V. Kovchegov, *Phys. Rev. D* **61** (Mar, 2000) 074018.

[26] Y. V. Kovchegov, J. Kuokkanen, K. Rummukainen and H. Weigert, *Nucl. Phys.* **A823** (2009) 47 [`arXiv:0812.3238 [hep-ph]`].

[27] T. DeGrand and C. E. Detar, *Lattice methods for quantum chromodynamics.* 2006.

[28] C. Ratti, *Rept. Prog. Phys.* **81** (2018)no. 8 084301 [`arXiv:1804.07810 [hep-lat]`].

[29] D. H. Rischke, *Prog. Part. Nucl. Phys.* **52** (2004) 197 [`arXiv:nucl-th/0305030 [nucl-th]`].

[30] U. W. Heinz, *Nucl. Phys.* **A685** (2001) 414 [`arXiv:hep-ph/0009170 [hep-ph]`].

[31] G. Baym, T. Hatsuda, T. Kojo, P. D. Powell, Y. Song and T. Takatsuka, *Rept. Prog. Phys.* **81** (2018)no. 5 056902 [`arXiv:1707.04966 [astro-ph.HE]`].

[32] J. N. Capdevielle, *Journal of Physics G: Nuclear Physics* **12** (may, 1986) L125.

[33] J. Rafelski and B. Müller, *Phys. Rev. Lett.* **48** (Apr, 1982) 1066.

[34] U. W. Heinz and M. Jacob, `arXiv:nucl-th/0002042 [nucl-th]`.

[35] P. Koch, B. Müller and J. Rafelski, *International Journal of Modern Physics A* **32** (2017)no. 31 1730024 [`arXiv:https://doi.org/10.1142/S0217751X17300241`].

[36] T. Matsui and H. Satz, *Phys. Lett.* **B178** (1986) 416.

[37] R. Granier de Cassagnac, *Nucl. Phys.* **A783** (2007) 293 [`arXiv:nucl-ex/0610003 [nucl-ex]`].

[38] A. Mocsy, P. Petreczky and M. Strickland, *Int. J. Mod. Phys.* **A28** (2013) 1340012 [`arXiv:1302.2180 [hep-ph]`].

[39] **PHENIX** collaboration, K. Adcox *et. al.*, *Phys. Rev. Lett.* **88** (2002) 022301 [`arXiv:nucl-ex/0109003 [nucl-ex]`].

[40] **STAR** collaboration, C. Adler *et. al.*, *Phys. Rev. Lett.* **90** (2003) 082302 [`arXiv:nucl-ex/0210033 [nucl-ex]`].

[41] **ATLAS** collaboration, G. Aad *et. al.*, *Phys. Rev. Lett.* **105** (2010) 252303 [`arXiv:1011.6182 [hep-ex]`].

[42] **CMS** collaboration, S. Chatrchyan *et. al.*, *Phys. Rev.* **C84** (2011) 024906 [`arXiv:1102.1957 [nucl-ex]`].

[43] **ALICE** collaboration, B. Abelev *et. al.*, *Phys. Lett.* **B720** (2013) 52 [`arXiv:1208.2711 [hep-ex]`].

[44] S. A. Voloshin, A. M. Poskanzer and R. Snellings, *Landolt-Bornstein* **23** (2010) 293 [`arXiv:0809.2949 [nucl-ex]`].

[45] A. M. Poskanzer and S. A. Voloshin, *Phys. Rev.* **C58** (1998) 1671 [`arXiv:nucl-ex/9805001 [nucl-ex]`].

[46] **STAR** collaboration, K. H. Ackermann *et. al.*, *Phys. Rev. Lett.* **86** (2001) 402 [`arXiv:nucl-ex/0009011 [nucl-ex]`].

[47] **ALICE** collaboration, K. Aamodt *et. al.*, *Phys. Rev. Lett.* **105** (2010) 252302 [`arXiv:1011.3914 [nucl-ex]`].

[48] C. Gale, S. Jeon, B. Schenke, P. Tribedy and R. Venugopalan, *Phys. Rev. Lett.* **110** (2013)no. 1 012302 [`arXiv:1209.6330 [nucl-th]`].

[49] U. Heinz and R. Snellings, *Ann. Rev. Nucl. Part. Sci.* **63** (2013) 123 [`arXiv:1301.2826 [nucl-th]`].

[50] B. Alver and G. Roland, *Phys. Rev.* **C81** (2010) 054905 [`arXiv:1003.0194 [nucl-th]`]. [Erratum: Phys. Rev.C82,039903(2010)].

[51] J. L. Albacete and C. Marquet, *Prog. Part. Nucl. Phys.* **76** (2014) 1 [`arXiv:1401.4866 [hep-ph]`].

[52] A. Mocsy and P. Sorensen, `arXiv:1008.3381 [hep-ph]`.

[53] P. Staig and E. Shuryak, *Phys. Rev.* **C84** (2011) 034908 [`arXiv:1008.3139 [nucl-th]`].

[54] T. Lappi and L. McLerran, *Nuclear Physics A* **772** (2006)no. 3 200 .

[55] T. Lappi, *Physics Letters B* **643** (2006)no. 1 11 .

[56] A. Dumitru, F. Gelis, L. McLerran and R. Venugopalan, *Nuclear Physics A* **810** (2008)no. 1 91 .

[57] K. Fukushima and F. Gelis, *Nuclear Physics A* **874** (2012) 108 .

[58] F. Gelis, *Int. J. Mod. Phys.* **A28** (2013) 1330001 [`arXiv:1211.3327 [hep-ph]`].

[59] F. Gelis, *Int. J. Mod. Phys.* **E24** (2015)no. 10 1530008 [`arXiv:1508.07974 [hep-ph]`].

[60] A. Kurkela, A. Mazeliauskas, J.-F. Paquet, S. Schlichting and D. Teaney, *Phys. Rev. Lett.* **122** (2019)no. 12 122302 [`arXiv:1805.01604 [hep-ph]`].

[61] M. P. Heller, R. A. Janik and P. Witaszczyk, *Phys. Rev. Lett.* **108** (2012) 201602 [`arXiv:1103.3452 [hep-th]`].

[62] I. Ya. Arefeva and I. V. Volovich, `arXiv:1211.6041 [hep-th]`.

[63] V. Skokov, A. Yu. Illarionov and V. Toneev, *Int. J. Mod. Phys.* **A24** (2009) 5925 [`arXiv:0907.1396 [nucl-th]`].

[64] D. E. Kharzeev, L. D. McLerran and H. J. Warringa, *Nucl. Phys.* **A803** (2008) 227 [`arXiv:0711.0950 [hep-ph]`].

[65] D. E. Kharzeev, J. Liao, S. A. Voloshin and G. Wang, *Prog. Part. Nucl. Phys.* **88** (2016) 1 [`arXiv:1511.04050 [hep-ph]`].

[66] **STAR** collaboration, B. I. Abelev *et. al.*, *Phys. Rev. Lett.* **103** (2009) 251601 [`arXiv:0909.1739 [nucl-ex]`].

[67] **ALICE** collaboration, B. Abelev *et. al.*, *Phys. Rev. Lett.* **110** (2013)no. 1 012301 [`arXiv:1207.0900 [nucl-ex]`].

[68] **STAR** collaboration, L. Adamczyk *et. al.*, *Phys. Rev. Lett.* **113** (2014) 052302 [`arXiv:1404.1433 [nucl-ex]`].

[69] **STAR** collaboration, L. Adamczyk *et. al.*, *Phys. Rev. Lett.* **114** (2015)no. 25 252302 [`arXiv:1504.02175 [nucl-ex]`].

[70] **STAR** collaboration, P. Tribedy, *Nucl. Phys.* **A967** (2017) 740 [`arXiv:1704.03845 [nucl-ex]`].

[71] A. Bzdak, V. Koch and J. Liao, *Phys. Rev.* **C83** (2011) 014905 [`arXiv:1008.4919 [nucl-th]`].

[72] S. Schlichting and S. Pratt, *Phys. Rev.* **C83** (2011) 014913 [`arXiv:1009.4283 [nucl-th]`].

[73] G.-L. Ma and B. Zhang, *Phys. Lett.* **B700** (2011) 39 [`arXiv:1101.1701 [nucl-th]`].

[74] S. A. Voloshin, *Phys. Rev.* **C70** (2004) 057901 [`arXiv:hep-ph/0406311 [hep-ph]`].

[75] A. Bzdak, V. Koch and J. Liao, *Lect. Notes Phys.* **871** (2013) 503 [`arXiv:1207.7327 [nucl-th]`].

[76] F. Wen, J. Bryon, L. Wen and G. Wang, *Chin. Phys.* **C42** (2018)no. 1 014001 [`arXiv:1608.03205 [nucl-th]`].

[77] H.-j. Xu, J. Zhao, X. Wang, H. Li, Z.-W. Lin, C. Shen and F. Wang, *Chin. Phys.* **C42** (2018)no. 8 084103 [`arXiv:1710.07265 [nucl-th]`].

[78] H. Huang *et. al.* in *Proceedings, 9th International Particle Accelerator Conference (IPAC 2018): Vancouver, BC Canada*, p. TUPAF006, 2018.

[79] A. Pich, *Rept. Prog. Phys.* **58** (1995) 563 [`arXiv:hep-ph/9502366 [hep-ph]`].

[80] A. Bazavov *et. al.*, *Phys. Rev.* **D80** (2009) 014504 [`arXiv:0903.4379 [hep-lat]`].

[81] **HotQCD** collaboration, A. Bazavov and P. Petreczky, *J. Phys. Conf. Ser.* **230** (2010) 012014 [`arXiv:1005.1131 [hep-lat]`].

[82] **Wuppertal-Budapest** collaboration, S. Borsanyi, Z. Fodor, C. Hoelbling, S. D. Katz, S. Krieg, C. Ratti and K. K. Szabo, *JHEP* **09** (2010) 073 [`arXiv:1005.3508 [hep-lat]`].

[83] Y. Aoki, S. Borsanyi, S. Durr, Z. Fodor, S. D. Katz, S. Krieg and K. K. Szabo, *JHEP* **06** (2009) 088 [`arXiv:0903.4155 [hep-lat]`].

[84] T. Hell, K. Kashiwa and W. Weise, *Phys. Rev. D* **83** (Jun, 2011) 114008.

[85] F. Lenz, *Lect. Notes Phys.* **659** (2005) 7 [`arXiv:hep-th/0403286 [hep-th]`]. [,7(2001)].

[86] T. Lappi and S. Schlichting, *Phys. Rev.* **D97** (2018)no. 3 034034 [`arXiv:1708.08625 [hep-ph]`].

[87] G. M. Newman, *JHEP* **01** (2006) 158 [`arXiv:hep-ph/0511236 [hep-ph]`].

[88] D. T. Son and P. Surowka, *Phys. Rev. Lett.* **103** (2009) 191601 [`arXiv:0906.5044 [hep-th]`].

[89] A. V. Sadofyev and M. V. Isachenkov, *Phys. Lett.* **B697** (2011) 404 [`arXiv:1010.1550 [hep-th]`].

[90] D. Kharzeev, A. Krasnitz and R. Venugopalan, *Phys. Lett.* **B545** (2002) 298 [`arXiv:hep-ph/0109253 [hep-ph]`].

[91] M. Mace, S. Schlichting and R. Venugopalan, *Phys. Rev.* **D93** (2016)no. 7 074036 [`arXiv:1601.07342 [hep-ph]`].

[92] A. Kovner, L. D. McLerran and H. Weigert, *Phys. Rev.* **D52** (1995) 6231 [`arXiv:hep-ph/9502289 [hep-ph]`].

[93] A. Kovner, L. D. McLerran and H. Weigert, *Phys. Rev.* **D52** (1995) 3809 [`arXiv:hep-ph/9505320 [hep-ph]`].

[94] E. Iancu, A. Leonidov and L. D. McLerran, *Nucl. Phys.* **A692** (2001) 583 [`arXiv:hep-ph/0011241 [hep-ph]`].

[95] J. P. Blaizot, F. Gelis and R. Venugopalan, *Nucl. Phys.* **A743** (2004) 13 [`arXiv:hep-ph/0402256 [hep-ph]`].

[96] E. Iancu, K. Itakura and L. McLerran, *Nucl. Phys.* **A724** (2003) 181 [`arXiv:hep-ph/0212123 [hep-ph]`].

[97] R. J. Fries, J. I. Kapusta and Y. Li, `arXiv:nucl-th/0604054 [nucl-th]`.

[98] G. Chen, R. J. Fries, J. I. Kapusta and Y. Li, *Phys. Rev.* **C92** (2015)no. 6 064912 [`arXiv:1507.03524 [nucl-th]`].

[99] C. S. Lam and G. Mahlon, *Phys. Rev.* **D61** (2000) 014005 [`arXiv:hep-ph/9907281 [hep-ph]`].

[100] H. Fujii, F. Gelis and R. Venugopalan, *Nucl. Phys.* **A780** (2006) 146 [`arXiv:hep-ph/0603099 [hep-ph]`].

[101] C. Marquet, *Nucl. Phys.* **A796** (2007) 41 [`arXiv:0708.0231 [hep-ph]`].

[102] C. Marquet and H. Weigert, *Nucl. Phys.* **A843** (2010) 68 [`arXiv:1003.0813 [hep-ph]`].

[103] K. Fukushima and Y. Hidaka, *JHEP* **06** (2007) 040 [`arXiv:0704.2806 [hep-ph]`].

[104] F. Fillion-Gourdeau and S. Jeon, *Phys. Rev.* **C79** (2009) 025204 [`arXiv:0808.2154 [hep-ph]`].

[105] A. Kovner and U. A. Wiedemann, *Phys. Rev.* **D64** (2001) 114002 [`arXiv:hep-ph/0106240 [hep-ph]`].

[106] P. Dittner, *Commun. Math. Phys.* **22** (1971) 238.

[107] R. Mertig, M. Bohm and A. Denner, *Comput. Phys. Commun.* **64** (1991) 345.

[108] V. Shtabovenko, R. Mertig and F. Orellana, *Comput. Phys. Commun.* **207** (2016) 432 [`arXiv:1601.01167 [hep-ph]`].

[109] A. Dumitru, K. Dusling, F. Gelis, J. Jalilian-Marian, T. Lappi and R. Venugopalan, *Phys. Lett.* **B697** (2011) 21 [`arXiv:1009.5295 [hep-ph]`].

[110] K. Dusling and R. Venugopalan, *Phys. Rev. Lett.* **108** (Jun, 2012) 262001.

[111] K. Dusling and R. Venugopalan, *Phys. Rev.* **D87** (2013)no. 5 054014 [`arXiv:1211.3701 [hep-ph]`].

[112] K. Dusling and R. Venugopalan, *Phys. Rev.* **D87** (2013)no. 9 094034 [`arXiv:1302.7018 [hep-ph]`].

[113] A. Dumitru, F. Gelis, L. McLerran and R. Venugopalan, *Nucl. Phys.* **A810** (2008) 91 [`arXiv:0804.3858 [hep-ph]`].

[114] S. Gavin, L. McLerran and G. Moschelli, *Phys. Rev.* **C79** (2009) 051902 [`arXiv:0806.4718 [nucl-th]`].

[115] K. Dusling, D. Fernandez-Fraile and R. Venugopalan, *Nucl. Phys.* **A828** (2009) 161 [`arXiv:0902.4435 [nucl-th]`].

[116] F. Gelis, T. Lappi and L. McLerran, *Nucl. Phys.* **A828** (2009) 149 [`arXiv:0905.3234 [hep-ph]`].

[117] K. Dusling, F. Gelis, T. Lappi and R. Venugopalan, *Nucl. Phys.* **A836** (2010) 159 [`arXiv:0911.2720 [hep-ph]`].

[118] T. Lappi and S. Schlichting, *Phys. Rev. D* **97** (Feb, 2018) 034034.

[119] T. Lappi, S. Srednyak and R. Venugopalan, *JHEP* **01** (2010) 066 [`arXiv:0911.2068 [hep-ph]`].

[120] J. E. Bernhard, J. S. Moreland, S. A. Bass, J. Liu and U. Heinz, *Phys. Rev. C* **94** (Aug, 2016) 024907.

[121] S. Floerchinger and U. A. Wiedemann, *Phys. Rev. C* **88** (Oct, 2013) 044906.

[122] S. Floerchinger and U. A. Wiedemann, *Physics Letters B* **728** (2014) 407 .

[123] K. J. Golec-Biernat and M. Wusthoff, *Phys. Rev.* **D59** (1998) 014017 [`arXiv:hep-ph/9807513 [hep-ph]`].

[124] E. Iancu, K. Itakura and S. Munier, *Phys. Lett.* **B590** (2004) 199 [`arXiv:hep-ph/0310338 [hep-ph]`].

[125] J. L. Albacete, N. Armesto, J. G. Milhano, C. A. Salgado and U. A. Wiedemann, *Eur. Phys. J.* **C43** (2005) 353 [`arXiv:hep-ph/0502167 [hep-ph]`].

[126] Y. V. Kovchegov and K. Tuchin, *Phys. Rev.* **D65** (2002) 074026 [`arXiv:hep-ph/0111362 [hep-ph]`].

[127] A. Dumitru, A. Hayashigaki and J. Jalilian-Marian, *Nucl. Phys.* **A765** (2006) 464 [`arXiv:hep-ph/0506308 [hep-ph]`].

[128] J. L. Albacete, N. Armesto, J. G. Milhano and C. A. Salgado, *Phys. Rev.* **D80** (2009) 034031 [`arXiv:0902.1112 [hep-ph]`].

[129] J. L. Albacete, N. Armesto, J. G. Milhano, P. Quiroga-Arias and C. A. Salgado, *Eur.Phys.J.* **C71** (2011) 1705 [`arXiv:1012.4408 [hep-ph]`].

[130] Y. Kovchegov and H. Weigert, *Nucl. Phys.* **A 784** (2007) 188 [`arXiv:hep-ph/0609090`].

[131] I. I. Balitsky, *Phys. Rev. D* **75** (2007) 014001 [`arXiv:hep-ph/0609105`].

[132] J. L. Albacete and Y. V. Kovchegov, *Phys. Rev.* **D75** (2007) 125021 [`arXiv:arXiv:0704.0612 [hep-ph]`].

[133] J. L. Albacete and A. Dumitru, `arXiv:1011.5161 [hep-ph]`.

[134] **H1, ZEUS** collaboration, F. D. Aaron *et. al.*, *JHEP* **01** (2010) 109 [`arXiv:0911.0884 [hep-ex]`].

[135] J. Pumplin *et. al.*, *JHEP* **07** (2002) 012 [`arXiv:hep-ph/0201195`].

[136] T. Altinoluk, N. Armesto, G. Beuf, A. Kovner and M. Lublinsky, *Phys. Rev.* **D91** (2015)no. 9 094016 [`arXiv:1411.2869 [hep-ph]`].

[137] G. A. Chirilli, B.-W. Xiao and F. Yuan, *Phys.Rev.* **D86** (2012) 054005 [`arXiv:1203.6139 [hep-ph]`].

[138] I. Balitsky and G. A. Chirilli, *Phys. Rev.* **D77** (2008) 014019 [`arXiv:0710.4330 [hep-ph]`].

[139] I. Balitsky and G. A. Chirilli, *Phys. Rev.* **D88** (2013) 111501 [`arXiv:1309.7644 [hep-ph]`].

[140] J. L. Albacete, A. Dumitru, H. Fujii and Y. Nara, *Nucl.Phys.* **A897** (2013) 1 [`arXiv:1209.2001 [hep-ph]`].

[141] A. M. Stasto, B.-W. Xiao and D. Zaslavsky, *Phys.Rev.Lett.* **112** (2014)no. 1 012302 [`arXiv:1307.4057 [hep-ph]`].

[142] T. Lappi and H. Mäntysaari, *Phys.Rev.* **D91** (2015)no. 7 074016 [`arXiv:1502.02400 [hep-ph]`].

[143] E. Iancu, J. Madrigal, A. Mueller, G. Soyez and D. Triantafyllopoulos, *Phys.Lett.* **B744** (2015) 293 [`arXiv:1502.05642 [hep-ph]`].

[144] T. Lappi and H. Mäntysaari, `arXiv:1601.06598 [hep-ph]`.

[145] J. L. Albacete, `arXiv:1507.07120 [hep-ph]`.

[146] E. Iancu, J. D. Madrigal, A. H. Mueller, G. Soyez and D. N. Triantafyllopoulos, *Phys. Lett.* **B750** (2015) 643 [`arXiv:1507.03651 [hep-ph]`].

[147] B. Ducloué, T. Lappi and Y. Zhu, `arXiv:1604.00225 [hep-ph]`.

[148] J. M. Butterworth, J. R. Forshaw and M. H. Seymour, *Z. Phys.* **C72** (1996) 637 [`arXiv:hep-ph/9601371 [hep-ph]`].

[149] L. Durand and P. Hong, *Phys. Rev. Lett.* **58** (Jan, 1987) 303.

[150] L. Durand and H. Pi, *Phys. Rev. D* **40** (Sep, 1989) 1436.

[151] B. Z. Kopeliovich, *Phys. Rev.* **C68** (2003) 044906 [`arXiv:nucl-th/0306044 [nucl-th]`].

[152] **CMS** collaboration, V. Khachatryan *et. al.*, `arXiv:1509.03893 [hep-ex]`.

[153] J. L. Albacete and C. Marquet, *Phys. Lett.* **B687** (2010) 174 [`arXiv:1001.1378 [hep-ph]`].

[154] T. Sjostrand, S. Mrenna and P. Z. Skands, *JHEP* **05** (2006) 026 [`arXiv:hep-ph/0603175 [hep-ph]`].

[155] T. Sjostrand, S. Mrenna and P. Z. Skands, *Comput. Phys. Commun.* **178** (2008) 852 [`arXiv:0710.3820 [hep-ph]`].

[156] W.-T. Deng, H. Fujii, K. Itakura and Y. Nara, *Phys. Rev.* **D91** (2015)no. 1 014006 [`arXiv:1410.2018 [hep-ph]`].

[157] **BRAHMS** collaboration, I. Arsene *et. al.*, *Phys. Rev. Lett.* **93** (2004) 242303 [`arXiv:nucl-ex/0403005`].

[158] **STAR** collaboration, J. Adams *et. al.*, *Phys. Rev. Lett.* **97** (2006) 152302 [`arXiv:nucl-ex/0602011`].

[159] J. Jalilian-Marian and A. H. Rezaeian, *Phys.Rev.* **D85** (2012) 014017 [`arXiv:1110.2810 [hep-ph]`].

[160] **LHCf** collaboration, O. Adriani *et. al.*, `arXiv:1507.08764 [hep-ex]`.

[161] R. Ulrich, R. Engel, S. Muller, T. Pierog, F. Schussler and M. Unger, `arXiv:0906.0418 [astro-ph.HE]`.

[162] G. Chen, R. J. Fries, J. I. Kapusta and Y. Li, *Phys. Rev. C* **92** (Dec, 2015) 064912.

[163] H. Fujii, K. Fukushima and Y. Hidaka, *Phys. Rev.* **C79** (2009) 024909 [`arXiv:0811.0437 [hep-ph]`].

List of Abbreviations

AAMQS	Albacete-Armesto-Milhano-Quiroga-Salgado
AdS	Anti-de Sitter
B-JIMWLK	Balitsky-Jalilian-Marian-Iancu-McLerran-Weigert-Leonidov -Kovner
BFKL	Balitsky-Fadin-Kuraev-Lipatov
BK	Balitsky-Kovchegov
BRAHMS	Broad Range Hadron Magnetic Spectrometers
CFT	Conformal Field Theory
CG	Clebsch-Gordan
CGC	Color Glass Condensate
CME	Chiral Magnetic Effect
CP	Charge-Parity
DESY	Deutsches Elektronen-Synchrotron
DGLAP	Dokshitzer-Gribov-Lipatov-Altarelli-Parisi
DHJ	Dumitru-Hayashigaki-Jalilian-Marian
DIS	Deep Inelastic Scattering
DLA	Double Logarithmic Approximation
EMT	Energy-Momentum Tensor
GBW	Golec-Biernat-Wüsthoff
HERA	Hadron-Electron Ring Accelerator
HIC	Heavy Ion Collision
IMF	Infinite Momentum Frame
LHC	Large Hadron Collider
LLA	Leading Logarithm Approximation
MIT	Massachusetts Institute of Technology
MV	McLerran-Venugopalan
NLO	Next-to-Leading Order
NNLO	Next-to-Next-to-Leading Order
PDF	Parton Distribution Function
PNJL	Polyakov-Nambu-Jona-Lasini
QCD	Quantum Chromodynamics
QED	Quantum Electrodynamics
QGP	Quark Gluon Plasma
RHIC	Relativistic Heavy Ion Collider
rcBK	running coupling Balitsky-Kovchegov
SLAC	Stanford Linear Accelerator Center
STAR	Solenoidal Tracker at RHIC
SPS	Super Proton Synchrotron
uGD	unintegrated Gluon Distribution
UHECR	Ultra-High Energy Cosmic Rays